Title
Engineered Transport in Microporous Membranes for Clean Energy Technologies

Author
Li, Changyi

Publication Date
2015

Engineered Transport in Microporous Membranes for Clean Energy Technologies

By

Changyi Li

A dissertation submitted in partial satisfaction of the

Requirements for the degree of

Doctor of Philosophy

in

Chemical Engineering

in the

Graduate Division

of the

University of California, Berkeley

Committee in charge:

Dr. Brett A. Helms, Co-Chair
Prof. Susan J. Muller, Co-Chair
Prof. Nitash P. Balsara
Prof. Matthew B. Francis

Fall 2015

Engineered Transport in Microporous Membranes for Clean Energy Technologies

by

Changyi Li

Abstract

Engineered Transport in Microporous Membranes for Clean Energy Technologies

By

Changyi Li

Doctor of Philosophy in Chemical Engineering

University of California, Berkeley

Dr. Brett A. Helms, Co-Chair

Professor Susan J. Muller, Co-Chair

Selective transport is a key component in many cutting edge clean technologies, including reverse osmosis, carbon capture and energy storage. At the center of these processes there is typically a membrane that preferentially selects for one of the constituents in the analyte mixture, at a fraction of the cost of the status quo technologies financially and energetically. The rapid developments of new classes of microporous materials within the last two decades have yielded a vast arsenal of building blocks poised to make an impact on membrane separation. Sporting pores that are less than 2 nm in size and approaching or commensurate with the molecular dimensions, microporous materials are capable of selecting for molecules based on sizes and shapes, and affecting transport by confinement. As a result, in many cases, properly designed molecular sieves can markedly improve both the selectivity and flux of the parent membrane. In this dissertation, I aim to discuss three classes of microporous materials – cyclic peptide nanotubes (CPNs), metal-organic frameworks (MOFs), and polymers of intrinsic microporosity (PIMs). Specifically I will elaborate upon the synthetic strategies to access interior functionalized CPNs and MOFs from metal oxide precursors; membrane fabrication involving MOFs and PIMs; and PIM membrane performance as applied to Li-S batteries. Using materials chemistry to precisely design and apply microporous molecular sieves, the work presented here spans the realms of both ion and gas selective transport, and technologies such as carbon capture and energy storage. At the same time I intend to offer a new general perspective on membrane component design.

Engineered Transport in Microporous Membranes for Clean Energy Technologies

Table of Contents

Acknowledgement

I would like to express my sincere gratitude for the support from family, friends and colleagues through the past arduous five and a half years. Thank you for being there for me through the good times and the bad.

First I would like to thank Dr. Brett Helms for his generous support throughout the latter half of my PhD career. I would not be writing this dissertation were it not for his willingness to take me on when my graduate career hit a bump on the road. Secondly I would like to thank Prof. Susan Muller for offering personal guidance through the maze that is graduate school, and for being the kindest spirit I have met in Berkeley. I would also like to thank Prof. Ting Xu for opening my eyes to the reality of research and academia in general and for giving me the opportunity to work in her lab. Prof. Sunney I. Chan has also given me many personal advices during my graduate career and I greatly appreciate his mentorship and friendship.

I have met many wonderful colleagues along the way. I am forever grateful for the friendship of Rami Hourani, Kari Thorkelsson, Ben Rancatore, Joseph Kao, Peter Bai from Ting's group, and Sean Doris, Stephen Meckler, Ashleigh Ward, Laura Gerber, Pete Frischmann, Andy Wills, Lorenzo Maserati from the Helms' Group, Andrew Pun, David Hanifi from Yi's lab. The many wonderful people I have met at the Molecular Foundry, at the LBNL Machine Shop, and within the Chemical and Biomolecular Engineering department at UC Berkeley, have all been very kind to me. I would also like to thank my many college friends who were there when I needed an escape from the day-to-day of scientific research.

Last but not least I would like to thank my parents, Junxian Zhang and Weiping Li. Without the personal sacrifices they have made, I would certainly not be wandering the halls of UC Berkeley and Caltech, and not be able to realize my full potentials. I owe all of my accomplishments and successes to them.

Chapter 1

Introduction

Introduction

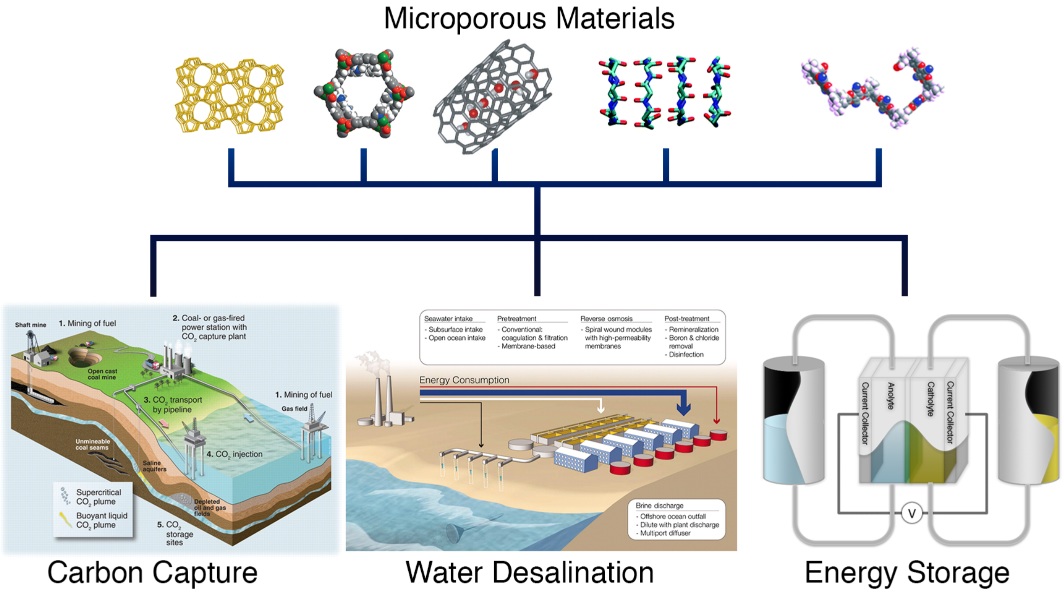

Figure 1.1 Microporous materials are leading a revolution in clean energy technologies: e.g., carbon capture[1], water desalination[2] and energy storage. Microporous membrane components span zeolites[3], MOFs[4], carbon nanotubes[5], organic nanotubes[6] and intrinsically microporous polymers[7]. The images are adapted with permission from the cited references. The carbon capture image is from R. S. Haszeldine, *Science*, 2009, **325**, 1647–1652. Reprinted with permission from AAAS. The water desalination image is from M. Elimelech and W. A. Phillip, *Science*, 2011, **333**, 712–717. Reprinted with permission from AAAS. The MOF image is reprinted by permission from Macmillan Publishers Ltd: *Nature,* **519,** 303–308 (2015), copyright 2015. The carbon nanotube image is reprinted by permission from Macmillan Publishers Ltd: *Nature* **414,** 188–190 (2001), copyright 2001. The organic nanotube image is reproduced in part from Ref 6 with permission of The Royal Society of Chemistry. The microporous polymer image is reproduced in part from Ref 7) with permission of The Royal Society of Chemistry.

Improving the efficiency of membrane-based separations is critical to the advancement of many clean energy technologies—including gas separations, carbon capture and sequestration (CCS), water desalination, dehumidification, and electrochemical energy storage (EES) (**Figure 1.1**). Schemes to engineer highly selective species transport across microporous membranes have progressed considerably in the past decade, in particular due to the advent of microporous membrane components with controlled pore architectures and pore chemistries. In contrast to conventional absorptive or adsorptive strategies, which often require energy-intensive regeneration procedures, microporous membranes can achieve high fluxes of the desired permeant at markedly lower energetic costs and can often be implemented in a continuous process.

Microporous membrane components considered here feature persistent free volume elements that discriminate between analytes primarily based on size, although there are cases where chemoselective recognition and transport can be conferred. In that the free volume elements of these materials are commensurate with the dimensions of molecules, microporous materials are also referred to as molecular sieves.

Microporous (or molecular sieve) membranes can either be single component or composites of several materials, of which at least one is microporous. With their rigid structures enforcing size-selectivity, lower framework mobility is expected. Therefore the motion of the microporous materials does not directly mediate the transport of analytes. As a result, the transport selectivity and flux can be decoupled from the mechanical robustness, allowing for independent optimization of the membrane's performance attributes.

The primary classes of molecular-sieving materials are: (1) microporous inorganics (e.g., zeolites[8,9]); (2) hybrids (e.g., metal-organic frameworks[10–12]), (3) microporous carbons (e.g., carbon nanotubes[13], carbon molecular sieves[14]); and (4) microporous organics (e.g., microporous polymers[15,16], organic nanotubes[17]). While significant attention has been given to molecular-sieving materials with exceptionally high surface areas as adsorbates[18] and catalysts[19–21], here we will discuss how their unique architectures impact transport selectivity and conductivity for gases, liquids, and ions). Furthermore, we will address how transport outcomes are affected by both nano-confinement within the materials' free volume and pore-analyte interactions. The emerging perspective, regardless of the type of transport process, is that the unique shape-persistent architectures of these materials permit molecular diffusive permeabilities as fast as or even exceeding bulk kinetics while forbidding the passage of other components of the analyte mixture.

Microporous Materials with Controlled Pore Architectures and Pore Chemistries

Zeolites and Related Inorganic Molecular Sieves

Zeolites are microporous aluminosilicate framework solids[22,23] that exhibit well-ordered and periodic arrangements of matter and empty space. They were the first reported molecular-sieving materials. Since then, related inorganic molecular sieves have included silicalites[24], metallosilicates[25,26], and metallophosphates[27–30]. Though discovered in the 1700s[31], zeolites did not find widespread industrial use for nearly two centuries[32,33]. Today, hundreds of zeolites are available with uniform pore sizes ranging from 3 Å to 1 nm. The strict size and shape selectivity[34] have not only made them ideal molecular sieves for selective transport, but also lead to their broad adoption as adsorbates[35] and catalysts[36,37,21]. Typical zeolite syntheses are carried out under hydrothermal conditions using silicates and aluminates. Variation of temperature, cations, reaction time, pH, among other parameters dictate framework outcomes[33]. Typically, the chemical make-up determines the structure of the zeolites. Occasionally minor pore size adjustments are possible. For instance, zeolite 3A, 4A and 5A are all derived from Zeolite A and incorporate different guest counterions: K^+, Na^+ and Ca^+, respectively[38–40]. Membrane incorporation could take the form of a solid dispersion or in situ synthesis on membrane by way of seeded growth[41].

Metal-Organic Frameworks

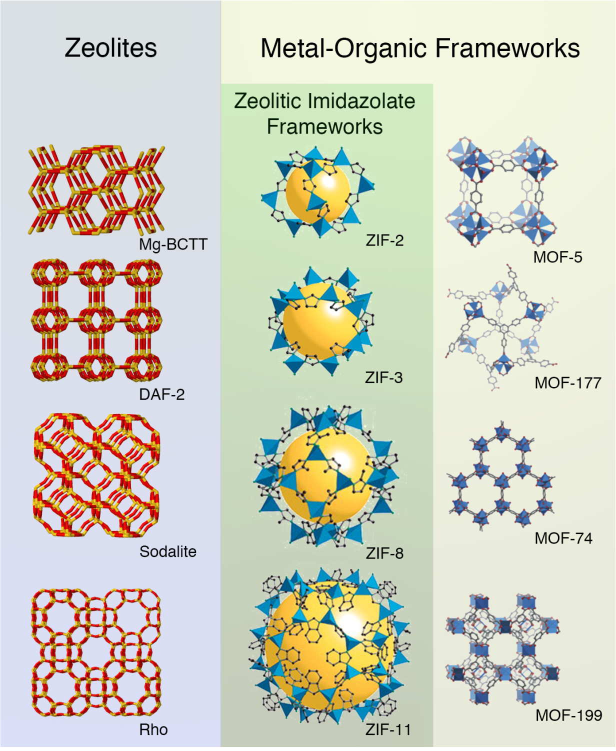

Figure 1.2 The variety of structures that MOFs[42] and zeolites[3] afford. ZIFs[43] and their isormorphic counterpart zeolites are listed together for comparison. The images are adapted with permission from the cited references. The MOF structures are reprinted from *Tetrahedron*, Vol 64, Tranchemontagne, D. J.; Hunt, J. R.; Yaghi, O. M., Room temperature synthesis of metal-organic frameworks: MOF-5, MOF-74, MOF-177, MOF-199, and IRMOF-0, 8553-8557, Copyright 2008, with permission from Elsevier. The ZIF structures are reproduced from Ref 43. Copyright 2006 National Academy of Sciences, USA.

Metal-Organic Frameworks[44], or MOFs, are hybrid microporous materials; MOFs are also referred to as porous coordination polymers (PCPs)[45]. Similar to zeolites, MOFs are made up of connected nodes in a periodic fashion. There are two types of building blocks, or secondary building units (SBUs)—metal-containing SBUs, and organic SBUs. The metal-containing SBUs, which could be a metal ion or a cluster containing multiple metal and other atoms, act as nodes that are connected by polytopic organic SBU linkers. In addition to forming architectural topologies that are isomorphic to zeolites at an expanded scale (as is the case with zeolitic imidazolate frameworks, or ZIFs[43]), organic SBU linkers can be designed to yield MOFs of more exotic nets[46,47] (**Figure 1.2**). MOF syntheses typically proceed under hydrothermal conditions or microwave irradiation[10,11,48,49]. Like zeolites, MOFs feature periodic arrangements of micropores, or in some instances mesopores, depending on the organic linker. They are also amenable to post-synthetic modifications to fine-tune interactions with analytes[50,51]. The diversity of architectures in this class of microporous materials is remarkable, with examples pushing the bounds of surface area (up to 7000 m_2/g [52]) and porosity (up to 90% [53]). MOFs can now adsorb and facilitate reactions for molecules that have been too bulky for zeolites and other inorganic molecular sieves; and SBUs, can be engineered synergistically to mediate interactions with analytes within the micropores[54,55]. These properties have been exploited for gas storage/adsorption[56,57], catalysis[19], sensing[58], and other types of selective transport[59,60].

Replacing the metal centers in MOFs with polytopic organic moieties yields covalent organic frameworks or COFs, e.g., as pioneered by Yaghi et al.[61] COFs have since attracted much attention; however they have not been used extensively in selective transport. Nonetheless, COFs have found early successes in gas storage[62] and electronic charge storage[63,64]. Interested readers are directed to the relevant reviews in the literature on those topics[65,66].

Carbon Nanostructures

Carbon nanotubes are a mainstay of nanoscience and nanotechnology[67].[68] They exhibit unique electrical[69,70], thermal and mechanical[71] properties, and are also a molecular-sieving material in their own right. Catalysts, precursors, and process conditions can be tuned to control nanotube diameters, either as single-walled or multi-walled nanostructures[72,73]. While a variety of routes have been reported to modify carbon nanotubes on the exterior or the openings,[74,75],[76] there are as yet no strategies to functionalize their interior space. Instead, they remain a continuous and atomically smooth hydrophobic surface that is capable of promoting faster-than-bulk, frictionless kinetics[77] via specular reflection of the molecules. In addition to having a confined geometry for molecular sieving, carbon nanotubes also have shown promise in chemically distinguishing between analytes, ranging from ions[78] to macromolecules[79].

Whereas carbon nanotubes are exemplars of 1-D microporous carbon nanostructures, carbon molecular sieves are 3-D. By pyrolizing a polymer precursor, microporous carbonaceous architectures emerge with high surface area, small pores (< 1 nm) and narrow pore-size distributions[80,81]. Most carbon molecular sieves are derived from polyimides[82–84], such as Matrimid®[85,86] or Kapton®[80,85,87]. Other polymer precursors have included poly(furfuryl alcohol)[88,89], phenol-based resins[90] and poly(vinyl chloride) copolymers[91]. Both precursor chain packing and pyrolizing procedure influence the final micropore architecture[92–94]. Unlike zeolites or MOFs, however, these shape-persistent microporous materials are random arrangements of matter and empty space. Through the stochastic stacking, the microvoids enable molecular sieving in membranes tailored for gas separations[14,95].

Organic Nanotubes

Organic nanotubes are, like carbon nanotubes, prototypical microporous 1-D nanostructures. Unlike carbon nanotubes, however, they are assembled from molecular components—either from wedges with directed supramolecular interactions (e.g., dendrimers[96], and guanosine quartets and their related analogues[97], etc) or from discrete macrocycles (e.g., arylene ethynylenes[98] or cyclic peptides[99]). This is achieved through non-covalent interactions, such as π-π stacking or hydrogen bonding. The structural diversity of organic nanotubes is vast. The size of their aperture can range from ~Å to ~nm, which is subject to precise synthetic control; the length of organic nanotubes, on the other hand, depends strongly on the strength of the non-covalent interactions and the assembly strategy. Uniquely, both their exteriors and interiors[100,101] can be modified with chemical functionality to enhance transport selectivity. Not surprisingly then, advances in synthetic methods have thus far focused on understanding these molecular structure–transport selectivity relationships, rather than on practical aspects associated with scale-up as might be required for membrane-based separations. In some instances, organic nanotubes benefit from exterior functionalization to align the nanotubes within a matrix (e.g., a mesostructured block copolymer film). This allows for facile membrane casting from solution. Owing to their ability to regulate transport, organic nanotubes have been explored as transmembrane protein analogues[102,103]. Aside from bio-inspired applications, they have also found use as sensors[104].

Microporous Polymers

In organic polymers, micropores naturally arise from imperfect packing. Synthetic polymers intrinsically possess a distribution of chain lengths and as a result have a substantive fractional free volume. Whereas conventional polymers have dynamic microporosity due to thermally-activated segmental chain motions, in recent years, researchers have engineered void-forming elements at the molecular level to deliberately both reduce segmental chain dynamics and induce a higher degree of microporosity. For microporous organic polymers (MOPs) such as poly(trimethylsilyl propyne) (PTMSP), 34% free fractional volume[105] has been reported. PTMSP features a bulky trimethylsilane group onto the backbone while maintaining a rigid sp2 hybridized carbon main chain. Likewise, polymers of intrinsic microporosity (PIMs) achieve high fractional free volume by introducing kinks into an otherwise rigid polymer backbone, which results in frustrated chain packing in the solid state[106] (**Figure 1.3**). For PIM-1, the free fractional volume approaches 20%, and consists primarily of micropores[107] (**Figure 1.4**). Conjugated microporous polymers (CMPs) generate porosity via a similar principle of maintaining rigidity to disrupt packing. For polymers that are considered dense, there are generally two ways to introduce porosity chemically—reductive or additive. The reductive strategy is more prevalent, and yields free volume elements through triggered rearrangement or loss of chemical moieties appended to the polymer. Thermally-rearranged (TR) polymers[108] accomplish microporosity often in a two-step process: first, monomers are polymerized into a processable precursor material; second, a thermal treatment is applied, which activates contracting rearrangement or partial decomposition of the pre-polymer, revealing the micropores (**Figure 1.3**). Carbon molecular sieves can be considered as an extreme of this case. The additive path, on the other hand, creates voids by chemically wedging spacers between polymer chains, often accomplished by crosslinking[109] (e.g., hyper-crosslinked polymers, or HCPs). In general, these polymers are processible in their non-crosslinked forms as large-area, flexible films. They often serve as highly permeable matrix for composites incorporating other molecular-sieving components. The ease of processing and low cost of these microporous polymers has led to the pervasive adoption of these materials across many technology areas, including gas separation[106,108,110], desalination[111], energy storage[107].

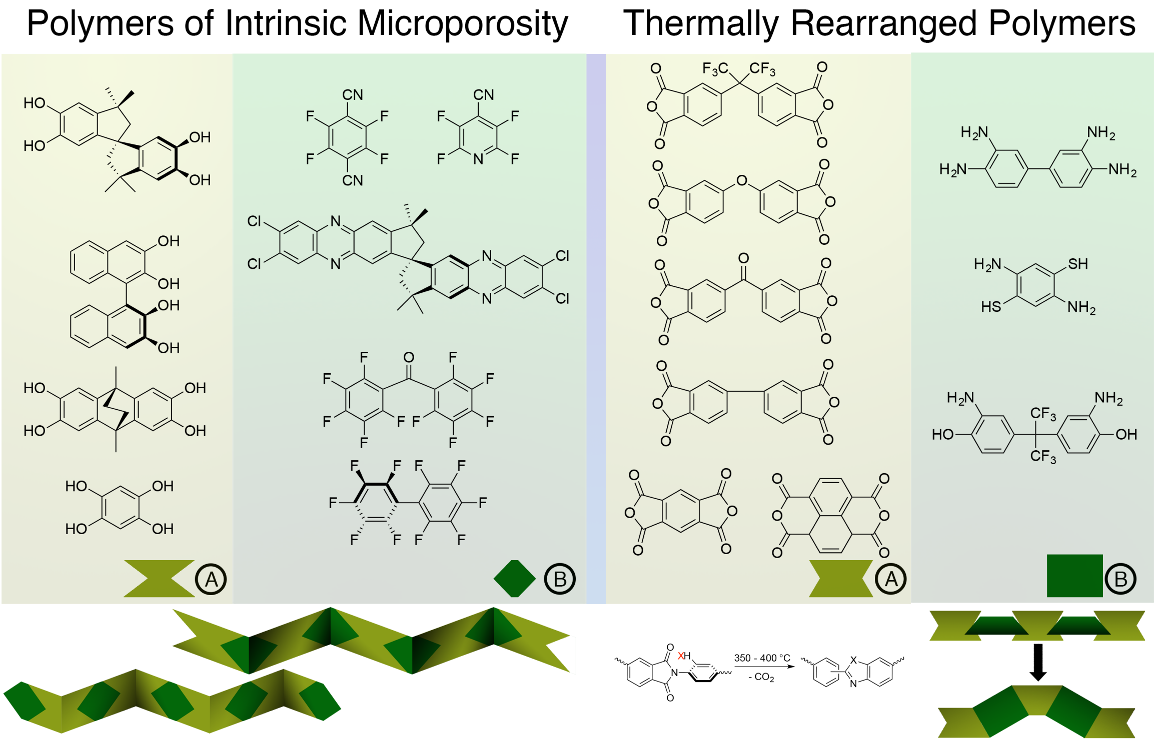

Figure 1.3 A selection of building blocks for polymers of intrinsic microporosity (PIMs)[16] and thermally rearranged polymers (TRs)[112]. PIMs incur porosity by having a tortuous structure, leading to frustrated packing. TRs incur porosity by post-

polymerization rearrangement. The PIM monomer structures are reproduced from Ref 16 with permission of The Royal Society of Chemistry. The TR monomer structures are reproduced from Ref 112 with permission of The Royal Society of Chemistry.

Selective Transport Properties Relevant to Clean Energy Technologies

Gas Transport – Carbon Capture

Permselective gas transport by microporous materials is being exploited for more efficient processes in hydrocarbon processing[113]. With looming concern over global climate change brought about by excessive emission of greenhouse gases, carbon capture and sequestration, the process by which atmospheric carbon dioxide is collected and pressurized underground, has become a major driving-force for membrane development. The incumbent CO_2-scrubbing technology implements aqueous solutions of aminoalcohols to capture carbon dioxide from flue gas streams[114]. Regeneration proceeds thermally, which is energy-intensive; up to 30% of the power output of the plant may be required to do so[115]. Gas separation membranes present a more cost-effective solution. This alternative technology landscape is dominated by polymeric and composite membranes due to their ease of processing. The widely accepted mechanism for gas transport through polymeric membranes is solution-diffusion[116]. Here micropores open and close according to thermally-activated segmental chain motions, which allows for random hopping of gas molecules from one free volume element to the next. Implicit to this description is a trade-off between selectivity and permeability, noted empirically by Robeson[110,117]. A simple mathematical argument presented by Freeman et al. more rigorously accounts for this phenomenon[118] where different transport regimes manifest based on pore sizes and pore geometries[119], which give rise to membrane permselectivity.

Single-Component Systems – Microporous Polymers and Carbon

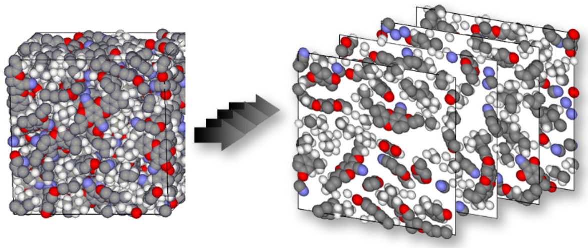

Figure 1.4 The simulated frustrated polymer chain packing of PIM-1 and the formation of the micropores[120]. The cross sectional cuts of the simulation volume (left) are shown on the right, explicitly revealing the micropores at each plane. Reprinted from *Journal of Membrane Science*, Vol 318, Heuchel, M.; Fritsch, D; Budd, P. M.; McKeown, N. B.; Hofmann, D., Atomistic packing model and free volume distribution of a polymer with intrinsic microporosity (PIM-1), 84-99, Copyright 2008, with permission from Elsevier.

In contrast to dense polymer membranes with transient micropores, polymer membranes with permanent micropores have achieved greater success in improving the separation efficiency for several industrially-relevant gas pairs. PIMs are particularly noteworthy in this regard (i.e., as upper-bound membrane materials). Since the mobility of the polymer backbone is not the limiting kinetic process in mediating gas transport, the optimization of the membrane in turn calls for the rigidification of the backbone, to the point of minimizing the number of rotatable bonds. PIMs have evolved from ladder polymers, bearing both spiro centers and mostly aromatic backbone[121], to rigid polymers that are fully constrained and decorated with bulky groups[122–124]. PIMs have demonstrated superior performance in separating CO_2/CH_4 and other gas pairs[125–128]: methanol-treated PIM-1 membranes have demonstrated CO_2-permeability as high as 11200 Barrer[129]. Moreover, tetrazolate derivatives of PIM-1—TZPIM-1 and TZPIM-2—offer CO_2/N_2 selectivity approaching 30 [127]. PIMs are likely to continue to push the bounds of the Robeson permeability-selectivity trade-off[7,16,112,130] (**Figure 1.5**).

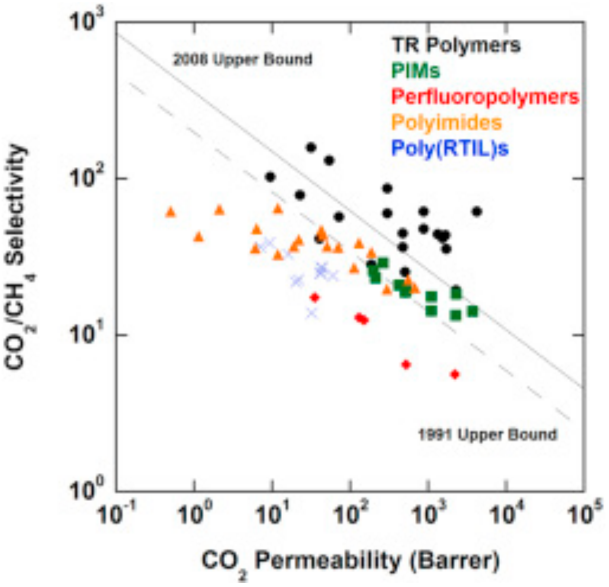

Figure 1.5 Robeson's plot for the CO_2/CH_4 gas pair[131]. The molecular sieving polymers are close to and exceeding the 2008 upper bound, outperforming traditional dense polymer membranes. Reprinted from *Polymer*, Vol 54, Sanders, D. F.; Smith, Z. P.; Guo, R.; Robeson, L. M.; McGrath, J. E.; Paul, D. R.; Freeman, B. D., Energy-efficient polymeric gas separation membranes for a sustainable future: A review, 4729-4761, Copyright 2013, with permission from Elsevier.

Thermally rearranged polymers have also found success in improving the efficiency of gas separations. Since their discovery in 2007[108], thermally-rearranged polymers exceeded the empirical upper-bound for the CO_2/CH_4 gas pair[110] (**Figure 1.5**). Similar to PIMs, thermally rearranged polymers can be diversified and optimized through molecular design principles. However, whereas PIM micropores are tuned by disrupting chain packing, thermally rearranged polymers are rendered microporous through an intramolecular rearrangement. As a result, they have a tighter pore-size distribution and smaller pores overall[132]. Soluble polymer precursors enabled solution-processing for what would otherwise be very rigid and insoluble aromatic polymers after thermal rearrangement[132]. Again, through rigidification, an amorphous dense polymer can exhibit high selectivity (CO_2/CH_4 selectivity as high as 58 and >30 CO_2/N_2 selectivity[132]) and high permeability (CO_2 permeability as much as 6000 Barrer[133]). Other microporous polymers such as conjugated microporous polymers[134–136] have achieved some success as well and the readers are directed to the relevant reviews for more detailed discussions.

Carbon molecular sieve membranes, sometimes referred to simply as carbon membranes, have been investigated for selective gas separations since the 1980s[88]. Though derived from a polymeric precursor, the carbon molecular sieve membranes boast performance metrics that exceed the polymer membrane upper-bound. By virtue of being molecular sieves, solution-diffusion no longer applies and transport permselectivity is not limited by polymer motion. This is evident in the improved permeability and selectivity seen in the pyrolized membrane compared to its precursor membrane[137,138]. A broader selection of materials and their application in gas separations can be found in recent reviews[14,95,139].

Multicomponent Systems – Composite Membranes

There are now countless examples where microporous molecular-sieving components have been incorporated into an external matrix, often polymeric, to facilitate their use as a membrane for gas separations. Owing to the rigid character of these filler components, gas transport does not take place via the solution-diffusion mechanism, thus the empirical trade-off between permeability and selectivity observed on Robeson's plot is not imposed on transport outcomes. The narrower pore size distribution derived from the crystallinity can enable a sharper size selection not possible with an amorphous system like a polymer. However some of the frameworks do afford a certain degree of flexibility, evident from "breathing" vibrational modes[140–142].

Two common classes of microporous fillers used in gas separation membranes are zeolites and MOFs[143]. In addition to size selection, both materials achieve permselectivity from selective adsorption[60,144,145]. Where size selection can be tuned by the length of the ligands, adsorption strength is less straightforward. Theoretically, an ideal candidate should have both a sufficiently high enthalpy of adsorption to effect selectivity without being too strongly bound[146]. Therefore, tuning the adsorptive enthalpies of gas molecules with the molecular sieves is key to realizing an ideal material candidate for each gas pair[147]. Experimentally, the community has identified several important archetypical MOFs for carbon capture and have adapted them as membranes, such as MFI[148,149], ZIF-8[150,151] and MOF-74[147,152]. These and other microporous materials have been chronicled extensively in the gas separations literature[45,59,153,154]. Nonetheless, the materials landscape remains vast for carbon capture. One such example stems from developments based on the MOF-74 topology. Expanding the organic linker one phenyl ring at a time, Yaghi et al. produced a series of expanded MOF-74s with linkers measuring as long as 5 nm[155]. Research that was taken on concurrently in the Long group determined that an expanded MOF-74, which uses the linker 4,4'-dioxido-3,3'-biphenyldicarboxylate (dobpdc), shows exceptional CO_2 adsorption selectivity when the open metal centers in the MOF structure were modified with alkyldiamines[156]. Further examination revealed the CO_2 transport is in fact cooperative in nature, forming a conveyer belt upon which CO_2 is delivered downstream[4]. The incorporation of mmen-M_2(dobpdc) MOFs in a hybrid membrane with selective-transport ability is an active area of research in the CCS community.

Most MOFs and inorganic molecular sieves are incorporated into membranes as part of a solid phase dispersion to make a mixed matrix membrane, leveraging the processibility of the polymer matrix and the superior sieving transport characteristics of the nanocrystalline microporous materials[157]. Alternatively, MOFs have been synthesized in situ on a support, forming layered composites[151,158] (**Figure 1.6**). Metal oxides have been explored as *in situ* MOF precursors to prepare similar layered composites. Leveraging the nanocrystal surface chemistry expertise, we have successfully prepared MOF coatings from ligand-free metal oxide nanocrystals. The preparation of ligand-free nanocrystals, and the resultant MOF films are discussed in Chapters 2-5.

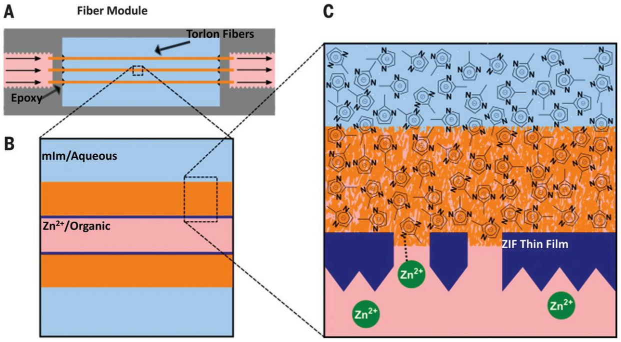

Figure 1.6 Construction of polymer-supported ZIF-8 in a hollow fiber format[151]. Using microfluidics and diffusion control, ZIF films are grown at the interface. From A. J. Brown, N. A. Brunelli, K. Eum, F. Rashidi, J. R. Johnson, W. J. Koros, C. W. Jones and S. Nair, *Science*, 2014, **345**, 72–75. Reprinted with permission from AAAS.

Carbon nanotubes membranes, where carbon nanotubes are sequestered in a pliable polymer matrix, are another multicomponent gas-separation membrane (**Figure 1.7**). In the microporous hollow interiors of carbon nanotubes, uniform level of confinement not only leads to size selectivity, but also sometimes dramatic improvements in permeability. Single-walled carbon nanotubes whose diameters are less than 2 nm, when carefully microfabricated on a membrane, demonstrated gas transport kinetics that are up to 120 times higher than what was to be expected using the Knudsen model[159]. These results have been attributed to the atomically smooth surface of the pore interior, which enables frictionless specular reflections not present in other microporous materials[160,161]. Additionally, carbon nanotube's unique characteristics also result in remarkable transport performance in liquid and ion tranasport[162], which will be discussed below.

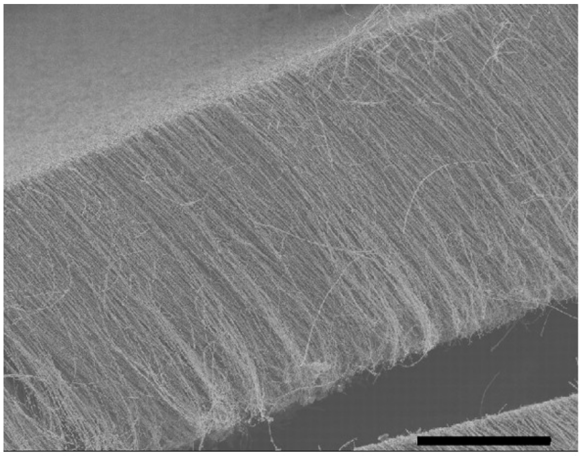

Figure 1.7 Carbon nanotube membrane prepared by Hinds *et al.*[163] The voids between the dense nanotube arrays are filled by polystyrene. From B. J. Hinds, N. Chopra, T. Rantell, R. Andrews, V. Gavalas and L. G. Bachas, *Science,* 2004, **303**, 62–65. Reprinted with permission from AAAS.

Liquid Transport – Reverse Osmosis and Dehydration

Desalination – Reverse Osmosis

Access to potable water is a pressing issue in many parts of the world. In coastal communities, sea water desalination is being implemented at increasingly larger scales. Desalination is also needed in other geographical areas, where water is confined to salted aquifers[164]. Reverse osmosis is the leading desalination technology in terms of overall capacity, and a reliable microporous membrane has been key to its success. Thin film composite membranes are featured prominently in reverse osmosis. These are typically made of an aromatic polyamide thin film (~0.2 μm) atop a thick polysulfone support layer (~40 μm). In practice, an additional support layer (~100 μm) is needed to uphold the membrane's structural integrity[165]. The permeability/selectivity trade off observed in gas separation is also applicable to membranes for water desalination under the framework of the solution-diffusion model[166–168] (**Figure 1.8**). Here membrane polymer chain dynamics delays that of water and salt, diminishing permeability. Microporous membranes, single-component or composite, featuring more shape-persistent micropores may provide advantages in future designs. One notable example of decoupling membrane-analyte interactions for aqueous transport involves carbon nanotubes. The interior surface promotes frictionless transport for water molecules in both simulation[169–171] and experiment[159,162]; additionally, the micropore orifice efficiently prevents hydrated ion translocation[171,172].

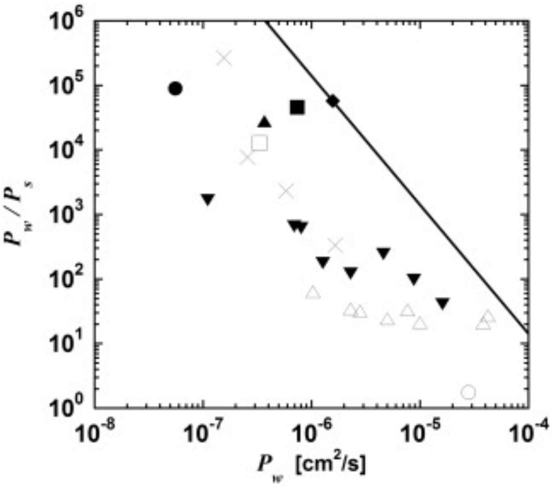

Polyimide	●
Aromatic polyamide	■,□
Poly(benzimi-dazopyrrolone)	♦
Poly(amide-hydrazide)	▲
Di-sulfonated poly(arylene ether sulfone)	▼
Cellulose acetate	×
Cross-linked poly(ethylene glycol diacrylate)	△
Poly(2-hydroxylethyl acrylate)	◇
Poly(acrylic acid)	◁
Hydrogels	+
Methacrylate-based copolymers	▽
Poly(hydroxylethyl methacrylamide)-based hydrogels	▷
Hypothetical membrane composed of water	○

Figure 1.8 The permselectivity tradeoff plot for reverse osmosis[166]. The legend is shown in the table. Reprinted from *Progress in Polymer Science*, Vol 39, Geise, G. M.; Paul, D. R.; Freeman, B. D., Fundamental water and salt transport properties of polymeric materials, 1-42, Copyright 2014, with permission from Elsevier.

Pervaporation – Dehydration of Organic Liquids

Pervaporation relates a process by which a mixture of liquids can be purified by partial vaporization, often through a porous membrane. One of its commercial applications is the dehydration of organic liquids; here water undergoes selective permeation through the membrane. While permeation is often times described by a solution-diffusion mechanism, indicative of membranes with transient pores, a selection of inorganic and hybrid membranes have emerged with behavior that deviates from this mechanism, including supported zeolite membranes[173–175 176,177], prepared by nucleation and growth of zeolites directly onto an inorganic support. Thus, while polymer-based membranes presently dominate the market, recently commercialized zeolite membranes for pervaporation may eventually overtake them[178]. MOF-based mixed matrix membranes have also been investigated for alcohol dehydration[179–181]. Pervaporation processes can also be applied to anhydrous liquid-liquid separations. Whereas in the past, organophilic sieving-materials were scarce, in recent years, zeolites and MOFs have shown promise and are poised to make an impact[182]. For example, ZIF-8 embedded in a polymethylphenylsiloxane membrane shows promise as a butanol recovery membrane in pervaporation mode[183]. On the other hand, silicalite-1-based membranes have shown efficacy in separating xylene isomers via pervaporation[184].

Dehumidification – Indoor Air Conditioning

Maintaining an comfortable indoor environment for building occupants is an energy-intensive process that may take up to 60% of a building's total energy consumption[185]. Dehumidification is an integral part of air conditioning systems. Conventional dehumidification cools humid indoor air to collect the condensed water before re-heating the dry air to the indoor temperature level for recirculation[186]. Liquid-to-air membrane energy exchangers are an alternative membrane-based approach to dehumidification. Here water transports through a porous membrane into a liquid dessicant, which can be regenerated with waste-heat elsewhere in the building. Techno-economic analysis on membrane-based dehumidifying systems can be found elsewhere[186,187]. While membranes presently used are generally macroporous or mesoporous[188,189], a few notable examples of microporous composite[190] and assymetric[191] membranes are showing promise. As a nascent area of membrane science that impacts one of the major sources of energy consumption, there is certainly a lot of space for adaptation from well-established liquid transport fields, such as leveraging friction-free water transport within microporous voids[159].

Ion Transport – Fuel Cells and Electrochemical Energy Storage

Renewable generation and storage[192–194] of electrical energy are critical to a sustainable future. To that end, fuel cells (FCs) offer on-demand energy generation by converting chemical potential energy into electrical energy. The source of chemical energy in fuel cells is either H_2 or an alcohol, such as methanol or ethanol. Hydrogen fuel cells in particular can achieve zero-emission when the hydrogen fuel is generated using renewable sources. Electrochemical energy storage (EES), on the other hand, is increasingly being paired with systems featuring intermittent energy generation, and in particular wind and solar. Doing so allows for multi-hour power delivery, frequency regulation, load-shifting, and other advantages depending on the scale of the system. For both FCs and EES, membrane technology is a critical determinant of system performance. The membrane is responsible for selective ion transport and other functions. Since the operation of these electrochemical devices occurs in aqueous and non-aqueous settings, across wide wide temperature ranges, and under extremes of chemically reactivity, there is no a universally applicable membrane platform. Instead, membranes are developed to balance systems needs for conductivity, selectivity, and structural integrity.

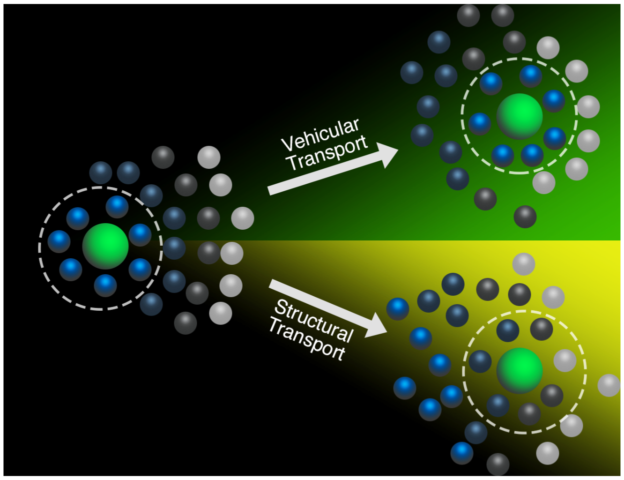

Figure 1.9 Two general pathways of ion transport. In vehicular transport, the ion retains its solvation shell as it moves through the medium (top). In structural transport, the solvent molecules in the first solvation shell exchanges with bulk solvent molecules.

In approaching the design of ion-transporting membranes for FCs and EES, it's important to first consider the fundamental aspects governing ion transport in polymeric materials. Poly(ethylene oxide)[195], or PEO, ubiquitous as a component in solid polymer electrolytes, conducts cations through reversible coordination to a neutrally-charged polymer backbone[196]. Solid and gel (or plasticized) polymer electrolytes are simply formulated by dissolving salts in PEO, or its derivatives, alongside other additives[197]. Poly(ionic liquids), on the other hand, feature a charged backbone or side chain alongside mobile counter-ions. The mobile counterions experience a repulsive electrostatic field from charges residing on the polymer, or Donnan exclusion, which results in perfect ion-transport selectivity. Nonetheless, these interactions, similar to strongly adsorptive interactions in gas separation, slow down the rate of ion transport, embodied by the ionic conductivity in this case. In doing so, the mobility of the ions is coupled to the polymer segmental chain dynamics, which are at least an order of magnitude slower than the bulk ionic mobility[197]. With that in mind, shape-persistent microporous membranes are increasingly attractive targets for engineering transport selectivity without sacrificing ionic conductivity. By deploying a microporous framework as the sieving elements, three desirable membrane attributes can be conferred: selectivity can be enforced through size exclusion, without necessarily using charged moieties featuring strong interactions; minimized membrane-analyte interactions decouple ion motion from the sieving material (rigidity and inertness can be deliberately introduced for dimensional and chemical stability); high conductivity can be realized with frictionless pore walls with additional transport enhancement possible through the confinement effects.

Aqueous Proton Transport – Proton Exchange Membrane Fuel Cell

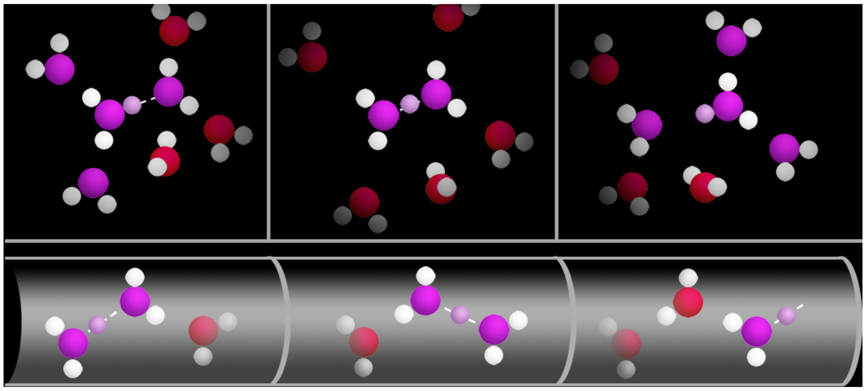

Figure 1.10 Aqueous proton transport in bulk (top) and confinement (bottom). In bulk, proton transfer undergoes the Eigen-Zundel-Eigen mechanism. On the other hand, only the Zundel-Zundel mechanism is observed in confinement. Oxygen atoms participating in the proton complexes and the corresponding excess protons are highlighted.

Aqueous proton transport is a key process in proton exchange membrane (PEM) fuel cells[198]. This fuel cell chemistry is not affected by unwanted active-material crossover; therefore here we will only discuss mechanically robust microporous membranes with high rate of proton conduction. Protons exhibit anomalously high diffusion rates compared to Na+ and K+ ions[199]. This is due to the large-scale non-covalent structure formed using hydrogen bonds where the lone electron pairs are coordinated to hydrogen atoms. However, unlike an ice crystal, the liquid structure is dynamic and can incur various defects. One of these defects is the ionic defect, where the O–H vibration is sufficiently large to release the proton to a neighbouring water molecule, effectively creating a hydroxide ion, OH–, and a hydronium ion, H3O+. Hydronium ion solvated by three water molecules is called the Eigen[200] cation, and the Zundel[201] cation is a proton coordinated between two water molecules. They are the principle complexed proton carriers, or vehicles in bulk water. Protons can diffuse by nature of its carrier's motion, a mechanism aptly called vehicular transport (**Figure 1.9**). On the other hand, fluctuation in the hydrogen bonding network structure enables transferring the excess proton to the appropriately aligned neighboring water molecule. This process is called the Grotthuss mechanism[202], named after the 19th century scientist who first hypothesized it[203] (**Figure 1.10**). Through a multitude of simulation methods, Omer et. al. have determined the multistep proton transfer process in bulk water goes through a Eigen-Zundel-Eigen transition[204]. The process is initiated by an assymetric Eigen cation with one shorter hydrogen bond, constantly rotating to find an appropriate proton transfer partner. As a result, the dynamic of the proton hopping mechanism is limited by the molecular rotation timescale. While vehicular transport is general to all ions in both aqueous and non-aqueous environments, Grotthuss transport is only present in hydrogen-bonded networks, and is the cause of the anomalously high proton diffusion in water. Detailed review of the ab initio simulations on the proton transfer processes can be found elsewhere[205] with finer nuances of the process emerging everyday[206].

Given the Grotthuss mechanism is faster, high rate of proton transport can be obtained if that is to be accentuated. As noted earlier, the limiting step in this proton transfer process is molecular rotation and alignment while in the Eigen form of the cation. As confinement is imposed upon the water molecules, the bulkier isotropic Eigen cation is destablized, giving way to the Zundel form as the only cation complex possible[207]. The directional nature of the hydrogen bonds in a confined space implies the water molecules are well aligned for proton transfer via the Zundel-Zundel pathway[199,208] (**Figure 1.10**). The proton diffusion is thus enhanced by an order of magnitude[207] due to the removal of the rate-limiting step. This serves as the motivation for the use of microporous materials in proton transport as confining frameworks and structured proton transfer mediators.

Though intrinsically not a microporous material, Nafion® and related perfluorosulfonic acids (PFSAs) are the standard bearers of proton exchange membranes. Nafion and other PFSAs feature a perfluoropolyether backbone and hydrophilic sulfonic acid side chains of variable length and loading. Both undergo microseparation upon hydration, leading to a bicontinuous network[209] featuring a mechanically robust phase and a hydrophilic ion-conducting phase. As water is the primary medium in which proton transport takes place within the hydrophilic phase, bulk-like proton diffusion at ~ 7.8 ×102 S cm–1 is observed in these microenvironments, and has been studied extensively through experiments[210,211] and simulations[212].

Nafion and PFSAs are not ideal membranes for fuel cells. Higher temperatures (> 80°C) are desirable for fuel cell efficiency due to enhanced catalytic activity; however, the critical role water plays in PFSA's proton conduction also signifies that the loss of hydration at higher temperature is detrimental to membrane performance. In light of this, there are classes of microporous materials that are offering promising alternatives to PFSAs. Their persistent micropores can not only emulate the liquid-infiltrated state, but also impose the effect of nano-confinement, leading to improved proton conductivity.

Carbon nanotubes present a simple model system where improved proton transfer has been observed when in confinement. Brewer et al.[207] used empirical valence bond method to simulate the diffusivity of protons under confinement. It was shown that a ten-fold improvement in proton diffusivity despite diminished vehicular transport behaviours in carbon nanotubes thinner than 5 Å in diameter. Dellago et al.[213] showed in their Car-Parrinello molecular dynamics simulation that the diffusion coefficients of protons are more than 40 times higher in a (6,6) carbon nanotube (~ 8 Å in diameter) than they are in bulk[214]. Furthermore, Voth et al. showed that proton transfer in a (6,6) carbon nanotube takes place exclusively via the Zundel-Zundel process, a sign of confinement-assisted conductivity enhancement[208]. The delocalized excess proton structure referenced therein, H7O3+, was corroborated by a recent path-integral molecular dynamics simulation[199], a gradual departure from the discrete description based solely on individual Eigen and Zundel complexes. In the context of PEM fuel cells, carbon nanotubes have not been used as a proton exchange membrane as yet, but extensively investigated as a catalyst support. Although, carbon-nanotube-based proton- and electron-conducting membrane does exist in the literature. Wu et al.[215] pioneered the epoxy-based carbon nanotube membranes, by microtoming an epoxy-nanotube composite. Pilgrim et al.[216] fabricated much thicker epoxy membranes with oriented nanotubes. These nanotubes were grown as a thick forest, which was infiltrated with epoxy as the membrane matrix post-synthesis. The demonstrated proton rate is approximately half of that of a Nafion membrane, still with room for improvement. Given the synthetic capabilities[217] and membrane precedents[159,163,215], a carbon-nanotube-based proton exchange membrane leveraging confinement-induced high proton transfer rate may still be within reach.

Nanotubes can also be constructed from bottom-up approaches from organic macrocycles via self-assembly. Though examples of proton transport exist for arylene ethynylene[218] and dendritic dipeptide[219], they have not moved beyond the lipid bilayer vesicle platform and not amenable for energy-related applications. Another notable class of organic nanotube material is cyclic peptides. Hypothesized in 1974[220] and first synthesized in 1993[99], cyclic peptides have sustained two decades of development. Proton transport was among the first properties investigated, also using a vesicle platform[221]. The class of materials has since then extended its applicability into ion channels in a bio-oriented context[222]. However in energy technology, membranes require greater dimensional stability than lipid bilayers. Xu et al.[223] used hierarchical assembly to achieve such a sub-nanometer microporous polymeric membrane by bringing together a block copolymer, a homopolymer, and cyclic peptide macrocycles. The macrocycles are covalently attached to chains of poly(ethylene oxide), which interfaces favourably with the hydrophilic block of polystyrene-b-poly(methyl methacrylate). The system undergoes self-assembly, sequestering the polymer-covered nanotubes in the lumens of cylindrical-morphology block copolymer. The nanotubes are shown to conduct protons much more effectively than the bare membranes. Even though the current material's selection cannot withstand the harsh conditions imposed by PEM fuel cells, the synthetic diversity that it can display could control liquid water structure with unprecedented specificity[6,224]. Additional synthetic developments in the interior functionalization of cyclic peptide nanotubes will be discussed in Chapter 2.

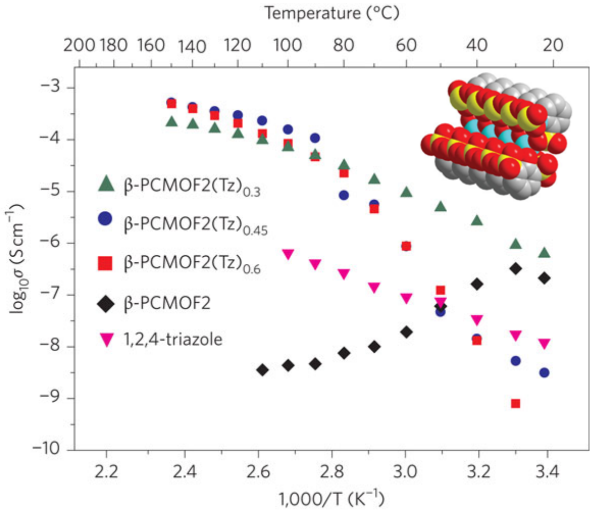

Figure 1.11 Anhydrous proton conduction in β-PCMOF2 by scaled introduction of 1*H*-1,2,4-triazole. Conductivity of the triazole-infused complexes maintains a monotonic increase in proton conductivity as temperature rises above 100 °C, demonstrating anhydrous proton transfer. Reprinted by permission from Macmillan Publishers Ltd: *Nature Chemistry,* **1,** 705–710 (2009), copyright 2009.

Metal-organic frameworks have recently garnered attention for their ability to facilitate anhydrous proton transport, directly addressing the shortcomings of Nafion and PFSAs at high temperature[226]. Shimizu[225] and Kitigawa[227–229] demonstrated that the installation acidic functionalities within the cavities of MOFs enables the direct mediation of proton transfer in the absence of water. Both aryl sulfonates and aryl phosphontes[230] within the framework serve as strongly acidic groups that facilitate proton transport. This was accomplished either through the use of a sulfonated or phosphonated ligands[227] or post-synthetic modification[231]. These sites, along with infiltrated water depending on the relative humidities, act as proton hopping stations, enabling proton conductivity typically in the range of 1×10^{-3} S cm^{-1} by promoting structured proton transfer[227,232,233]. For high temperature operations, water can be substituted for less volatile proton hopping mediators such as 1*H*-1,2,4-triazole[234]. Its introduction enabled proton conduction at 150 °C, well above the boiling point of water[225] (

Figure 1.11). Exceptional conductivity can be achieved at more than 1×10^{-2} S cm^{-1} by lubricating the framework, or weakening the water-framework interaction[228]. An alternative proton conduction strategy involves the use of a guest proton conductor in a micropore[229]. In this case, the adsorbed imidazole molecules, effectively plays the role of proton hopping mediators. For interested readers, a more detailed review on proton-conducting MOFs can be found elsewhere[235,236].

Non-Aqueous Ion Transport – Electrochemical Energy Storage

As the renewed interests in energy storage continues to catalyse innovations in battery chemistries and device architectures, battery membranes are steadily transforming from mesoporous polypropylene or polyethylene membranes[237] to ion-conducting membranes capable of functioning in battery-relevant solvents. With the wide selection of organic solvents and supporting electrolytes available[238], new membranes need to be tailored for the specific non-aqueous environments and cater to the transport mechanisms of ions of interests, such as Li^+, Na^+, $Mg_2{}^+$, $BF_4{}^-$ or $PF_6{}^-$. Unfortunately, less mechanistic detail is available for ion-transporting membranes in non-aqueous settings. Several groups have looked into the solvent-stabilized lithium salt dynamics in various battery relevant solvents such as ethylene carbonate[239–243] and propylene carbonate[240,241]. Borodin and Smith[243] posited that there are two diffusion mechanisms at work for non-aqueous ions—vehicular diffusion and structural diffusion. Vehicular diffusion is similar to that within the context of proton transport in that the ions diffuse with its solvation shell of solvent molecules. Structural diffusion on the other hand implies the uncoordinated motion of the ion and its solvation shell. The faster the resultant exchange of the solvation shell molecules, the greater diffusion contribution from structural diffusion. Since most electrolytes coordinate to the cations, the counter-ions, be it the $BF_4{}^-$ ion[241] or the $PF_6{}^-$ ion[239], tend to diffuse faster than the lithium ion. It follows naturally that the coordinating strength of the solvent plays a large part in determining the ion mobility[239–241]. Microporous materials are well positioned to both allow for the vehicular transport of appropriately sized moieties and mediate structural transport with weakly coordinating functional groups in confinement. Here we will highlight two classes of microporous materials that are seeing development as lithium-or magnesium-ion conductors in ion-selective membranes.

MOFs have found their way into non-aqueous lithium transport, in addition to their aforementioned growing presence in aqueous proton transport. The Long group has been instrumental in developing solid MOF electrolytes featuring Li^+ ions[244,245] and $Mg_2{}^+$ ions[246]. By merely solvating the ions occupying the porous space, these MOF electrolyte can yield lithium ion conductivity upward of 1×10^{-5} S cm^{-1}. The addition of supporting electrolyte could increase the conductivity by another order of magnitude[244,247] (**Figure 1.12**). Other MOF electrolytes not covered here can be found at these specialized reviews[236,248].

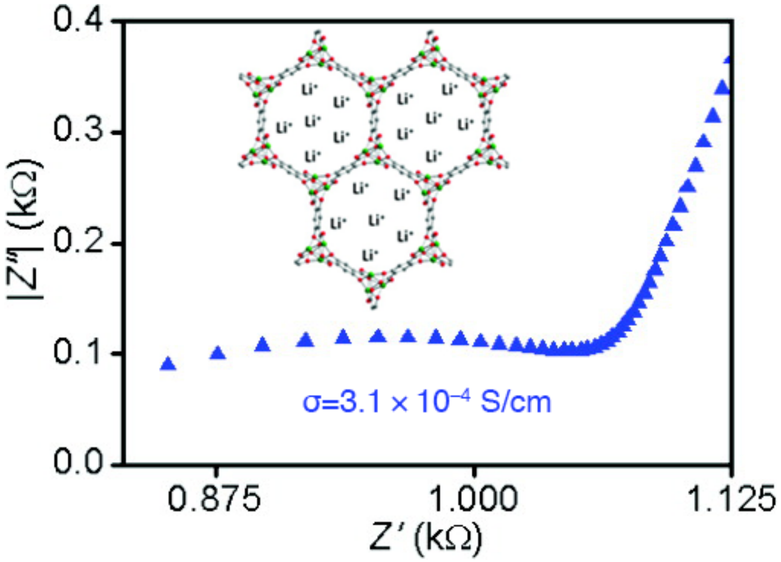

Figure 1.12 Electrochemical impedance spectra (EIS) of lithium ion conduction in Mg_2(dobdc) with 0.35 equivalent of LiO^iPr and 0.25 equivalent of $LiBF_4$[244]. Adapted with permission from Wiers, B. M.; Foo, M.-L.; Balsara, N. P.; Long, J. R. *J. Am. Chem. Soc.* **2011**, *133* (37), 14522–14525. Copyright 2011 American Chemical Society.

Even though MOFs can serve as solid-state electrolytes for lithium ion batteries where no selective transport is required, it would require much more precise pore size tuning for some next-generation battery chemistries. Lithium-sulfur (Li-S) flow battery is a promising grid-scale energy storage solution, boasting high specific capacities both gravimetrically and volumetrically. Unlike the simpler case of lithium ion batteries, the active materials in Li–S batteries are a series of soluble lithium polysulfides. One major bottleneck of this technology is the prevention of unwanted active material crossover. Our approach[107] to this problem involves the use of a microporous membrane which can 1) maintain a rigid and robust framework which can withstand device operating conditions, both chemically and mechanically; 2) host micropores for size-selectivity, such that semi-permeability can happen without too much perturbation to the analyte ions' energy landscape; 3) curate an environment where bulk transport can be emulated, so that the ions are mainly coordinated by infiltrating media. We recently applied PIM-1[121] to the polysulfide crossover problem. With pore size distribution peaking at 7.7 Å (**Figure 1.13(a)**), it is at an ideal position to reject solvated polysulfide complexes, most of which feature radii of gyration, obtained from molecular dynamics simulations, greater than 8 Å. This is evident by the crossover test performed in an H-cell where the diffusion of polysulfide in PIM-1 is 500-fold slower compared to a conventional battery separator such as Celgard® 2325 (**Figure 1.13(b)**), without drastically sacrificing conductivity. This is the first proof-of-concept demonstration that microporous molecular sieve membranes can be used to carry out permselective ion transport without significantly compromising its stability, conductivity and selectivity. Further details regarding this work are presented in Chapter 6.

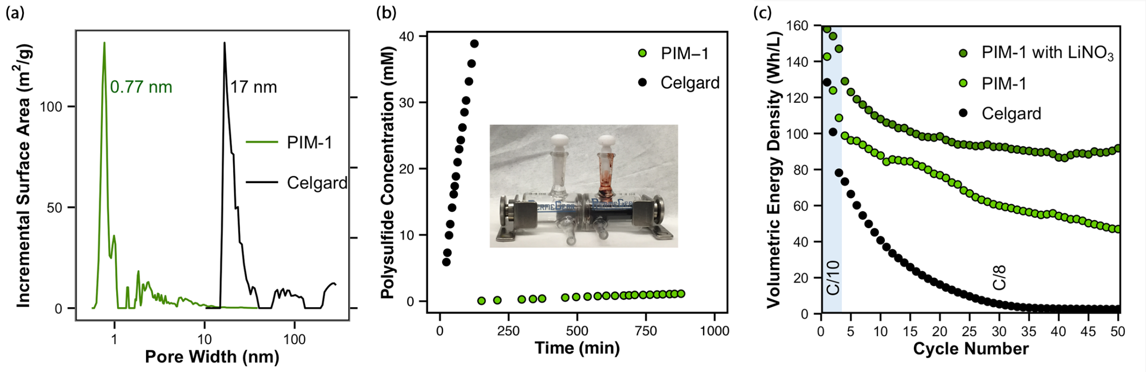

Figure 1.13 (a) Pore size distributions of PIM-1 and Celgard 2325. PIM-1 has primarily micropores while Celgard has mesopores. (b) The crossover rates of lithium poly as performed in an H-cell. The microporosity of PIM-1 is capable of screening out a the majority of lithium polysulfides, significantly delaying the unwated species crossover. (c) Significant improvement in capacity retention by replacing Celgard with PIM-1. Additional capacity gain is possible when PIM-1 is used in conjunction with the anode-protecting additive LiNO$_3$[107]. Adapted with permission from Li, C.; Ward, A. L.; Doris, S. E.; Pascal, T. A.; Prendergast, D.; Helms, B. A. *Nano Lett.* **2015**. Copyright 2015 American Chemical Society.

References

(1) Haszeldine, R. S. *Science* **2009**, *325* (5948), 1647–1652.

(2) Elimelech, M.; Phillip, W. A. *Science* **2011**, *333* (6043), 712–717.

(3) Ch. Baerlocher; L. B. McCusker. Database of Zeolite Structures http://www.iza-structure.org/databases/.

(4) McDonald, T. M.; Mason, J. A.; Kong, X.; Bloch, E. D.; Gygi, D.; Dani, A.; Crocellà, V.; Giordanino, F.; Odoh, S. O.; Drisdell, W. S.; Vlaisavljevich, B.; Dzubak, A. L.; Poloni, R.; Schnell, S. K.; Planas, N.; Lee, K.; Pascal, T.; Wan, L. F.; Prendergast, D.; Neaton, J. B.; Smit, B.; Kortright, J. B.; Gagliardi, L.; Bordiga, S.; Reimer, J. A.; Long, J. R. *Nature* **2015**, *519* (7543), 303–308.

(5) Hummer, G.; Rasaiah, J. C.; Noworyta, J. P. *Nature* **2001**, *414* (6860), 188–190.

(6) Ruiz, L.; Wu, Y.; Keten, S. *Nanoscale* **2014**, *7* (1), 121–132.

(7) Budd, P. M.; McKeown, N. B. *Polym. Chem.* **2010**, *1*, 63–68.

(8) Cundy, C. S.; Cox, P. A. *Chem. Rev.* **2003**, *103* (3), 663–702.

(9) Cundy, C. S.; Cox, P. A. *Microporous Mesoporous Mater.* **2005**, *82* (1–2), 1–78.

(10) Stock, N.; Biswas, S. *Chem. Rev.* **2012**, *112* (2), 933–969.

(11) Farha, O. K.; Hupp, J. T. *Acc. Chem. Res.* **2010**, *43* (8), 1166–1175.

(12) Furukawa, H.; Cordova, K. E.; O'Keeffe, M.; Yaghi, O. M. *Science* **2013**, *341* (6149), 1230444.

(13) Dai, H. *Acc. Chem. Res.* **2002**, *35* (12), 1035–1044.

(14) Saufi, S. M.; Ismail, A. F. *Carbon* **2004**, *42* (2), 241–259.

(15) Dawson, R.; Cooper, A. I.; Adams, D. J. *Prog. Polym. Sci.* **2012**, *37* (4), 530–563.

(16) McKeown, N. B.; Budd, P. M. *Chem. Soc. Rev.* **2006**, *35* (8), 675.

(17) Bong, D. T.; Clark, T. D.; Granja, J. R.; Ghadiri, M. R. *Angew. Chem. Int. Ed.* **2001**, *40* (6), 988–1011.

(18) Rosi, N. L.; Eckert, J.; Eddaoudi, M.; Vodak, D. T.; Kim, J.; O'Keeffe, M.; Yaghi, O. M. *Science* **2003**, *300* (5622), 1127–1129.

(19) Lee, J.; Farha, O. K.; Roberts, J.; Scheidt, K. A.; Nguyen, S. T.; Hupp, J. T. *Chem. Soc. Rev.* **2009**, *38* (5), 1450–1459.

(20) Tanabe, K.; Hölderich, W. F. *Appl. Catal. Gen.* **1999**, *181* (2), 399–434.

(21) Corma, A. *J. Catal.* **2003**, *216* (1–2), 298–312.

(22) Baerlocher, C.; McCusker, L. B.; Olson, D. H. *Atlas of Zeolite Framework Types*; Elsevier, 2007.

(23) Breck, D. W. *Zeolite molecular sieves: structure, chemistry, and use*; R.E. Krieger, 1984.

(24) Flanigen, E. M.; Bennett, J. M.; Grose, R. W.; Cohen, J. P.; Patton, R. L.; Kirchner, R. M.; Smith, J. V. *Nature* **1978**, *271* (5645), 512–516.

(25) Chapman, D. M.; Roe, A. L. *Zeolites* **1990**, *10* (8), 730–737.

(26) Tanev, P. T.; Chibwe, M.; Pinnavaia, T. J. *Nature* **1994**, *368* (6469), 321–323.

(27) Davis, M. E.; Saldarriaga, C.; Montes, C.; Garces, J.; Crowdert, C. *Nature* **1988**, *331* (6158), 698–699.

(28) Wilson, S. T.; Lok, B. M.; Messina, C. A.; Cannan, T. R.; Flanigen, E. M. *J. Am. Chem. Soc.* **1982**, *104* (4), 1146–1147.

(29) Estermann, M.; McCusker, L. B.; Baerlocher, C.; Merrouche, A.; Kessler, H. *Nature* **1991**, *352* (6333), 320–323.

(30) Lok, B. M.; Messina, C. A.; Patton, R. L.; Gajek, R. T.; Cannan, T. R.; Flanigen, E. M. *J. Am. Chem. Soc.* **1984**, *106* (20), 6092–6093.

(31) Cronsted, A. F. *Akad Handl 17*, 20.

(32) Davis, M. E.; Lobo, R. F. *Chem. Mater.* **1992**, *4* (4), 756–768.

(33) Cheetham, A. K.; Férey, G.; Loiseau, T. *Angew. Chem. Int. Ed.* **1999**, *38* (22), 3268–3292.

(34) Chen, N. Y.; Jr, T. F. D.; Smith, C. M. *Molecular Transport and Reaction in Zeolites: Design and Application of Shape Selective Catalysis*; John Wiley & Sons, 1994.

(35) Babel, S.; Kurniawan, T. A. *J. Hazard. Mater.* **2003**, *97* (1–3), 219–243.

(36) Hölderich, W.; Hesse, M.; Näumann, F. *Angew. Chem. Int. Ed. Engl.* **1988**, *27* (2), 226–246.

(37) Venuto, P. B. *Microporous Mater.* **1994**, *2* (5), 297–411.

(38) Pluth, J. J.; Smith, J. V. *J. Phys. Chem.* **1979**, *83* (6), 741–749.

(39) Pluth, J. J.; Smith, J. V. *J. Am. Chem. Soc.* **1980**, *102* (14), 4704–4708.

(40) Pluth, J. J.; Smith, J. V. *J. Am. Chem. Soc.* **1983**, *105* (5), 1192–1195.

(41) Gascon, J.; Kapteijn, F.; Zornoza, B.; Sebastián, V.; Casado, C.; Coronas, J. *Chem. Mater.* **2012**, *24* (15), 2829–2844.

(42) Tranchemontagne, D. J.; Hunt, J. R.; Yaghi, O. M. *Tetrahedron* **2008**, *64* (36), 8553–8557.

(43) Park, K. S.; Ni, Z.; Côté, A. P.; Choi, J. Y.; Huang, R.; Uribe-Romo, F. J.; Chae, H. K.; O'Keeffe, M.; Yaghi, O. M. *Proc. Natl. Acad. Sci. U. S. A.* **2006**, *103* (27), 10186–10191.

(44) Yaghi, O. M.; Li, G.; Li, H. *Nature* **1995**, *378* (6558), 703–706.

(45) Kitagawa, S.; Kitaura, R.; Noro, S. *Angew. Chem. Int. Ed.* **2004**, *43*, 2334–2375.

(46) O'Keeffe, M.; Yaghi, O. M. *Chem. Rev.* **2012**, *112* (2), 675–702.

(47) Ockwig, N. W.; Delgado-Friedrichs, O.; O'Keeffe, M.; Yaghi, O. M. *Acc. Chem. Res.* **2005**, *38* (3), 176–182.

(48) Férey, G. *Chem Soc Rev* **2008**, *37* (1), 191–214.

(49) Meek, S. T.; Greathouse, J. A.; Allendorf, M. D. *Adv. Mater.* **2011**, *23* (2), 249–267.

(50) Wang, Z.; Cohen, S. M. *Chem. Soc. Rev.* **2009**, *38* (5), 1315–1329.

(51) Cohen, S. M. *Chem. Rev.* **2012**, *112* (2), 970–1000.

(52) Farha, O. K.; Eryazici, I.; Jeong, N. C.; Hauser, B. G.; Wilmer, C. E.; Sarjeant, A. A.; Snurr, R. Q.; Nguyen, S. T.; Yazaydın, A. Ö.; Hupp, J. T. *J. Am. Chem. Soc.* **2012**, *134* (36), 15016–15021.

(53) Furukawa, H.; Ko, N.; Go, Y. B.; Aratani, N.; Choi, S. B.; Choi, E.; Yazaydin, A. Ö.; Snurr, R. Q.; O'Keeffe, M.; Kim, J.; Yaghi, O. M. *Science* **2010**, *329* (5990), 424–428.

(54) Chen, B.; Xiang, S.; Qian, G. *Acc. Chem. Res.* **2010**, *43* (8), 1115–1124.

(55) Eddaoudi, M.; Kim, J.; Rosi, N.; Vodak, D.; Wachter, J.; O'Keeffe, M.; Yaghi, O. M. *Science* **2002**, *295* (5554), 469–472.

(56) Ma, S.; Zhou, H.-C. *Chem. Commun.* **2010**, *46* (1), 44–53.

(57) Murray, L. J.; Dincă, M.; Long, J. R. *Chem. Soc. Rev.* **2009**, *38* (5), 1294–1314.

(58) Kreno, L. E.; Leong, K.; Farha, O. K.; Allendorf, M.; Van Duyne, R. P.; Hupp, J. T. *Chem. Rev.* **2012**, *112* (2), 1105–1125.

(59) Li, J.-R.; Sculley, J.; Zhou, H.-C. *Chem. Rev.* **2012**, *112* (2), 869–932.
(60) Li, J.-R.; Kuppler, R. J.; Zhou, H.-C. *Chem. Soc. Rev.* **2009**, *38* (5), 1477–1504.
(61) Côté, A. P.; Benin, A. I.; Ockwig, N. W.; O'Keeffe, M.; Matzger, A. J.; Yaghi, O. M. *Science* **2005**, *310* (5751), 1166–1170.
(62) Furukawa, H.; Yaghi, O. M. *J. Am. Chem. Soc.* **2009**, *131* (25), 8875–8883.
(63) DeBlase, C. R.; Silberstein, K. E.; Truong, T.-T.; Abruña, H. D.; Dichtel, W. R. *J. Am. Chem. Soc.* **2013**, *135* (45), 16821–16824.
(64) DeBlase, C. R.; Hernández-Burgos, K.; Silberstein, K. E.; Rodríguez-Calero, G. G.; Bisbey, R. P.; Abruña, H. D.; Dichtel, W. R. *ACS Nano* **2015**, *9* (3), 3178–3183.
(65) Xiang, Z.; Cao, D. *J. Mater. Chem. A* **2013**, *1* (8), 2691–2718.
(66) Ding, S.-Y.; Wang, W. *Chem. Soc. Rev.* **2012**, *42* (2), 548–568.
(67) Iijima, S. *Nature* **1991**, *354* (6348), 56–58.
(68) Hone, J.; Whitney, M.; Piskoti, C.; Zettl, A. *Phys. Rev. B* **1999**, *59* (4), R2514–R2516.
(69) Dai, H.; Wong, E. W.; Lieber, C. M. *Science* **1996**, *272* (5261), 523–526.
(70) Ebbesen, T. W.; Lezec, H. J.; Hiura, H.; Bennett, J. W.; Ghaemi, H. F.; Thio, T. *Nature* **1996**, *382* (6586), 54–56.
(71) Treacy, M. M. J.; Ebbesen, T. W.; Gibson, J. M. *Nature* **1996**, *381* (6584), 678–680.
(72) Kanzow, H.; Lenski, C.; Ding, A. *Phys. Rev. B* **2001**, *63* (12), 125402.
(73) Ago, H.; Komatsu, T.; Ohshima, S.; Kuriki, Y.; Yumura, M. *Appl. Phys. Lett.* **2000**, *77* (1), 79–81.
(74) Balasubramanian, K.; Burghard, M. *Small* **2005**, *1* (2), 180–192.
(75) Tasis, D.; Tagmatarchis, N.; Bianco, A.; Prato, M. *Chem. Rev.* **2006**, *106* (3), 1105–1136.
(76) Wong, S. S.; Joselevich, E.; Woolley, A. T.; Cheung, C. L.; Lieber, C. M. *Nature* **1998**, *394* (6688), 52–55.
(77) Bhatia, S. K.; Chen, H.; Sholl, D. S. *Mol. Simul.* **2005**, *31* (9), 643–649.
(78) Lee, C. Y.; Choi, W.; Han, J.-H.; Strano, M. S. *Science* **2010**, *329* (5997), 1320–1324.
(79) Liu, H.; He, J.; Tang, J.; Liu, H.; Pang, P.; Cao, D.; Krstic, P.; Joseph, S.; Lindsay, S.; Nuckolls, C. *Science* **2010**, *327* (5961), 64–67.
(80) Suda, H.; Haraya, K. *J. Phys. Chem. B* **1997**, *101* (20), 3988–3994.
(81) Koresh, J.; Soffer, A. *J. Chem. Soc. Faraday Trans. 1 Phys. Chem. Condens. Phases* **1980**, *76* (0), 2457–2471.
(82) Hayashi, J.; Yamamoto, M.; Kusakabe, K.; Morooka, S. *Ind. Eng. Chem. Res.* **1995**, *34* (12), 4364–4370.
(83) Jones, C. W.; Koros, W. J. *Carbon* **1994**, *32* (8), 1419–1425.
(84) Sedigh, M. G.; Xu, L.; Tsotsis, T. T.; Sahimi, M. *Ind. Eng. Chem. Res.* **1999**, *38* (9), 3367–3380.
(85) Fuertes, A. B.; Nevskaia, D. M.; Centeno, T. A. *Microporous Mesoporous Mater.* **1999**, *33* (1–3), 115–125.
(86) Vu, D. Q.; Koros, W. J.; Miller, S. J. *Ind. Eng. Chem. Res.* **2002**, *41* (3), 367–380.
(87) Hatori, H.; Yamada, Y.; Shiraishi, M.; Nakata, H.; Yoshitomi, S. *Carbon* **1992**, *30* (2), 305–306.
(88) Bird, A. J.; Trimm, D. L. *Carbon* **1983**, *21* (3), 177–180.

(89) Chen, Y. D.; Yang, R. T. *Ind. Eng. Chem. Res.* **1994**, *33* (12), 3146–3153.
(90) Shusen, W.; Meiyun, Z.; Zhizhong, W. *J. Membr. Sci.* **1996**, *109* (2), 267–270.
(91) Centeno, T. A.; Fuertes, A. B. *Carbon* **2000**, *38* (7), 1067–1073.
(92) Salleh, W. N. W.; Ismail, A. F. *Sep. Purif. Technol.* **2012**, *88*, 174–183.
(93) Fuertes, A. B. *Carbon* **2001**, *39* (5), 697–706.
(94) Salleh, W. N. W.; Ismail, A. F.; Matsuura, T.; Abdullah, M. S. *Sep. Purif. Rev.* **2011**, *40* (4), 261–311.
(95) Ismail, A. F.; David, L. I. B. *J. Membr. Sci.* **2001**, *193* (1), 1–18.
(96) Percec, V.; Dulcey, A. E.; Balagurusamy, V. S. K.; Miura, Y.; Smidrkal, J.; Peterca, M.; Hummelin, S.; Edlund, U.; Hudson, S. D.; Heiney, P. A.; Duan, H.; Magonev, S. N.; Vinogradov, S. A. *Nature* **2004**, *430* (7001), 764–768.
(97) Davis, J. T.; Spada, G. P. *Chem. Soc. Rev.* **2007**, *36* (2), 296–313.
(98) Zhao, D.; Moore, J. S. *Chem. Commun.* **2003**, No. 7, 807–818.
(99) Ghadiri, M. R.; Granja, J. R.; Milligan, R. A.; McRee, D. E.; Khazanovich, N. *Nature* **1993**, *366* (6453), 324–327.
(100) Hourani, R.; Zhang, C.; van der Weegen, R.; Ruiz, L.; Li, C.; Keten, S.; Helms, B. A.; Xu, T. *J. Am. Chem. Soc.* **2011**, *133* (39), 15296–15299.
(101) Reiriz, C.; Amorín, M.; García-Fandiño, R.; Castedo, L.; Granja, J. R. *Org. Biomol. Chem.* **2009**, *7* (21), 4358–4361.
(102) Sánchez-Quesada, J.; Isler, M. P.; Ghadiri, M. R. *J. Am. Chem. Soc.* **2002**, *124* (34), 10004–10005.
(103) Fernandez-Lopez, S.; Kim, H.-S.; Choi, E. C.; Delgado, M.; Granja, J. R.; Khasanov, A.; Kraehenbuehl, K.; Long, G.; Weinberger, D. A.; Wilcoxen, K. M.; Ghadiri, M. R. *Nature* **2001**, *412* (6845), 452–455.
(104) Zang, L.; Che, Y.; Moore, J. S. *Acc. Chem. Res.* **2008**, *41* (12), 1596–1608.
(105) Shantarovich, V. P.; Kevdina, I. B.; Yampolskii, Y. P.; Alentiev, A. Y. *Macromolecules* **2000**, *33* (20), 7453–7466.
(106) Budd, P. M.; Ghanem, B. S.; Makhseed, S.; McKeown, N. B.; Msayib, K. J.; Tattershall, C. E. *Chem. Commun.* **2004**, No. 2, 230–231.
(107) Li, C.; Ward, A. L.; Doris, S. E.; Pascal, T. A.; Prendergast, D.; Helms, B. A. *Nano Lett.* **2015**, *15* (9), 5724–5729.
(108) Park, H. B.; Jung, C. H.; Lee, Y. M.; Hill, A. J.; Pas, S. J.; Mudie, S. T.; Wagner, E. V.; Freeman, B. D.; Cookson, D. J. *Science* **2007**, *318* (5848), 254–258.
(109) Qiao, Z.-A.; Chai, S.-H.; Nelson, K.; Bi, Z.; Chen, J.; Mahurin, S. M.; Zhu, X.; Dai, S. *Nat. Commun.* **2014**, *5*.
(110) Robeson, L. M. *J. Membr. Sci.* **2008**, *320* (1–2), 390–400.
(111) Setiawan, L.; Wang, R.; Li, K.; Fane, A. G. *J. Membr. Sci.* **2011**, *369* (1–2), 196–205.
(112) Du, N.; Park, H. B.; Dal-Cin, M. M.; Guiver, M. D. *Energy Environ. Sci.* **2012**, *5* (6), 7306–7322.
(113) Koros, W. J.; Fleming, G. K. *J. Membr. Sci.* **1993**, *83* (1), 1–80.
(114) Vaidya, P. D.; Kenig, E. Y. *Chem. Eng. Technol.* **2007**, *30* (11), 1467–1474.
(115) Rochelle, G. T. *Science* **2009**, *325* (5948), 1652–1654.
(116) Wijmans, J. G.; Baker, R. W. *J. Membr. Sci.* **1995**, *107* (1–2), 1–21.
(117) Robeson, L. M. *J. Membr. Sci.* **1991**, *62* (2), 165–185.
(118) Freeman, B. D. *Macromolecules* **1999**, *32* (2), 375–380.

(119) Thornton, A. W.; Hilder, T.; Hill, A. J.; Hill, J. M. *J. Membr. Sci.* **2009**, *336* (1–2), 101–108.

(120) Heuchel, M.; Fritsch, D.; Budd, P. M.; McKeown, N. B.; Hofmann, D. *J. Membr. Sci.* **2008**, *318* (1–2), 84–99.

(121) Budd, P. M.; Elabas, E. S.; Ghanem, B. S.; Makhseed, S.; McKeown, N. B.; Msayib, K. J.; Tattershall, C. E.; Wang, D. *Adv. Mater.* **2004**, *16* (5), 456–459.

(122) Tocci, E.; De Lorenzo, L.; Bernardo, P.; Clarizia, G.; Bazzarelli, F.; Mckeown, N. B.; Carta, M.; Malpass-Evans, R.; Friess, K.; Pilnáček, K.; Lanč, M.; Yampolskii, Y. P.; Strarannikova, L.; Shantarovich, V.; Mauri, M.; Jansen, J. C. *Macromolecules* **2014**, *47* (22), 7900–7916.

(123) Rose, I.; Carta, M.; Malpass-Evans, R.; Ferrari, M.-C.; Bernardo, P.; Clarizia, G.; Jansen, J. C.; McKeown, N. B. *ACS Macro Lett.* **2015**, *4* (9), 912–915.

(124) Carta, M.; Bernardo, P.; Clarizia, G.; Jansen, J. C.; McKeown, N. B. *Macromolecules* **2014**, *47* (23), 8320–8327.

(125) Budd, P. M.; Msayib, K. J.; Tattershall, C. E.; Ghanem, B. S.; Reynolds, K. J.; McKeown, N. B.; Fritsch, D. *J. Membr. Sci.* **2005**, *251* (1–2), 263–269.

(126) Ghanem, B. S.; McKeown, N. B.; Budd, P. M.; Fritsch, D. *Macromolecules* **2008**, *41* (5), 1640–1646.

(127) Du, N.; Park, H. B.; Robertson, G. P.; Dal-Cin, M. M.; Visser, T.; Scoles, L.; Guiver, M. D. *Nat. Mater.* **2011**, *10* (5), 372–375.

(128) Carta, M.; Malpass-Evans, R.; Croad, M.; Rogan, Y.; Jansen, J. C.; Bernardo, P.; Bazzarelli, F.; McKeown, N. B. *Science* **2013**, *339* (6117), 303–307.

(129) Budd, P. M.; McKeown, N. B.; Ghanem, B. S.; Msayib, K. J.; Fritsch, D.; Starannikova, L.; Belov, N.; Sanfirova, O.; Yampolskii, Y.; Shantarovich, V. *J. Membr. Sci.* **2008**, *325* (2), 851–860.

(130) Kim, S.; Lee, Y. M. *Prog. Polym. Sci.* **2015**, *43*, 1–32.

(131) Sanders, D. F.; Smith, Z. P.; Guo, R.; Robeson, L. M.; McGrath, J. E.; Paul, D. R.; Freeman, B. D. *Polymer* **2013**, *54* (18), 4729–4761.

(132) Park, H. B.; Han, S. H.; Jung, C. H.; Lee, Y. M.; Hill, A. J. *J. Membr. Sci.* **2010**, *359* (1–2), 11–24.

(133) Choi, J. I.; Jung, C. H.; Han, S. H.; Park, H. B.; Lee, Y. M. *J. Membr. Sci.* **2010**, *349* (1–2), 358–368.

(134) Cooper, A. I. *Adv. Mater.* **2009**, *21* (12), 1291–1295.

(135) Lindemann, P.; Tsotsalas, M.; Shishatskiy, S.; Abetz, V.; Krolla-Sidenstein, P.; Azucena, C.; Monnereau, L.; Beyer, A.; Gölzhäuser, A.; Mugnaini, V.; Gliemann, H.; Bräse, S.; Wöll, C. *Chem. Mater.* **2014**, *26* (24), 7189–7193.

(136) Cheng, G.; Bonillo, B.; Sprick, R. S.; Adams, D. J.; Hasell, T.; Cooper, A. I. *Adv. Funct. Mater.* **2014**, *24* (33), 5219–5224.

(137) Favvas, E. P.; Kouvelos, E. P.; Romanos, G. E.; Pilatos, G. I.; Mitropoulos, A. C.; Kanellopoulos, N. K. *J. Porous Mater.* **2007**, *15* (6), 625–633.

(138) Tin, P. S.; Chung, T.-S.; Liu, Y.; Wang, R. *Carbon* **2004**, *42* (15), 3123–3131.

(139) Buonomenna, M. G.; Yave, W.; Golemme, G. *RSC Adv.* **2012**, *2* (29), 10745–10773.

(140) Hamon, L.; Llewellyn, P. L.; Devic, T.; Ghoufi, A.; Clet, G.; Guillerm, V.; Pirngruber, G. D.; Maurin, G.; Serre, C.; Driver, G.; Beek, W. van; Jolimaître, E.; Vimont, A.; Daturi, M.; Férey, G. *J. Am. Chem. Soc.* **2009**, *131* (47), 17490–17499.

(141) Ryder, M. R.; Civalleri, B.; Bennett, T. D.; Henke, S.; Rudić, S.; Cinque, G.; Fernandez-Alonso, F.; Tan, J.-C. *Phys. Rev. Lett.* **2014**, *113* (21), 215502.
(142) Férey, G.; Serre, C. *Chem. Soc. Rev.* **2009**, *38* (5), 1380–1399.
(143) Rangnekar, N.; Mittal, N.; Elyassi, B.; Caro, J.; Tsapatsis, M. *Chem. Soc. Rev.* **2015**, *44* (20), 7128–7154.
(144) Keizer, K.; Burggraaf, A. J.; Vroon, Z. A. E. P.; Verweij, H. *J. Membr. Sci.* **1998**, *147* (2), 159–172.
(145) Goj, A.; Sholl, D. S.; Akten, E. D.; Kohen, D. *J. Phys. Chem. B* **2002**, *106* (33), 8367–8375.
(146) Lin, L.-C.; Berger, A. H.; Martin, R. L.; Kim, J.; Swisher, J. A.; Jariwala, K.; Rycroft, C. H.; Bhown, A. S.; Deem, M. W.; Haranczyk, M.; Smit, B. *Nat. Mater.* **2012**, *11* (7), 633–641.
(147) Britt, D.; Furukawa, H.; Wang, B.; Glover, T. G.; Yaghi, O. M. *Proc. Natl. Acad. Sci.* **2009**, *106* (49), 20637–20640.
(148) Zhou, M.; Korelskiy, D.; Ye, P.; Grahn, M.; Hedlund, J. *Angew. Chem. Int. Ed.* **2014**, *53* (13), 3492–3495.
(149) Sandström, L.; Sjöberg, E.; Hedlund, J. *J. Membr. Sci.* **2011**, *380* (1–2), 232–240.
(150) Venna, S. R.; Carreon, M. A. *J. Am. Chem. Soc.* **2010**, *132* (1), 76–78.
(151) Brown, A. J.; Brunelli, N. A.; Eum, K.; Rashidi, F.; Johnson, J. R.; Koros, W. J.; Jones, C. W.; Nair, S. *Science* **2014**, *345* (6192), 72–75.
(152) Bae, T.-H.; Long, J. R. *Energy Environ. Sci.* **2013**, *6* (12), 3565–3569.
(153) Phan, A.; Doonan, C. J.; Uribe-Romo, F. J.; Knobler, C. B.; O'Keeffe, M.; Yaghi, O. M. *Acc. Chem. Res.* **2010**, *43* (1), 58–67.
(154) Aceituno Melgar, V. M.; Kim, J.; Othman, M. R. *J. Ind. Eng. Chem.* **2015**, *28*, 1–15.
(155) Deng, H.; Grunder, S.; Cordova, K. E.; Valente, C.; Furukawa, H.; Hmadeh, M.; Gándara, F.; Whalley, A. C.; Liu, Z.; Asahina, S.; Kazumori, H.; O'Keeffe, M.; Terasaki, O.; Stoddart, J. F.; Yaghi, O. M. *Science* **2012**, *336* (6084), 1018–1023.
(156) McDonald, T. M.; Lee, W. R.; Mason, J. A.; Wiers, B. M.; Hong, C. S.; Long, J. R. *J. Am. Chem. Soc.* **2012**, *134* (16), 7056–7065.
(157) Zimmerman, C. M.; Singh, A.; Koros, W. J. *J. Membr. Sci.* **1997**, *137* (1–2), 145–154.
(158) Huang, K.; Dong, Z.; Li, Q.; Jin, W. *Chem. Commun.* **2013**, *49* (87), 10326–10328.
(159) Holt, J. K.; Park, H. G.; Wang, Y.; Stadermann, M.; Artyukhin, A. B.; Grigoropoulos, C. P.; Noy, A.; Bakajin, O. *Science* **2006**, *312* (5776), 1034–1037.
(160) Skoulidas, A. I.; Ackerman, D. M.; Johnson, J. K.; Sholl, D. S. *Phys. Rev. Lett.* **2002**, *89* (18), 185901.
(161) Cooper, S. M.; Cruden, B. A.; Meyyappan, M.; Raju, R.; Roy, S. *Nano Lett.* **2004**, *4* (2), 377–381.
(162) Majumder, M.; Chopra, N.; Hinds, B. J. *ACS Nano* **2011**, *5* (5), 3867–3877.
(163) Hinds, B. J.; Chopra, N.; Rantell, T.; Andrews, R.; Gavalas, V.; Bachas, L. G. *Science* **2004**, *303* (5654), 62–65.
(164) Shannon, M. A.; Bohn, P. W.; Elimelech, M.; Georgiadis, J. G.; Marĩas, B. J.; Mayes, A. M. *Nature* **2008**, *452* (7185), 301–310.
(165) Lee, K. P.; Arnot, T. C.; Mattia, D. *J. Membr. Sci.* **2011**, *370* (1–2), 1–22.
(166) Geise, G. M.; Paul, D. R.; Freeman, B. D. *Prog. Polym. Sci.* **2014**, *39* (1), 1–42.

(167) Geise, G. M.; Park, H. B.; Sagle, A. C.; Freeman, B. D.; McGrath, J. E. *J. Membr. Sci.* **2011**, *369* (1–2), 130–138.
(168) Paul, D. R. *J. Membr. Sci.* **2004**, *241* (2), 371–386.
(169) Kalra, A.; Garde, S.; Hummer, G. *Proc. Natl. Acad. Sci.* **2003**, *100* (18), 10175–10180.
(170) Falk, K.; Sedlmeier, F.; Joly, L.; Netz, R. R.; Bocquet, L. *Nano Lett.* **2010**, *10* (10), 4067–4073.
(171) Corry, B. *J. Phys. Chem. B* **2008**, *112* (5), 1427–1434.
(172) Fornasiero, F.; Park, H. G.; Holt, J. K.; Stadermann, M.; Grigoropoulos, C. P.; Noy, A.; Bakajin, O. *Proc. Natl. Acad. Sci.* **2008**, *105* (45), 17250–17255.
(173) Bowen, T. C.; Noble, R. D.; Falconer, J. L. *J. Membr. Sci.* **2004**, *245* (1–2), 1–33.
(174) Coronas, J.; Santamaría, J. *Sep. Purif. Rev.* **1999**, *28* (2), 127–177.
(175) Korelskiy, D.; Leppäjärvi, T.; Zhou, H.; Grahn, M.; Tanskanen, J.; Hedlund, J. *J. Membr. Sci.* **2013**, *427*, 381–389.
(176) Tavolaro, A.; Drioli, E. *Adv. Mater.* **1999**, *11* (12), 975–996.
(177) Bein, T. *Chem. Mater.* **1996**, *8* (8), 1636–1653.
(178) Morigami, Y.; Kondo, M.; Abe, J.; Kita, H.; Okamoto, K. *Sep. Purif. Technol.* **2001**, *25* (1–3), 251–260.
(179) Hua, D.; Ong, Y. K.; Wang, Y.; Yang, T.; Chung, T.-S. *J. Membr. Sci.* **2014**, *453*, 155–167.
(180) Kang, C.-H.; Lin, Y.-F.; Huang, Y.-S.; Tung, K.-L.; Chang, K.-S.; Chen, J.-T.; Hung, W.-S.; Lee, K.-R.; Lai, J.-Y. *J. Membr. Sci.* **2013**, *438*, 105–111.
(181) Shi, G. M.; Yang, T.; Chung, T. S. *J. Membr. Sci.* **2012**, *415–416*, 577–586.
(182) Zhang, K.; Lively, R. P.; Zhang, C.; Chance, R. R.; Koros, W. J.; Sholl, D. S.; Nair, S. *J. Phys. Chem. Lett.* **2013**, *4* (21), 3618–3622.
(183) Liu, X.-L.; Li, Y.-S.; Zhu, G.-Q.; Ban, Y.-J.; Xu, L.-Y.; Yang, W.-S. *Angew. Chem. Int. Ed.* **2011**, *50* (45), 10636–10639.
(184) Qu, X. Y.; Dong, H.; Zhou, Z. J.; Zhang, L.; Chen, H. L. *Ind. Eng. Chem. Res.* **2010**, *49* (16), 7504–7514.
(185) Awbi, H. B. *Renew. Sustain. Energy Rev.* **1998**, *2* (1–2), 157–188.
(186) Abdel-Salam, M. R. H.; Fauchoux, M.; Ge, G.; Besant, R. W.; Simonson, C. J. *Appl. Energy* **2014**, *127*, 202–218.
(187) Abdel-Salam, M. R. H.; Ge, G.; Fauchoux, M.; Besant, R. W.; Simonson, C. J. *Renew. Sustain. Energy Rev.* **2014**, *39*, 700–728.
(188) Khayet, M. *Adv. Colloid Interface Sci.* **2011**, *164* (1–2), 56–88.
(189) Woods, J. *Renew. Sustain. Energy Rev.* **2014**, *33*, 290–304.
(190) Zhang, L.-Z.; Wang, Y.-Y.; Wang, C.-L.; Xiang, H. *J. Membr. Sci.* **2008**, *308* (1–2), 198–206.
(191) Zhang, X.-R.; Zhang, L.-Z.; Liu, H.-M.; Pei, L.-X. *J. Membr. Sci.* **2011**, *366* (1–2), 158–165.
(192) Lewis, N. S.; Nocera, D. G. *Proc. Natl. Acad. Sci.* **2006**, *103* (43), 15729–15735.
(193) Carrasco, J. M.; Franquelo, L. G.; Bialasiewicz, J. T.; Galvan, E.; Guisado, R. C. P.; Prats, M. A. M.; Leon, J. I.; Moreno-Alfonso, N. *IEEE Trans. Ind. Electron.* **2006**, *53* (4), 1002–1016.
(194) Barton, J. P.; Infield, D. G. *IEEE Trans. Energy Convers.* **2004**, *19* (2), 441–448.
(195) Fenton, D. E.; Parker, J. M.; Wright, P. V. *Polymer* **1973**, *14* (11), 589.

(196) Lightfoot, P.; Mehta, M. A.; Bruce, P. G. *Science* **1993**, *262* (5135), 883–885.
(197) Hallinan, D. T.; Balsara, N. P. *Annu. Rev. Mater. Res.* **2013**, *43* (1), 503–525.
(198) Kreuer, K.-D.; Paddison, S. J.; Spohr, E.; Schuster, M. *Chem. Rev.* **2004**, *104* (10), 4637–4678.
(199) Chen, J.; Li, X.-Z.; Zhang, Q.; Michaelides, A.; Wang, E. *Phys. Chem. Chem. Phys.* **2013**, *15* (17), 6344–6349.
(200) Eigen, M. *Angew. Chem.-Int. Ed.* **1964**, *3* (1), 1 – &.
(201) G. Zundel; J. Fritsch. In *The Chemical Physics of Solvation*; R. R. Dogonadze, E. Kálmán, A. A. Kornyshev, J. Ulstrup, Eds.; Elsevier: Amsterdam, 1986; Vol. 2.
(202) Cukierman, S. *Biochim. Biophys. Acta BBA - Bioenerg.* **2006**, *1757* (8), 876–885.
(203) De Grotthuss, C. J. T. *Ann Chim* **1806**, *58*, 54–74.
(204) Markovitch, O.; Chen, H.; Izvekov, S.; Paesani, F.; Voth, G. A.; Agmon, N. *J. Phys. Chem. B* **2008**, *112* (31), 9456–9466.
(205) Marx, D. *ChemPhysChem* **2006**, *7* (9), 1848–1870.
(206) Hassanali, A.; Giberti, F.; Cuny, J.; Kühne, T. D.; Parrinello, M. *Proc. Natl. Acad. Sci.* **2013**, *110* (34), 13723–13728.
(207) Brewer, M. L.; Schmitt, U. W.; Voth, G. A. *Biophys. J.* **2001**, *80* (4), 1691–1702.
(208) Cao, Z.; Peng, Y.; Yan, T.; Li, S.; Li, A.; Voth, G. A. *J. Am. Chem. Soc.* **2010**, *132* (33), 11395–11397.
(209) Allen, F. I.; Comolli, L. R.; Kusoglu, A.; Modestino, M. A.; Minor, A. M.; Weber, A. Z. *ACS Macro Lett.* **2015**, *4* (1), 1–5.
(210) Sone, Y.; Ekdunge, P.; Simonsson, D. *J. Electrochem. Soc.* **1996**, *143* (4), 1254–1259.
(211) Mauritz, K. A.; Moore, R. B. *Chem. Rev.* **2004**, *104* (10), 4535–4586.
(212) Paddison, S. J.; Paul, R. *Phys. Chem. Chem. Phys.* **2002**, *4* (7), 1158–1163.
(213) Dellago, C.; Naor, M. M.; Hummer, G. *Phys. Rev. Lett.* **2003**, *90* (10), 105902.
(214) Day, T. J. F.; Soudackov, A. V.; Čuma, M.; Schmitt, U. W.; Voth, G. A. *J. Chem. Phys.* **2002**, *117* (12), 5839–5849.
(215) Wu, J.; Gerstandt, K.; Zhang, H.; Liu, J.; Hinds, B. J. *Nat. Nanotechnol.* **2012**, *7* (2), 133–139.
(216) Pilgrim, G. A.; Leadbetter, J. W.; Qiu, F.; Siitonen, A. J.; Pilgrim, S. M.; Krauss, T. D. *Nano Lett.* **2014**, *14* (4), 1728–1733.
(217) Baughman, R. H.; Zakhidov, A. A.; Heer, W. A. de. *Science* **2002**, *297* (5582), 787–792.
(218) Zhou, X.; Liu, G.; Yamato, K.; Shen, Y.; Cheng, R.; Wei, X.; Bai, W.; Gao, Y.; Li, H.; Liu, Y.; Liu, F.; Czajkowsky, D. M.; Wang, J.; Dabney, M. J.; Cai, Z.; Hu, J.; Bright, F. V.; He, L.; Zeng, X. C.; Shao, Z.; Gong, B. *Nat. Commun.* **2012**, *3*, 949.
(219) Kaucher, M. S.; Peterca, M.; Dulcey, A. E.; Kim, A. J.; Vinogradov, S. A.; Hammer, D. A.; Heiney, P. A.; Percec, V. *J. Am. Chem. Soc.* **2007**, *129* (38), 11698–11699.
(220) De Santis, P.; Morosetti, S.; Rizzo, R. *Macromolecules* **1974**, *7* (1), 52–58.
(221) Ghadiri, M. R.; Granja, J. R.; Buehler, L. K. *Nat. Lond. U. K.* **1994**, *369*, 301–304.
(222) Montenegro, J.; Ghadiri, M. R.; Granja, J. R. *Acc. Chem. Res.* **2013**, *46* (12), 2955–2965.
(223) Xu, T.; Zhao, N.; Ren, F.; Hourani, R.; Lee, M. T.; Shu, J. Y.; Mao, S.; Helms, B. A. *ACS Nano* **2011**, *5*, 1376–1384.

(224) Ruiz, L.; Benjamin, A.; Sullivan, M.; Keten, S. *J. Phys. Chem. Lett.* **2015**, *6* (9), 1514–1520.

(225) Hurd, J. A.; Vaidhyanathan, R.; Thangadurai, V.; Ratcliffe, C. I.; Moudrakovski, I. L.; Shimizu, G. K. H. *Nat. Chem.* **2009**, *1* (9), 705–710.

(226) Shimizu, G. K. H.; Taylor, J. M.; Kim, S. *Science* **2013**, *341* (6144), 354–355.

(227) Ramaswamy, P.; Matsuda, R.; Kosaka, W.; Akiyama, G.; Jeon, H. J.; Kitagawa, S. *Chem. Commun.* **2013**, *50* (9), 1144–1146.

(228) Horike, S.; Kamitsubo, Y.; Inukai, M.; Fukushima, T.; Umeyama, D.; Itakura, T.; Kitagawa, S. *J. Am. Chem. Soc.* **2013**, *135* (12), 4612–4615.

(229) Bureekaew, S.; Horike, S.; Higuchi, M.; Mizuno, M.; Kawamura, T.; Tanaka, D.; Yanai, N.; Kitagawa, S. *Nat. Mater.* **2009**, *8* (10), 831–836.

(230) Shimizu, G. K. H.; Vaidhyanathan, R.; Taylor, J. M. *Chem. Soc. Rev.* **2009**, *38* (5), 1430.

(231) Goesten, M. G.; Juan-Alcañiz, J.; Ramos-Fernandez, E. V.; Sai Sankar Gupta, K. B.; Stavitski, E.; van Bekkum, H.; Gascon, J.; Kapteijn, F. *J. Catal.* **2011**, *281* (1), 177–187.

(232) Taylor, J. M.; Dawson, K. W.; Shimizu, G. K. H. *J. Am. Chem. Soc.* **2013**, *135* (4), 1193–1196.

(233) Colodrero, R. M. P.; Olivera-Pastor, P.; Losilla, E. R.; Hernández-Alonso, D.; Aranda, M. A. G.; Leon-Reina, L.; Rius, J.; Demadis, K. D.; Moreau, B.; Villemin, D.; Palomino, M.; Rey, F.; Cabeza, A. *Inorg. Chem.* **2012**, *51* (14), 7689–7698.

(234) Li, S.; Zhou, Z.; Zhang, Y.; Liu, M.; Li, W. *Chem. Mater.* **2005**, *17* (24), 5884–5886.

(235) Yoon, M.; Suh, K.; Natarajan, S.; Kim, K. *Angew. Chem. Int. Ed.* **2013**, *52* (10), 2688–2700.

(236) Morozan, A.; Jaouen, F. *Energy Environ. Sci.* **2012**, *5* (11), 9269–9290.

(237) Arora, P.; Zhang, Z. (John). *Chem. Rev.* **2004**, *104* (10), 4419–4462.

(238) Xu, K. *Chem. Rev.* **2004**, *104* (10), 4303–4417.

(239) Ong, M. T.; Verners, O.; Draeger, E. W.; van Duin, A. C. T.; Lordi, V.; Pask, J. E. *J. Phys. Chem. B* **2015**, *119* (4), 1535–1545.

(240) Li, T.; Balbuena, P. B. *J. Electrochem. Soc.* **1999**, *146* (10), 3613–3622.

(241) Soetens, J.-C.; Millot, C.; Maigret, B. *J. Phys. Chem. A* **1998**, *102* (7), 1055–1061.

(242) Bhatt, M. D.; Cho, M.; Cho, K. *Model. Simul. Mater. Sci. Eng.* **2012**, *20* (6), 065004.

(243) Borodin, O.; Smith, G. D. *J. Phys. Chem. B* **2006**, *110* (10), 4971–4977.

(244) Wiers, B. M.; Foo, M.-L.; Balsara, N. P.; Long, J. R. *J. Am. Chem. Soc.* **2011**, *133* (37), 14522–14525.

(245) Ameloot, R.; Aubrey, M.; Wiers, B. M.; Gómora-Figueroa, A. P.; Patel, S. N.; Balsara, N. P.; Long, J. R. *Chem. – Eur. J.* **2013**, *19* (18), 5533–5536.

(246) Aubrey, M. L.; Ameloot, R.; Wiers, B. M.; Long, J. R. *Energy Environ. Sci.* **2014**, *7* (2), 667–671.

(247) Park, J. H.; Suh, K.; Rohman, M. R.; Hwang, W.; Yoon, M.; Kim, K. *Chem. Commun.* **2015**, *51* (45), 9313–9316.

(248) Ke, F.-S.; Wu, Y.-S.; Deng, H. *J. Solid State Chem.* **2015**, *223*, 109–121.

Chapter 2

Processable Cyclic Peptide Nanotubes with Tunable Interiors

Adapted with permission from *J. Am. Chem. Soc.*, **2011**, *133* (39), pp 15296–15299. **Copyright © 2011 American Chemical Society.**

Introduction

Organic nanotubes have unique advantages over carbon nanotubes and inorganic counterparts since their supramolecular assembly, often governed by secondary interactions, is fully reversible. They are useful building blocks to fabricate membranes for applications such as carbon capture, water desalination, and protective coatings[1-4]. There have been extensive efforts to design and synthesize nanotubes using dendrimers[5], peptides[6], peptidomimetics[7], DNAs[8], foldamers[9], and J-type rosettes[10]. However, in order to fabricate technologically relevant membranes using organic nanotubes, there are two barriers: synthesizing nanotubes with a molecularly defined size, shape, and interior chemistry to control selectivity[11–14]; and modulating the nanotube assembly process to be compatible with polymers processing toward membrane fabrication[4].

Cyclic peptides (CPs), comprised of an even number of alternating D- and L-α-amino acids, are particularly attractive since hydrogen bonding between adjacent cyclic peptides leads to stable 1-D hollow cyclic peptide nanotubes (CPNs) that exhibit transport properties similar to those seen in transmembrane proteins[15,16]. To further control mass transport through CPNs, attempts to modify their interiors have focused on incorporating artificial amino acids containing cyclohexanes and aromatic rings, or unsaturated amino acids at multiple positions in the canonical CP sequence to project a specific chemical functionality toward the pore interior[11–14,17–29]. Most of these approaches involve amino acid derivatives that are synthetically nontrivial, making it difficult to fabricate membranes at large scales. Synthesizing CPs using the solid phase peptide synthesis (SPPS) methodologies provides full control of the number and location of modifications in the peptide sequence[30]. These aspects of the synthesis are particularly important to modify the exterior of CPNs for dispersion and directed nanotube growth in polymeric matrices. Also, the number and placement of noncannonical amino acids can have undesirable effects on the conformation of the ring and its potential for self-assembly. In many cases, the CP ring contorts owing to ring strain or otherwise rotates the backbone amide bonds. As a result, the efficacy of inter-ring hydrogen bonding is reduced and, in some cases, the formation of high aspect ratio CPNs is compromised.

Prototypical CPs have a strong tendency to form nanotube aggregates that are highly insoluble[31–35]. The solubility and the aspect ratio of CPNs can be tailored by attaching polymers to the exterior of nanotubes[36–38]. However, due to the obvious difficulties in vertically aligning 1-D nanotubes with a high aspect ratio in thin films, as is required for membrane fabrication, there is a need to modulate the assembly of CPN growth in a confined framework to macroscopically align nanotubes. There may also be additional opportunities to modulate the assembly through structural modifications to the primary sequence[4].

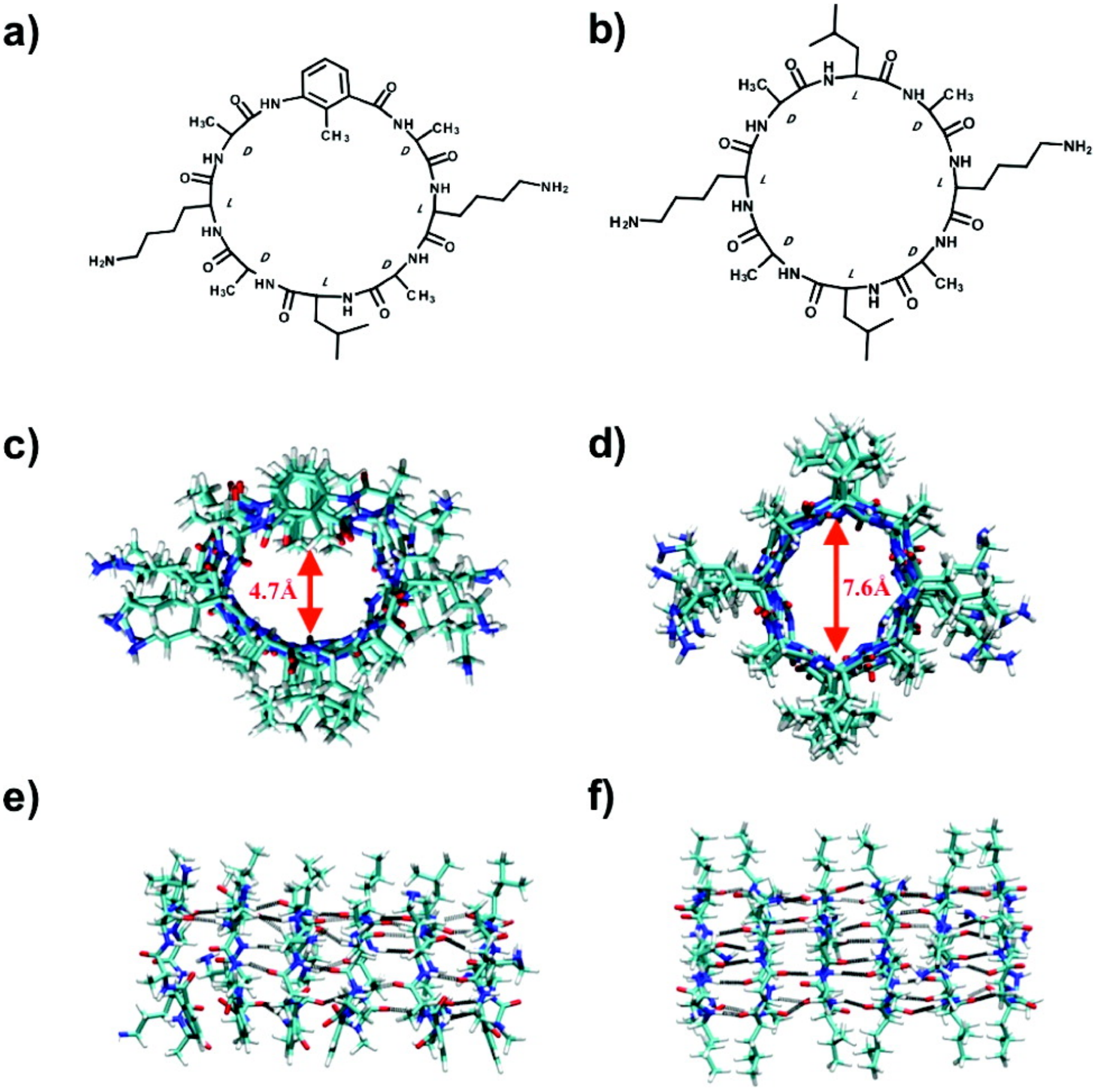

Figure 2.1 Chemical structures of (a) Mba-8CP and (b) its conventional analogue 8CP; Snapshots of equilibrium structures calculated from molecular dynamics (MD) simulations, showing cross-sectional (c,d) and lateral (e,f) views of Mba-8CP and 8CP nanotubes respectively. The internal diameters of Mba-8CP and 8CP are ~4.7 and ~7.6 Å, respectively, based on van der Waals radii.

We present here a minimalist approach that overcomes barriers to both generate peptide nanotubes with interior modification and dynamically tune the assembly process within the processing window of polymeric membranes. As an initial demonstration, a methyl group is introduced to the interior, although other functional groups might also be incorporated using orthogonal peptide chemistries and will be explored separately[39,40]. This was achieved by substituting one of the L-Leu in the primary sequence of a protypical CP sequence cyclo-[L-Lys-D-Ala-L-Leu-D-Ala]2 (8CP) using a single aromatic amino acid, 3-amino-2-methylbenzoic acid (γ-Mba-OH). The chemical structure of the Mba-modified cyclic peptide, *cyclo*-(L-Lys-D-Ala-L-Leu-D-Ala-L-Lys-D-Ala-γ-Mba-D-Ala) (Mba-8CP, **Figure 2.1**a), is shown alongside the 8CP (**Figure 2.1**b) for comparison.

Results

3-(9-Fluorenylmethyloxycarbonyl)amino-2-methylbenzoic acid (Fmoc-γ-Mba-OH) was prepared from 3-amino-2-methylbenzoic acid and *N*-(9-fluorenylmethoxy-carbonyloxy) succinimide (Fmoc-OSu) in 80% yield. Both starting materials are commercially available, and the resulting Fmoc-protected amino acid can be made in large quantities and readily used in the SPPS. Mba-8CP and 8CP were synthesized on and cleaved from a 2-chlorotrityl chloride resin prior to head-to-tail cyclization at high dilution in the presence of propane phosphonic acid anhydride (T3P) in 85% yield. After deprotection of the Boc groups on the lysine side chains, the crude materials were purified using preparative HPLC in an overall yield of 30%.

Molecular dynamics (MD) simulations were carried out to compare the structure and stability of the assemblies of Mba-8CP and 8CP. The simulations were performed using the COMPASS force field. Top views and side views of the equilibrated structures obtained from MD simulations are shown in **Figure 2.1**c–f. For Mba-8CP, the L-Leu to γ-Mba mutation points the methyl group into the interior of the pore as designed. This prominent hydrophobic group substantially reduces the internal diameter which is estimated to be ~4.7 ± 0.6 Å based on van der Waals radii (**Figure 2.1**c), a 38% reduction in size from the 7.6 Å pore size of the 8CP nanotube (**Figure 2.1**d). The aromatic rings of γ-Mba-OH are configured along one side of the nanotube, with slight tilts. The lateral views (**Figure 2.1**e,f) of the formed nanotubes showed that the mutation disproportionately elongates the ring structure and disrupts the symmetry of its amide bonds, and consequently the alignment of the carbonyl and amide groups in the antiparallel assembly. As a result, the number of hydrogen bonds between adjacent cyclic peptide rings is reduced from an average of 7.3 hydrogen bonds for 8CP to 5.9 for Mba-8CP. The average inter-ring distance is 4.8 Å in both cases (**Figure 2.S1**).

Mba-8CP readily assembles into nanotubes in acetonitrile (ACN). Inter-ring hydrogen bonding for Mba-8CP was clearly observed at 3284 cm^{-1} using Fourier transform infrared (FT-IR) spectroscopy (**Figure 2.2**a). Characteristic peaks for the amide Ia, amide Ib, and amide II regions at ν 1673, 1628, and 1538 cm^{-1} were consistent with those reported for 8CP[41–43]. Transmission electron microscopy (TEM) revealed bundles of nanotubes, ~100–500 nm in length (**Figure 2.2**b). The width of the bundles is between 20 and 40 nm, which corresponds to approximately over 20 individual Mba-8CPNs in a single aggregate. The dynamic light scattering (DLS) profile of Mba-8CP showed a nominal nanotube length of 235 nm, slightly smaller than that of 377 nm for 8CP (**Figure 2.S2**).

Detailed spectroscopic characterizations using ^{1}H and ^{1}H–^{1}H-COSY (**Figure 2.S3**) NMR experiments were used to confirm the structure of Mba-8CP. A through-space 2D NOESY experiment was also carried out on a molecularly dissolved (i.e., disassembled) sample in DMSO to determine the orientation of the substituent at the 2-position of the aromatic amino acid in the modified CP (**Figure 2.S4**). The methyl group of γ-Mba-OH at δ 2.19 ppm showed distinctive through-space interactions with each of the amide resonances in the CP backbone between 7.80 and 9.20 ppm (**Figure 2.3**a). This correlation was absent for the aromatic protons, except for the two neighboring amide protons on either side of the aromatic ring (**Figure 2.3**b). Similar studies were carried out in the ACN solution but were unsuccessful. The 2D NOSEY results reflect the solution conformation of the Mba-8CP, which most likely represent the favorable conformation of the monomer in a CPN. This agrees well with the MD simulation that the methyl group was directed toward the inside of the CPN, while the aromatic protons were directed outward. Thus, by simply inserting this single aromatic amino acid into the primary sequence of the cyclic peptide 8-mer, its associated functional groups were presented in the interior of the nanotubes without compromising the formation of high aspect ratio assemblies. Theoretical calculations were also carried out to investigate the incorporation of two or more unnatural amino acids in the modified cyclic peptides. However, introduction of multiple modifications lead to either blocked pores or puckered cyclic peptide structures largely incapable of assembling into CPNs, as illustrated in **Figure 2.S5**.

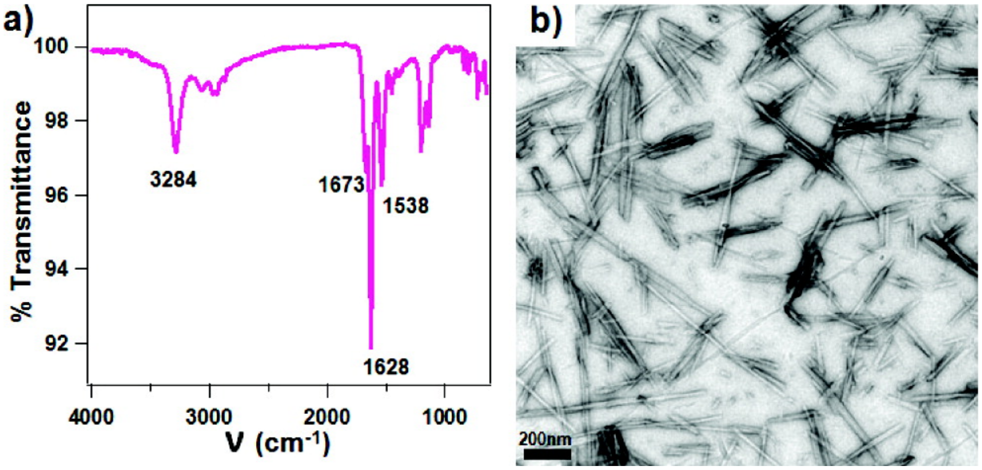

Figure 2.2 (a) FTIR spectrum of a thin film of Mba-8CP cast from ACN at room temperature. (b) TEM image of Mba-8CP nanotubes that aggregated into bundles, likely during the drying process. Scale bar: 200 nm.

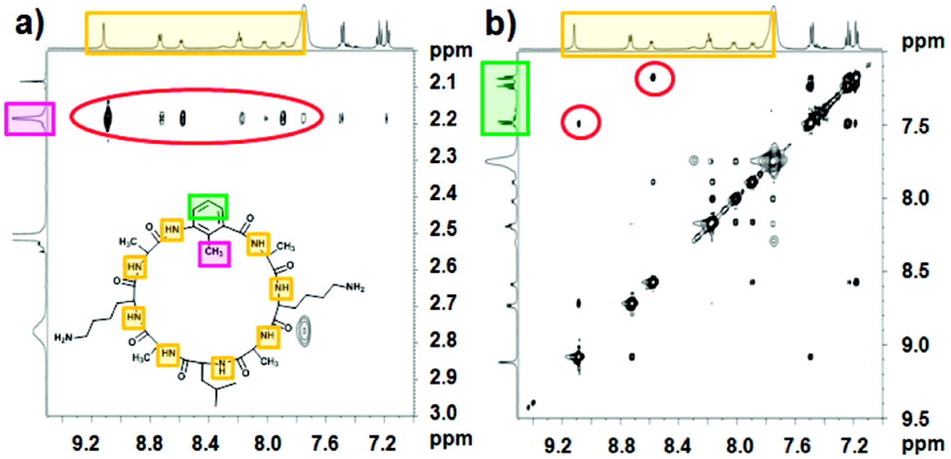

Figure 2.3 2D NOESY spectra in d_6-DMSO of molecularly dissolved Mba-8CP indicating the through space correlations between the aromatic methyl group's protons in purple (a) and the aromatic protons in red (b) with the proton resonances of the amides in orange. The key cross-peaks are shown in red.

The mutation in the Mba-8CP sequence also suppressed to some extent the nanotube growth. The solution phase assembly of Mba-8CP was studied as a function of concentration and temperature using circular dichroism (CD) spectroscopy. CPNs from Mba-8CP in ACN showed a distinctive negative Cotton effect at $\lambda = 210$ nm (**Figure 2.4**a). Increasing the concentration of Mba-8CP increased the intensity of the CD signal at 210 nm, toward a plateau at ~40 μM. The dissociation constant K_d was found to be 21 ± 5 μM. The assembly process of Mba-8CP was determined to be completely thermoreversible within the experimental conditions applied. **Figure 2.4**b relates the magnitude of the Cotton effect at 210 nm for Mba-CP derived nanotubes in ACN at different concentrations upon heating from 20 to 70 °C. The effect of temperature on the CD signal profile was dependent on the concentration of the Mba-8CP. As the temperature is increased, the CD signals of all profiles approach a similar equilibrium state closer to the molecularly dissolved state. Similar studies with the regular 8CP could not be achieved due to its lower solubility and much stronger hydrogen bonding among the rings, which showed little thermal losses in the CD signal. The dependence of the reversible assembly process on concentration and temperature in the case of CPNs derived from Mba-8CP points to distinct opportunities to process smooth polymer thin films from solution.

To ensure the reversible assembly process of Mba-8CP does not compromise the formation of high aspect ratio CPNs, we monitored the nanotube growth using polyethylene glycol (PEG)-covered CPNs of Mba-8CP. HO-PEG-$NHCOCH_2CH_2COOH$ ($M_w = 3000$ g/mol) was conjugated to Mba-8CP by coupling to the amino groups of lysine residues of Mba-8CP as described previously[4]. The nanotube growth process of PEG-conjugated Mba-8CP in the solid state was studied *in situ* using FTIR spectroscopy by monitoring the N–H stretching vibration at 3292 cm^{-1}upon heating from 30 to 180 °C. The nanotubes reformed upon cooling with only a slight hysteresis (**Figure 2.5**a). Upon spin-casting onto a silicon substrate with a native silicon oxide layer, the PEG-conjugated Mba-8CPNs that are 50–150 nm in length can be easily visualized (**Figure 2.5**b). The width of the formed nanotube is ~5.5 nm (the height is ~0.5 nm), which corresponds to individual PEG-covered Mba-8CPNs[36–38]. This confirms the advantage of attaching polymers to CPNs in reducing their tendency to aggregate, hence rendering them more processable. The assembly of the casted CPNs can be readily disrupted by thermal or solvent annealing; typical treatments to prepare polymeric membranes (**Figure 2.5**c). The high aspect ratio nanotubes reform upon thermal annealing followed by slow cooling (**Figure 2.5**d).

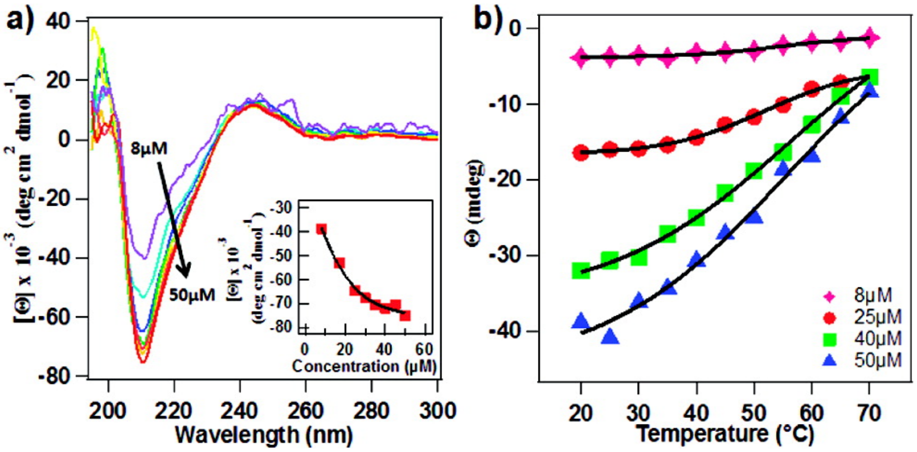

Figure 2.4 (a) CD spectra of Mba-8CP in ACN at different concentrations upon heating from 20 to 70 °C. The inset illustrates the dependence of molar ellipticity at 210 nm as a function of concentration. (b) The CD signal of Mba-8CP in ACN at 210 nm as a function of temperature for different concentrations. The heating rate is 5 °C/min with an equilibration time of 5 min.

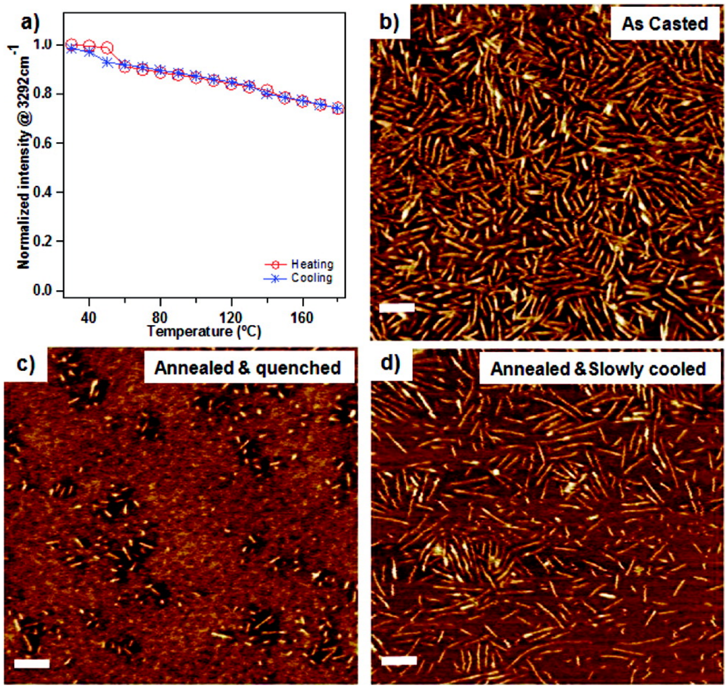

Figure 2.5 (a) Normalized absorptions of PEG-conjugated Mba-8CP for the heating and cooling cycles (30–180 °C) as a function of temperature using the intensity of the peak maximum at $\upsilon = 3292$ cm^{-1} at 30 °C. AFM images of a spin-casted THF solution of PEG-conjugated Mba-8CP nanotubes (b), followed by solvent-annealing and quenching (c), followed by thermal annealing at 80 °C for 1 h and slow cooling (d) (Scale bar: 50 nm). Reversible growth of high aspect ratio PEG-covered CPNs of Mba-8CP can be clearly seen.

Diversification of Interior Functionalization

Syntheses of 2-substituted-3-aminobenzoic acid precursors

Building upon the previous success, I have synthesized a set of non-canonical amino acids as part of an ongoing research effort focusing on functionalizing the interior of these cyclic peptide rings as a means to access unexplored transport regimes. These specific functionalities will add to the molecular sieving property of nanotubes to further discriminate moieties, allowing the system to transport specific analytes at high flux. Amines, regardless of substitution have been the standard functionality for CO_2 capture[44] and work in the related metal organic framework[45–47] has demonstrated that amines are an essential motif in this regard. On the other hand, in the energy storage sector, selective transport of ions is crucial. Biological channels achieved this goal with carboxylate and carboxamide functionalities[48,49]. We are interested in realizing the same motifs in a polymeric thin-film membrane containing cyclic peptide nanotubes. We hope to not only achieve high selectivity, but also high flux due to both the short diffusion paths and straight pores. Thus we aim to synthesize cyclic peptides with primary amine and carboxylic acid respectively and assess their transport properties.

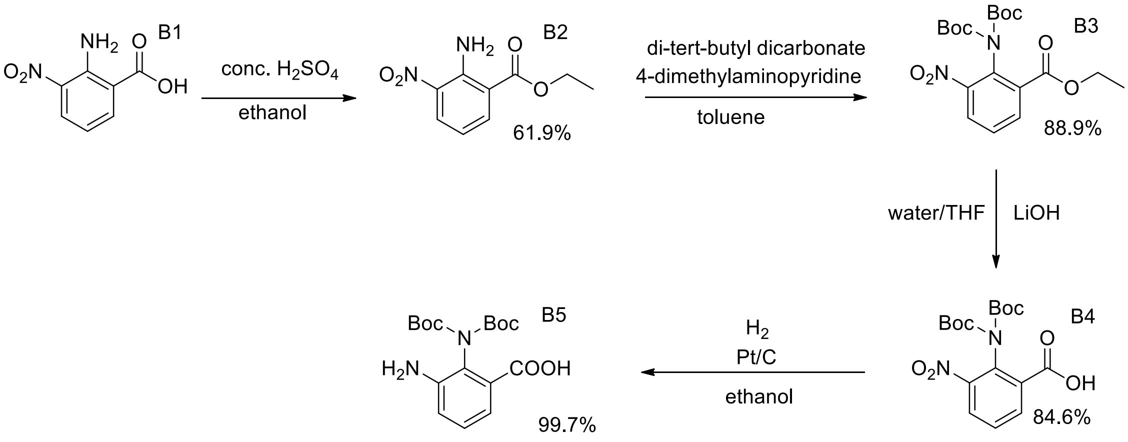

Figure 2.6 Synthesis of amine-functionalized non-canonical amino acid, B5. DCM is dichloromethane.

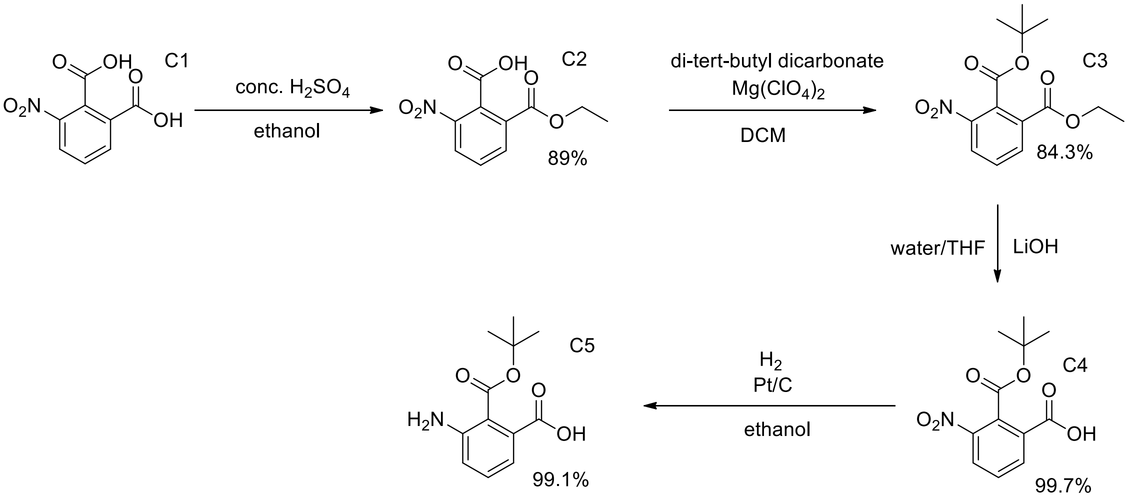

Figure 2.7 Synthesis of the carboxylate-functionalized non-canonical amino acid, C5. THF is tetrahydrofuran.

The second non-canonical amino acid (B5, **Figure 2.6**) synthesized aimed to project a primary amine towards the interior of the resultant cyclic peptide nanotubes (CP-B). To avoid the steric bulk of substituted amines, a primary amine was chosen. In addition, from the simulation performed by our collaborator[50], employing 2,3-diaminobenzoic acid as the non-canonical amino acid in the cyclic peptide sequence would lead to greater nanotube stability compared to our previously reported methyl-interior-modified cyclic peptide nanotubes. In the meantime, a carboxylic acid-functionalized aminobenzoic acid (C5, **Figure 2.7**) was also synthesized. As the polar opposite of Unit B, which exhibited a nucleophilic species, it featured an electrophilic group. Inspired by biological ion channels, it is primarily motivated by having a self-assembled framework to conduct ions, which will lead to applications in energy storage.

As we moved from an inert methyl group towards a reactive primary amine or a carboxylic acid, it became necessary to use protecting groups to preserve functionalities and avoid side reactions. In order to be compatible with the ensuing 9-fluorenylmethyl carbamate (Fmoc) solid phase peptide synthesis, tert-butyloxycarbonyl (Boc) and tert-butyl ester (tBu) were used in the synthetic schemes for the precursor aminobenzoic acids based on amine and carboxylate groups, respectively in the 2-position. For the amino group needed at the 3-position, a nitro group was chosen as a pseudo-protecting group for the amine due to the quantitative interconversion using platinum-catalyzed hydrogenation, which also tolerates both Boc- and tBu-protected moieties mentioned above for B5 and C5. In all cases, synthetic routes were devised using starting materials which were both inexpensive and available commercially in large quantities, which would allow for economical scale-ups when technologies based on these materials are ready for deployment. In some cases, individual steps in the syntheses were adapted from previous work on related compounds of similar structure[51–53]. Most of the intermediates in the synthetic plans were purified via recrystallization with minimal usage of column chromatography.

Fmoc solid phase peptide synthesis

The majority of coupling chemistry was done using Fmoc solid phase peptide synthesis. Compared to the traditional Boc solid phase peptide synthesis, the Fmoc alternative utilized a set of orthogonal protecting groups which were labile at milder conditions, avoiding the use of hydrofluoric acid as the final cleavage step. In our experiments, the resin of choice was 2-chlorotrityl chloride resin. It provided an efficient cleavage (1~2% trifluoroacetic acid) while leaving all the protecting groups intact. The resin was manually functionalized with the first amino acid in the sequence, D-alanine. This was followed by the manual coupling of the 2-substituted-3-aminobenzoic acid and a third residue, which was also a D-alanine. The typical cyclic peptide macrocycle consisted of eight amino acids, one of which was replaced by one of the units synthesized above. The insertion of the aminobenzoic acid into the sequence preserved the longest chain of D,L-alternating amino acids possible, which would follow its natural secondary structure and brings together the *N* and *C* termini, facilitating the cyclization reaction later on. Two approaches to installing the amino-functionalized aminobenzoic acids were investigated.

The first approach (**Figure 2.8**, top) attempted was of a step-wise nature. Analogous to conventional solid phase peptide synthesis, one residue was added at a time sequentially. This method was adequate for synthesizing the cyclic peptide with a methyl interior projection due to the appreciable reactivity of the two termini of the aminobenzoic acid. In our experience, the aminobenzoic acids with amine and carboxylic acid projections (B5 and C5) suffered from drastically reduced reactivity compared to their predecessor. The difficulty was attributed to the steric effects of the tert-butyl groups and the electron-withdrawing nature of the substituents. Even though the carboxylic acid terminus of the aminobenzoic acid attached onto the D-alanine-functionalized resin with seemingly high yield, the amine terminus showed less than 5% yield when it was coupled to the next residue, regardless of reaction condition, coupling reagent and solvent system.

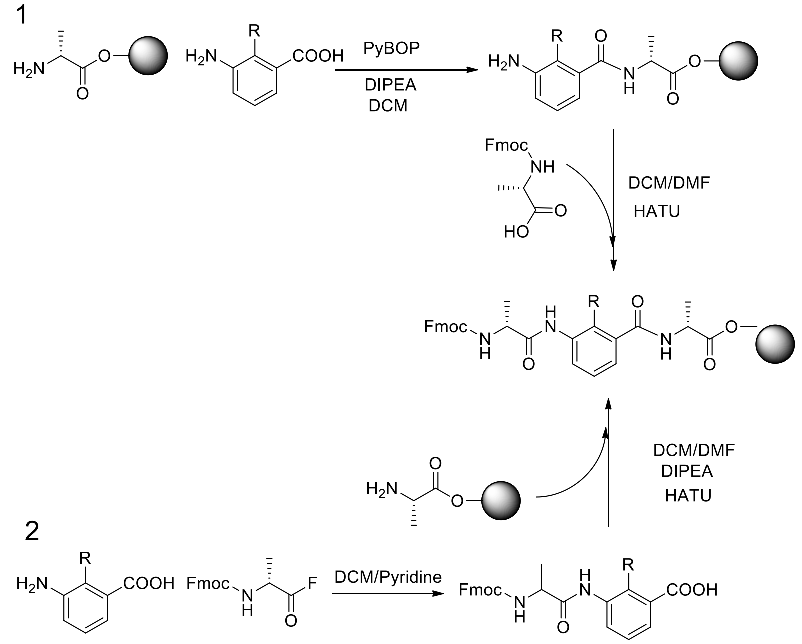

Figure 2.8 The two approaches to immobilizing 2-substituted-3-aminobenzoic acid on resin. DCM is dichloromethane, DMF is dimethylformamide. HATU is 2-(*1H*-7-Aza-benzotriazol-1-yl)--1,1,3,3-tetramethyl uronium hexafluorophosphate Methanamini-um. PyBOP is Benzotriazol-1-yl-oxytripyrrolidinophosphonium hexafluorophosphate.

The second approach (**Figure 2.8**, bottom) isolated the problematic reaction center, aryl amine, and applied harsher conditions to coerce the amide formation. Specifically, a dipeptide was first generated in solution, which was then subsequently linked to the D-alanine-functionalized resin. Acid fluoride activation was found to be sufficiently potent and compact for bond formation, overcoming the inert nature of an electronically deficient and sterically hindered nucleophile. Pure dipeptides were separated, subsequently coupled onto the D-alanine-functionalized resin.

After the trimer sequence was generated on resin manually, standard solid phase peptide synthesis protocol was used to complete the peptide sequence. So far the model system is limited to an eight-peptide sequence of *K-A-L-A-K-A-M-A* where M represented the insertion site of B5. Linear sequence containing B5 was synthesized and confirmed by MALDI (**Figure 2.Error**! Bookmark not defined.).

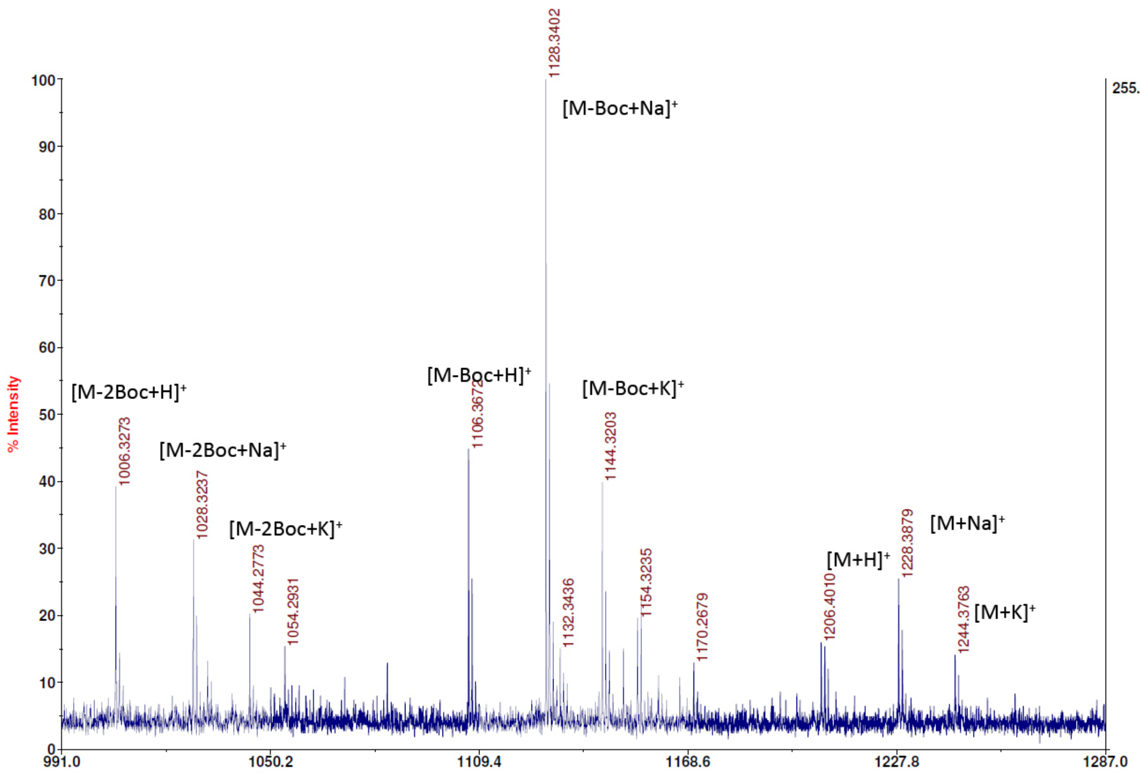

Figure 2. Error! Bookmark not defined. MALDI-TOF spectrum of the linear peptide sequence containing B5. Major peaks are assigned and noted. These include the molecular species and deblocked products. Calculated [M+H]$^+$: 1206.70; Found: 1206.40.

Deprotection and Subsequent Rearrangement

After peptide synthesis, conventional Boc procedure was carried out to accomplish deblocking. However, the strongly acidic environment that it demanded allowed for rapid intramolecular condensation. Multiple alternative deblocking methods have been attempted to circumvent the irreversible rearrangement to no avail. The condensation products resulted a benzimidazole moiety in the peptide backbone (**Figure 2.9**).

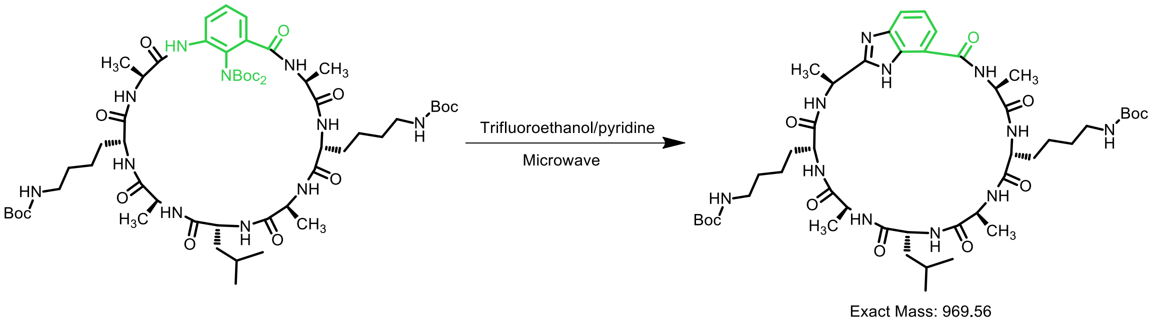

Figure 2.9 Deblocking and subsequent intramolecular condensation of CP-B.

The structure of the benzimidazole-functionalized cyclic peptide was confirmed with the combination of COrrelation SpectroscopY (COSY) and Nuclear Overhauser Effect SpectroscopY (NOESY), validated by MALDI. COSY is a 2D NMR technique which correlates NMR-active nuclei, proton in this case, through bonds. On the other hand, NOESY correlates these nuclei through spatial proximity. The combination of the two 2D NMR techniques is frequently used in protein sequence analysis by alternatingly correlating amide protons with α protons (**Figure 2.10**). All amide protons and α protons are accounted for within the region. Further identifications of specific amino acids can be traced by the correlations between side chain protons and α protons. However the imidazole proton has been elusive, possibly due to the its delocalized nature.

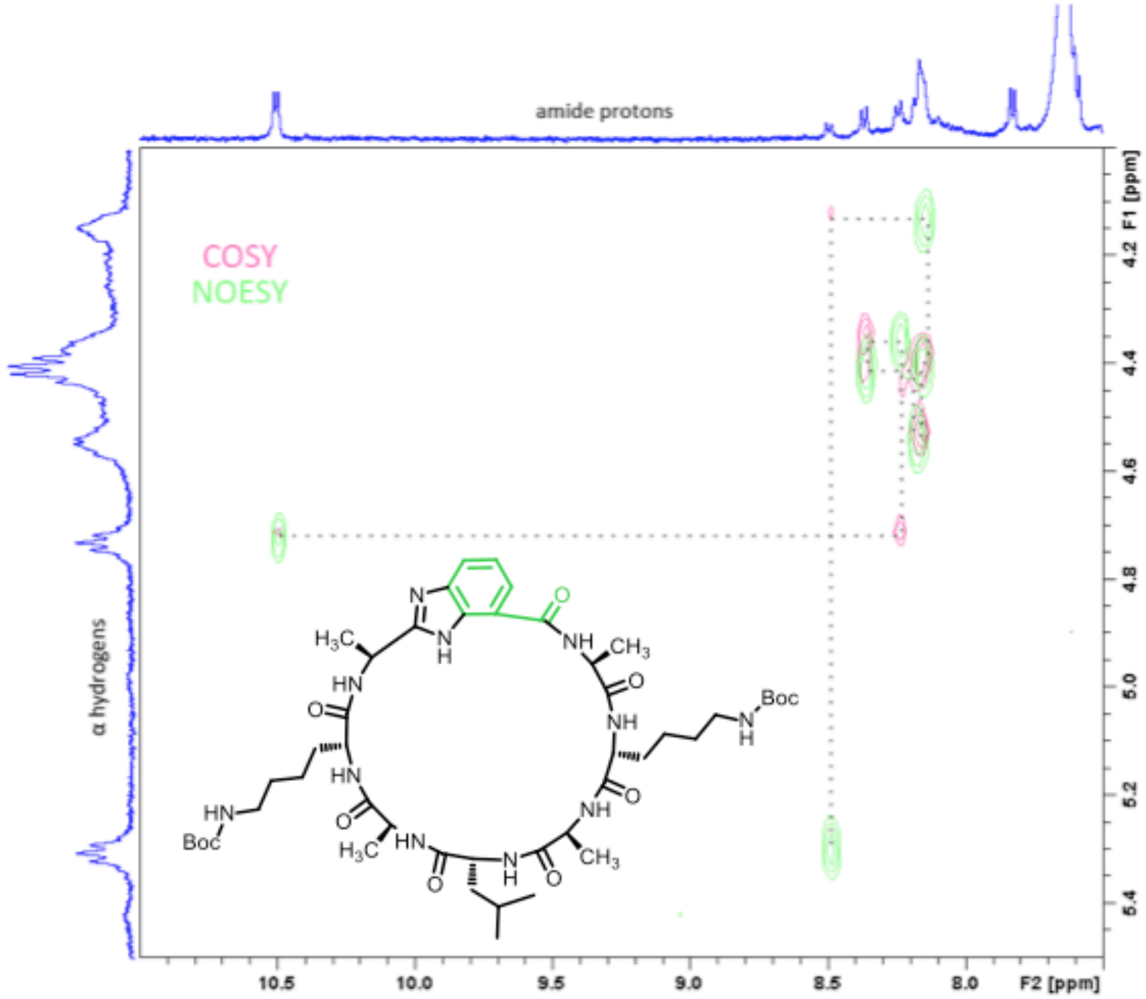

Figure 2.10 Superimposed COSY/NOESY spectra of relevant backbone proton regions. Correlations between α protons and side chain protons are outside of the shown region.

The inception of benzimidazole, imbued the CP with pH-switching ability. The doubly-protonated/charged state could disrupt the native self-assembly behavior of the CP backbone, allowing for a dynamic assembly system. Preliminary pH switching was investigated using UV/vis spectroscopy with phosphate buffer. As pH increases, multiple isosbestic emerged, indicative a two state protonation system (**Figure 2.11**). Two select wavelength were chosen for a more quantitative measure of the switching characteristics (**Figure 2.12**). By fitting the sigmoidal curves, pKa of 4.9 was extracted, which was comparable to published pKa values of benzimidazole derivatives[54].

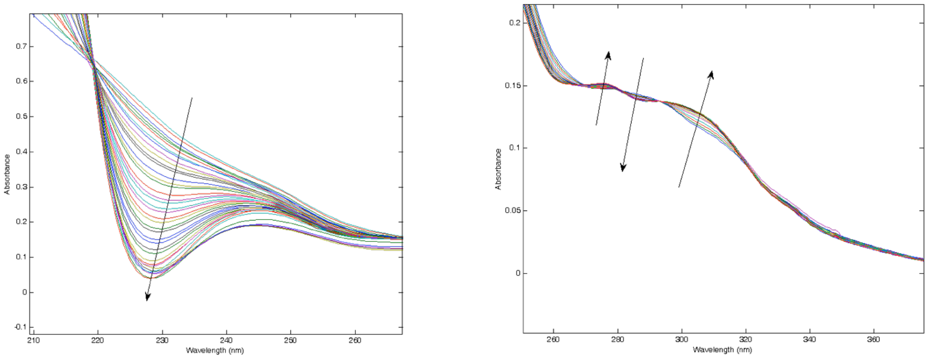

Figure 2.11 UV/vis spectra of benzimidazole-functionalized CP at various pHs. The arrows indicate the direction of higher pH.

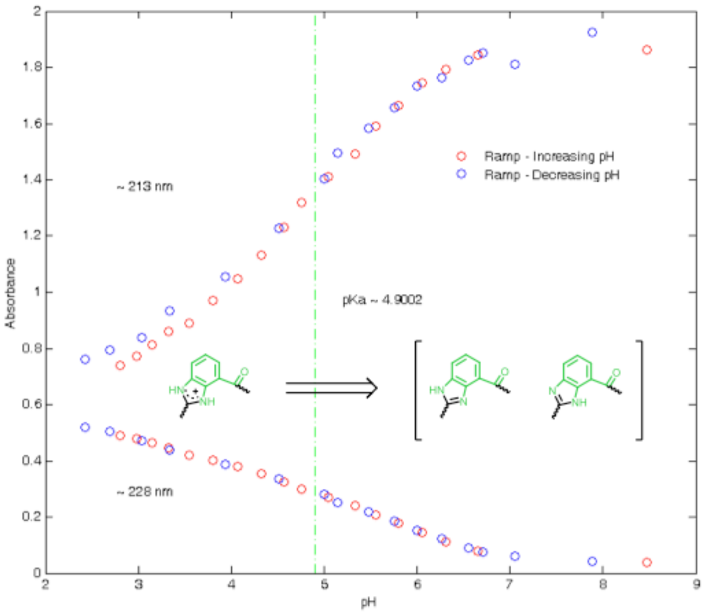

Figure 2.12 Absorbances at 213 nm and 228 nm respectively. Both traces exhibit reversible pH switching between two states.

Conclusion

Since the assembly of cyclic peptides is a highly directional 1-D growth process and the overall properties of nanotubes are influenced by the molecular scale building blocks, we see a viable path toward organic nanotubes with molecularly defined interiors to mimic transmembrane proteins for enhanced selectivity in molecular recognition, transport, and separation processes. The added advantage of this new design is the ability to manipulate the nanotube formation to be compatible with the processing window of polymeric membranes so that subunits or short nanotubes, rather than high aspect ratio nanotubes, can be incorporated into a polymer matrix and, subsequently, grow nanotubes *in situ* to fabricate functional membranes.

Additional functionalization has been carried out to moderate transport within the next generation of self-assembled cyclic peptide nanotubes. Our first attempt lead to the benzimidazole-functionalized CP. After thoroughly validating the structure using MALDI and 2D NMR, the pH switching ability of this CP was directly probed using UV/vis spectroscopy, yielding a pKa similar to small molecular benzimidazole derivatives. At the same time, the precursor (C5) to carboxylate-functionalized CP was synthesized and the associated CP was well within reach.

Supporting Information

Materials & Methods

Fmoc-D-Ala-OH, Fmoc-L-Lys(Boc)-OH, Fmoc-L-Leu-OH, polystyrene-(2-chlorotrityl) resin (loading: 1.5 mmol/g), and 2-(6-Chloro-1H-benzotriazole-1-yl)-1,1,3,3-tetramethylaminium hexafluorophosphate (HCTU) were purchased from Nova Biochem. 2-Propanephosphonic acid anhydride (T3P) in DMF was purchased from Advanced ChemTech. 3-amino-2-methylbenzoic acid (**B**), Carboxylic acid-terminated polyethylene glycol (PEG) (HO-PEG-NHCOCH2CH2COOH) (Mw=3000 g/mol) was purchased from Rapp Polymere, 2-amino-3-nitrobenzoic acid (B1) was purchased from Matrix Scientific. All of the solvents used were freshly acquired from a JC Meyer Solvent Purification System. PEG-covered CPNs of Mba-8CP were prepared as described previously using 2 equivalents of PEG to the Mba-8CP, N-(9-fluorenylmethoxycarbonyloxy)succinimide (Fmoc-OSu), and all other reagents were purchased from Aldrich without further purification. All solvents used were of HPLC grade. The ^{1}H NMR spectra were recorded on a Bruker 500 UltraShield™ spectrometer. The MALDI-TOF spectra were recorded on an Applied Biosystems 4800 MALDI TOF/TOF spectrometer. The UV/vis absorption spectra were recorded on a Varian Cary 5000 UV-Vis-NIR spectrophotometer.

Solid Phase Peptide Synthesis was performed on a Protein Technologies Prelude solid phase synthesizer using standard 9-fluorenylmethyl carbamate (Fmoc) protection chemistry and HCTU as coupling reagent.

Analytical HPLC was performed on a C18 column (Vydac), 0-50% ACN in H2O over 30 minutes at a flow rate of 1 mL min^{-1} using a Varian Prostar 335 CC UV detector. Peptides were purified by RP-HPLC (Beckman Coulter) on a C18 column (Vydac). The flow rate was 10 mL min^{-1} for semipreparative runs and peptides were injected at a concentration of 10 mg/mL. Peptide elution was monitored with a diode array detector at wavelengths of 220 and 280 nm. Water-soluble conjugates were eluted with a linear AB gradient, where solvent A consisted of MilliQ water containing 0.1% v/v TFA and solvent B consisted of acetonitrile containing 0.1% v/v TFA. UV-Vis spectra were recorded on a Varian 5000 UV-VIS-NIR spectrophotometer. Matrix-assisted laser desorption/ionization time-of-flight (MALDI-ToF) mass spectrometry has been performed on an Applied Biosystems 4800 MALDI-ToF/ToF Analyzer. All spectra were recorded in positive ion mode operating in reflector mode. **Circular dichroism (CD)** and UV-Vis spectra were recorded on a Jasco J-815 CD spectrophotometer equipped with a Jasco PTC- 4245/15 cooling element. DLS measurements were performed on a Malvern Zetasizer ZS. **FT-IR** spectra were recorded on a Perkin Elmer Spotlight 200 FTIR Microscope System. **Transmission electron microscopy (TEM)** samples were prepared from solutions of the lyophilized materials in ACN at concentration of 0.25mg/mL by placing 5 µl of the peptide suspension on holey carbon-coated copper grid (TED Pella 01824) for 10 seconds before removing the excess solution by filter paper blotting. The sample on the grid was negatively stained with a 2% (w/v) phosphotungstic acid (adjusted to pH = 3 with NaOH) for 10 seconds. Excess stain solution was wicked off. TEM images were collected on a FEI Tecnai 12 transmission electron microscope at an accelerating voltage of 120 kV. **Tapping mode AFM** images were collected using silicon cantilevers (RTESP from Veeco, Inc.) with a resonant frequency of 255 Hz. ATR-FTIR spectra were collected using a NICOLET 6700 FT-IR Spectrometer. **Molecular Modeling** calculations were performed using HyperChem software, where the optimized molecular models were generated using the Molecular Mechanics method with the MM+ force field[55,56]. The geometry optimization was carried out using the Polak–Ribiere conjugate gradient, set to terminate at an RMS gradient of 0.01 kcal Å^{-1} mol^{-1}.

Molecular Dynamics Simulations: A wide range of computational approaches such as molecular dynamics (MD)[57–64] or quantum mechanics methods[65–70] have been employed in earlier studies of CPNs. Encouraged by earlier MD studies that corroborated experimental data such as pore size, intersubunit distances, and crystal structure lattice constants, we carried out MD simulations to obtain long time scale dynamical data on nanotube structure and stability in non-S3 periodic, explicit solvent conditions relevant to self-assembly in solution, taking into account short as well as long-range interactions.

Initial coordinates for the CP subunit structures were taken from optimized geometries calculated using MM+ force field in HyperChem. Molecular Dynamics simulations were carried out in Materials Studio using the ab-initio based COMPASS[71] force field. In order to explore the conformational space and find the minimum energy configuration of the CP monomers in the tubular morphology, three subunits were stacked and subjected to five annealing cycles with a temperature range of 298K to 600K in the NVT ensemble, where each cycle was followed by minimization calculations. The final configuration of the central subunit was selected to build the CPNs used for equilibration simulations. The structures computed from these final equilibration runs were used for the comparative analysis. CPNs were composed of eight subunits stacked in an antiparallel fashion. These simulations were carried out in an isothermal-isobaric ensemble (NPT) with the Berendsen method and the Nose thermostat to control pressure and temperature at 1 atm and 298 K respectively. The system is solvated in explicit water and periodic boundary conditions are employed for a cubic box that is 50Åx30Åx30Å. To calculate the electrostatic interactions and the Van der Waals forces, we use the Ewald summation method with a repulsive cutoff of 6 Å and a cutoff distance of 12.5 Å. The time-step is fixed to 1 fs and the total duration of the simulations is 1.5 ns. Post-processing was done using Visual Molecular Dynamics[72] (VMD) and .tcl scripts. The cutoff distance for the hydrogen bonds was 3.4 Å and the minimum D-H-A angle for bond formation is taken as 130°. The inter-subunit distance was calculated as the center of mass distance between the alpha-carbon atoms of each subunit. For all calculations, measurements are taken every 2 ps, excluding the first 200 ps of the equilibration runs.

Compounds Synthesis & Characterization

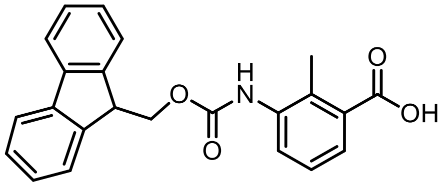

Synthesis of Fmoc-Mba-OH: Sodium bicarbonate (3.84 g, 45.7 mmol) was added slowly to an aqueous solution (50 mL) of 3-amino-2-methylbenzoic acid (γ-Mba) (10.0 g, 29.7 mmol). The resulting solution was cooled in an ice bath, and N-(9-fluorenylmethoxycarbonyloxy)succinimide (Fmoc-OSu) (3.45 g, 22.8 mmol) was added slowly as a solution in p-dioxane (50 mL). The solution mixture was left to stir at 0 °C for 1 h, and then was left to stir at RT overnight. Water (50 mL) was added, and the aqueous solution was extracted 3 times with ethyl acetate (150 mL). The organic layer was washed twice with saturated solution of sodium bicarbonate (100 mL). The aqueous layers were combined, and the resulting solution was acidified to pH 1 by addition of 1 M HCl. The acidified solution was then extracted with 3 x 50 mL portions of ethyl acetate. The organic layers were combined, dried over sodium sulfate, filtered and solvent was evaporated in vacuum. The product was redissolved in minimal amount of THF, and dried under vacuum. The product was obtained as a white solid (6.80g, 80%). ^{1}H NMR (500 MHz, DMSO-d_6): δ (ppm) 2.32 (s, 3H), 4.29 (s, broad, 1H), 4.44 (d, *J* = 8.8 Hz, 2H), 7.23 (t, *J* = 7.5 Hz, 1H), 7.34 (m, 3H), 7.43 (t, *J* =7.6 Hz, 2H), 7.56 (d, *J* =7.5 Hz, 1H), 7.72 (s, broad, 2H), 7.90 (d, *J* = 7.5 Hz, 2H), 9.16 (s, 1H), 12.96 (s, 1H). 13C{1 H} NMR (125 MHz, DMSO-d_6): δ 15.5, 47.2, S4 66.1, 120.6, 125.6, 126.0, 127.1, 127.5, 128.1, 129.4, 133.2, 133.6, 137.6, 141.2, 144.2, 154.9, 169.6. MALDI-TOF for C23H19NO4 Calculated: 374.13 [M+H]$^+$; Found 374.21.

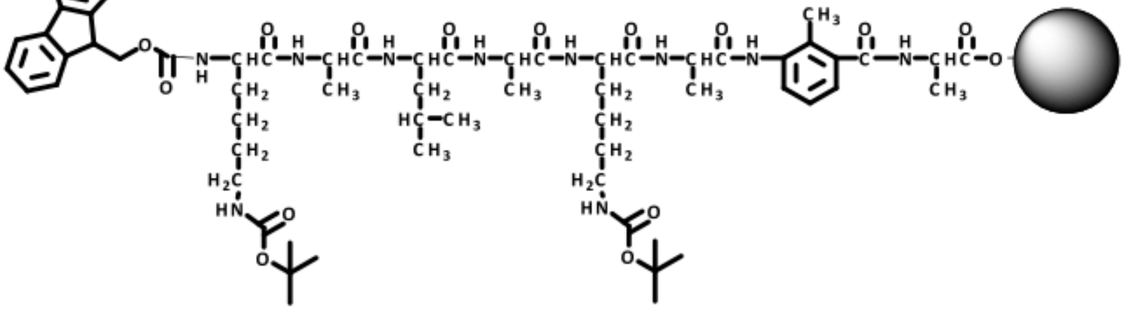

Procedure for solid phase peptide synthesis: 2-Chlorotrityl chloride resin was swelled for two hours in DMF. Fmoc-D-Ala-OH (2 eq.) was dissolved in DMF and DIPEA (4 eq.) was added. The amino acid mixture was added to the resin suspension and stirred for two hours. Methanol was then added to block remaining chloride residues. The resin was filtered and washed with DMF, DCM and methanol, and left to dry under vacuum. The Fmoc protecting group was then removed by stirring the resin in 20% v/v piperidine in DMF solution for 15 minutes. The liquid was removed and the mixing procedure repeated twice. The remaining solid was washed intensively with DMF. A solution of HCTU (5 eq.) and Fmoc-Mba-OH (5 eq.) in DMF was added to the loaded resin, followed by the addition of DIPEA (10 eq.). The mixture was left to stir for one hour, the liquids were then filtered out, and the reaction was repeated with a fresh reagents. The resin was then washed with DMF, DCM, and methanol, and left to dry under vacuum. The Fmoc protecting group was then removed as described above, and the same coupling procedure for Fmoc-Mba-OH was done using Fmoc-D-Alanine-OH. All consequent coupling reactions were performed using the automated prelude solid phase synthesizer using standard Fmoc protection chemistry. For the conventional CP, Fmoc-L-Lys(Boc)-OH was loaded first on the resin and all subsequent AA couplings were performed on the prelude solid phase synthesizer (PTI) using standard Fmoc protection chemistry. The Fmoc protecting group of the final linear sequence was removed as described earlier.

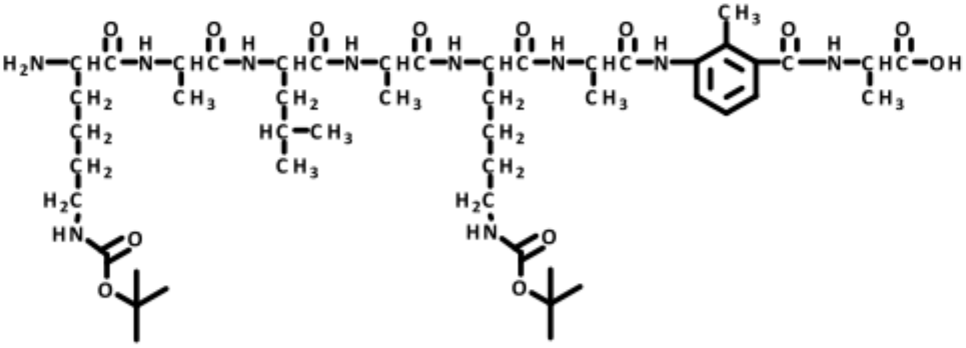

Procedure for resin cleavage of H2N-L-Lys-D-Ala-L-Leu-D-Ala-L-Lys-D-Ala-γ-Mba-D-Ala-OH: The H_2N-L-Lys-D-Ala-L-Leu-D-Ala-L-Lys-D-Ala-γ-Mba-D-Ala-OH loaded resin (200 μmol) was gently stirred in a solution (20 mL) of 1% v/v TFA, 5% v/v TIS in DCM for 20 minutes. The solid residue was then removed by vacuum filtration and extensively washed with DCM. The filtrate volume was reduced under vacuum to ~5mL, and the product was precipitated using cold ether (50 ml). The mixture was centrifuged, and ether was then decanted. This step was repeated twice, resulting in an off-white precipitate. The solid residue was dried under vacuum to yield 0.119 g (60%). MALDI-TOF for C48H80N10O13 Calculated: 1005.51 $[M+H]^+$; Found 1005.56 $[M+H]^+$, 1027.64 $[M+Na]^+$, 1043.52 $[M+K]^+$.

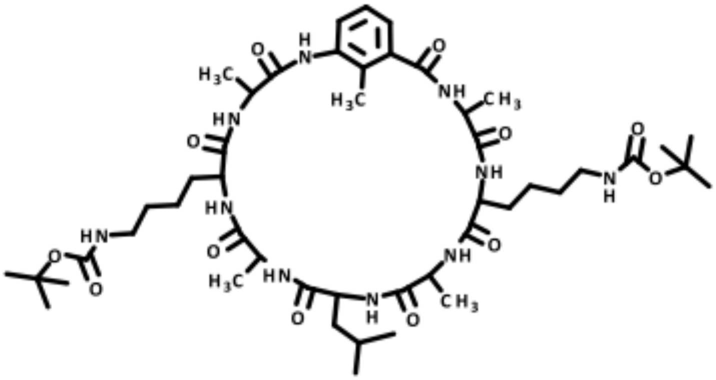

Procedure for peptide cyclization, cyclo-(L-Lys-D-Ala-L-Leu-D-Ala-L-Lys-D-Ala-γ-Mba-D-Ala): H_2N-L-Lys-D-Ala-L-Leu-D-Ala-L-Lys-D-Ala-γ-Mba-D-Ala-OH (0.119 g, 118 µmol) was dissolved in DMF (90 mL). The solution was cooled to 0 °C in an ice bath. T3P (50% w/w in DMF), (375 mg, 589 µmol) was dissolved in DMF (30 mL), cooled to 0 °C, was slowly added to the solution mixture while stirring at 0 °C. DIPEA (218 µL, 1180 mmol) was added slowly to the mixture. The reaction mixture was left to stir for 6 hours at 0 °C and then at room temperature for two days. The same amounts of T3P and DIPEA were added, and left stirring for another two days at RT. DMF was removed by vacuum distillation at 55 °C, resulting in a gel-like residue. The crude product *cyc*-K(Boc)ALAK(Boc)ABA was used without further purification.

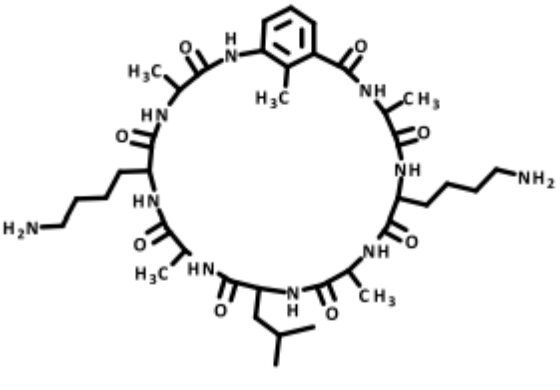

Procedure for Boc removal from cyclo-(L-Lys-D-Ala-L-Leu-D-Ala-L-Lys-D-Ala-γ-Mba-D-Ala): The cyclized product (cyc-K(Boc)ALAK(Boc)ABA) (118 µmol) was dissolved in 10 mL of 95% v/v TFA, 2.5% v/v TIS and 2.5% v/v H2O. The mixture was left to stir for two hours at room temperature. The deprotected product was then precipitated using cold ether (100 mL). The mixture was centrifuged, and ether was then decanted. This step was repeated twice, resulting in an off-white precipitate. The product was then dissolved in H_2O (5 mL), and lyophilized giving an off-white fluffy solid. The yield of the cyclized and deprotected product was found to be 85% using analytical HPLC. The crude product was purified using preparative HPLC (0% to 50% ACN in

H_2O in 30 minutes). The product fraction was lyophilized yielding a white solid (27.8 mg, 30%).

Syntheses of 2-substituted-3-aminobenzoic acids

Synthesis of B2. To a solution of 2-amino-3-nitrobenzoic acid (B1, 30.8 g, 0.17 mol) in 170 mL ethanol was added concentrated (20 mL) sulfuric acid dropwise using an addition funnel. The reaction mixture was refluxed overnight. It was then added to a mixture of ice and sodium hydroxide, from which the product precipitated. The solid was re-dissolved in an excess amount of ethanol at an elevated temperature and any insoluble solid was filtered off. The ethanol solution was concentrated in vacuo. The product (22.0 g, 62%) was recovered from recrystallization in ethanol. ^{1}H NMR (CD3OD, 500 MHz) δ 8.39 (dd, J = 1.8, 8.5 Hz, 1H), 8.30(dd, J = 1.8, 7.7 Hz, 1H), 6.72(t, J = 8.0 Hz, 1H), 4.31(q, J = 7.2 Hz, 2H), 1.42(t, J = 7.1 Hz, 3H) ppm.

Synthesis of B3. To a solution of (13.3 g, 63 mmol) of B2 in 200 mL of toluene was added of di-tert-butyl dicarbonate (56 g, 256 mmol). 4-dimethylaminopyridine (1 g, 8.1 mmol) was then added to the reaction mixture. The reaction was stirred at 75°C overnight. The reaction mixture was cooled down to room temperature and 200 mL of CHCl3 was added. The mixture was washed with water and dried over sodium sulfate. The solvent was removed in vacuo and the product (23.1 g, 89%) was recovered from recrystallization with hexane. ^{1}H NMR (CDCl3, 500 MHz) δ 8.23 (dd, J = 1.6, 7.9 Hz, 1H), 8.09 (dd, J = 1.6, 8.1 Hz, 1H), 7.59 (t, J = 8.0 Hz, 1H), 4.40 (q, J = 7.1 Hz, 2H), 1.41 (t, J = 7.1 Hz, 3H), 1.39 (s, 18H) ppm.

Synthesis of B4. To a solution of B3 (7 g, 17 mmol) in 68 mL of tetrahydrofuran was added a solution of lithium hydroxide monohydrate (1.12 g, 27 mmol) in 17 mL of water. The reaction was stirred overnight. After the addition of approximately 100 mL of ethyl acetate, the mixture was carefully acidified, first with 2 M hydrochloric acid, followed by 0.1 M citric acid. The organic phase was washed three times with water, dried over sodium sulfate and concentrated in vacuo. 5.5 g of product was recovered from recrystallization in a mixture of chloroform and hexane. ^{1}H NMR (CD3OD, 500 MHz) δ 8.29 (dd, J = 1.6, 7.8 Hz, 1H), 8.18 (d, J = 1.6, 8.2 Hz, 1H), 7.72 (t, J = 8.2 Hz, 1H), 1.35 (s, 18H) ppm.

Synthesis of B5. B4 (5 g, 13 mmol) was hydrogenated in 100 mL of ethanol with 5% w/w platinum on carbon (500 mg). The reaction mixture was filtered and concentrated in vacuo. Product (4.6 g, 100%) was used without further purification. ^{1}H NMR (CD3OD, 500 MHz) δ 8.31 (dd, J = 1.4, 7.8 Hz, 1H), 8.16 (t, J = 7.8 Hz, 1H), 7.01 (d, J = 1.4, 8.1 Hz, 1H), 1.36 (s, 18H) ppm.

Synthesis of dipeptides

Synthesis of (9H-fluoren-9-yl)methyl (1-chloro-1-oxopropan-2-yl)carbamate (Fmoc-D-Ala-F). To a solution of 2-((((9H-fluoren-9-yl)methoxy)carbonyl)amino)propanoic acid (Fmoc-D-Ala-OH, 2 g, 6.4 mmol) in approximately 150 mL of dichloromethane(DCM) was added cyanuric fluoride (1.1 mL, 12.8 mmol) and pyridine (0.51 mL, 6.4 mmol). The reaction was left stirring overnight. The reaction mixture was extracted three times using DCM. The organic phase was then washed with water and dried over anhydrous sodium sulfate. The solution was then concentrated in vacuo, obtaining the solid product (1.97 g, 98%). ^{1}H NMR (CDCl3, 500 MHz) δ 7.8 (d, J = 7.5 Hz, 2H), 7.62 (t, J = 6.5 Hz, 2H), 7.44 (t, J = 7.5 Hz, 2H), 7.36 (t, J = 7.5 Hz, 2H), 5.29 (d, J = 6.0 Hz, 1H), 4.64 (m, 1H), 4.54 (dd, J = 6.7, 10.6 Hz, 1H), 4.45 (m, 1H), 4.26 (t, J = 6.7 Hz, 1H), 1.57 (d, J = 7.2 Hz, 3H) ppm.

Synthesis of DP-B. To a solution of Unit B (1.1 g, 3.2 mmol) in 30 mL of DCM was added Fmoc-D-Ala-F (1.3 g, 4.15 mol) and sodium bicarbonate (0.75 g, 8.93 mmol). The reaction was stirred for 30 min before it was transferred to a separation funnel where additional DCM was added. The resultant mixture was washed with water and dried over anhydrous sodium sulfate. The organic phase was dried over sodium sulfate and concentrated in vacuo. Purification by chromatography (DCM/MeOH) yielded the target compound (1.6 g, 76%). ^{1}H NMR (CDCl3, 500 MHz) δ 8.83 (s, 1H), 8.39 (d, J = 7.7 Hz, 1H), 7.93 (d, J = 7.5 Hz, 1H), 7.79 (d, J = 7.5 Hz, 2H), 7.69 (t, J = 8.4 Hz, 1H), 7.45 (t, J = 8.0 Hz, 2H), 7.42 (t, J = 7.4 Hz, 2H), 7.33 (m, 3H), 4.52 (m, 3H), 4.28 (t, J = 7.0 Hz, 1H), 1.49 (d, J = 7.0 Hz, 3H), 1.37 (s, 9H), 1.30 (s, 9H) ppm.

Benzimidazole-functionalized Cyclic Peptide Synthesis

D-Ala resin functionalization. To 4 mL of DCM was added 1 g (1.7 mmol/g loading) of 2-chlorotrityl chloride resin. The mixture was stirred for an hour before adding a solution of Fmoc-D-Ala-OH (1.1 g, 3.2 mmol) in 3 mL of DMF. DIPEA (3.0 mL, 17 mmol) was added dropwise to the mixture. The reaction mixture was stirred for 2 hours before it was quenched by the addition of MeOH. The liquid phase was filtered off and the resin was washed sequentially with DMF, DCM and MeOH for three times. The resin was dried in vacuum before loading (1.1 mmol/g, 65%) was assessed using UV-vis spectroscopy. The Fmoc-protected resin was then deprotected by suspending it in 20% piperidine in DMF for 2 hours. The resin was filtered and washed in the same manner and stored in vacuum.

DP-B immobilization on resin. To a solution of DP-B (123 mg, 190 µmol) and (2-(7-Aza-1H-benzotriazole-1-yl)-1,1,3,3-tetramethyluronium hexafluorophosphate) (HATU, 72 mg, 190 µmol) in 1mL of 1:1 DCM/DMF mixture was injected N,N-diisopropylethylamine (DIPEA, 66 µl, 380 µmol). The solution was stirred for 30 min before D-Ala-functionalized resin (100 mg, 0.95 mmol/g) was added. The reaction was stirred for 2 hours before the resin was filtered and washed with three iterations of DMF, DCM and methanol. The loading (0.73 mmol/g, 66%) was assessed using UV-Vis spectroscopy.

Peptide cyclization. To a solution of the linear peptide, synthesized using the peptide synthesizer, (300 mg, 0.25 mmol) in 300 mL was added DIPEA (3 mL, 0.5 mmol) and 50% propane phosphonic acid anhydride solution in DMF (T3P, 3 mL). The reaction was stirred for two days and an additional 3 mL of T3P was added at the 24th hour.azzxc

^{1}H NMR (500 MHz, DMSO-*d*$_6$) for Mba-CP: δ (ppm) 0.80 (d, *J* = 6.5 Hz, 3H), 0.84 (d, *J* = 6.6 Hz, 3H), 1.11 (d, *J* = 7.0 Hz, 3H), 1.16 (d, *J* = 7.0 Hz, 3H), 1.24 (s, 3H), 1.31 (dt, *J* = 16.8 Hz, 8.4, 12H), 1.34-1.53 (m, 8H), 1.65 (m, 1H), 1.76 (d, *J* = 7.0 Hz, 1H), 2.19 (s, 3H), 2.77 (s, broad, 4H), 4.28-4.33 (m, 6H), 4.42 (m, 1H), 7.17 (d, *J* = 6.9 Hz, 1H), 7.24 (t, *J* = 7.8 Hz, 1H), 7.48 (d, *J* = 7.9 Hz, 1H), 7.75 (s, broad, 6H), 7.82 (d, *J* = 7.4 Hz, 1H), 7.89 (d, *J* = 8.7 Hz, 1H), 8.02 (d, *J* = 7.4 Hz, 1H), 8.19 (t, *J* = 7.0 Hz, 2H), 8.58 (d, *J* = 5.7 Hz, 1H), 8.72 (d, *J* = 7.2 Hz, 1H), 9.12 (s, 1H). MALDI-TOF for $C_{38}H_{62}N_{10}O_8$ Calculated: 787.48 [M+H]$^+$; Found 787.65 [M+H]$^+$, 809.69 [M+Na]$^+$, 825.69 [M+K]$^+$.

^{1}H NMR (500 MHz, DMSO-*d*$_6$) for 8CP: δ (ppm) 0.82 (d, *J* = 6.5 Hz, 6H), 0.85 (d, *J* = 6.6 Hz, 6H), 1.10-1.70 (m, 30H), 2.74 (m, 4H), 4.20 (m, 2H), 4.35-4.50 (m, 6H), 7.65 (s, 6H), 8.10-8.20 (m, 6H), 8.30 (d, *J* = 7.7 Hz, 2H). MALDI-TOF for $C_{36}H_{66}N_{10}O_8$ Calculated: 767.51 [M+H]$^+$; Found 767.59 [M+H]$^+$, 789.63 [M+Na]$^+$, 805.65 [M+K]$^+$.

^{1}H NMR spectrum of Fmoc-Mba-OH in DMSO-*d*$_6$

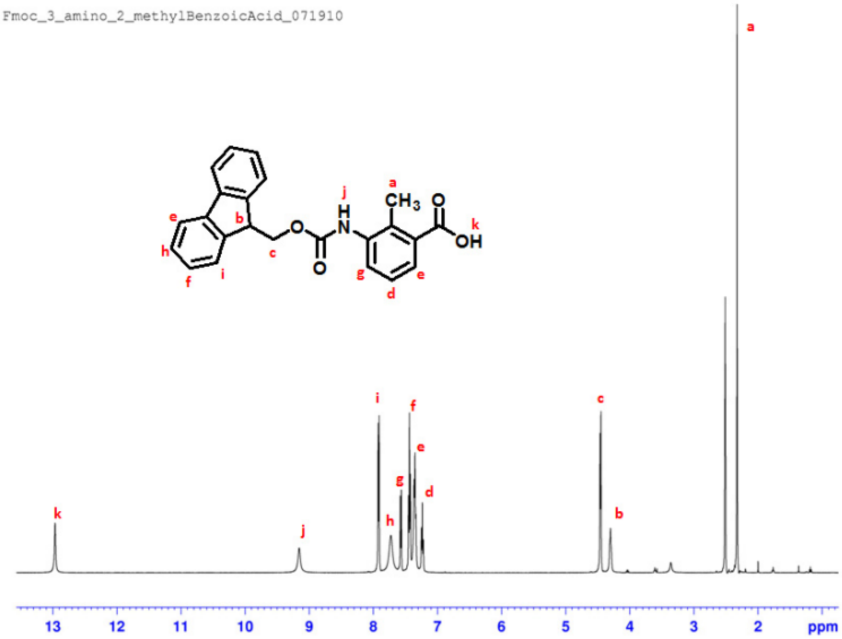

^{1}H NMR spectrum of Mba-8CP in DMSO-d_6

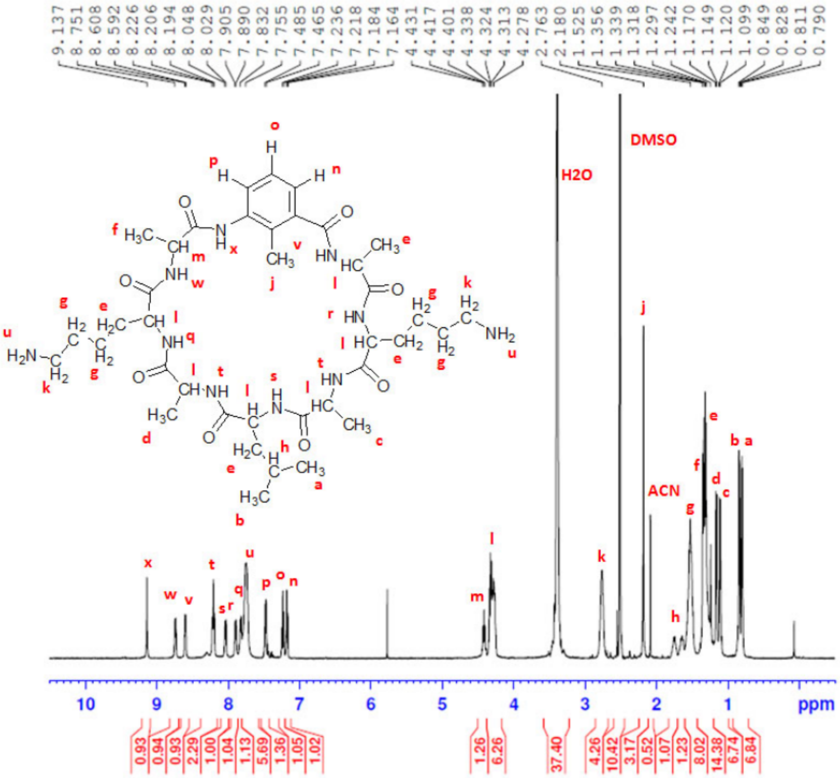

^{1}H NMR spectrum of regular 8CP in DMSO-d_6

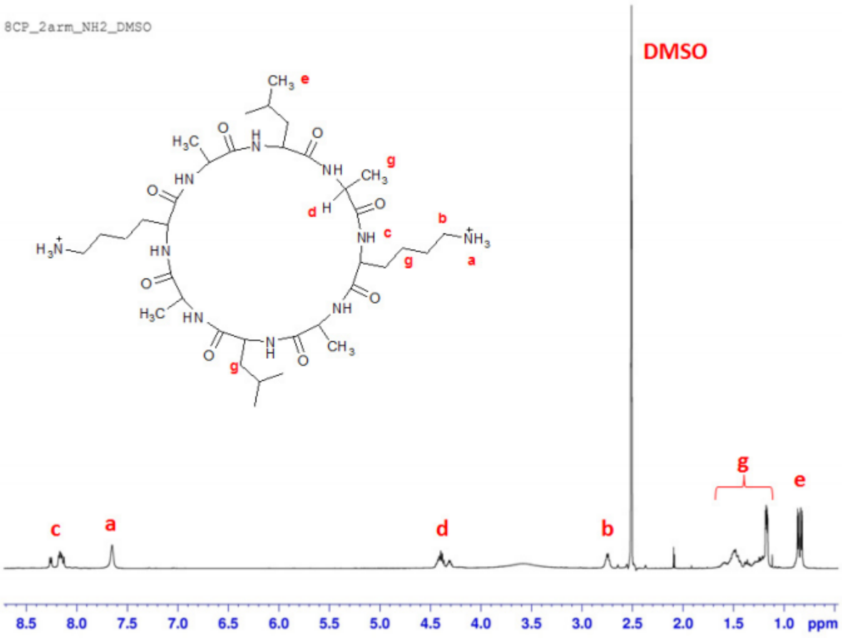

Other Characterization of Nanotubes

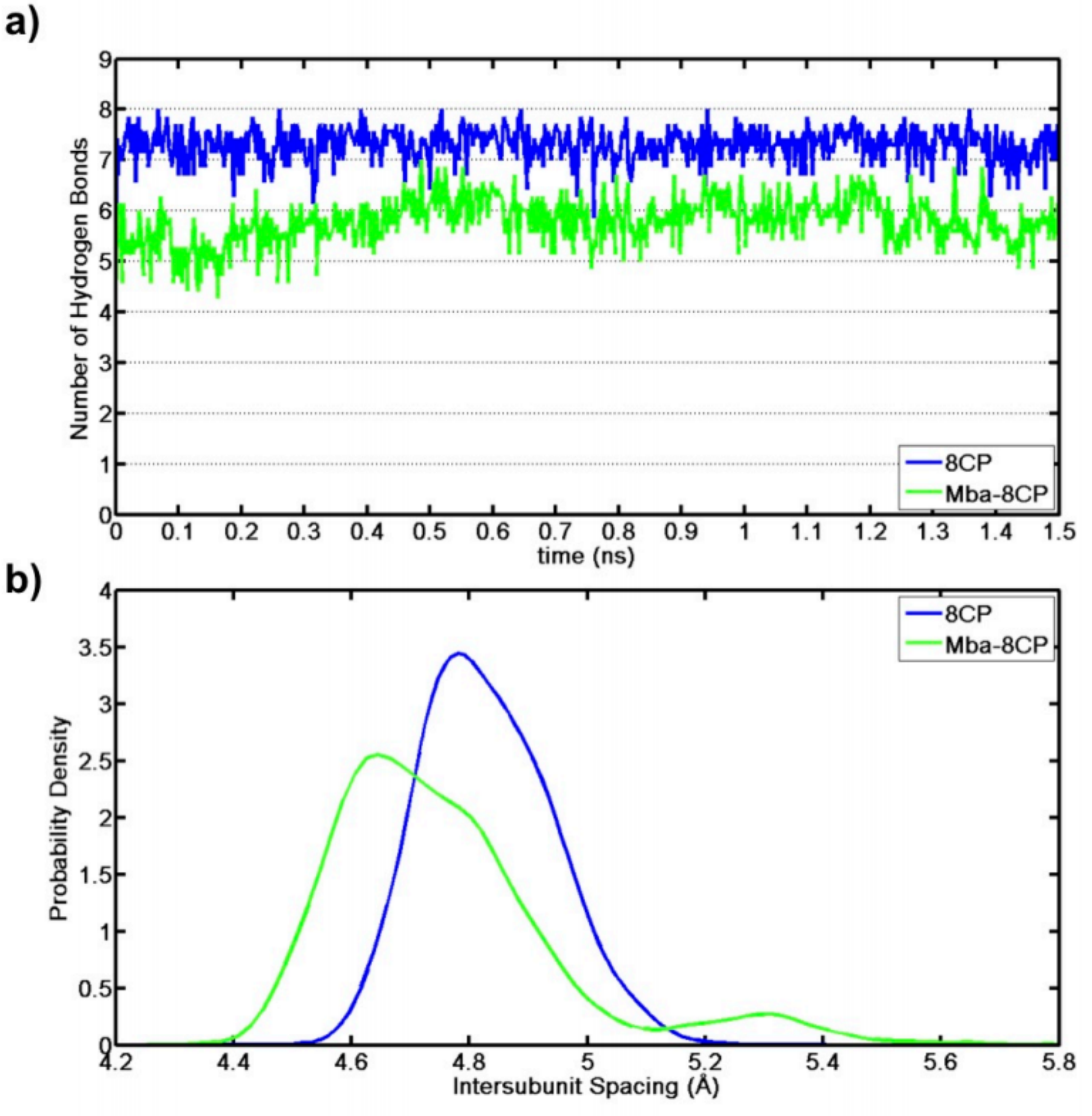

Figure 2.S1 Time history of the average number of interring backbone hydrogen bonds. The number of H-bonds remains stable during the simulation for both cases, with a lower average value for Mba-8CP than the 8CP nanotubes. Intersubunit distance distribution (b) is comparable in both cases and agree with reported experimental values (4.7-4.8 Å) for CPNs.

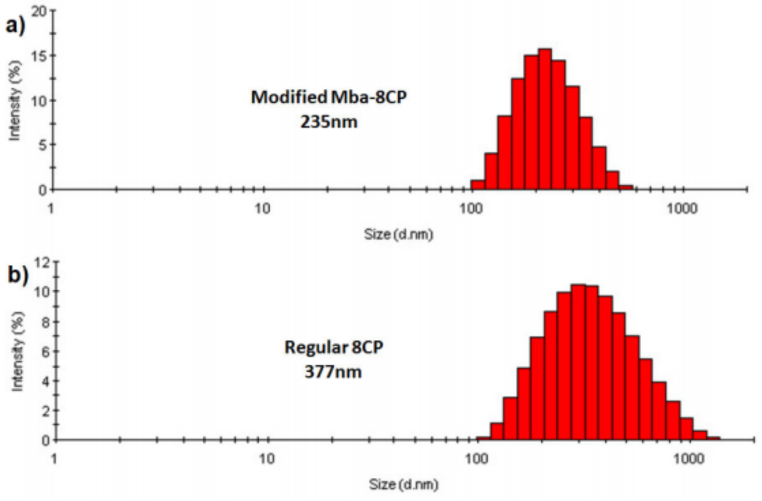

Figure 2.S2 Dynamic Light Scattering (DLS) of bundles of cyclic peptide nanotubes derived from (a) Modified (Mba-8CP) and (b) conventional 8CP in ACN (0.25mg/mL).

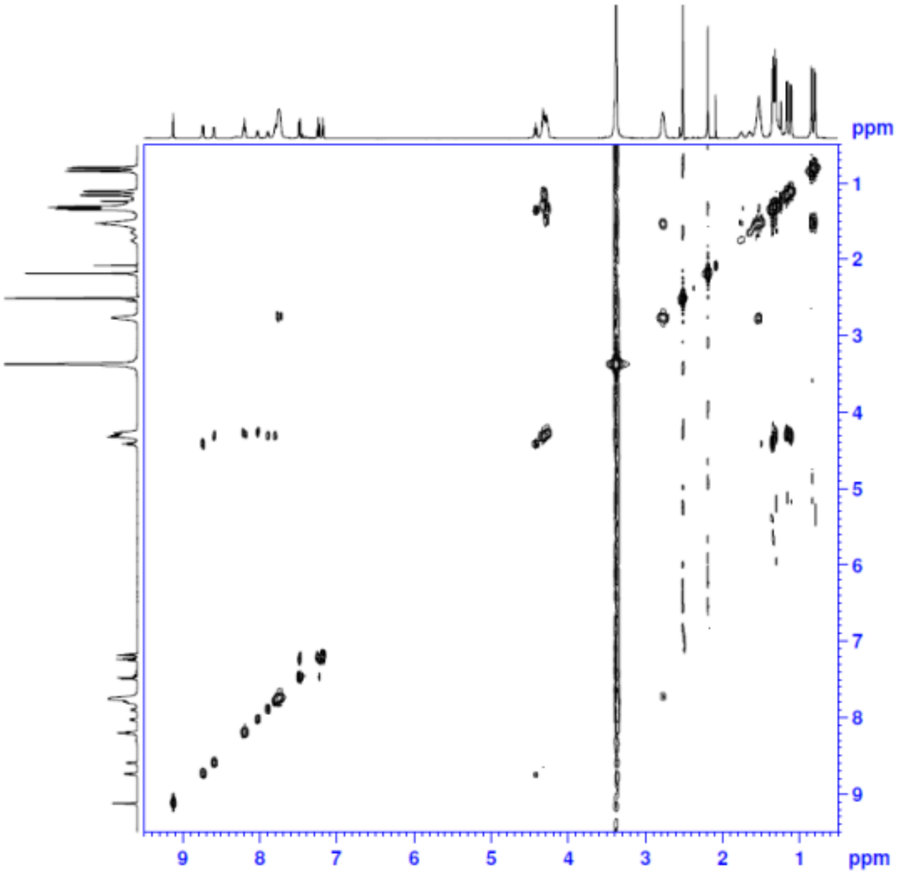

Figure 2.S3 2D COSY spectrum of molecularly dissolved Mba-8CP in DMSO-d_6 (~4mg/mL). Data were acquired over 1 h at room temperature.

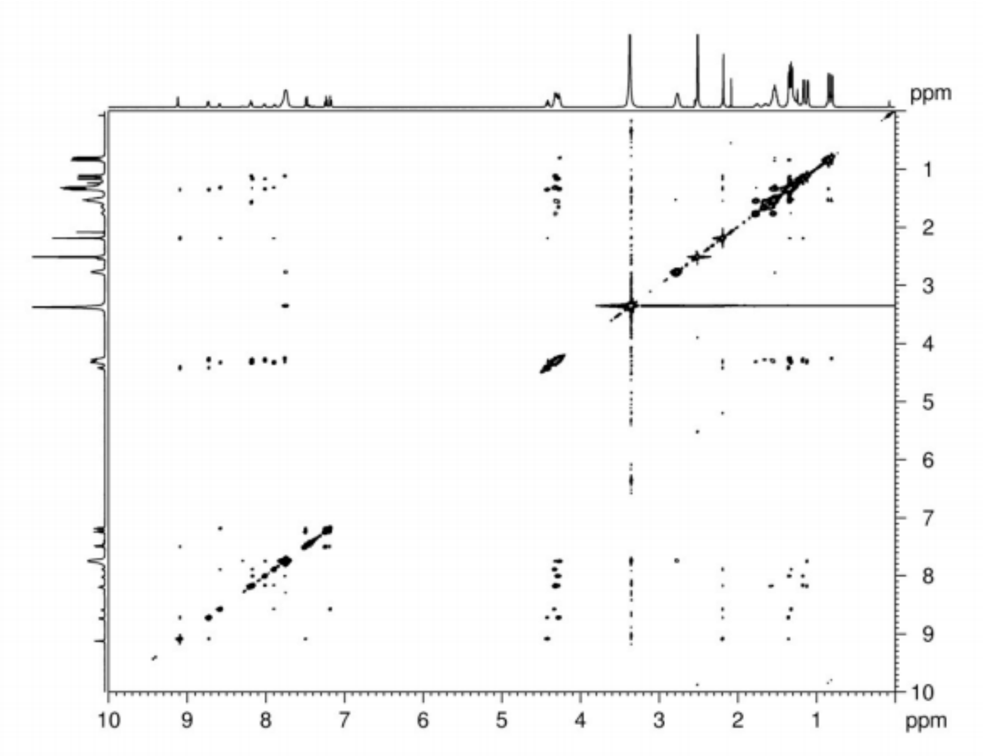

Figure 2.S4 2D NOESY spectrum of molecularly dissolved Mba-8CP in DMSO-d_6 (~4mg/mL). Data were acquired over 12 h at room temperature.

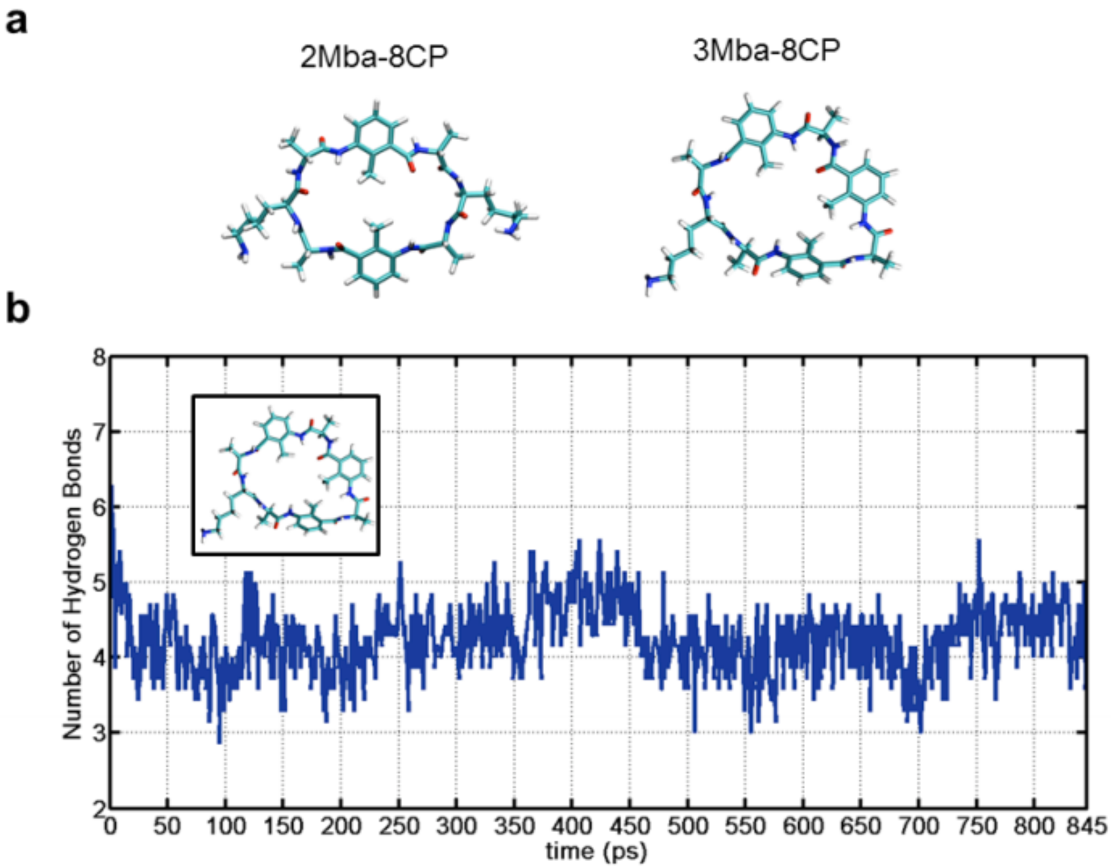

Figure 2.S5 Stability of CPNs containing multiple modifications. a) Snapshots of a double and triple modified CP. A distorted shape is observed in both 2Mba-8CP and 3Mba-8CP cases. b) Number of hydrogen bonds in the triple modified CP. The preliminary studies show that the number of hydrogen bonds in the 3Mba-8CP is well below the optimum number of hydrogen bonds, 8, and much lower than in the cases of the Mba-8CP or the regular 8CP. Simulations suggest that due to the distorted structure of the rings, the H-bonds are generally less likely to be perpendicular to the plane of the ring, leading to less-stable assemblies.

References

(1) Gin, D. L.; Noble, R. D. *Science* **2011**, *332* (6030), 674–676.

(2) Kaucher, M. S.; Peterca, M.; Dulcey, A. E.; Kim, A. J.; Vinogradov, S. A.; Hammer, D. A.; Heiney, P. A.; Percec, V. *J. Am. Chem. Soc.* **2007**, *129* (38), 11698–11699.

(3) Shannon, M. A.; Bohn, P. W.; Elimelech, M.; Georgiadis, J. G.; Marĩas, B. J.; Mayes, A. M. *Nature* **2008**, *452* (7185), 301–310.

(4) Xu, T.; Zhao, N.; Ren, F.; Hourani, R.; Lee, M. T.; Shu, J. Y.; Mao, S.; Helms, B. A. *ACS Nano* **2011**, *5* (2), 1376–1384.

(5) Percec, V.; Dulcey, A. E.; Balagurusamy, V. S. K.; Miura, Y.; Smidrkal, J.; Peterca, M.; Hummelin, S.; Edlund, U.; Hudson, S. D.; Heiney, P. A.; Duan, H.; Magonev, S. N.; Vinogradov, S. A. *Nature* **2004**, *430* (7001), 764–768.

(6) Kholkin, A.; Amdursky, N.; Bdikin, I.; Gazit, E.; Rosenman, G. *ACS Nano* **2010**, *4* (2), 610–614.

(7) Hartgerink, J. D.; Granja, J. R.; Milligan, R. A.; Ghadiri, M. R. *J. Am. Chem. Soc.* **1996**, *118* (1), 43–50.

(8) Davis, J. T.; Spada, G. P. *Chem. Soc. Rev.* **2007**, *36* (2), 296–313.

(9) Zang, L.; Che, Y.; Moore, J. S. *Acc. Chem. Res.* **2008**, *41* (12), 1596–1608.

(10) Sakai, N.; Kamikawa, Y.; Nishii, M.; Matsuoka, T.; Kato, T.; Matile, S. *J. Am. Chem. Soc.* **2006**, *128* (7), 2218–2219.

(11) Amorín, M.; Castedo, L.; Granja, J. R. *J. Am. Chem. Soc.* **2003**, *125* (10), 2844–2845.

(12) Reiriz, C.; Brea, R. J.; Arranz, R.; Carrascosa, J. L.; Garibotti, A.; Manning, B.; Valpuesta, J. M.; Eritja, R.; Castedo, L.; Granja, J. R. *J. Am. Chem. Soc.* **2009**, *131* (32), 11335–11337.

(13) Horne, W. S.; Stout, C. D.; Ghadiri, M. R. *J. Am. Chem. Soc.* **2003**, *125* (31), 9372–9376.

(14) Reiriz, C.; Amorín, M.; García-Fandiño, R.; Castedo, L.; Granja, J. R. *Org. Biomol. Chem.* **2009**, *7* (21), 4358–4361.

(15) Ghadiri, M. R.; Granja, J. R.; Buehler, L. K. *Nature* **1994**, *369* (6478), 301–304.

(16) Brea, R. J.; Reiriz, C.; Granja, J. R. *Chem. Soc. Rev.* **2010**, *39* (5), 1448–1456.

(17) Kubik, S.; Goddard, R. *J. Org. Chem.* **1999**, *64* (26), 9475–9486.

(18) Kubik, S. *J. Am. Chem. Soc.* **1999**, *121* (25), 5846–5855.

(19) Ishida, H.; Qi, Z.; Sokabe, M.; Donowaki, K.; Inoue, Y. *J. Org. Chem.* **2001**, *66* (9), 2978–2989.

(20) Kubik, S.; Goddard, R. *Chem. Commun.* **2000**, No. 7, 633–634.

(21) Kubik, S. *Chem. Soc. Rev.* **2009**, *38* (2), 585–605.

(22) Gauthier, D.; Baillargeon, P.; Drouin, M.; Dory, Y. L. *Angew. Chem. - Int. Ed.* **2001**, *40* (24), 4635–4638.

(23) Leclair, S.; Baillargeon, P.; Skouta, R.; Gauthier, D.; Zhao, Y.; Dory, Y. L. *Angew. Chem. - Int. Ed.* **2004**, *43* (3), 349–353.

(24) Amorín, M.; Castedo, L.; Granja, J. R. *Chem. - Eur. J.* **2005**, *11* (22), 6543–6551.

(25) Amorín, M.; Villaverde, V.; Castedo, L.; Granja, J. R. *J. Drug Deliv. Sci. Technol.* **2005**, *15* (1), 87–92.

(26) Brea, R. J.; Castedo, L.; Granja, J. R. *Chem. Commun.* **2007**, No. 31, 3267–3269.

(27) Brea, R. J.; Amorín, M.; Castedo, L.; Granja, J. R. *Angew. Chem. - Int. Ed.* **2005**, *44* (35), 5710–5713.
(28) Amorín, M.; Brea, R. J.; Castedo, L.; Granja, J. R. *Org. Lett.* **2005**, *7* (21), 4681–4684.
(29) Amorín, M.; Castedo, L.; Granja, J. R. *Chem. - Eur. J.* **2008**, *14* (7), 2100–2111.
(30) Atherton, E.; Sheppard, R. C. *Solid Phase Pept. Synth. Pract. Approach* **1989**.
(31) Khazanovich, N.; Granja, J. R.; McRee, D. E.; Milligan, R. A.; Ghadiri, M. R. *J. Am. Chem. Soc.* **1994**, *116* (13), 6011–6012.
(32) Ghadiri, M. R.; Kobayashi, K.; Granja, J. R.; Chadha, R. K.; McRee, D. E. *Angew. Chem. Int. Ed. Engl.* **1995**, *34* (1), 93–95.
(33) Kobayashi, K.; Granja, J. R.; Ghadiri, M. R. *Angew. Chem. Int. Ed. Engl.* **1995**, *34* (1), 95–98.
(34) Clark, T. D.; Ghadiri, M. R. *J. Am. Chem. Soc.* **1995**, *117* (49), 12364–12365.
(35) Ghadiri, M. R.; Granja, J. R.; Milligan, R. A.; McRee, D. E.; Khazanovich, N. *Nature* **1993**, *366* (6453), 324–327.
(36) Cate, M. G. J. Ten; Severin, N.; Börner, H. G. *Macromolecules* **2006**, *39* (23), 7831–7838.
(37) Couet, J.; Biesalski, M. *Small* **2008**, *4* (7), 1008–1016.
(38) Couet, J.; Samuel, J. D. J. S.; Kopyshev, A.; Santer, S.; Biesalski, M. *Angew. Chem. - Int. Ed.* **2005**, *44* (21), 3297–3301.
(39) Hermanson, G. T. *Bioconjugate Tech.* **1996**.
(40) Chan, W. C.; White, P. D. *Fmoc Solid Phase Pept. Synth. Pract. Approach* **2000**.
(41) Krimm, S.; Bandekar, J. *Adv. Protein Chem.* **1986**, 181–364.
(42) Haris, P. I.; Chapman, D. *Biopolym. - Pept. Sci. Sect.* **1995**, *37* (4), 251–263.
(43) Clark, T. D.; Buehler, L. K.; Ghadiri, M. R. *J. Am. Chem. Soc.* **1998**, *120* (4), 651–656.
(44) Vaidya, P. D.; Kenig, E. Y. *Chem. Eng. Technol.* **2007**, *30* (11), 1467–1474.
(45) McDonald, T. M.; Lee, W. R.; Mason, J. A.; Wiers, B. M.; Hong, C. S.; Long, J. R. *J. Am. Chem. Soc.* **2012**, *134* (16), 7056–7065.
(46) Couck, S.; Denayer, J. F. M.; Baron, G. V.; Rémy, T.; Gascon, J.; Kapteijn, F. *J. Am. Chem. Soc.* **2009**, *131* (18), 6326–6327.
(47) Vaidhyanathan, R.; Iremonger, S. S.; Shimizu, G. K. H.; Boyd, P. G.; Alavi, S.; Woo, T. K. *Science* **2010**, *330* (6004), 650–653.
(48) Andersen, O. S.; Koeppe, R. E. *Physiol. Rev.* **1992**, *72* (suppl 4), S89–S158.
(49) Jasti, J.; Furukawa, H.; Gonzales, E. B.; Gouaux, E. *Nature* **2007**, *449* (7160), 316–323.
(50) Ruiz, L. .
(51) Lubish, W.; Kock, M.; Hoeger, T.; Grandel, R.; Schult, S.; Mueller, R. Cyclo-alkyl substituted benzimidazoles and their use as PARP inhibitors. US6737421 B1, May 18, 2004.
(52) Naka, T.; Nishikawa, K.; Kato, T. 1-(cyclohexyloxycarbonyloxy)ethyl 2-ethoxy-1-[[2’-(1H-tetrazol-5-yl)biphenyl-4-yl]methyl]benzimidazole-7-carboxylate and compositions and methods of pharmaceutical use thereof. US5196444 A, March 23, 1993.

(53) Satake, S.; Bando, S.; Sato, N.; Iida, Y. METHOD FOR PRODUCING 3-NITRO-2-(N-t-BUTOXYCARBONYL)- AMINOBENZOATES AND INTERMEDIATE FOR PRODUCING THE SAME ESTERS.
(54) Lipka, E.; Folly-Klan, M.; Charton, J.; Vaccher, M.-P.; Bonte, J.-P.; Vaccher, C. *J. Pharm. Biomed. Anal.* **2010**, *53* (5), 1267–1271.
(55) *HyperChem release 5.11. For Windows molecular modeling system*; Hypercube Inc., 419 Philip Street, Waterloo, Ont., Canada N2L 3X2, 1999.
(56) *Computational Chemistry*; HyperChem Manual; Hypercube Inc., Waterloo, Ontario, Canada.
(57) Engels, M.; Bashford, D.; Ghadiri, M. R. *J. Am. Chem. Soc.* **1995**, *117* (36), 9151–9158.
(58) Tarek, M.; Maigret, B.; Chipot, C. *Biophys. J.* **2003**, *85* (4), 2287–2298.
(59) Hwang, H.; Schatz, G. C.; Ratner, M. A. *J. Phys. Chem. B* **2006**, *110* (13), 6999–7008.
(60) Khurana, E.; Nielsen, S. O.; Ensing, B.; Klein, M. L. *J. Phys. Chem. B* **2006**, *110* (38), 18965–18972.
(61) Hwang, H.; Schatz, G. C.; Ratner, M. A. *J. Phys. Chem. B* **2006**, *110* (51), 26448–26460.
(62) Cheng, J.; Zhu, J.; Liu, B. *Chem. Phys.* **2007**, *333* (2–3), 105–111.
(63) García-Fandiño, R.; Granja, J. R.; Marco D'Abramo; Orozco, M. *J. Am. Chem. Soc.* **2009**, *131* (43), 15678–15686.
(64) Carvajal Diaz, J. A.; Çağin, T. *Nanotechnology* **2010**, *21* (11), 115703.
(65) Carloni, P.; Andreoni, W.; Parrinello, M. *Phys. Rev. Lett.* **1997**, *79* (4), 761–764.
(66) Gailer, C.; Feigel, M. *J. Comput. Aided Mol. Des.* **1997**, *11* (3), 273–277.
(67) Lewis, J. P.; Pawley, N. H.; Sankey, O. F. *J. Phys. Chem. B* **1997**, *101* (49), 10576–10583.
(68) Jishi, R. A.; Flores, R. M.; Valderrama, M.; Lou, L.; Bragin, J. *J. Phys. Chem. A* **1998**, *102* (48), 9858–9862.
(69) Chen, G.; Su, S.; Liu, R. *J. Phys. Chem. B* **2002**, *106* (7), 1570–1575.
(70) Tan, H.; Qu, W.; Chen, G.; Liu, R. *Chem. Phys. Lett.* **2003**, *369* (5–6), 556–562.
(71) Sun, H. *J. Phys. Chem. B* **1998**, *102* (38), 7338–7364.
(72) Humphrey, W.; Dalke, A.; Schulten, K. *J. Mol. Graph.* **1996**, *14* (1), 33–38.

Chapter 3

Mechanistic Insight into the Formation of Cationic Naked Nanocrystals Generated under Equilibrium Control

Adapted with permission from *J. Am. Chem. Soc.*, **2014**, *136* (44), pp 15702–15710. **Copyright © 2014 American Chemical Society.**

Introduction

Nanocyrstals have been in development for more than three decades[1–7]. A mature part of nanoscience, they have been integrated in a myriad of devices such as sensors[8,9], photovoltaics[10–13], display[14–16] and electrochromics[17–19]. By shrinking the material dimensions down to the nanoscale, nanoparticles display unique properties not found in bulk materials. In particular, the small size inherently brings about the increase in the ratio between surface area and volume, into a regime where surface property plays a crucial role in determining the overall properties. It is thus imperative that precise chemistry control be in place to tune the surface properties of nanocrystals. Typically, as-synthesized, nanocrystals are capped by native ligands, which are often times alkyl chains with minimal function other than modulating the growth and nucleation. One strategy of surface control is to replace the native ligands with functional ones, synthesized *ex situ*[20–31]. Alternatively, instead of replacing ligands, one can also remove, or "strip" the native ligands to reveal a bare nanocrystal surface and hence modify the surface properties[32–35].

Specifically, pertinent to the topic of this dissertation, the display of ligand-free nanocrystalline metal oxides surfaces is critical in enabling scalable access to microporous frameworks such as extended MOF-74, M2(dobpdc) (Chapter 4), and ZIF-7/ZIF-8 (Chapter 5). These metal oxide nanocrystals constitute a source of metal ions to be incorporated in the resultant microporous framework. Thus rendering them to be predisposed to linkers/etchants is crucial in the process. The details of the interconversion process will be elaborated upon in the noted chapters. In this chapter, I will discuss our effort in preparing these "stripped" or "naked" nanocrystals, and my specific contribution in understanding the underlying mechanism.

With such a selection of ligand exchange and removal techniques available, we are only beginning to understand the mechanistic underpinnings of those transformations[21,24,29,36–41]. It is still difficult to explain and predict trends in reactivity for different NC compositions for a given transformation. For example, some NC compositions have not been amenable to native ligand removal while also maintaining colloidal dispersibility—e.g., the lead chalcogenides[33,42]. Disparities in surface reactivity and stability are related to structure and bonding available to the material and demand that we develop an arsenal of reagents that can be tailored as needed for the desired transformation of a NC of interest.

In the past, we and others have used irreversible chemical reactions, including alkylation with Meerwein's salt or oxidation by the nitrosyl cation, to drive the removal of ligands from NC surfaces[33,35,42]. These reactions yield charge-stabilized colloids in polar dispersants due to open metal coordination sites left at the NC surface following ligand stripping (**Figure 3.1**a). Chemical approaches based on such irreversible reactions leave behind a transiently unstable surface (i.e., absent any stabilizing adsorbates), which can lead to desorption of excess metal cations from the surface and loss of dispersibility (due to loss of surface charge) on a time scale similar to repassivation with coordinating solvent.

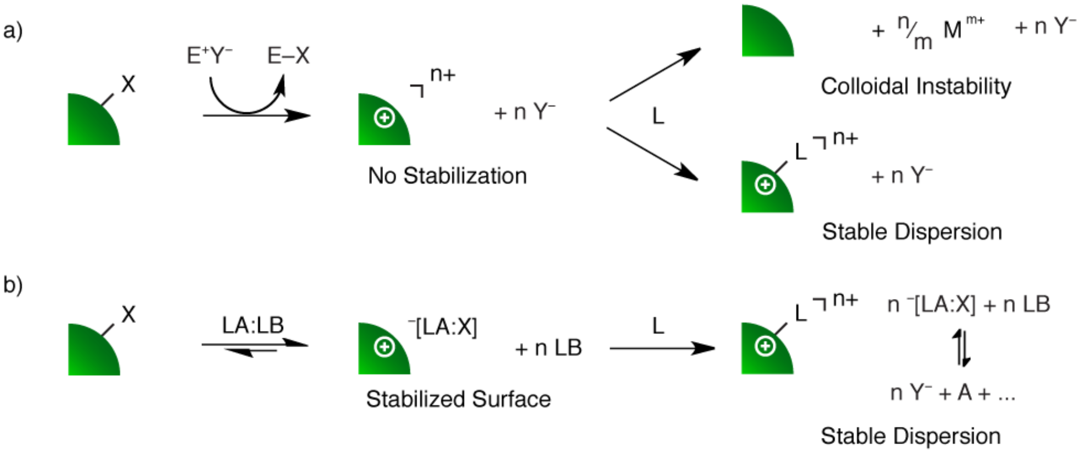

Figure 3.1 Mechanistic grounds distinguishing various native ligand stripping chemitries that yield cationic naked NCs. X^- = anionic ligand, E^+ = electrophile, Y^- = non-coordinating anion, M^{m+} = metal ion, LA:LB = Lewis acid-base adduct, L = charge-neutral coordinating solvent (e.g., DMF). a) Irreversible ligand stripping by strong electrophiles yields a cationic NC surface with no electrostatic stabilization. For sensitive NC compositions, loss of M^{m+} from the surface leads to colloidal instability, particularly when re-passivation of surface M^{m+} by L is not competitive with M^{m+} desorption. b) Ligand stripping under equilibrium control stabilizes the cationic NC surface through dynamic interactions with an anionic physisorbed species $[LA:X]^-$ until it can be re-passivated with L. In the approach described herein, Y^- is generated through disproportionation of $[LA:X]^-$ as described in the main text.

We hypothesized that this undesirable outcome could be avoided if it were possible to stabilize the NC surface through the entire ligand-stripping pathway. Here, we introduce the concept of native ligand stripping under equilibrium control, where reversible Lewis acid–base chemistry is used to generate adduct-stabilized surfaces during ligand stripping (**Figure 3.1**b). The dynamic exchange of these adducts on and off the NC surface allows for ligand displacement while imparting surface stabilization, in contrast to previous approaches that leave the surface without stabilization. Our concept of equilibrium control over ligand stripping is demonstrated using Lewis base adducts of BF_3, which yield for the first time naked NC inks of PbSe, along with a wide range of other semiconductor and metallic NCs. Our analysis of excess surface Pb(II) before and after stripping under equilibrium control indicated near-complete retention of excess Pb(II), in contrast with irreversible ligand stripping approaches. To rationalize differences in ligand-stripping outcomes with different reagents, we investigated in detail the mechanism of oleate ligand removal from PbSe NCs using complementary in situ techniques, including both 1D and 2D nuclear magnetic resonance (NMR) spectroscopy for both ^{1}H- and ^{19}F-containing reaction intermediates, as well as electrospray ionization mass spectrometry (ESI-MS) in order to validate our structure assignments.

Unique to the chemistry developed herein, we show that BF_3 reacts with the carboxylate terminus of PbSe-bound oleate ligands (OA^-) to form a physisorbed $[OA:BF_3]^-$ adduct that is in dynamic exchange (equilibrium) on and off the NC surface throughout the stripping reaction. We reason that this dynamic layer of $[OA:BF_3]^-$ at PbSe is responsible for the observed surface stabilization and refer to this effect as equilibrium control over surface stabilization. We further show that anionic $[OA:BF_3]^-$ undergoes disproportionation reactions in the presence of excess BF_3, ultimately leading to the loss of oleate as neutral $OA_x(B_yF_z)$ species and the formation of BF_4^- as the sole charge-compensating species at the cationic NC surface in the final naked nanocrystal dispersion. The quality of these nanoinks allows PbSe NCs to be assembled into either single-component ordered NC films or periodic mesostructured composites using block copolymer directed assembly, highlighting the versatility of these functional nanoscale building units in mesoscale chemistry.

Results and Discussion

As a test case to highlight the versatility of native ligand stripping under equilibrium control over previously reported procedures, we investigated in detail the removal of oleate ligands from the surface of PbSe NCs (PbSe-OA) using Lewis base adducts of BF_3. As Se^{2-} in the NC lattice is easily oxidized, PbSe NCs require mild chemical reagents to strip them of their native ligands. While reagents such as trialkyloxonium salts (e.g., Meerwein's salt) and 1-alkoxy-*N*,*N*-dimethylmethaminium salts have so far proven capable of stripping ligands from the NC surface, by either method, the resulting naked PbSe NCs are not dispersible in organic solvents[33,42]. javascript:void(0);Both alkylating agents are high-energy reactants, and their use is commensurate with rapid and irreversible removal of chemisorbed organic ligands from NC surfaces. For NCs such as PbSe, loss of native ligands from the coordination sphere of surface Pb(II) can lead to desorption of Pb(II) from the NC surface. Here, we show that by changing the ligand-stripping chemistry to one that allows for equilibrium control over surface stabilization, we are able to completely avoid loss of surface Pb(II) and thereby preserve colloidal stability in the cationic naked PbSe NC inks.

Stable dispersions of cationic naked PbSe NCs with BF_4^- counterions were obtained by direct transfer of PbSe-OA into *N*,*N*-dimethylformamide (DMF) containing BF_3:Et_2O. The resulting PbSe dispersions—purified first by hexane washes and then precipitation from DMF with toluene—were stable to centrifugation and filtration for days. The efficient removal of ligands by Lewis base adducts of BF_3 (BF_3:LB) was confirmed by FT-IR and EDX, which showed a dramatic decrease in intensity of the C–H vibrational stretching frequencies and carbon content, respectively (Figure 3.S1 and **Figure 3.S2**). Ligand removal was further verified by carrying out the stripping procedure in DMF-d_7 and acquiring the ^{1}H NMR spectrum (**Figure 3.S3**), which showed no residual oleate. In order to establish the compositional diversity afforded by ligand stripping under equilibrium control, we showed that charge-stabilized dispersions of naked ZnO, Mn_3O_4, TiO_2, and Ni can be prepared in a manner similar to that described for PbSe (**Figure 3.S4** and **Figure 3.S5**). Despite the dramatic change in NC surface chemistry, we did not observe dramatic changes in size or crystal structure, as evidenced by TEM and XRD (**Figure 3.S5** and **Figure 3.S6**). Thus, this approach efficiently removes organic ligands from NC surfaces while preserving the integrity of the inorganic NC core.

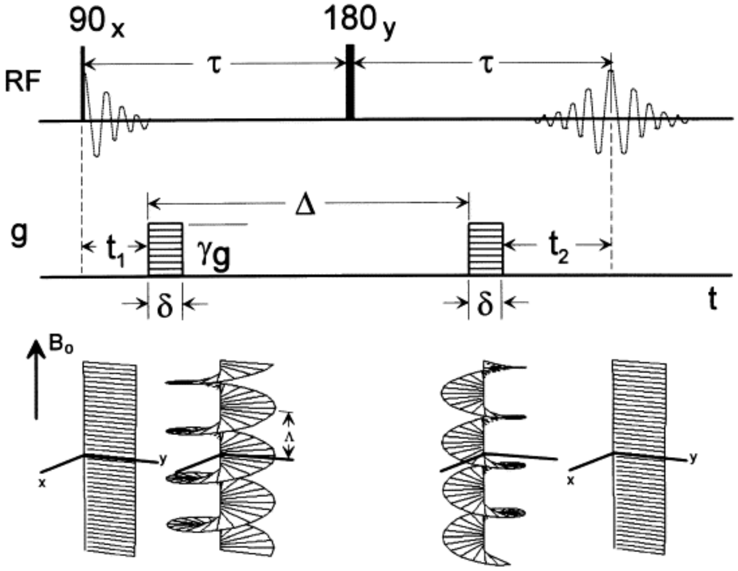

Figure 3.2 A simple spin echo DOSY experiment. Reproduced with permission[43].

In order to understand the microscopic chemical processes leading to stable dispersions of naked PbSe NCs, we followed the ligand-stripping chemistry of PbSe-OA in situ in toluene-$d_8$using diffusion-ordered spectroscopy (DOSY). DOSY is a 2D NMR technique that provides information about the chemical shifts and diffusion coefficients of NMR-active species and has been used to identify and track the dynamics of ligand exchange (but not stripping) on a variety of NC surfaces[37,38,41,44–46]. I was instrumental in establishing the technique at the Foundry NMR, leading to its pervasive use in this project. It measures the diffusion coefficients of molecules, by using pulse field gradients. The most simplistic implementation of DOSY applies a pulsed field gradient to dephase the nuclear spins differentially according to its position in the sample. A regular 1D NMR

(1H or 19F) echo pulse (180°x) in the proton channel combined with a second gradient is then applied to reverse the gradient created by the first pulse. At very short time, little diffusion has happened, and almost complete recovery of the proton signal strength is observed (**Figure 3.2**). As the time lag between the two gradient pulses, commonly denoted as Δ, increases, molecular motion has more time to jumble the positions of the nuclei. Upon refocusing with the echo pulse and the pulsed gradient, the random displacements lead to misaligned nuclear spin and hence signal attenuation. In practice, adjusting the gradient field strength also leads to signal attenuation and is the adjustable parameter used in the experiment. Thus, after optimizing program parameters such as Δ and other delays, the strength of the gradient is varied as snapshots of ^{1}H NMRs at varying stages of attenuation are taken. Depending on the specific DOSY pulse sequence used, the diffusion coefficients can be modeled using the corresponding equations which generally takes on an exponential form:

$$I = I_0 e^{-DQ(g)} \qquad \textbf{(Eq. 3.1)}$$

where I is the intensities obtained during the experiment, I_0 is the unperturbed signal intensity (i.e. intensity without the pulsed gradient), D is the diffusion coefficient, g is the gradient strength and Q is an function of g along with other information about the pulse sequence. Consequently, the sizes of the diffusing particulates can be deduced as well. As one would expect, larger objects move slower and have a smaller diffusion coefficient. Such an intuition is echoed in the Stokes-Einstein equation:

$$D = \frac{k\,T}{6\,\pi\,\eta\,r_s} \qquad \textbf{(Eq. 3.2)}$$

where k is the Boltzmann constant, T is the temperature, η is the viscosity and r_s is the hydrodynamic radius of the diffusing object. For example, by modeling the decay of The ^{1}H DOSY spectrum of 6.8 ± 0.5 nm PbSe-OA NCs (**Figure 3.S7**) showed broad peaks with chemical shifts characteristic of bound oleate and a diffusion coefficient of $(0.75 \pm 0.01) \times 10^{-10}$ m^{2} s^{-1}. This contrasts significantly with the diffusion coefficient of free oleic acid of $(7.75 \pm 0.05) \times 10^{-10}$ m^{2} s^{-1} (**Figure 3.S8**). The measured diffusion coefficient for PbSe-OA corresponds to a hydrodynamic diameter of 10.0 ± 0.5 nm, which agrees well with a 6.8 nm PbSe core and a tightly bound ~1.6 nm ligand shell on each side.

The broad alkene resonance at δ 5.7 ppm is well separated from other resonances in the ^{1}H NMR spectrum and provides an ideal handle for tracking the fate of oleate as ligand stripping progresses. As BF_3:Et_2O was added to the NC dispersion, the broad oleate alkene resonance shifted upfield and decreased in intensity while a sharp resonance at δ 5.4–5.5 ppm, which we assign to $[OA:BF_3]^-$, appeared and grew in intensity (**Figure 3.3**a). The measured diffusion coefficient of the broad resonance increased only slightly throughout the experiment (from $(0.75 \pm 0.01) \times 10^{-10}$ to $(1.20 \pm 0.02) \times 10^{-10}$ m^{2} s^{-1}), but the measured diffusion coefficient of the sharp resonance increased from $(1.02 \pm 0.03) \times 10^{-10}$ m^2 s^{-1} at 0.2 equiv of BF_3 to $(4.43 \pm 0.02) \times 10^{-10}$ m^2 s^{-1} at 2.3 equiv of BF_3 (**Figure 3.3**b and **Figure 3.S9**). This can be explained by oleate reacting with BF_3:Et_2O to form $[OA:BF_3]^-$ and Et_2O. As the negative charge of $[OA:BF_3]^-$ is more diffuse than that of OA^-, $[OA:BF_3]^-$ is expected to bind much less strongly to the nanocrystal surface. As a result, $[OA:BF_3]^-$ rapidly exchanges on and off the nanocrystal, and the observed diffusion coefficient is a weighted average between the bound and unbound states.

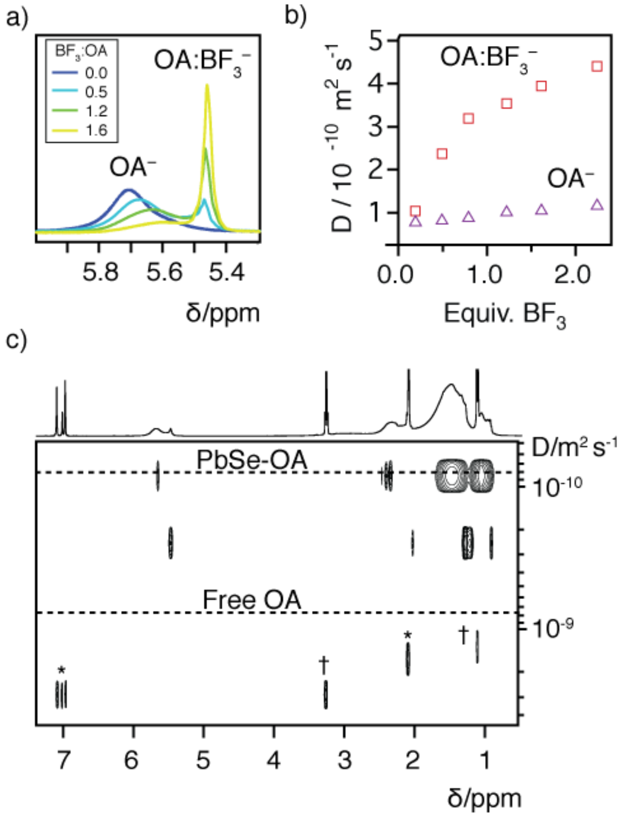

Figure 3.3 Titration of PbSe-OA in toluene-d_8 with BF_3:Et_2O. a) ^1H spectra of the alkene resonance of oleate after addition of 0, 0.5, 1.2, and 1.6 equivalents (with respect to oleate) BF_3:Et_2O. b) Measured diffusion coefficient for the broad (OA^-) and sharp ($[OA:BF_3]^-$) resonances as a function of added BF_3:Et_2O. c) Representative DOSY plot of PbSe-OA + 0.5 equivalents BF_3:Et_2O. For clarity, integration regions for the DOSY spectrum were manually defined to avoid regions where overlapping peaks led to artifacts in the DOSY spectrum. Dashed lines corresponding to the diffusion coefficients of PbSe-OA and free oleic acid, measured separately, are included for comparison. * indicates solvent and † indicates Et_2O.

As the titration proceeded, $[OA:BF_3]^-$ became increasingly liberated from the surface. On the other hand, unreacted oleate remained tightly bound to the NC. As more of the ligand shell was removed, the remaining oleate ligands experienced more configurational entropy (or conformational degrees of freedom), allowing them to reconfigure at the ligand–NC interface. As a result, the hydrodynamic diameter of the NC, as measured by DOSY of the broad resonance at δ 5.7 ppm, decreased from 10.0 ± 0.5 nm (inorganic core + ligand shell) to 6.3 ± 0.3 nm (inorganic core alone) over the course of the titration. Changes in the chemical shift for tightly bound oleate can be explained by changes in the local dielectric environment as neighboring oleate ligands are removed. These results provide strong support that $[OA:BF_3]^-$ adducts are exchanging on and off the surface of PbSe nanocrystals during the stripping process, thus stabilizing the surface against surface metal cation desorption. Alternate explanations for the sharp peak at δ 5.5 ppm were considered but found to be inconsistent with our observations. For example, we considered that the sharp resonance at δ 5.5 ppm could be due to the exchange of charge-neutral $Pb(OA)_2$, which Hens and co-workers observed in the case of PbSe-OA oxidation[37]. However, we found that $Pb(OA)_2$ is unstable in the presence of BF_3, making this hypothesis unlikely (**Figure 3.S10**). Furthermore, all experiments were carried out in tightly sealed screw-top NMR tubes, which were immediately transferred from a glovebox into the NMR spectrometer in order to avoid oxygen exposure. We also ruled out the possibility that $[OA:BF_3]^-$was merely becoming entangled in the ligand shell rather than exchanging on and off the nanocrystal surface by considering that the diffusion coefficient measured at 2.3 equiv of added $BF_3:Et_2O$ indicated that the species was still spending some time diffusing with the nanocrystal, despite the almost complete loss of the ligand shell at this point in the titration.

Support that $BF_3:Et_2O$-mediated equilibrium-controlled ligand stripping avoids loss of surface excess Pb(II) was provided by measurement of the PbSe NC's surface excess Pb(II) before and after stripping using inductively coupled plasma atomic emission spectroscopy (ICP-AES). As-synthesized 5.8 ± 0.5 nm diameter PbSe-OA NCs gave a Pb:Se ratio of 1.24 ± 0.03, while naked PbSe returned with a 1.23 ± 0.02 Pb:Se ratio. This retention of surface excess Pb(II) during ligand stripping is unique among agents that generate naked PbSe nanocrystals: a ~1:1 ratio is typically observed when using Meerwein's salt directly, while a 1.15:1 ratio is observed when using 1-ethoxy-*N,N*-dimethylmethaminium tetrafluoroborate[42]. Moreover, our new BF_3:LB approach is the only procedure that yields dispersible naked PbSe, most likely due to the enhanced electrostatic stabilization that follows retention of excess surface Pb(II). On the basis of these data, it is then appropriate to describe the composition of naked PbSe nanocrystals as $(Pb^{2+})_{0.23n}(Y^-)_{0.46n}(PbSe)_n$, where n is ~1600 and Y^- is the counterion generated during ligand stripping[47].

Given that no exogenous ions of the type Y^- were added to the ligand-stripping solution, it was necessary to establish the chemical identity of Y^- and its mechanistic origins as the compensating charge at the cationic naked PbSe NC surface. FT-IR of a thin film of naked PbSe NCs showed a strong peak at 1120 cm^{-1}, suggesting the presence of BF_4^- even though no $BF_4^-$was added to the ligand-stripping solution. To confirm that BF_4^- was present in the purified dispersions of naked PbSe NCs, ^{19}F NMR was carried out. Strong peaks at δ −151.72 and −151.77 ppm with a 1:4 ratio in integrated intensity were observed, consistent with isotopic shifts due to bonding of ^{19}F to ^{10}B and ^{11}B, respectively (**Figure 3.4**). The assignment of this peak to BF_4^- was made by acquiring the ^{19}F NMR spectrum of $NaBF_4$ in DMF and noting a chemical shift similar to that observed for our naked PbSe dispersions (**Figure 3.4**a,b). We also noted that BF_4^- in naked PbSe dispersions is only weakly, if at all, associating with the NC surface in DMF (**Figure 3.4**c,d).

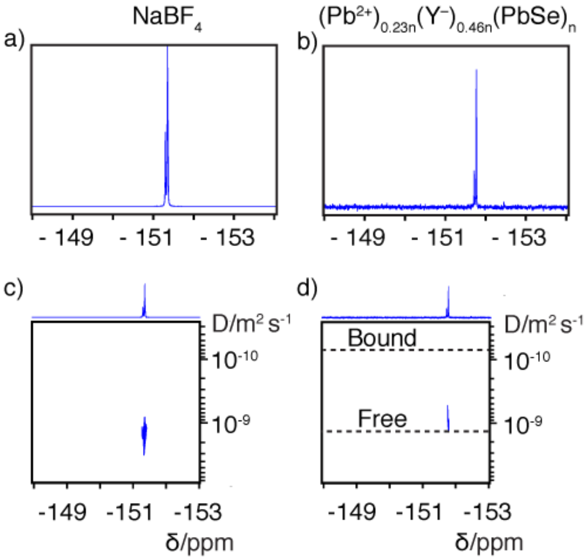

Figure 3.4 ^{19}F NMR evidence for BF_4^- as a non-coordinating counter-ion in naked PbSe NC dispersions. a) and b) depict ^{19}F NMR of $NaBF_4$ and naked PbSe NC in DMF, respectively. Identification of the species as BF_4^- was made on the basis of similar chemical shifts. The slight difference in chemical shifts can be attributed to concentration and dielectric effects. c) and d) depict ^{19}F-DOSY spectra for $NaBF_4$ and naked PbSe NC in DMF, respectively. On the basis of this data, it is clear that BF_4^- is only weakly, if at all, associating with the NC surface in this high dielectric constant dispersant.

In order to establish the origins of the formation of BF_4^-, we acquired the ^{19}F NMR spectrum for BF_3:Et_2O in DMF-d_7 (**Figure 3.S11**). The major chemical species present was the DMF adduct of BF_3 at δ −152.4 ppm, this adduct accounting for 96% of the fluorine in the system, alongside two minor fluorine-containing species. The chemical shifts of these minor species were δ −150.8 and −151.8 ppm and were present in an ~1:2 ratio in integrated intensity. On the basis of the chemical shift, the peak at δ −151.8 ppm can be assigned to BF_4^-. These data are consistent with the disproportionation of DMF:BF_3 to form $[(DMF)_2BF_2]^+$ and BF_4^-, thus accounting for one possible source of BF_4^- counterions in naked PbSe NC dispersions (**Figure 3.5**)[48].

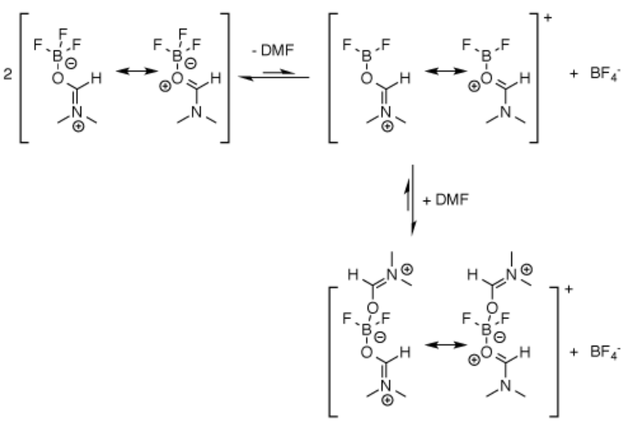

Figure 3.5 Disproportionation of DMF:BF_3. DMF:BF_3 initially forms via an exchange of BF_3 from the weaker Lewis base diethyl ether to the more basic DMF (not shown). The DMF:BF_3 adduct is resonance stabilized. This adduct can react with a second equivalent of BF_3:DMF in a fluoride transfer reaction to yield BF_4^- and $[BF_2DMF]^+$. Finally, the open coordination site on boron is filled by DMF to yield $[BF_2(DMF)_2]^+$.

From the view of electroneutrality, the replacement of anionic oleate ligands with non-coordinating BF_4^- counterions at the NC surface requires both generation of BF_4^- and either conversion of oleate anions to a neutral species or pairing of oleate with a cationic species (i.e., OA^- with $[(DMF)_2BF_2]^+$). We sought to understand oleate speciation post-stripping by performing ESI-MS on a reaction mixture of $Pb(OA)_2$ and $BF_3:Et_2O$ in benzene-*d*$_6$ (Figure 3.6). It is known from previous work that carboxylates can coordinate 1 or 2 equiv of BF_3 and that carboxylate BF_3 adducts can undergo disproportionation reactions to generate BF_4^- and $[B(O_2CR)_nF_{4-n}]^-$[49]. In accordance with this known reactivity pathway, ESI-MS indicated that our reaction mixture contained OA^- (**1**, *m*/*z* 281.25, calcd 281.25), $[OA:BF_3]^-$ (**2**, *m*/*z* 349.26, calcd 349.25), $[OA(BF_3)_2]^-$ (**3**, *m*/*z* 417.26, calcd 417.26), and $[B(OA)_2F_2]^-$ (**4**, *m*/*z* 611.50, calcd 611.50) (**Figure 3.6**, **Figure 3.7**). In addition to anionic disproportionation products, we also observed species that resulted from the hydrolysis of neutral disproportionation products in the presence of adventitious water. For example, fluoride transfer from $[OA:BF_3]^-$ (**2**) to $BF_3:Et_2O$ generates BF_4^- and $OA(BF_2)$ (**5**), which readily dimerizes to form the neutral $(OA)_2(BF_2)_2$species. While this dimer is not directly observable by ESI-MS due to its lack of charge, the deprotonated hydrolysis product $[(OA)_2(BF_2)(BFO)]^-$ (**6**, *m*/*z* 657.50, calcd 657.51) was observed. The $[OA(BF_3)_2]^-$ adduct **3** can also undergo fluoride loss to generate BF_4^- and neutral $OA(BF_3)(BF_2)$. Again, this neutral species is undetectable by ESI-MS, but we observed the deprotonated form of the hydrolysis product, $[OA(BF_2)(BF_2O)]^-$ (**7**, *m*/*z* 395.26, calcd 395.26). The transfer of fluoride from BF_3 oleate adducts to excess $BF_3:Et_2O$ provides a pathway for the conversion of anionic oleate ligands into neutral species along with the generation of non-coordinating BF_4^-. It is also worth noting that, in addition to $[\mathrm{OA:BF_3}]^-$, the anionic species formed along this pathway also have the ability to stabilize NC surfaces during the stripping process.

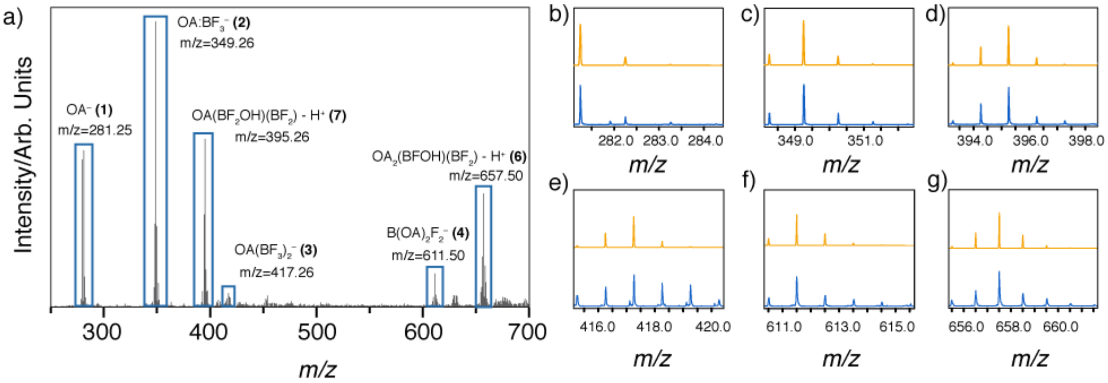

Figure 3.6 a) High resolution negative-ion mode ESI-MS of $\mathrm{Pb(OA)_2}$ + $\mathrm{BF_3{:}Et_2O}$. Six of the species proposed in **Figure 3.7** were identified in the mass spectrum and are boxed for clarity. Isotope distribution patterns for b) OA^-, c) $[\mathrm{OA:BF_3}]^-$, d) $[\mathrm{OA(BF_2)(BF_2O)}]^-$, e) $[\mathrm{OA(BF_3)_2}]^-$, f) $[\mathrm{B(OA)_2F_2}]^-$, and g) $[\mathrm{(OA)_2(BF_2)(BFO)}]^-$ are shown in blue (bottom trace) along with predicted patterns (orange, top trace). Fully annotated isotope distribution patterns can be found in **Figure 3.S11**.

The unprecedented access to stable dispersions of cationic naked PbSe NCs allowed us to better control their mesoscale order in thin films and composites, yielding new classes of mesostructured materials with applications as energy conversion materials. For example, thin films of lead chalcogenide NCs are common active layers in Schottky-type solar cells, field effect transistors, NIR photodetectors, and thermoelectrics[13,23,27,42,50–58]. As synthesized (i.e., with ligands intact), they can be assembled into periodic lattices with hexagonal close packing (*hcp*). Where controlled propagation of energy in the film is required for the function of the device, ligand removal can be advantageous. As shown here and elsewhere, order is usually lost upon stripping ligands in thin films (**Figure 3.8** and **Figure 3.S13**)[50,59]. In addition, cracks and defects can manifest as a result of the dramatic volume change that occurs when organics are liberated. In contrast to the colloidal glasses produced by in-film ligand removal, ordered thin films of naked PbSe can be prepared simply by casting their dispersions directly onto substrates. Apparent cubic packing is evidenced in the top-down SEM images (**Figure 3.8**d), indicating significant differences in the preferred packing geometry for ligand-coated and ligand-stripped NCs. To further distinguish packing geometries between the different PbSe NC films, grazing incidence small-angle X-ray scattering (GISAXS) was carried out. Both ligand-stripped PbSe NC films in **Figure 3.8**c,d showed a decrease in interparticle spacing from ~1.3 to ~0.4 nm, consistent with ligand removal. However, films that were spin-coated from stripped dispersions of PbSe exhibited a tendency toward in-plane ordering as opposed to the isotropic packing observed in films that were stripped in-film (**Figure 3.8**d and **Figure 3.S13**).

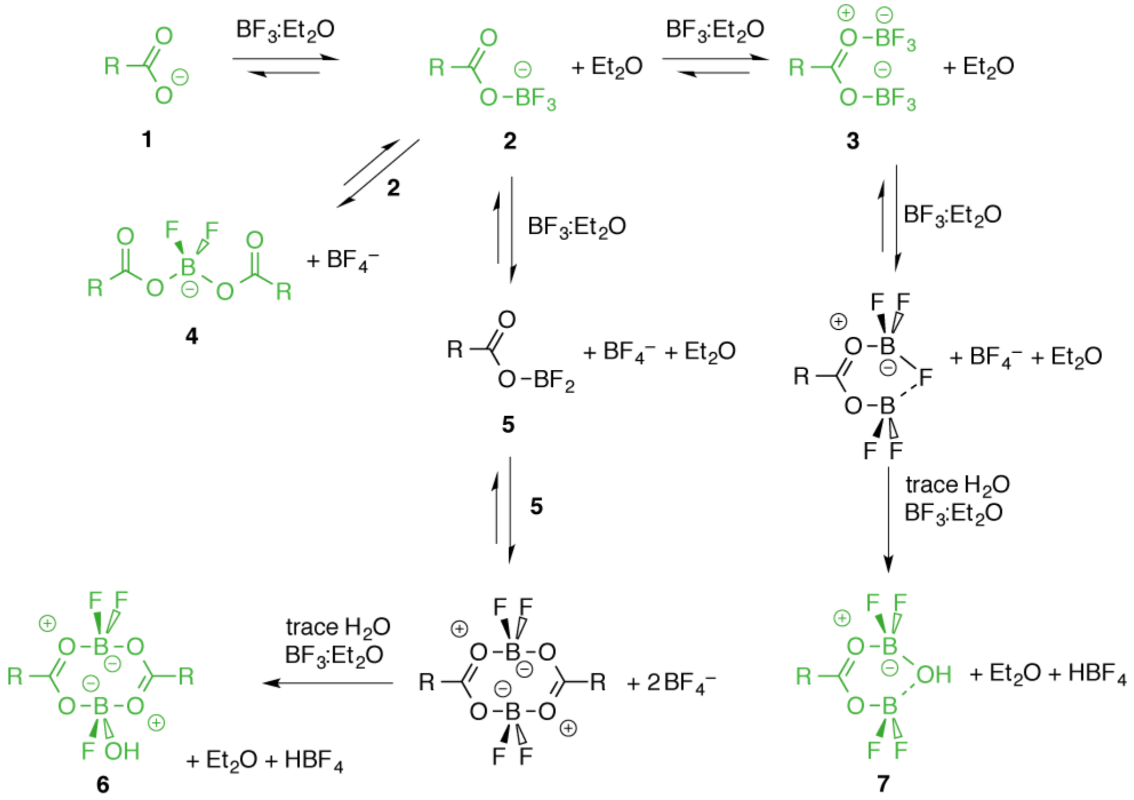

Figure 3.7 Reaction pathways available to OA^- in the presence of $BF_3:Et_2O$ to yield BF_4^-. OA^- forms adducts with either one or two equivalents of BF_3 to give intermediates **2** and **3**, respectively. Compound **2** undergoes disproportionation, yielding $[B(OA)_2F_2]^-$ and BF_4^-. Alternatively, **2** can transfer a fluoride to $BF_3:Et_2O$ to give a charge-neutral species **5** and BF_4^-. Species **5** dimerizes readily, and is observable as compound **6** in the presence of adventitious H_2O during the ESI-MS measurement. BF_3-mediated disproportionation of **3** is also observable along the reaction pathway proposed. Chemical structures for **1**, **2**, **3**, **4**, **6**, and **7** (*green*) were verified by ESI-MS.

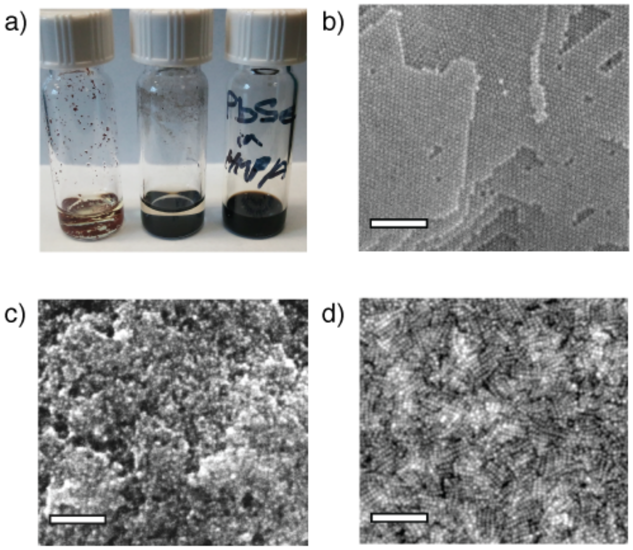

Figure 3.8 a) Comparison of different ligand stripping reagents for PbSe-OA: $NOBF_4$ rapidly oxidizes PbSe yielding the red allotrope of Se^0 (left); application of Meerwein's salt yields stoichiometric PbSe with poor dispersability (middle); ligand stripping with Lewis base adducts of BF_3 (right) yields stable dispersions of cationic naked PbSe NCs. b) PbSe-OA form *hcp* superlattices when deposited from stable dispersions in aliphatic hydrocarbons. c) In-film removal of oleates in *hcp*-ordered PbSe-OA films by Lewis-base adducts of BF_3 destroys ordering and can introduce cracking. d) Film deposition from cationic naked PbSe NC inks yields large-area, ordered films with improved film quality. All scale bars are 100 nm.

The observed packing in films deposited from ligand-coated vs ligand-stripped PbSe NCs can arise from differences in surface energies of exposed facets leading to preferred NC-to-NC orientations[60], differences in packing preferences for nondeformable objects (i.e., the naked PbSe) in comparison to partially deformable ligand-coated particles[61], and differences in interaction potentials available to the system to guide the assembly trajectory during solvent evaporation (van der Waals vs electrostatics)[62]. As such, our work suggests new opportunities to control energy propagation in NC films through their packing in the active layers.

Conclusion

The mechanistic insights gained in this work provide a much-needed framework for rationalizing the successes and failures of different chemical approaches for removing surface-bound ligands from nanocrystals while maintaining colloidal dispersibility. We hypothesized that earlier approaches based on irreversible severing of NC–ligand bonds failed to maintain colloidal dispersibility for sensitive compositions due to a lack of surface stabilization and concomitant desorption of excess metal cations from the NC surface. To address this shortcoming, we proposed the use of reversible Lewis acid–base chemistry to generate physisorbed anionic species that stabilize the NC surface until coordinating solvent is able to repassivate the surface. Using PbSe NC as a model system, we demonstrated that anionic BF_3 adducts of surface-bound ligands exchanged on and off the NC surface, providing stabilization. Furthermore, we showed that NCs stripped under equilibrium control maintained colloidal stability and did not suffer from the excess surface metal desorption that can be problematic when using some irreversible ligand stripping reagents. As a result, ligand stripping under equilibrium control represents a powerful new class of reactions for modifying the surface chemistry of colloidal NC while maintaining colloidal stability.

More importantly, the new ligand removal technique discovered herein not only enabled the wider applicability of the stripping chemistry, it also opened up new avenues for production of microporous materials, specifically metal-organic frameworks (MOFs). By reliably revealing a bare surface with only loosely coordinating moieties, etching ligands can easily penetrate and react with the nanocrystal, making them a class of versatile MOF precursors. This avenue of research has led to the successes of two related but separate projects, where two different classes of MOFs are produced from stripped metal oxide nanocrystal precursors, upon which I will elaborate in the ensuing chapters.

Experimental Section

Materials and Methods

Acetone (anhydrous, 99.9%), benzene-d_6 (99.6% atom D), 1,4-dioxane (anhydrous, 99.8%), diphenylphosphine (98%), ethanol (anhydrous, 99.5%), hexamethylphosphoramide (HMPA, 99%), hexanes (anhydrous, 99%), lead(II) nitrate (99.99%), lead(II) oxide (99.999% trace metals grade), *N*,*N*-dimethylformamide (anhydrous, 99.8%), *N*,*N*-dimethylformamide-d_7 (99.5% atom D), nitric acid (70%, 99.999% trace metals grade), 1-octadecene (90% tech grade), octane (anhydrous, 99%), oleic acid (90% tech grade), selenium shot (99.999% trace metals grade), toluene (anhydrous, 99.8%), toluene-d_8 (99.6% atom D), and α,α,α-trifluorotoluene (anhydrous, 99%) were obtained from Sigma-Aldrich. Boron trifluoride etherate (BF_3:Et_2O, 48% BF_3 basis) was obtained from Acros Organics. Tri-*n*-octylphosphine (TOP, 90% tech grade) was obtained from Alfa Aesar. Pb and Se standards for ICP-AES were obtained from Fluka. Sodium oleate (97%) was obtained from Pfaltz & Bauer. All chemicals were used as received. Lead oleate was prepared by metathesis of lead(II) nitrate and sodium oleate. NMR spectra were acquired on a Bruker Biospin 500 MHz NMR spectrometer at 500 MHz for ^1H and 470 MHz for ^{19}F. ^1H chemical shifts were referenced with respect to residual solvent peaks, and ^{19}F shifts were internally referenced to α,α,α-trifluorotoluene (−63.72 ppm from $CFCl_3$) as a secondary standard. Pb and Se contents of NC samples were measured by ICP-AES on a Varian 720-ES spectrometer using an argon plasma. Prior to analysis, dried NC samples were digested in 70% nitric acid in a closed Teflon container for several days. High-resolution ESI-MS spectra were obtained in negative ion mode on a Bruker microTOF Q high-resolution mass spectrometer. SEM images were obtained with a Zeiss Gemini Ultra-55 analytical scanning electron microscope equipped with in-lens and secondary electron detectors at a beam energy of 2–5 keV. Grazing incidence small-angle X-ray scattering measurements were made at beamline 7.3.3 of the Advanced Light Source, Lawrence Berkeley National Laboratory, using an incident angle of 0.16°, a wavelength of 0.124 nm (10 keV), a detector distance of 3.9 m, and recorded on a Pilatus 1 M flat detector[63]. The resulting data were processed with the Nika 2D SAS software package in Igor Pro[64].

Synthesis of Oleate-Passivated Lead Selenide Nanocrystals (PbSe-OA)

Lead selenide nanocrystals were synthesized under an inert atmosphere following slightly modified reported procedures[65]. Briefly, selenium shot (960 mg, 12.2 mmol) was added to TOP (8.64 g, 23.3 mmol) in a 40 mL septum-capped vial and the mixture was stirred overnight in a nitrogen glovebox prior to the addition of diphenylphosphine (84 mg, 0.45 mmol). Separately, in a 100 mL three-necked flask, lead(II) oxide (1.34 g, 6 mmol), oleic acid (4.24 g, 15 mmol), and 1-octadecene (23.4 mL) were placed under vacuum at room temperature for 15 min and then at 110 °C for 1 h to dry and degas the solution. After the solution became colorless and transparent, the temperature was raised to 180 °C under N_2, at which point the TOP-Se solution was rapidly injected. After this TOP-Se injection, the reaction temperature was dropped to ~150 °C and was kept at this temperature for the desired reaction time (5 min gave PbSe nanocrystals with ~7 nm diameter). The reaction mixture was cooled in a water bath. The nanocrystals were then purified by precipitation three times from hexanes using first ethanol (1×) and then acetone (2×) to give 460 mg of purified NC (1.2 mmol of $(PbOA)_{0.2}PbSe$, 24% yield).

Ligand Stripping Procedure

Activated DMF was prepared in a nitrogen glovebox by adding $BF_3{:}Et_2O$ (20 μL, 0.16 mmol) to 500 μL of DMF and mixing vigorously. Next, 500 μL of a stock solution of nanocrystals in hexanes (5–10 mg mL^{-1}) was added to the activated DMF and the mixture was mixed vigorously. Toluene (3.5 mL) was then added to induce mixing of the two layers and precipitation of stripped nanocrystals, which were redispersed in DMF. The resulting naked nanocrystal dispersion was purified by multiple washes with hexanes and precipitation from DMF with toluene.

In Situ NMR

A known amount of PbSe-OA was dried under vacuum and redispersed in toluene-d_8. The amount of oleate in the system was determined by quantitative NMR using 1,4-dioxane as an internal standard and 45 s interscan delays. Diffusion ordered spectroscopy (DOSY) was carried out at room temperature using standard bipolar convection compensating pulses. The diffusion delay, Δ, was set to 200 ms and the gradient pulse length, δ, was set to achieve at least 90% signal attenuation between 95% and 5% gradient strength. For the BF_3 titration experiment, the gradient pulse length was held at 5 ms, but for other experiments it varied from 1 to 2 ms. The gradient strength was varied between 5 and 95% of the calibrated maximum gradient strength of 51.1 G cm^{-1} in 16 steps. The resulting data were processed in the Bruker Topspin and Bruker Dynamics Center software packages, where it was fit to the appropriate form of the Stejskal–Tanner equation.

ESI-MS

A reaction mixture of $Pb(OA)_2$ and BF_3:Et_2O was prepared by dissolving $Pb(OA)_2$ (3 mg, 4 μmol) in 700 μL of benzene-d_6 and adding BF_3:Et_2O (8 μmol). For improved ionization efficiency, the reaction mixture was diluted 5-fold with dry acetonitrile to prepare the final ESI-MS sample. ESI-MS was run in negative ion mode.

Preparation of Naked Nanocrystal Thin Films and Polymer Composites

Thin films of PbSe-OA were prepared by spin coating a solution of PbSe-OA in 1/1 hexane/octane onto a silicon wafer. To strip the NC film in the solid state, the film was dipped into a solution of BF_3:Et_2O (50 μL) in HMPA (1 mL) and rinsed with hexanes. Ordered thin films of naked PbSe NC could be prepared by spin coating a solution (~10 mg mL^{-1}) of naked PbSe NC directly onto a silicon wafer. Architecture-directing 60 kDa–20 kDa PS-*b*-PDMA block copolymers were prepared as described by us elsewhere[66] and dissolved in DMF to form a stock solution at a concentration of 50 mg mL^{-1}. Separately, a 30 mg mL^{-1} stock solution of naked PbSe NC in DMF was prepared. The stock solutions were mixed along with excess DMF to yield a solution with a final concentration of 10 mg of polymer mL^{-1} and 3–10 mg of NC mL^{-1}, which was dropcast directly onto a Si wafer to produce ordered polymer-NC composites.

Supporting Information

Nanocrystal Syntheses

Synthesis of copper selenide nanocrystals (Cu2-xSe). Copper selenide nanocrystals were synthesized under an inert atmosphere following slightly modified reported procedures[67]. Briefly, selenium powder (94.8 mg, 1.2 mmol) was added to 1-octadecene (9 mL) and OAm (6 mL) in a 50 mL three-necked flask and placed under vacuum at room temperature and 110 °C for 15 min and 1 h, respectively to dry and degass the solution. Afterwards, the Se solution was placed under nitrogen flow and raised to 310 °C. The solution was orange and transparent. Separately, in a 25 mL three-necked flask, CuCl (198 mg, 2 mmol), OAm (2 mL), and 1-octadecene (3 mL) were placed under vacuum at 110 °C for 15 min to dry and degas the solution. The solution was light green and transparent. Next, the copper-containing solution was rapidly injected into the Se-containing solution and the reaction temperature dropped to ~285 °C. The reaction temperature was allowed to recover to 300 °C and was kept at this temperature for 20 min before cooling in a water bath. The particles were then purified by precipitation three times from hexanes/toluene (50% *v/v*) using ethanol.

Synthesis of nickel nanocrystals (Ni). Nickel nanocrystals were synthesized under an inert atmosphere following slightly modified standard procedures[68]. Briefly, nickel(II) 2,4-pentanedionate hydrate (84.7 mg, 0.33 mmol) was added to TOP (1 mL) in a 40 mL septum capped vial and in a nitrogen glovebox and then sonicated for 10 min to form a green/blue solution. In a separate 25 mL three-necked flask, OAm (10 mL) was placed under vacuum at room temperature and 110 °C for 15 min and 1 h, respectively to dry and degas the solvent. The OAm was cooled to RT prior to the injection of the Ni-TOP solution. The reaction temperature was raised at a rate of 10 °C min^{-1} to 250 °C and allowed to react for 30 min. The reaction was cooled in a water bath. The particles were then purified by precipitation three times from hexanes/toluene (50% *v/v*) using ethanol.

Synthesis of manganese oxide nanocrystals (Mn3O4). Manganese oxide nanocrystals were synthesized in air following established procedures[69]. Briefly, manganese acetate (513 mg, 3.0 mmol), stearic acid (1.71g, 6.0 mmol), and OAm (9.9 mL, 30 mmol) were dissolved in xylene (45 mL) in a 250 mL two neck flask with redox condenser and heated to 90 ˚C with stirring. Water (3 mL) was rapidly injected and the solution turned from clear dark brown to cloudy and light brown. The reaction temperature was held at 90 ˚C for 3 h, followed by cooling to room temperature. All solids were removed from the reaction mixture by centrifugation, and 350 mL ethanol was added to precipitate Mn_3O_4 nanocrystals. The nanocrystals were purified by precipitation three times from hexanes using acetone.

Synthesis of zinc oxide nanocrystals (ZnO). Zinc oxide nanocrystals were synthesized in air following slightly modified procedures[70,71]. Briefly, potassium hydroxide (902 mg, 16 mmol) was dissolved in methanol (150 mL) in a 500 mL round-bottom flask. The solution was heated to 60 ˚C with stirring and held at this temperature for 30 min. Next, a stock solution of zinc acetate dihydrate (1.757 g, 8.0 mmol) in methanol (50 mL) was added to the potassium hydroxide solution. The reaction was allowed to proceed for 2 h at 60 ˚C, after which time the mixture was allowed to cool to RT naturally. The reaction mixture volume was reduced to 50 mL under reduced pressure at 40 ˚C. Zinc oxide nanocrystals were precipitated by adding 5 equivalents of hexanes and 1 equivalent of isopropanol followed by centrifugation. The nanocrystals were redispersed in the minimal volume of methanol, and the precipitation and redispersion steps were repeated twice. On the final redispersion step the nanocrystals were redispersed in chloroform (3 mL) containing 375 µL OAm and 121 µL OA. The nanocrystals were precipitated with acetone and purified by precipitation three times from hexanes using acetone.

Synthesis of TiO2 nanocrystals. TiO_2 nanocrystals were synthesized under an inert atmosphere following established procedures[72]. Briefly, OA (35.0 g, 124 mmol) was dried under vacuum at 120 ˚C for 60 min in a 100 mL 3-neck flask. The temperature was reduced to 90 ˚C and the flask was filled with nitrogen. Titanium tetraisopropoxide (1.5 mL, 5.1 mmol) was rapidly injected to yield a clear, yellow solution. After 5 minutes, a stock aqueous solution of trimethylamine-*N*-oxide (2 M, 5 mL, 10 mmol) was injected, at which point the reaction mixture turned white and cloudy. The reaction was held at 90 ˚C with stirring for 5 hours and allowed to cool to RT naturally. The nanocrystals were precipitated by adding 120 mL ethanol. The nanocrystals were recovered by centrifugation and purified three times by precipitation from hexanes using acetone.

Additional Figures

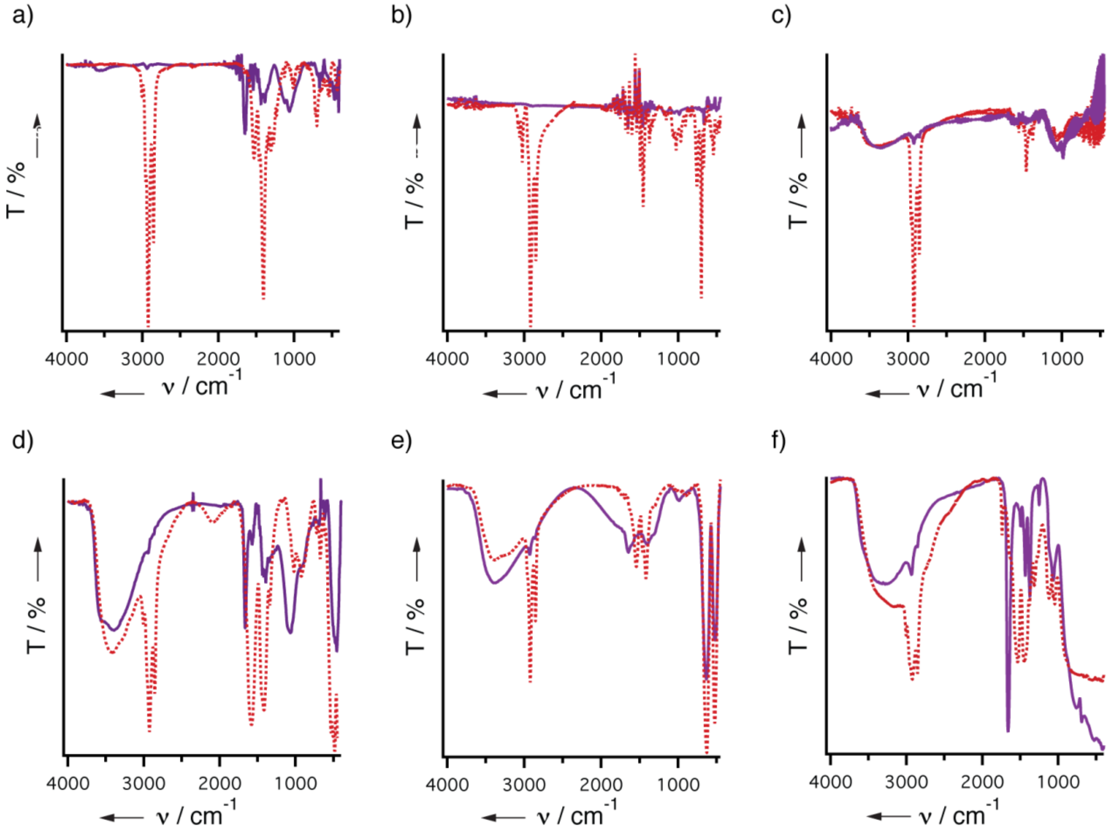

Figure 3.S1 FT-IR of ligand-coated (red, dashed) and ligand-stripped (purple, solid) NCs of a) PbSe, b) Cu1.7Se, c) Ni, d) ZnO, e) Mn3O4 and f) TiO2. The decrease in intensity of the C-H stretch peaks around 2900 cm–1 and the carbonyl stretch around 1400 cm–1 indicate highly efficient ligand removal. Additionally, in the case of PbSe, ZnO, Mn3O4, and TiO2, new peaks are observed around 1100 and 1670 cm–1, which correspond to BF4– and adsorbed DMF, respectively.

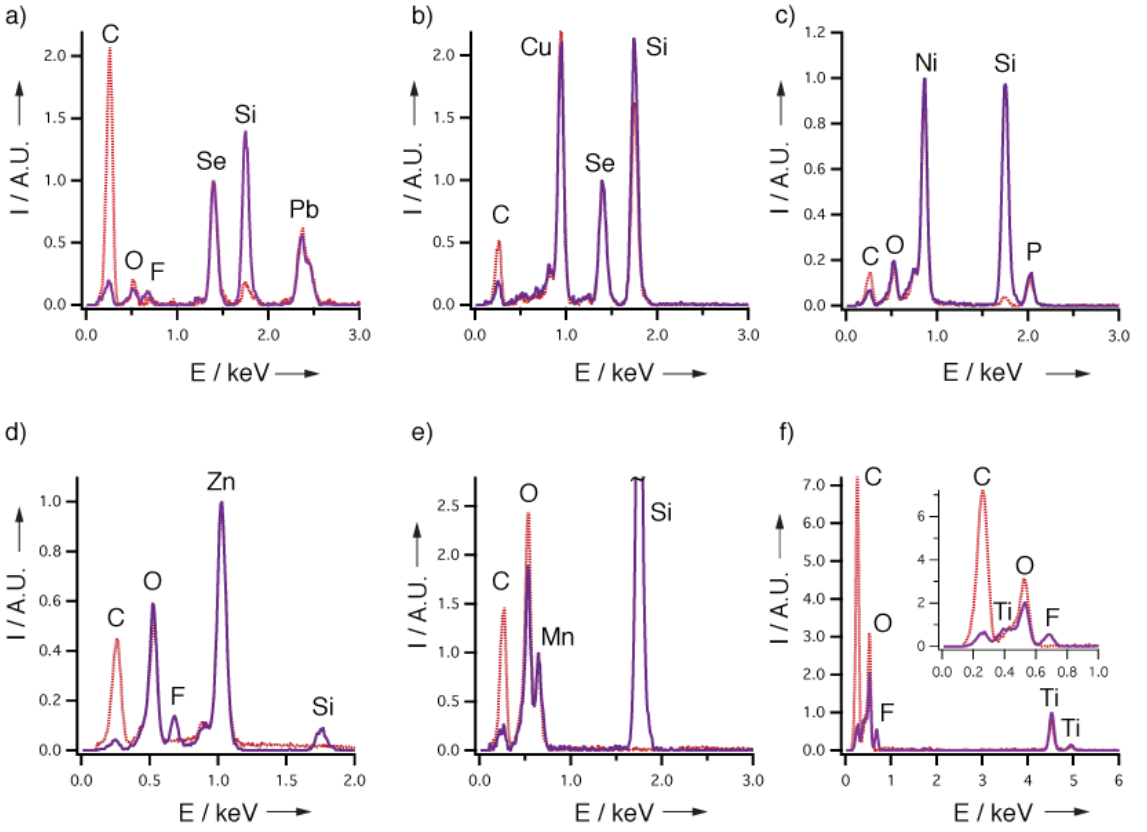

Figure 3.S2 Energy dispersive X-ray (EDX) spectra of a) PbSe, b) Cu$_{1.7}$Se, c) Ni, d) ZnO, e) Mn$_3$O$_4$ and f) TiO$_2$ nanocrystals on Si before (red, dashed) and after (purple, solid) ligand stripping. All spectra are scaled to aid in comparison. In all cases, a dramatic decrease in carbon content indicates ligand removal. Additionally, a new peak for fluorine is commonly observed, which agrees with FT-IR and NMR evidence for BF$_4^-$ counter-ions. Changes in the Si peak are indicative of different film thicknesses and are not related to the stripping process. All measurements were performed with an electron beam energy of 5 keV except for TiO$_2$, which was performed at a beam energy of 10 keV.

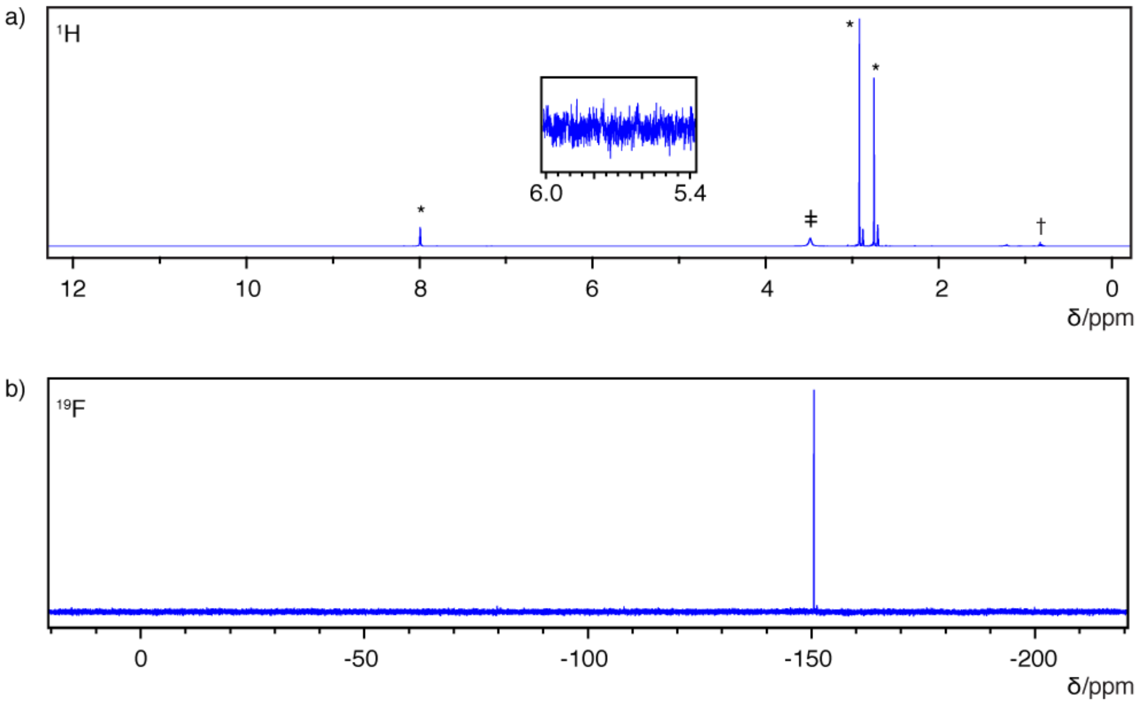

Figure 3.S3 a) ^{1}H and b) ^{19}F NMR spectra of cationic naked PbSe NC in DMF. The ^{1}H spectrum shows only DMF (*) and trace amounts of hexanes (†), along with a broad peak corresponding to a pool of exchanging protons, which is attributed to the presence of trace water (ǂ). Oleate is notably absent, as evidenced by the inset showing the region where the oleate alkene resonance normally appears. The ^{19}F spectrum is an expanded view of the same spectrum from **Figure 3.4**b and is included to demonstrate that no fluorine-containing species other than BF_4^- were present in the naked NC dispersion.

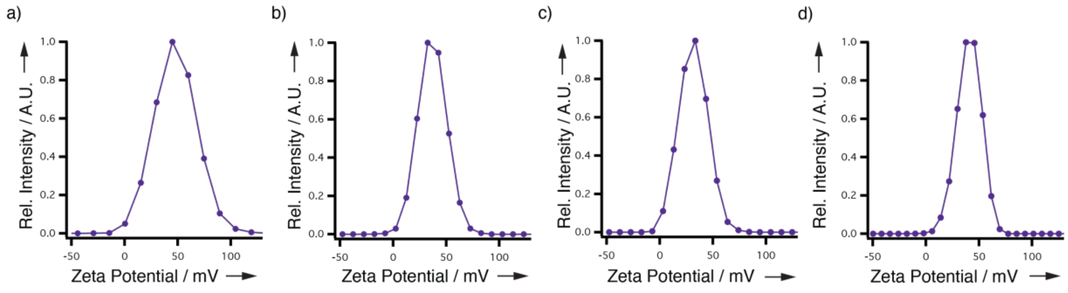

Figure 3.S4 Zeta potential distributions for cationic naked NC dispersions of a) ZnO, b) Mn_3O_4, c) TiO_2, and d) PbSe in DMF. Their average (N = 5) zeta potentials were 48 ± 2, 37 ± 1, 32 ± 1 mV, and 41 ± 2 mV, respectively.

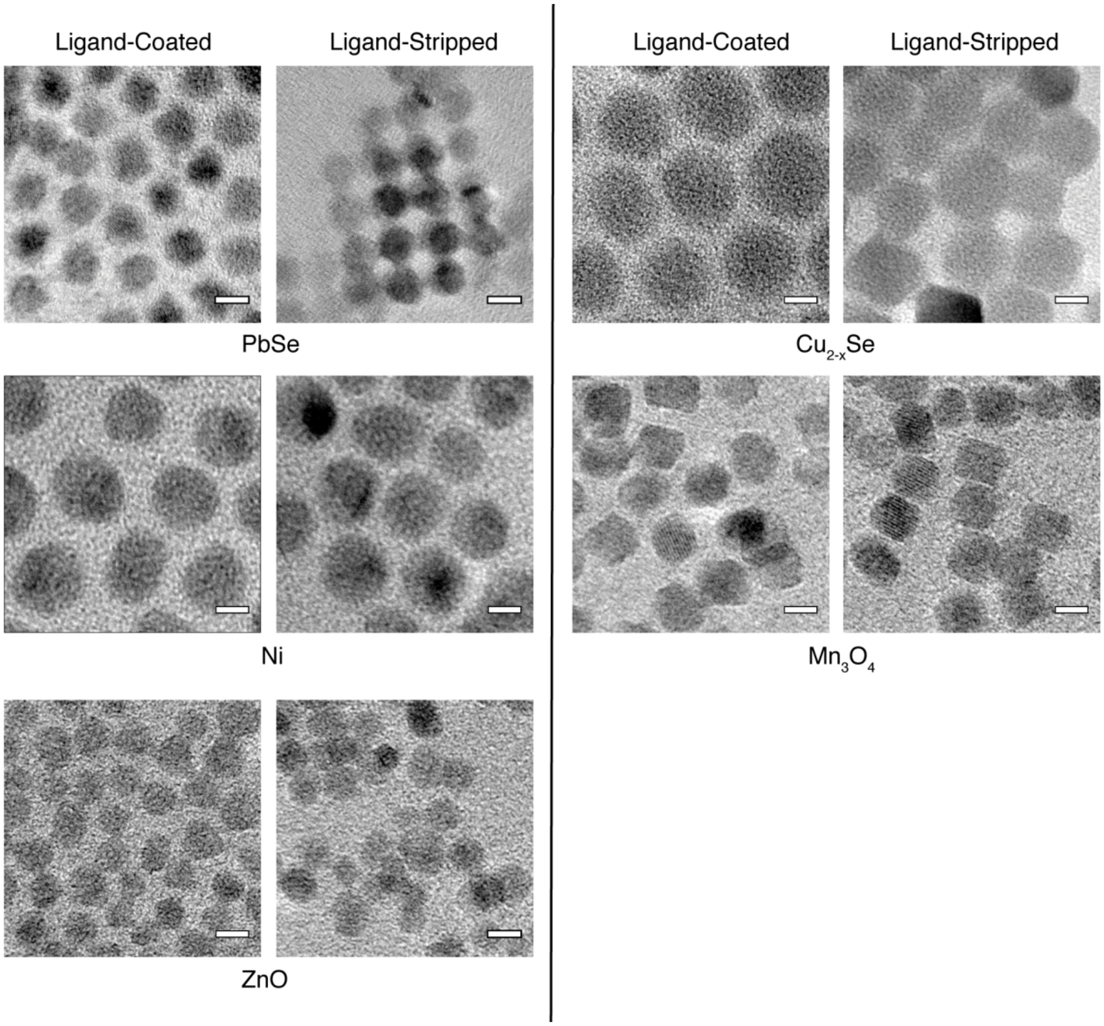

Figure 3.S5 TEM of ligand-coated and ligand-stripped NC. For each composition, ligand-coated NCs are on the left and ligand-stripped on the right. Removal of native ligands from the nanocrystal surface results in decreased inter-particle spacing, but does not result in significant etching or damage to the inorganic NC core. All scale bars are 5 nm.

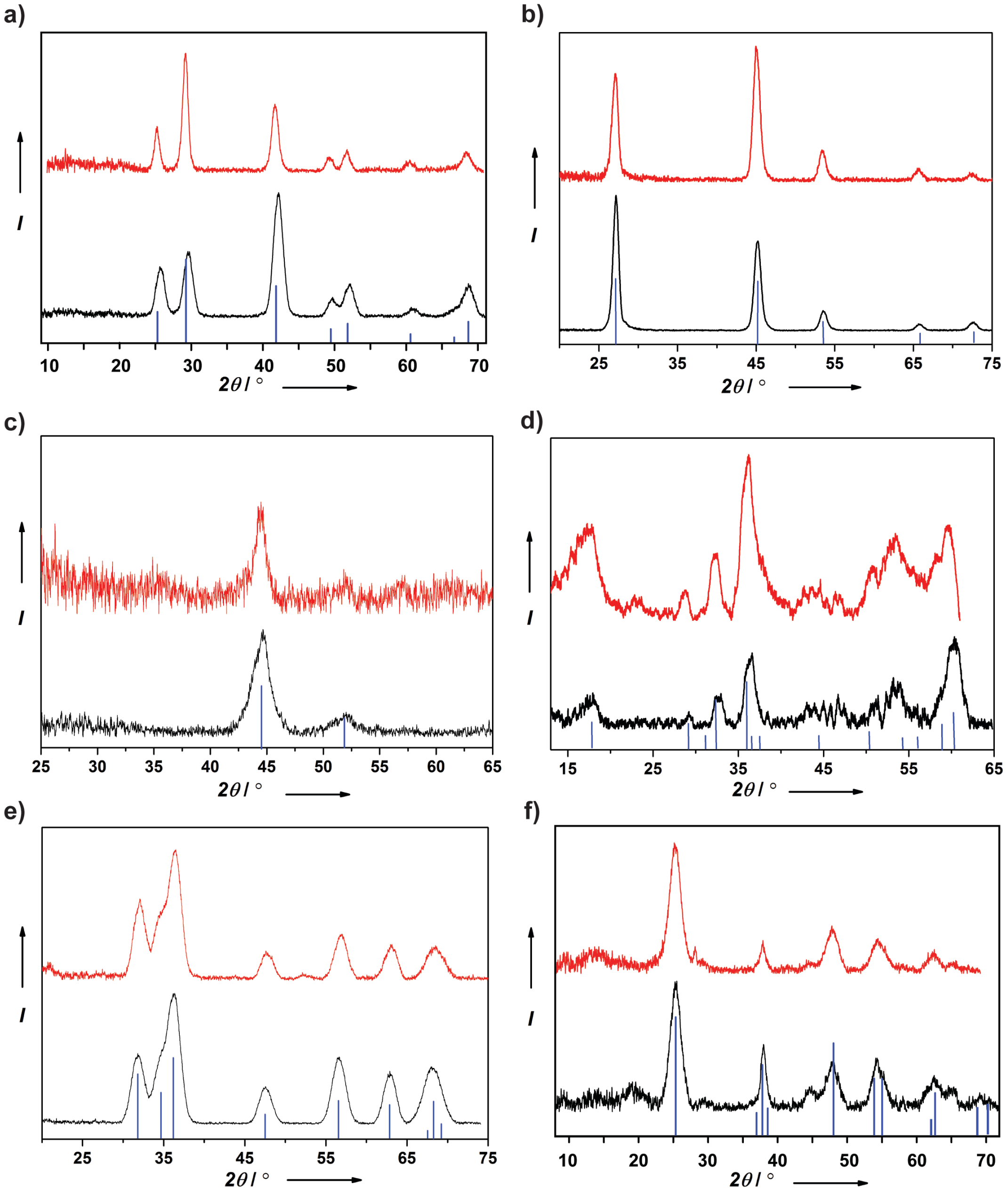

Figure 3.S6 XRD of ligand-coated (black, bottom) and ligand-stripped (red, top) NCs: a)PbSe, b) $Cu_{1.7}Se$, c) Ni, d) Mn_3O_4, e) ZnO, and f) TiO_2. Peaks were assigned according to JCPDS files 01-078-1903, 01-088-2043, 03-065-2865, 00-024-0734, 00-036-1451, and 00-021-1272, respectively.

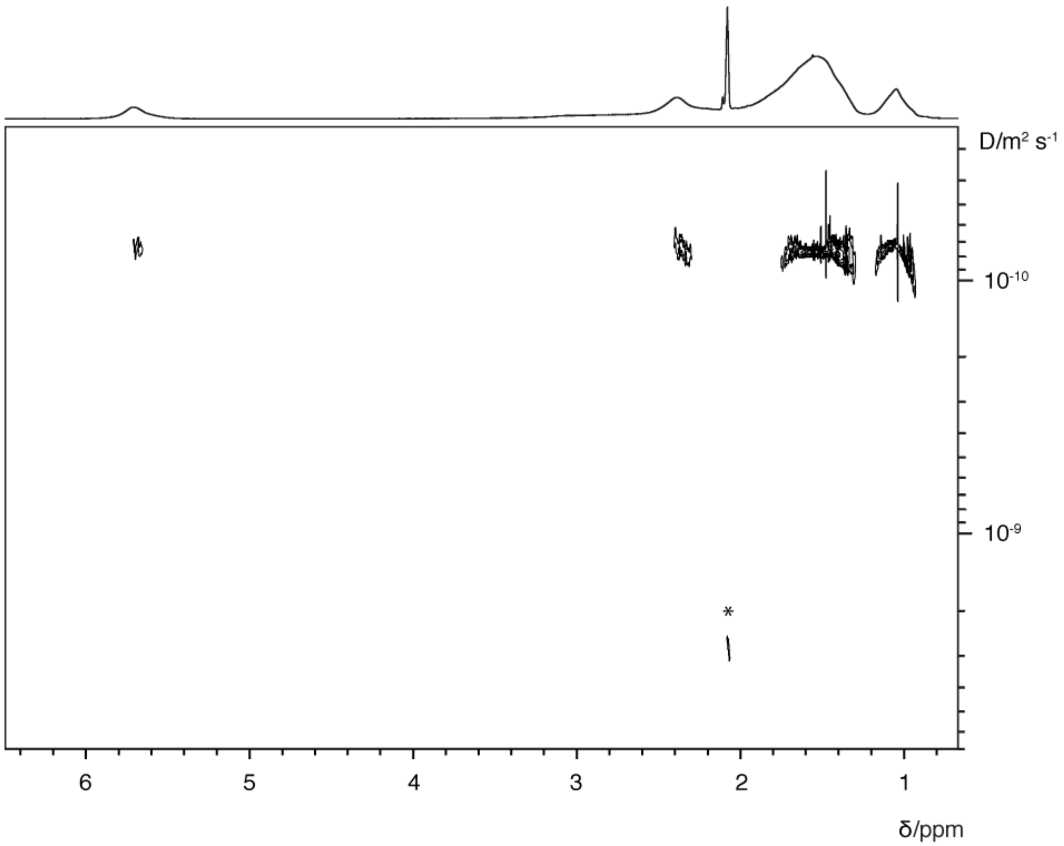

Figure 3.S7 ^{1}H-DOSY of PbSe-OA in toluene-d_8. The measured diffusion coefficient of (0.75 ± 0.01) x 10^{-10} m^2 s^{-1} corresponds to a particle with hydrodynamic radius of 10.0 ± 0.5 nm, which is consistent with a 6.8 ± 0.5 nm nanocrystal with a ~1.6 nm ligand shell on each side. * indicates toluene-d_8

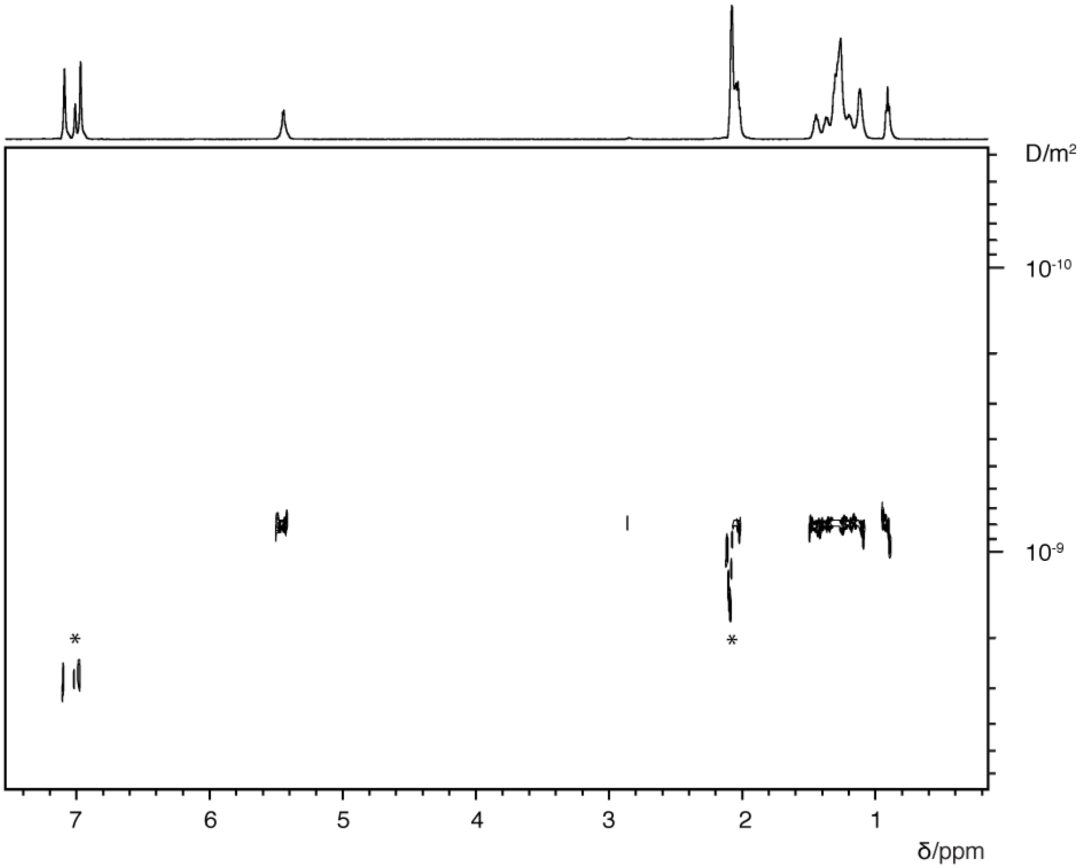

Figure 3.S8 ^{1}H-DOSY of oleic acid in toluene-d_8. The measured diffusion coefficient was (7.75 ± 0.05) x 10^{-10} m^2 s^{-1}. * indicates toluene-d_8

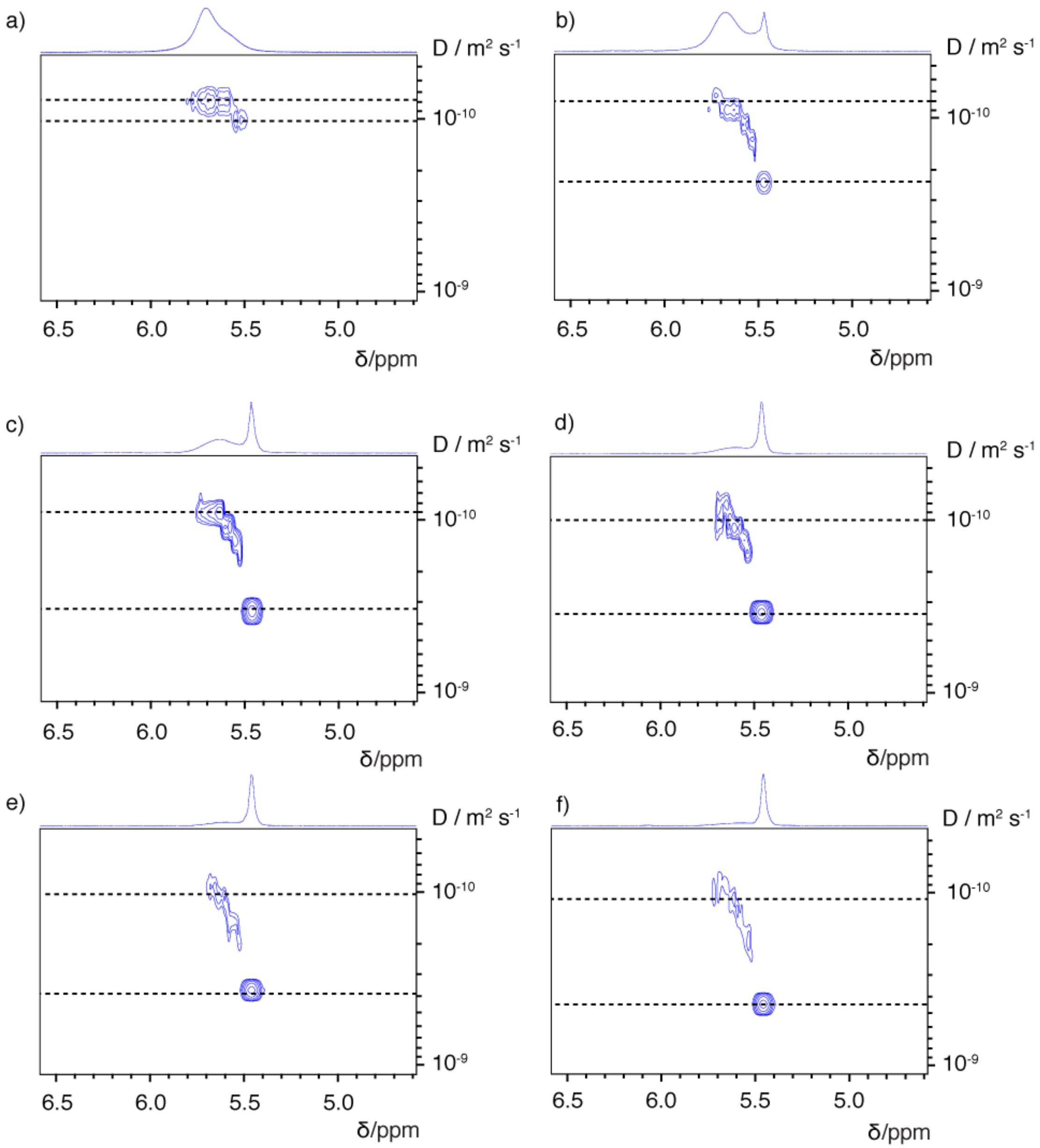

Figure 3.S9 ^{1}H-DOSY of alkene resonances of PbSe-OA during BF_3:Et_2O titration. After addition of a) 0.2, b) 0.5, c) 0.8, d) 1.2, e) 1.6, and f) 2.3 molar equivalents of BF_3:Et_2O with respect to oleate. Dashed lines indicate the measured diffusion coefficient for the broad and sharp resonances.

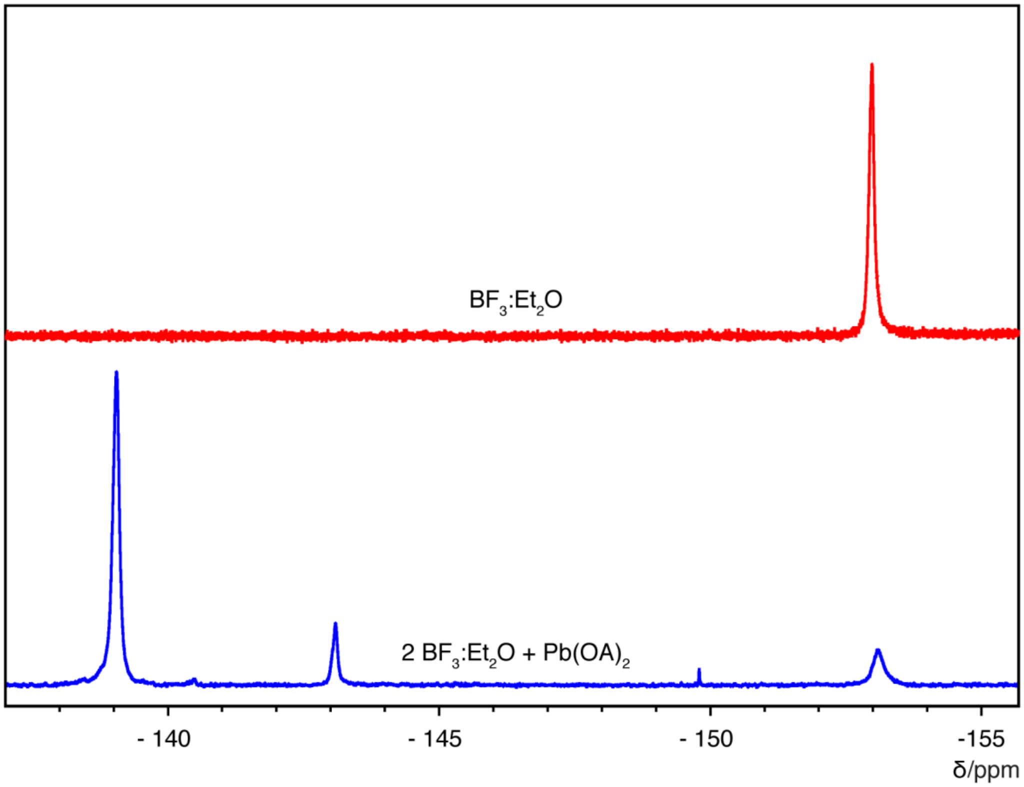

Figure 3.S10 ^{19}F NMR spectrum of BF_3:Et_2O (top, red) and $Pb(OA)_2$ + 2 BF_3:Et_2O (bottom, blue) in benzene-d_6. Upon the addition of $Pb(OA)_2$ to BF_3:Et_2O, the peak for BF_3:Et_2O is dramatically reduced in intensity and is replaced by peaks corresponding to OA:BF_3 and related species. This provides evidence for the chemical instability of $Pb(OA)_2$ in the presence of BF_3:Et_2O.

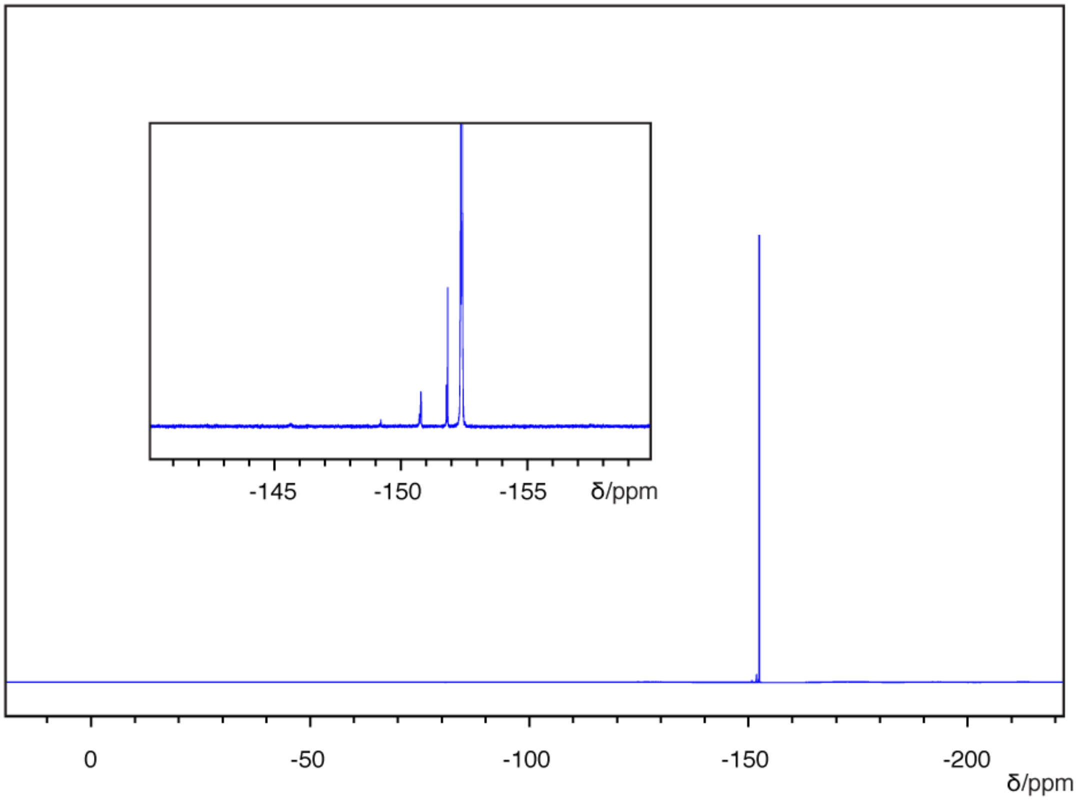

Figure 3.S11 ^{19}F NMR spectrum of BF_3:Et_2O in DMF-*d*$_7$. The peak at δ –152.4 ppm accounts for 96% of the fluorine in the system and corresponds to BF_3:DMF. Minor peaks at δ –150.8 and –151.8 ppm correspond to $[(DMF)_2BF_2]^+$ and BF_4^-, respectively.

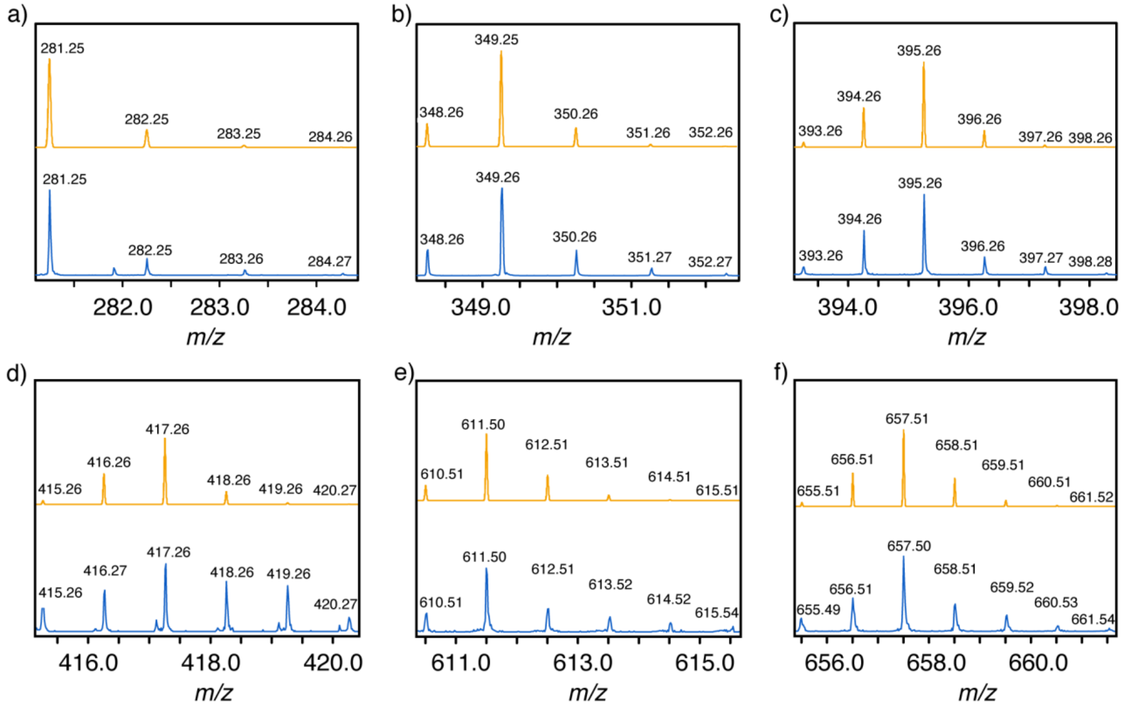

Figure 3.S12 Isotope distribution patterns for ESI-MS of Pb(OA)$_2$ + BF$_3$:Et$_2$O. Measured patterns are shown in blue (bottom) and predicted patterns shown in orange (top) for a) OA$^-$ (**1**), b) [OA:BF$_3$]$^-$ (**2**), c) OA(BF$_2$OH)(BF$_2$) – H$^+$ (**7**), d) [OA(BF$_3$)$_2$]$^-$ (**3**), e) [B(OA)$_2$F$_2$]$^-$ (**4**), and f) (OA)$_2$(BF$_2$)(BFOH) – H$^+$ (**6**).

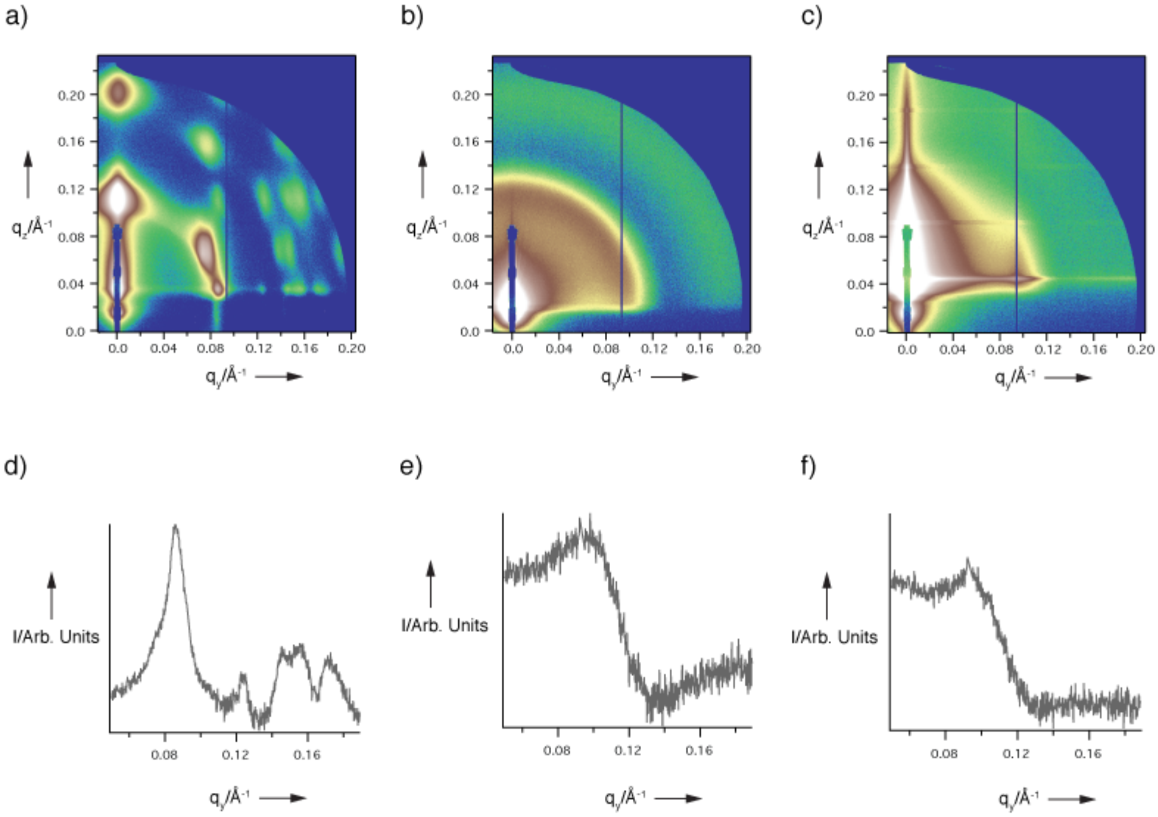

Figure 3.S13 Grazing incidence small angle scattering (GISAXS) patterns for: a) PbSe-OA superlattice, b) PbSe stripped in the solid state, and c) PbSe stripped in solution and spin-coated to form an ordered film. Panels d-f) are the corresponding line scans along the q_y axis for GISAXS data in panels a-c), respectively. The measured particle-particle spacing was 7.3 nm in the case of PbSe-OA and 6.5 and 6.4 nm for PbSe stripped in solution and film. Given the average nanocrystal size of 6.0 ± 0.5 nm (determined by TEM), these spacings correspond to nanocrystal separations of ~1.3 and 0.4 nm before and after stripping.

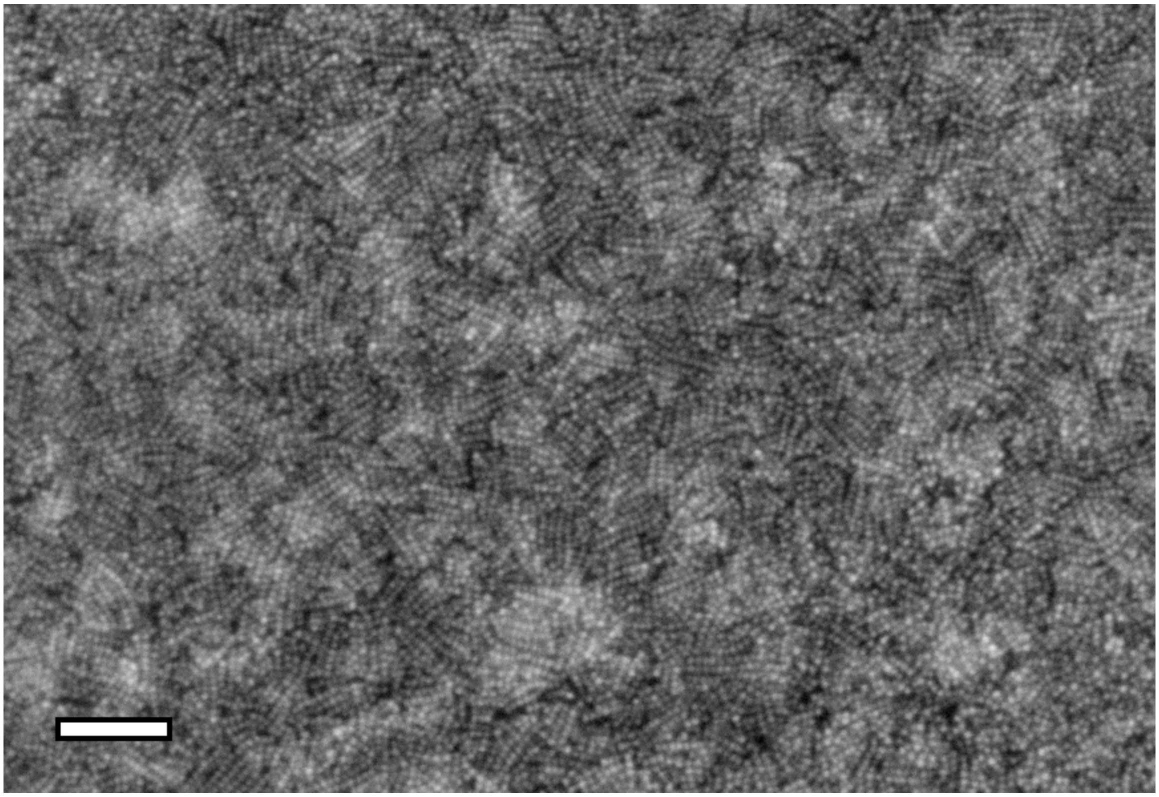

Figure 3.S14 SEM of ligand-stripped PbSe thin-film deposited from solution: an enlarged field of view of the data presented in main text **Figure 3.8**d. Scale bar is 100 nm.

References

(1) Alivisatos, A. P.; Harris, A. L.; Levinos, N. J.; Steigerwald, M. L.; Brus, L. E. *J. Chem. Phys.* **1988**, *89* (7), 4001–4011.

(2) Brus, L. *J. Phys. Chem.* **1986**, *90* (12), 2555–2560.

(3) Steigerwald, M. L.; Alivisatos, A. P.; Gibson, J. M.; Harris, T. D.; Kortan, R.; Muller, A. J.; Thayer, A. M.; Duncan, T. M.; Douglass, D. C.; Brus, L. E. *J. Am. Chem. Soc.* **1988**, *110* (10), 3046–3050.

(4) Murray, C. B.; Kagan, C. R.; Bawendi, M. G. *Annu. Rev. Mater. Sci.* **2000**, *30* (1), 545–610.

(5) Yin, Y.; Alivisatos, A. P. *Nature* **2005**, *437* (7059), 664–670.

(6) Xia, Y.; Xiong, Y.; Lim, B.; Skrabalak, S. E. *Angew. Chem. Int. Ed.* **2009**, *48* (1), 60–103.

(7) Grim, J. Q.; Manna, L.; Moreels, I. *Chem. Soc. Rev.* **2015**, *44* (16), 5897–5914.

(8) Somers, R. C.; Bawendi, M. G.; Nocera, D. G. *Chem. Soc. Rev.* **2007**, *36* (4), 579–591.

(9) Aricò, A. S.; Bruce, P.; Scrosati, B.; Tarascon, J.-.; Van Schalkwijk, W. *Nat. Mater.* **2005**, *4* (5), 366–377.

(10) McDonald, S. A.; Konstantatos, G.; Zhang, S.; Cyr, P. W.; Klem, E. J. D.; Levina, L.; Sargent, E. H. *Nat. Mater.* **2005**, *4* (2), 138–142.

(11) Panthani, M. G.; Akhavan, V.; Goodfellow, B.; Schmidtke, J. P.; Dunn, L.; Dodabalapur, A.; Barbara, P. F.; Korgel, B. A. *J. Am. Chem. Soc.* **2008**, *130* (49), 16770–16777.

(12) Steinhagen, C.; Panthani, M. G.; Akhavan, V.; Goodfellow, B.; Koo, B.; Korgel, B. A. *J. Am. Chem. Soc.* **2009**, *131* (35), 12554–12555.

(13) Luther, J. M.; Law, M.; Beard, M. C.; Song, Q.; Reese, M. O.; Ellingson, R. J.; Nozik, A. J. *Nano Lett.* **2008**, *8* (10), 3488–3492.

(14) Alivisatos, A. P. *Science* **1996**, *271* (5251), 933–937.

(15) Haase, M.; Schäfer, H. *Angew. Chem. Int. Ed.* **2011**, *50* (26), 5808–5829.

(16) Colvin, V. L.; Schlamp, M. C.; Alivisatos, A. P. *Nature* **1994**, *370* (6488), 354–357.

(17) Wang, C.; Shim, M.; Guyot-Sionnest, P. *Science* **2001**, *291* (5512), 2390–2392.

(18) Runnerstrom, E. L.; Llordés, A.; Lounis, S. D.; Milliron, D. J. *Chem. Commun.* **2014**, *50* (73), 10555–10572.

(19) Llordés, A.; Garcia, G.; Gazquez, J.; Milliron, D. J. *Nature* **2013**, *500* (7462), 323–326.

(20) Law, M.; Luther, J. M.; Song, Q.; Hughes, B. K.; Perkins, C. L.; Nozik, A. J. *J. Am. Chem. Soc.* **2008**, *130* (18), 5974–5985.

(21) Owen, J. S.; Park, J.; Trudeau, P.-.; Alivisatos, A. P. *J. Am. Chem. Soc.* **2008**, *130* (37), 12279–12281.

(22) Kovalenko, M. V.; Scheele, M.; Talapinl, D. V. *Science* **2009**, *324* (5933), 1417–1420.

(23) Zarghami, M. H.; Liu, Y.; Gibbs, M.; Gebremichael, E.; Webster, C.; Law, M. *ACS Nano* **2010**, *4* (4), 2475–2485.

(24) Caldwell, M. A.; Albers, A. E.; Levy, S. C.; Pick, T. E.; Cohen, B. E.; Helms, B. A.; Milliron, D. J. *Chem. Commun.* **2010**, *47* (1), 556–558.

(25) Nag, A.; Kovalenko, M. V.; Lee, J.-S.; Liu, W.; Spokoyny, B.; Talapin, D. V. *J. Am. Chem. Soc.* **2011**, *133* (27), 10612–10620.

(26) Fafarman, A. T.; Koh, W.-.; Diroll, B. T.; Kim, D. K.; Ko, D.-.; Oh, S. J.; Ye, X.; Doan-Nguyen, V.; Crump, M. R.; Reifsnyder, D. C.; Murray, C. B.; Kagan, C. R. *J. Am. Chem. Soc.* **2011**, *133* (39), 15753–15761.

(27) Tang, J.; Kemp, K. W.; Hoogland, S.; Jeong, K. S.; Liu, H.; Levina, L.; Furukawa, M.; Wang, X.; Debnath, R.; Cha, D.; Chou, K. W.; Fischer, A.; Amassian, A.; Asbury, J. B.; Sargent, E. H. *Nat. Mater.* **2011**, *10* (10), 765–771.

(28) Anderson, N. C.; Owen, J. S. *Chem. Mater.* **2013**, *25* (1), 69–76.

(29) Anderson, N. C.; Hendricks, M. P.; Choi, J. J.; Owen, J. S. *J. Am. Chem. Soc.* **2013**, *135* (49), 18536–18548.

(30) Dirin, D. N.; Dreyfuss, S.; Bodnarchuk, M. I.; Nedelcu, G.; Papagiorgis, P.; Itskos, G.; Kovalenko, M. V. *J. Am. Chem. Soc.* **2014**, *136* (18), 6550–6553.

(31) Zhang, H.; Jang, J.; Liu, W.; Talapin, D. V. *ACS Nano* **2014**, *8* (7), 7359–7369.

(32) Zhang, H.; Hu, B.; Sun, L.; Hovden, R.; Wise, F. W.; Muller, D. A.; Robinson, R. D. *Nano Lett.* **2011**, *11* (12), 5356–5361.

(33) Rosen, E. L.; Buonsanti, R.; Llordes, A.; Sawvel, A. M.; Milliron, D. J.; Helms, B. A. *Angew. Chem. Int. Ed.* **2012**, *51* (3), 684–689.

(34) Zanella, M.; Maserati, L.; Pernia Leal, M.; Prato, M.; Lavieville, R.; Povia, M.; Krahne, R.; Manna, L. *Chem. Mater.* **2013**, *25* (8), 1423–1429.

(35) Dong, A.; Ye, X.; Chen, J.; Kang, Y.; Gordon, T.; Kikkawa, J. M.; Murray, C. B. *J. Am. Chem. Soc.* **2011**, *133* (4), 998–1006.

(36) Ji, X.; Copenhaver, D.; Sichmeller, C.; Peng, X. *J. Am. Chem. Soc.* **2008**, *130* (17), 5726–5735.

(37) Moreels, I.; Fritzinger, B.; Martins, J. C.; Hens, Z. *J. Am. Chem. Soc.* **2008**, *130* (45), 15081–15086.

(38) Fritzinger, B.; Capek, R. K.; Lambert, K.; Martins, J. C.; Hens, Z. *J. Am. Chem. Soc.* **2010**, *132* (29), 10195–10201.

(39) Morris-Cohen, A. J.; Vasilenko, V.; Amin, V. A.; Reuter, M. G.; Weiss, E. A. *ACS Nano* **2012**, *6* (1), 557–565.

(40) Peterson, M. D.; Jensen, S. C.; Weinberg, D. J.; Weiss, E. A. *ACS Nano* **2014**, *8* (3), 2826–2837.

(41) De Roo, J.; Van Den Broeck, F.; De Keukeleere, K.; Martins, J. C.; Van Driessche, I.; Hens, Z. *J. Am. Chem. Soc.* **2014**, *136* (27), 9650–9657.

(42) Rosen, E. L.; Sawvel, A. M.; Milliron, D. J.; Helms, B. A. *Chem. Mater.* **2014**, *26* (7), 2214–2217.

(43) Johnson Jr., C. S. *Prog. Nucl. Magn. Reson. Spectrosc.* **1999**, *34* (3–4), 203–256.

(44) Kohlmann, O.; Steinmetz, W. E.; Mao, X.-.; Wuelfing, W. P.; Templeton, A. C.; Murray, R. W.; Johnson Jr., C. S. *J. Phys. Chem. B* **2001**, *105* (37), 8801–8809.

(45) Hens, Z.; Moreels, I.; Martins, J. C. *ChemPhysChem* **2005**, *6* (12), 2578–2584.

(46) Hens, Z.; Martins, J. C. *Chem. Mater.* **2013**, *25* (8), 1211–1221.

(47) Moreels, I.; Lambert, K.; De Muynck, D.; Vanhaecke, F.; Poelman, D.; Martins, J. C.; Allan, G.; Hens, Z. *Chem. Mater.* **2007**, *19* (25), 6101–6106.

(48) Hartman, J. S.; Ilnicki, E. I.; Shoemaker, J. A. W.; Szerminski, W. R.; Yuan, Z. *Can. J. Chem.* **1998**, *76* (9), 1317–1326.

(49) Brownstein, S.; Latremouille, G. *Can.J.Chem.* **1978**, *56*.

(50) Talapin, D. V.; Murray, C. B. *Science* **2005**, *310* (5745), 86–89.
(51) Konstantatos, G.; Howard, I.; Fischer, A.; Hoogland, S.; Clifford, J.; Klem, E.; Levina, L.; Sargent, E. H. *Nature* **2006**, *442* (7099), 180–183.
(52) Hillhouse, H. W.; Beard, M. C. *Curr. Opin. Colloid Interface Sci.* **2009**, *14* (4), 245–259.
(53) Choi, J. J.; Lim, Y.-.; Santiago-Berrios, M. B.; Oh, M.; Hyun, B.-.; Sun, L.; Bartnik, A. C.; Goedhart, A.; Malliaras, G. G.; Abruña, H. D.; Wise, F. W.; Hanrath, T. *Nano Lett.* **2009**, *9* (11), 3749–3755.
(54) Semonin, O. E.; Luther, J. M.; Choi, S.; Chen, H.-.; Gao, J.; Nozik, A. J.; Beard, M. C. *Science* **2011**, *334* (6062), 1530–1533.
(55) Liu, Y.; Tolentino, J.; Gibbs, M.; Ihly, R.; Perkins, C. L.; Liu, Y.; Crawford, N.; Hemminger, J. C.; Law, M. *Nano Lett.* **2013**, *13* (4), 1578–1587.
(56) Sandeep, C. S. S.; Ten Cate, S.; Schins, J. M.; Savenije, T. J.; Liu, Y.; Law, M.; Kinge, S.; Houtepen, A. J.; Siebbeles, L. D. A. *Nat.Commun.* **2013**, *4*.
(57) Ocier, C. R.; Whitham, K.; Hanrath, T.; Robinson, R. D. *J. Phys. Chem. C* **2014**, *118* (7), 3377–3385.
(58) Chuang, C.-. M.; Brown, P. R.; Bulović, V.; Bawendi, M. G. *Nat. Mater.* **2014**, *13* (8), 796–801.
(59) Baumgardner, W. J.; Whitham, K.; Hanrath, T. *Nano Lett.* **2013**, *13* (7), 3225–3231.
(60) Fang, C.; Van Huis, M. A.; Vanmaekelbergh, D.; Zandbergen, H. W. *ACS Nano* **2010**, *4* (1), 211–218.
(61) Thomas, E. L.; Kinning, D. J.; Alward, D. B.; Henkee, C. S. *Macromolecules* **1987**, *20* (11), 2934–2939.
(62) Bishop, K. J. M.; Wilmer, C. E.; Soh, S.; Grzybowski, B. A. *Small* **2009**, *5* (14), 1600–1630.
(63) Hexemer, A.; Bras, W.; Glossinger, J.; Schaible, E.; Gann, E.; Kirian, R.; Macdowell, A.; Church, M.; Rude, B.; Padmore, H. *JPhys ConfSer* **2010**, *247*.
(64) Ilavsky, J. *J. Appl. Crystallogr.* **2012**, *45* (2), 324–328.
(65) Yu, W. W.; Falkner, J. C.; Shih, B. S.; Colvin, V. L. *Chem. Mater.* **2004**, *16* (17), 3318–3322.
(66) Buonsanti, R.; Pick, T. E.; Krins, N.; Richardson, T. J.; Helms, B. A.; Milliron, D. J. *Nano Lett.* **2012**, *12* (7), 3872–3877.
(67) Kriegel, I.; Jiang, C.; Rodríguez-Fernández, J.; Schaller, R. D.; Talapin, D. V.; da Como, E.; Feldmann, J. *J. Am. Chem. Soc.* **2012**, *134* (3), 1583–1590.
(68) Carenco, S.; Boissière, C.; Nicole, L.; Sanchez, C.; Le Floch, P.; Mézailles, N. *Chem. Mater.* **2010**, *22* (4), 1340–1349.
(69) Yu, T.; Moon, J.; Park, J.; Park, Y. I.; Na, H. B.; Kim, B. H.; Song, I. C.; Moon, W. K.; Hyeon, T. *Chem. Mater.* **2009**, *21* (11), 2272–2279.
(70) Koch, U.; Fojtik, A.; Weller, H.; Henglein, A. *Chem. Phys. Lett.* **1985**, *122* (5), 507–510.
(71) Sun, D.; Wong, M.; Sun, L.; Li, Y.; Miyatake, N.; Sue, H.-J. *J. Sol-Gel Sci. Technol.* **2007**, *43* (2), 237–243.
(72) Cozzoli, P. D.; Kornowski, A.; Weller, H. *J. Am. Chem. Soc.* **2003**, *125* (47), 14539–14548.

Chapter 4

Minute-MOFs: Ultrafast Synthesis of High-Quality Expanded M-MOF-74 via Dissolution-Crystallisation from MO Precursors

Adapted from unpublished work in preparation.

Introduction

Metal-organic frameworks (MOFs) are microporous crystalline solids constructed from metal ions or clusters, which are covalently linked by organic ligands[1,2]. The tunability of their composition, architecture and properties has advanced the fields of drug delivery[3,4], catalysis[5–7], sensors[8–10], optoelectronics[11–17] and electrochemistry[18–22]. In particular, the rigid framework maintains pores which are commensurate with the sizes of molecular species, rendering this class of materials uniquely positioned to mediate transport via short-range interactions, prompting their uses in gas separations[23–30] and gas storage[31–33]. During MOF crystallization, molecular precursors chemically transform into active monomers that crystallize into reticular architectures through a nucleation and growth process, in some cases requiring the formation of metal-oxo clusters from several metal ions and an endogenous source of oxygen[34,35]. While the mechanistic underpinnings of these transformations are still under investigation[36,37], kinetic factors involving reaction by-products may ultimately limit the rate of MOF formation from molecular precursors.

Here we report an exceptionally rapid synthesis of high quality M_2(dobpdc) MOFs (dobpdc = 4,4′-dioxido-3,3′-biphenyldicarboxylate)—i.e., the expanded M-MOF-74 series— that substitutes conventional divalent metal salts with divalent metal oxides: MO = MgO, MnO, CoO, NiO, or ZnO. This (pseudo)halide-free route avoids the generation of acidic by-products otherwise inherent to conventional M_2(dobpdc) syntheses; as a result, the reaction time needed decreases significantly[38] — in some cases, by several orders of magnitude (**Figure 4.1**). We investigated in detail the reaction pathway using *ex situ* x-ray diffraction (XRD) and scanning electron microscopy (SEM), which indicated that M_2(dobpdc) formation proceeded via a dissolution-crystallisation mechanism. Through our analysis of MO precursor morphology, surface area, and composition-dependent etch rate, we determined that MO dissolution is rate-limiting. Notably, then, scaling the dimensions of the MO precursor to nanoscopic dimensions allows these MOFs to be prepared in high quality in mere minutes without residual MO. As an ultimate demonstration, we synthesized Zn_2(dobpdc) MOFs from 7 nm ligand-stripped[39] ZnO colloidal nanocrystals (NCs) in less than 1 minute. While metal oxides have been used as precursors for a select group of MOFs, in particular ZnO[40–45], to the best of our knowledge, this is the first synthesis of M_2(dobpdc) using them; moreover, ours is the most rapid M_2(dobpdc) synthesis from any starting material.

Results and discussion

M_2(dobpdc) MOFs and their diamine-modified derivatives have shown exceptional promise as next-generation materials for energy-efficient CO_2 capture[27,46–48]. For diamine-modified M_2(dobpdc) MOFs, CO_2 adsorption involves the insertion of CO_2 into metal-amine bonds, which initiates rapid reorganization of the diamines into ordered chains of ammonium carbamates along the open channels[47,49–51]. The thermodynamics governing CO_2 uptake in these sorbents change dramatically with swings in either pressure or temperature; the sensitivity to those swings depends on the metal and the diamine. As a result, this scheme for CO_2 adsorption/desorption heralds an alternative, low-cost approach to CO_2 scrubbing in power plants[52]. Methods allowing their scalable and expedient production would significantly improve their prospects in this regard, and in the short-term aid in their validation in pilot-scale prototypes.

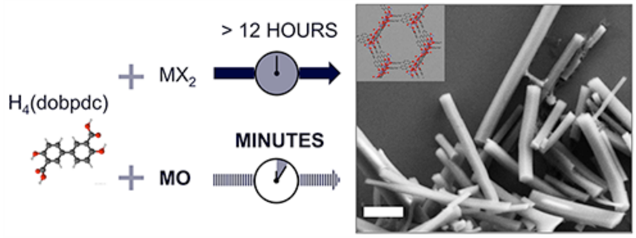

Figure 4.1 Minute-MOFs concept and realization: MOFs, such as M_2(dobpdc), are generated in minutes under controlled reaction conditions from divalent metal oxides as precursors. Conventional syntheses from metal (pseudo)halide salts, on the other hand, require multi-hour reaction times. Scale bar is 0.50 μm.

Currently limiting their expedient production is that reaction times in excess of 12 h are required when preparing M_2(dobpdc) in solution (e.g., *N,N*-diethylformamide) from metal halide or metal pseudohalide salts and H_4(dobpdc) ligand. We hypothesized that the generation of acidic by-products during this sequence of reactions may contribute to slow reaction times for this MOF. Recent studies have concluded as much in the synthesis of porous flexible iron fumarate MIL-88A MOF when acids were present. Organic acids were shown to inhibit crystallisation, while also contributing to a lower yield and a smaller particle size; conversely, increasing the pH had the opposite effect[38]. Were it possible to avoid acidic by-products, e.g., via dissolution of MO solids as precursors, then the integration of H_4(dobpdc) into M_2(dobpdc) MOFs could, in principle, proceed at a faster rate.

Our optimized (pseudo)halide-free M_2(dobpdc) synthesis involves the temperature-assisted dissolution of H_4(dobpdc) in *N,N*-dimethylformamide at 120°C, where $[H_4(\text{dobpdc})]_0 = 0.50$ M, and subsequent addition of the MO solid. The reaction was allowed to proceed until the solid-to-solid transformation was complete (minutes to hours, depending on the MO). Several of the reactions generated highly coloured products, which was most evident after clean-up (**Figure 4.2**).

In navigating the reaction space for this chemical transformation, we noted that the composition and morphology of the MO precursor played central roles in the rate of M_2(dobpdc) formation (**Figure 4.2**). The most rapid transformations were observed using

MgO and ZnO solids as precursors to Mg_2(dobpdc) and Zn_2(dobpdc), respectively, with yields of 28% isolated yield for Mg_2(dobpdc) and 38% isolated yield for Zn_2(dobpdc).

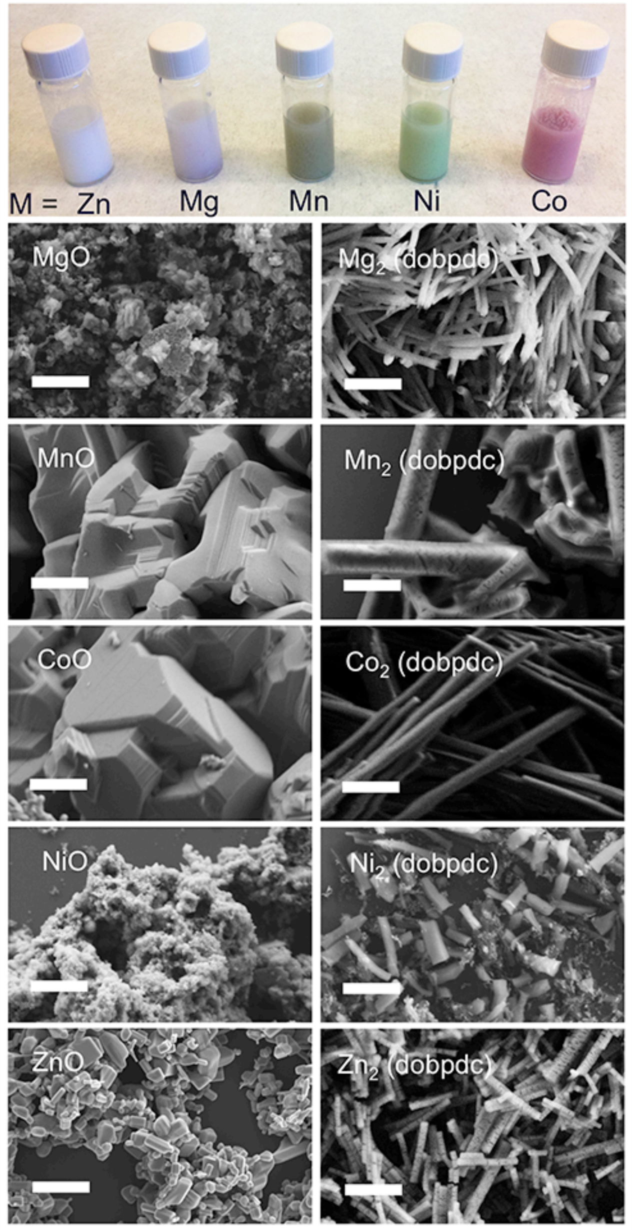

Figure 4.2 Top: Photograph of the M_2(dobpdc) MOFs dispersed in methanol. Bottom: scanning electron micrographs of MO precursors (left column) and their respective reaction products after high-temperature treatment with H_4(dobpdc) in DMF. Scale bars are 2.0 μm.

Crystallinity and porosimetry as quality metrics

Despite their unconventional method of preparation, the M_2(dobpdc) MOFs generated were of outstanding quality as evidenced by their high crystallinity (**Figure 4.3**a-c, **Figure 4.S1**), high surface areas (**Figure 4.3**c-d) and TGA analysis (**Figure 4.S2**).

All XRD spectra were well-matched to their expected and previously reported data. Furthermore, their BET surface areas—2294 ± 33 m^2 g^{-1} for Zn_2(dobpdc) and 2842 ± 28 m^2 g^{-1} for Mg_2(dobpdc)—were in line with previous reports[47,53]; the lack of hysteresis in the adsorption/desorption curves further indicated excellent measurement reliability.

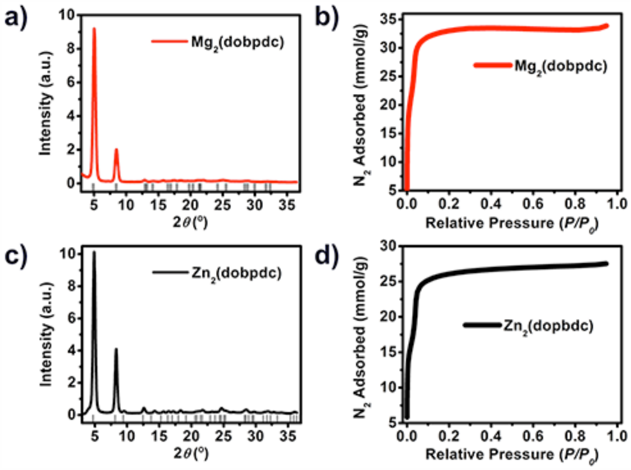

Figure 4.3 (a,b) XRD patterns and (c,d) BET surface area measurements for the Mg_2(dobpdc) (red curves) and Zn_2(dobpdc) (black curves).

Assessment of the reaction trajectory from MO dissolution to M_2(dobpdc) crystallization

In contrast to previously reported metal oxide-to-MOF chemical transformations[42,43], we did not observe significant pseudomorphic replication or self-limited growth of the MOF around the MO starting materials (**Figure 4.2**). To understand this outcome better, we monitored in greater detail the dissolution-crystallisation trajectory of MgO to Mg_2(dobpdc) at different reaction times by sampling aliquots and analysing the intermediates using *ex situ* SEM (**Figure 4.4**). Within the first 30 s of the transformation, we found that clusters of Mg_2(dobpdc) had sprouted from common nucleation points across the MgO surface (**Figure 4.4**a-b). After 2 min, these growths elongated (**Figure 4.4**c) and after 5 min, urchin-like morphologies were prevalent (**Figure 4.4**d). At this stage of the reaction, the XRD pattern matched that for Mg_2(dobpdc) with a small peak at 44° attributed to unreacted MgO (**Figure 4.S3**). After 10 min, the characteristic, highly anisotropic M_2(dobpdc) rod morphology (**Figure 4.4**e) was distinguishable from the faster forming clusters and the MgO signature in the XRD was no longer present (**Figure 4.S3**a). The crystal shape and crystallinity did not change significantly as reaction times were increased further, e.g., after 60 min (**Figure 4.4**f & **Figure 4.S3**b). The presence of MgO while M_2(dobpdc) rods are forming suggests MO etching is the rate-limiting step, signifying M^{2+} availability as a critical factor in optimizing this reaction pathway.

MO etching kinetics

In order to quantify the precursor dissolution rate underpinning the availability of M^{2+} during MOF formation, we introduced MO solids to a solution of salicylic acid (H_2(sal)) in DMF at 120 °C (i.e., our optimized reaction conditions). Salicylic acid here serves as a mono-functional analogue to H_4(dobpdc), which allowed us to track MO dissolution without contributing influence from other chemical species also involved in MOF crystallisation. The time-evolution of MO etching by salicylic acid was observed using *in situ* Fourier transform infrared spectroscopy (FT-IR). Spectra were collected every 15 s over a spectral range of 600 to 2000 cm^{-1} (**Figure 4.S4**). Metal salicylate formation $M[H(sal)]_2$ coincided with the disappearance of the H_2(sal) C–O stretch at 1219 cm^{-1}. This phenomenon was observed in all samples analysed, and was therefore a useful and selective marker for MO dissolution. **Figure 4.5** shows the IR spectral changes over time from 1180 to 1300 cm^{-1} and the decrease in signal intensity at 1219 cm^{-1} during the etching of ZnO, MgO, and CoO.

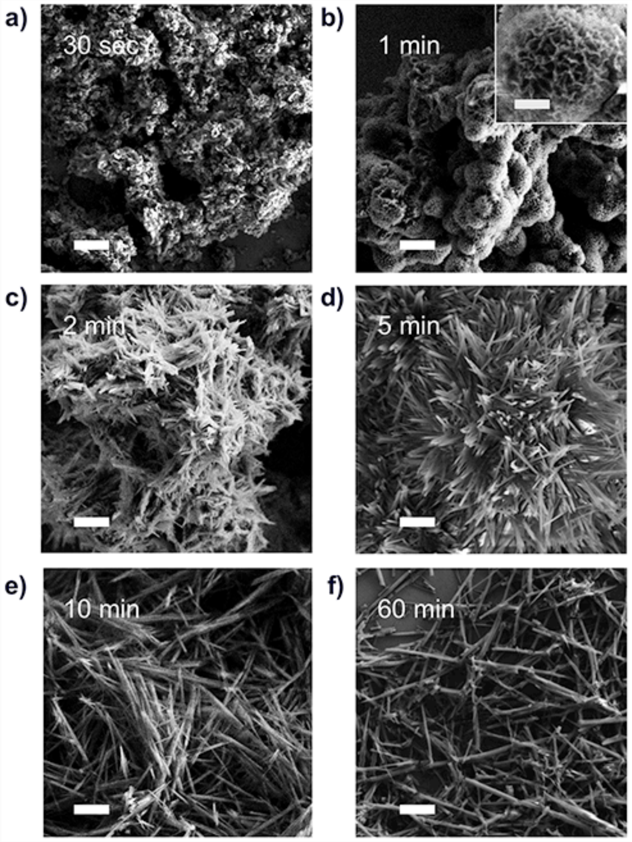

Figure 4.4 SEM along the reaction trajectory of MgO to Mg_2(dobpdc): (a) 30 sec; (b) 1 min; (c) 2 min; (d) 5 min; (e) 10 min; (f) 60 min. Scale bars for all panels are 2.0 µm; the inset scale bar is 500 nm.

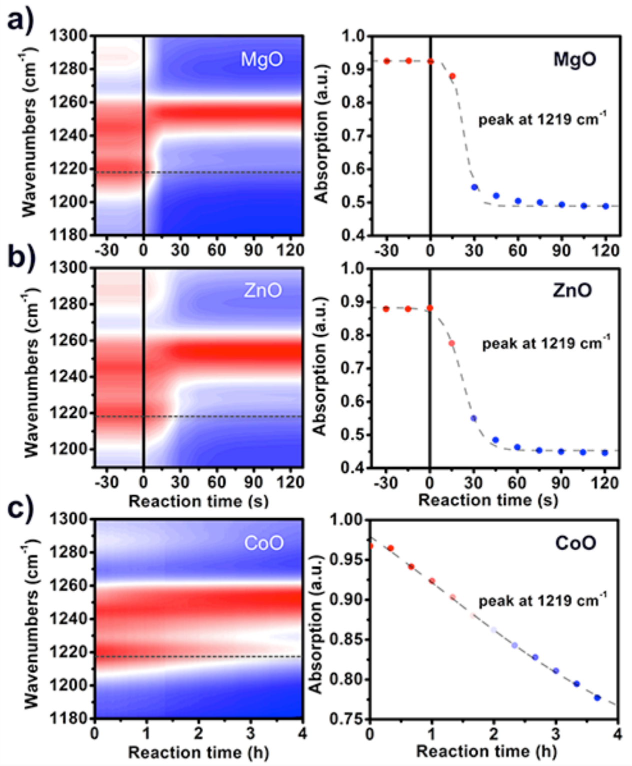

Figure 4.5 *In situ* FTIR spectra was used to quantify the etch rates of divalent metal oxides in the presence of salicylic acid, H_2(sal). Solid MO precursors were added to solution of H_2(sal) in DMF (2.0 M) at 120 °C and the spectra were recorded *in situ* at 15 s intervals. MgO (a) dissolved within 30 s, ZnO (b) in 1 min, while CoO (c) took 8 h to completely dissolve. The right column shows the time-evolution of the interconversion of H_2(sal) to M[H(sal)]$_2$, which could be fit to the Prout-Tompkins equation (dotted lines) to extract MO etch rates under these conditions.

Our investigation of the etching process by *ex situ* SEM had indicated that salicylic acid first etches channels on the surface and within MO (**Figure 4.S5**), rather than proceeding via a gradual dissolution of the solid. This outcome highlights a unique aspect of this chemistry in that the surface area of the MO increases along the reaction trajectory, while the primary dimensions of the particle do not change dramatically at early stages in the reaction. It was at this junction that I contributed to the judicious selection of a kinetics model and to the interpretation of experimental data. Using the disappearing/emerging peaks in the *in situ* FT-IR as a proxy for the extent of reaction, f, one can visually distinguish between two kinetic regimes, with initial acceleratory regime and a deceleratory regime as the conversion nears completion. Combined with the SEM observations, we can conlude that: for short time, etchants removed matter non-uniformly, creating wells and cracks where further branched etching can occur, effectively increasing the active surface area and is autocatalytic in nature; as the metal oxide depletes, the etching slows and eventually stops. The simplest reaction-mechanism-agnostic model is the Prout-Tompkins equation[54] ((**Eq. 4.3**):

$$log\ (f/(1-f)) = k(t-t_0) \qquad \textbf{(Eq. 4.3)}$$

where f is the extent of reaction, k is the etching rate constant and t_0 is the characteristic time of etching. Our treatment of the data in this manner allowed us to extract effective rate constants for MO etching by salicylic acid for MgO, ZnO, and CoO (**Table 4.S1**). The kinetic parameters can be seen to have a weak correlation with the BET surface areas (**Table 4.S2**) of the MO powders used. As etching is a surface reaction, maximizing the surface area of the MO precursor is a viable route to further accelerate the etching rates, and consequently, the conversion process.

The modeled time constants indicated that complete etching of the MO under these reaction conditions varied from tens of seconds for ZnO and MgO to hours for CoO. These data were consistent with the relative rates of M_2(dobpdc) formation (fast for M = Zn and Mg, slower for M = Co), supporting our hypothesis that fast MO etching is critical for optimized M_2(dobpdc) synthesis and that etching is rate-limiting overall.

1 Minute Zn_2(dobpdc)

Based on this insight into the rate-determining step, we were able to further push M_2(dobpdc) synthesis to its fringe kinetic limit by substituting commercially-available ZnO powders (BET surface area 11.3 $m^2\ g^{-1}$) with custom-prepared colloidal ZnO NCs (calculated surface area 118.8 $m^2\ g^{-1}$). To maximize interfacial contact area between ZnO NCs and the transforming solution of H_4(dobpdc) in DMF, we first removed the native coordinating oleate ligands using BF_3-mediated chemistry recently developed in our group[39]. We then added this dispersion of naked ZnO NCs (100 μL, 100 mg mL^{-1}) to H_4(dobpdc) in DMF (0.50 M) at 120 °C. Instantaneously, the transparent reaction mixture became white and cloudy. The reaction product was washed with DMF and methanol prior to analysis by SEM and XRD (**Figure 4.6**). For comparison, a second reaction was carried out from naked ZnO NCs for 1 h.

As was observed in the chemical transformation of commercial MO nanopowders, the morphology of the M_2(dobpdc) evolved in time from urchins (after 1 min) to individual rods (after 1 h) microns in length. Nonetheless, the XRD clearly demonstrated Zn_2(dobpdc) formation without residual ZnO at incredibly short reaction times. We anticipate that for MO materials that are slower to etch (e.g., MnO, CoO, and NiO), it may be possible in the future to accelerate their growth trajectory similarly by configuring them as naked MO nanocrystals[55–60].

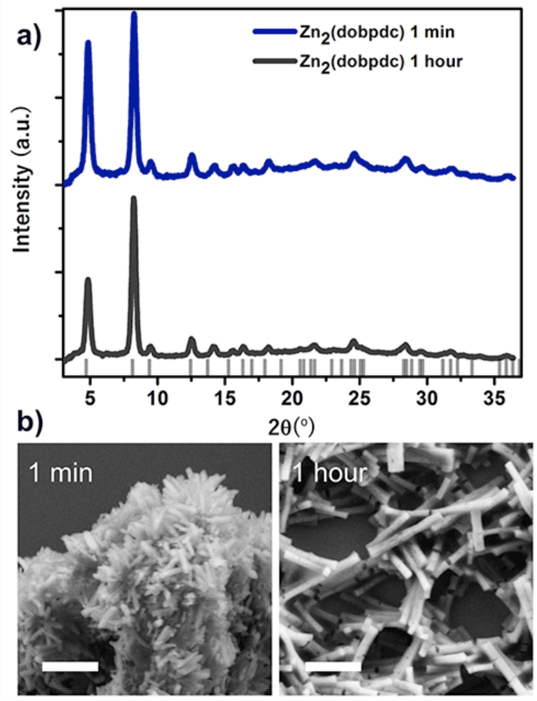

Figure 4.6 (a) XRD patterns for 1 min (blue curve) and 1 h (dark grey curve) Zn_2(dobpdc) derived from ligand-stripped ZnO NCs. (b) SEM images of Zn_2(dobpdc) after 1 min and 1 h of reaction in DMF at 120 °C where 0.50 M H_4(dobpdc) was added. Scale bars are 0.50 µm.

Conclusions

As we continue to translate new MOF discoveries into robust CO_2-capture technologies, the materials requirements to do so demand that we also lay the foundations for expedient and scalable MOF production. Our focus here on the fundamental materials chemistry governing expedient M_2(dobpdc) formation from metal oxide precursors via dissolution-crystallization identified MO etching as rate-limiting. We show that for fast-etching MO materials (e.g., MgO and ZnO), their application as nanopowders is sufficient to reduce reaction times from hours (or days) to minutes. We also demonstrate the fringe kinetic limit of this scheme by employing colloidal MO nanocrystals as M_2(dobpdc) precursors: notably, the interconversion of ZnO to Zn_2(dobpdc) was achieved in less than one minute using 7 nm ligand-free ZnO nanocrystals. Our understanding of the reaction trajectory was informed by both *ex situ* SEM and *in situ* FT-IR, which revealed an unexpected metal oxide-to-MOF mechanism that did not proceed via pseudomorphic replication or incur self-limited growth of MOF onto the MO substrate. While there is still much to be learned from this new reaction scheme at the atomic-and molecular-scales, our understanding at the nano- to macro- continues to highlight the underexplored opportunities in precursor design and reaction engineering—with Minute-MOFs as an important guidepost on that path.

Supporting Information

Materials

Cobalt oxide was purchased from Alfa Aesar, all the other chemicals, reagents, and solvents were purchased from Sigma Aldrich and used as received without further purification. Naked ZnO nanocrystals were synthesized using our previously reported procedure[39].

Methods

Synthesis of 4,4′-Dihydroxy-(1,1′-biphenyl)-3,3′-dicarboxylic Acid (H4(dobpdc)). H_4(dobpdc) was synthesized using a previously reported procedure[46]. Briefly, 4,4′-dihydroxybiphenyl (1.16 g, 6.24 mmol), $KHCO_3$ (2.00 g, 20.0 mmol), solid CO_2 (4.2 g), and 1,2,4-trichlorobenzene (3 mL) were added to a PTFE insert within a 20 mL steel pressure reactor and heated at 255 °C for 17 h. After cooling to room temperature, the mixture was rinsed with diethyl ether and filtered. The collected solid was suspended in 300 mL of distilled water and filtered again. To the filtrate, HCl was added drop-wise until a pH between 1 and 2 was reached. The resulting crude product was re-collected via filtration. The material was recrystallized overnight at 4° C in 50 mL of acetone and 50 mL of water per gram of crude material. ^{1}H NMR (500 MHz, DMSO-d_6): δ = 14.40−13.90 (br, 2H) 11.20−11.30 (br, 2H), 7.97 (d, 2H, J = 2.4 Hz), 7.80 (dd, 2H, J = 8.6 Hz, J = 2.4 Hz), 7.05 (d, 2H, J = 8.6 Hz).

Synthesis of M2(dobpdc) (M = Zn, Mg, Mn, Co, Ni) from commercial MO powders. A 4-mL dram vial was charged with DMF (2 mL) and H_4(dobpdc) (274 mg, 1 mmol). The vial was heated to 120 °C in a thermo-block allowing for the complete dissolution of the ligand, resulting in an initial ligand concentration of $[H_4(\text{dobpdc})]_0$ = 0.50 M. The desired MO powder (2 mmol) was added, and the reaction was kept at 120 °C for a defined reaction time: 10 min for Mg_2(dobpdc), 1 h for Zn_2(dobpdc), 3 h for Co_2(dobpdc), 3 h for Mn_2(dobpdc), and 20 h for Ni_2(dobpdc). After cooling the reaction mixture, an additional portion of DMF was added, and the product isolated after centrifugation of the crude M_2(dobpdc) solids. The solids were further washed with DMF (2x) and then methanol (3x). M_2(dobpdc) solids were activated under dynamic vacuum (<20 μTorr) at 250 °C for 12 h. Porosimetry measurements were carried out immediately after activation, reducing to a minimum the MOF’s exposure to air.

Synthesis of Zn2(dobpdc) from ligand-stripped ZnO NCs. H_4(dobpdc) (27.4 mg, 100 μmol) in DMF (100 μL) was heated to 120 °C before adding naked ZnO NCs as a dispersion in DMF (100 μL, 100 mg mL^{-1}). The reaction was heated at 120 °C for 1 min or 1 h before quenching. Zn_2(dobpdc) MOFs thus produced were washed with DMF and methanol as described above prior to analysis.

Brunauer–Emmett–Teller (BET) surface area measurements. Dry, freshly activated MOF samples were transferred to a pre-weighed glass sample tube under nitrogen atmosphere. In a typical experiment, 40 mg of adsorbent were loaded into a Micromeritics TriStar II, put under vacuum (<10 mTorr) and cooled to 77 K. The adsorption measurement was performed using N_2.

SEM. Images were obtained with a Zeiss Gemini Ultra-55 analytical scanning electron microscope equipped with secondary electron detectors at beam energy of 3 keV. Samples were deposited onto silicon wafers from a dispersion of M_2(dobpdc) in methanol; loaded substrates were dried in air prior to imaging.

XRD. Spectra were recorded in air on a Bruker Gadds-8 diffractometer with Cu-Kα source operating at 40 kV and 20 mA.

Additional Figures

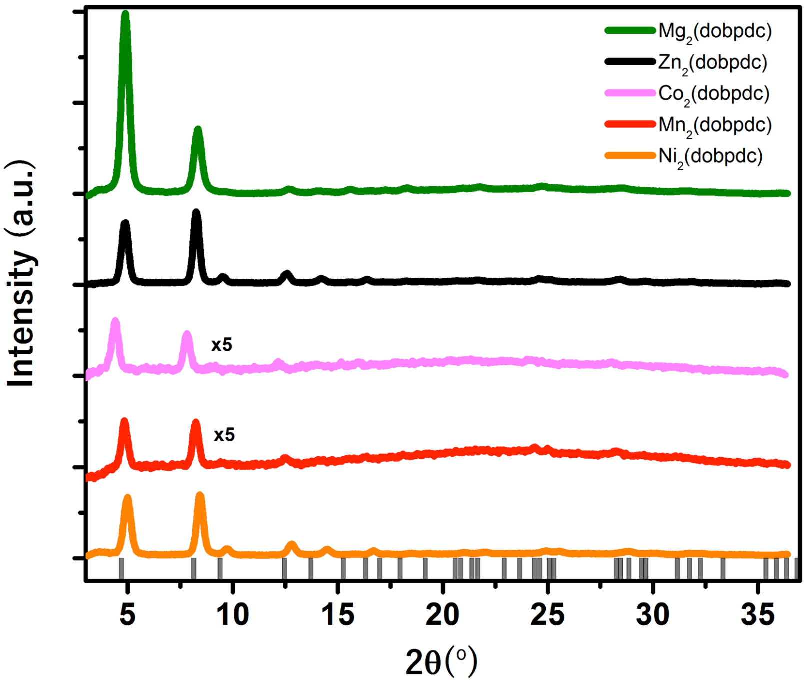

Figure 4.S1 XRD patterns for M$_2$(dobpdc) obtained from MO precursors. Slight shifts in peak positions are due to residual solvent present in the 1D MOF channels.

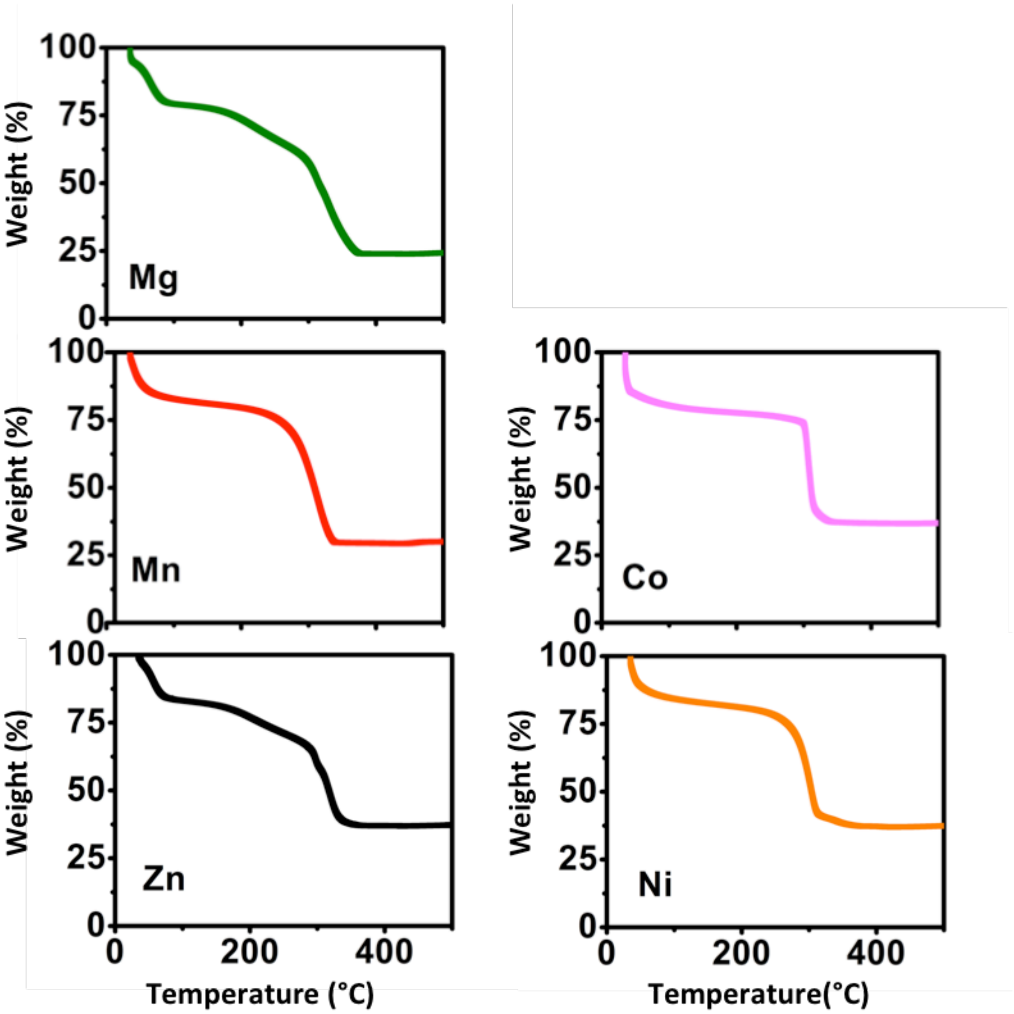

Figure 4.S2 Thermogravimetric analysis of M_2(dobpdc) solids, each indicating MOF decomposition ~300°C, as previously observed[47].

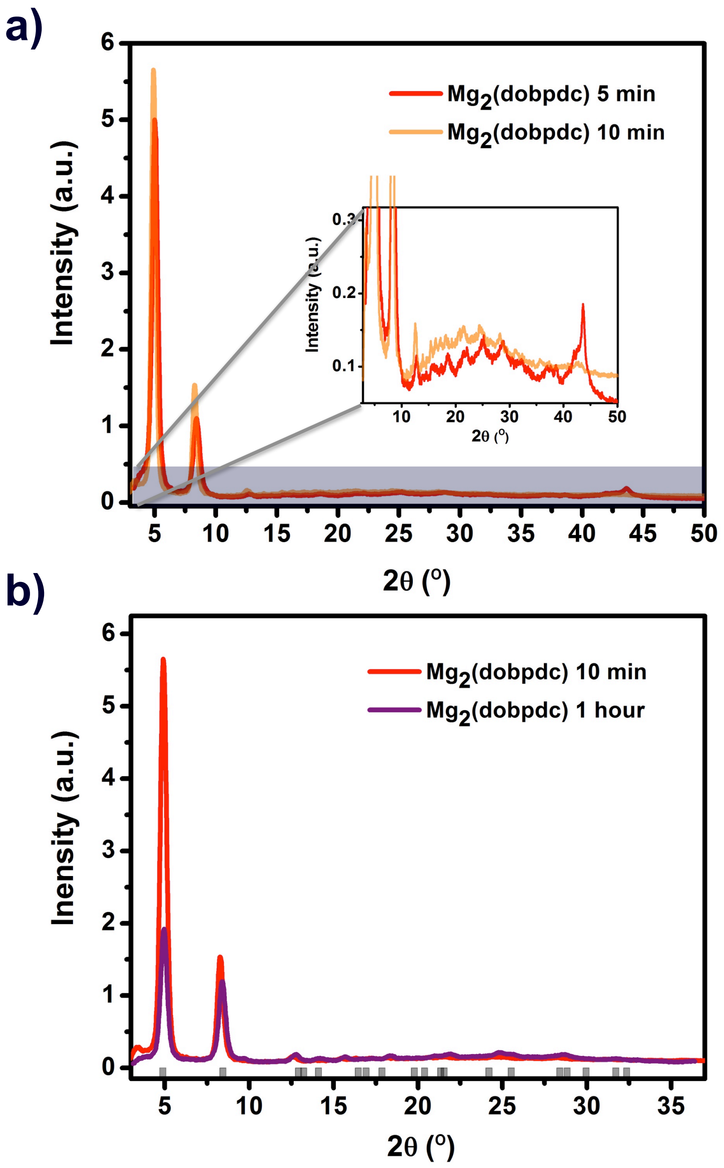

Figure 4.S3 (a) XRD patterns of 5 min (red curve) and 10 min (orange curve) of Mg_2(dobpdc) aliquots during crystallization. The peak at 44° assigned to residual MgO is still present after 5 min of reaction, and subsequently disappears after 10 min. (b) XRD patterns showing no peak position variation after 1 h.

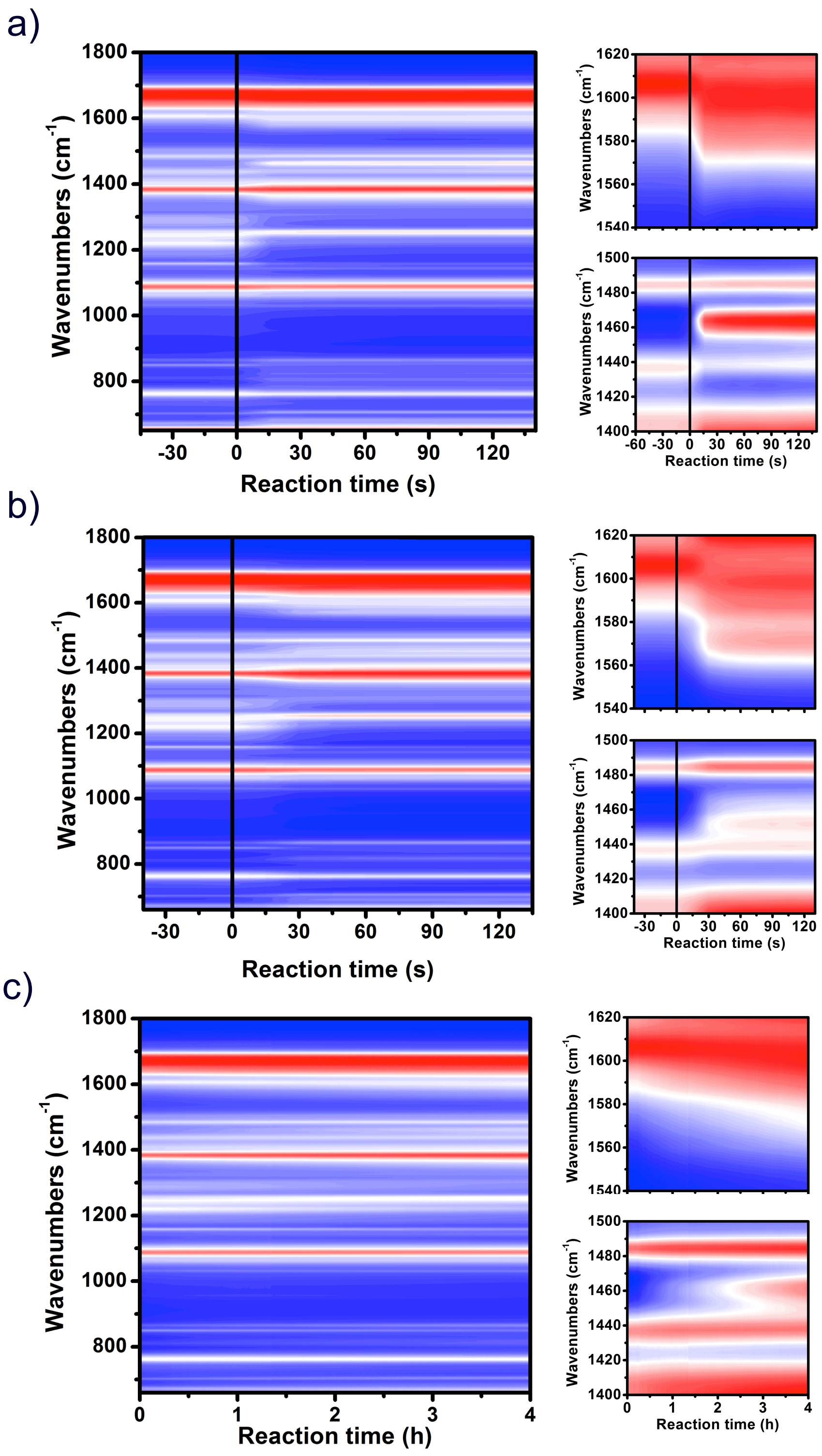

Figure 4.S4 *In situ* FT-IR: (a) MgO dissolution by salicylic acid, yielding magnesium salicylate. (b) ZnO dissolution by salicylic acid, yielding zinc salicylate. (c) CoO dissolution by salicylic acid, yielding cobalt salicylate.

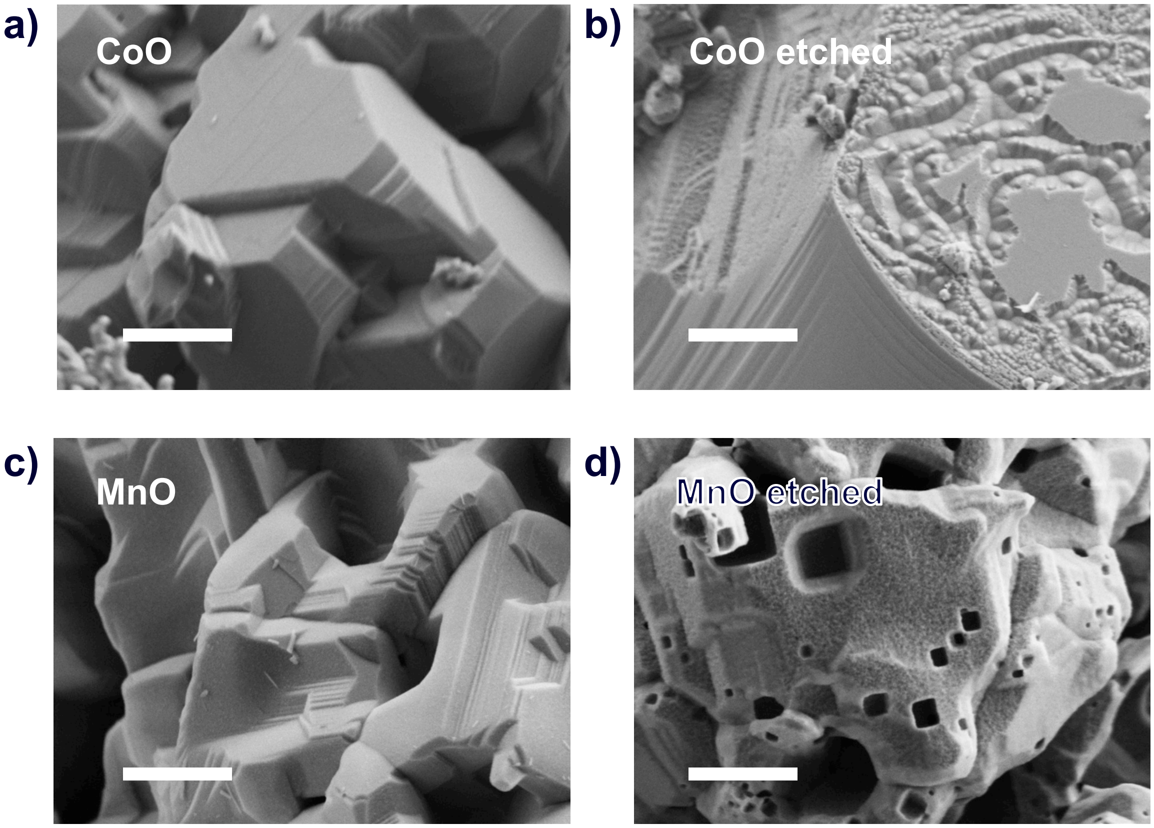

Figure 4.S5 Scanning electron micrographs of two slow-reacting metal-oxide precursors: commercial powders of CoO (a) and MnO (c); and etched MO after 1 h for CoO (b) and MnO (d). Anisotropic etching seems to proceed along crystallographic facets of the metal oxides. Scale bars are 1.0 μm.

Table 4.S1 MO etch rate constants (*k*) and time constants (t_0) extracted from the FT-IR spectra in **Figure 4.5** and **Figure 4.S4** after fitting to the Prout-Tompkins Equation[54].

Fitted Parameter / MO	MgO	ZnO	CoO
k **(s^{-1})**	0.265	0.152	0.000156
t_0 (s)	3.77	6.57	6410

Table 4.S2 BET surface area of MO powder used for *in situ* FTIR etching experiments.

MO	MgO	ZnO	CoO
BET Surface Area	74.15	8.16	Below Detection Limit

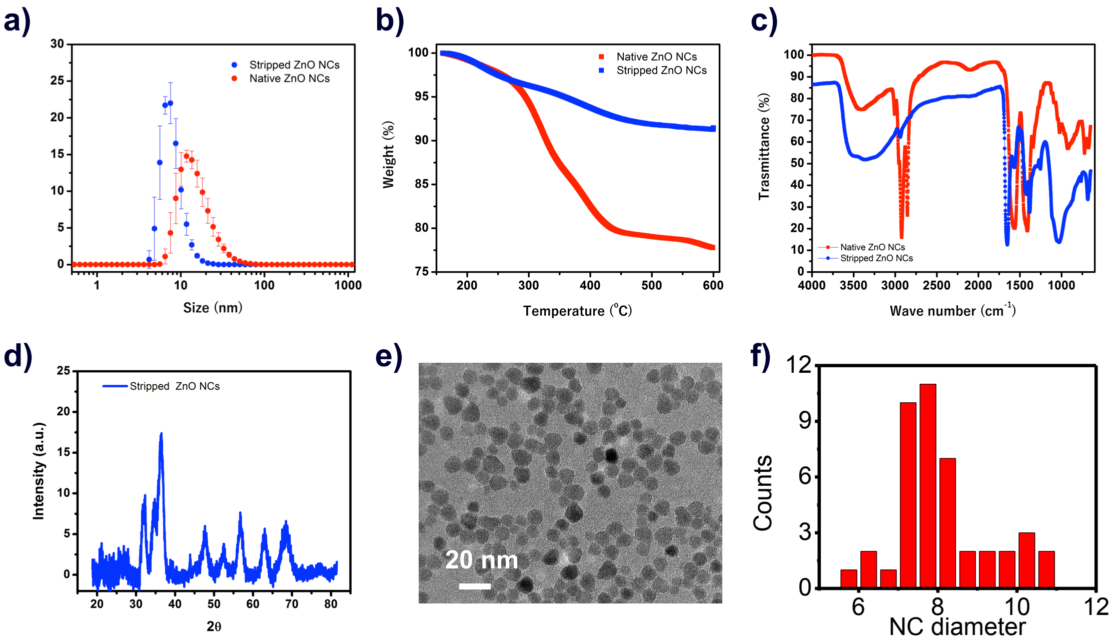

Figure 4.S6 Characterization of ligand-coated (red curves) and ligand-stripped (blue curves) colloidal ZnO nanocrystals by dynamic light scattering (a), thermogravimetric analysis (b), and FT-IR (c). All highlight that the removal of native ligands is commensurate with smaller solvodynamic radius, and vanishingly low degree of contamination by residual organic surfactant. Additional characterization of the naked ZnO nanocrystals by XRD (d) and transmission electron microscopy (e) and associated size distribution.

References

(1) Davis, M. E. *Nature* **2002**, *417* (6891), 813–821.

(2) Yaghi, O. M.; O'Keeffe, M.; Ockwig, N. W.; Chae, H. K.; Eddaoudi, M.; Kim, J. *Nature* **2003**, *423* (6941), 705–714.

(3) Horcajada, P.; Gref, R.; Baati, T.; Allan, P. K.; Maurin, G.; Couvreur, P.; Férey, G.; Morris, R. E.; Serre, C. *Chem. Rev.* **2012**, *112* (2), 1232–1268.

(4) Horcajada, P.; Chalati, T.; Serre, C.; Gillet, B.; Sebrie, C.; Baati, T.; Eubank, J. F.; Heurtaux, D.; Clayette, P.; Kreuz, C.; Chang, J.-S.; Hwang, Y. K.; Marsaud, V.; Bories, P.-N.; Cynober, L.; Gil, S.; Férey, G.; Couvreur, P.; Gref, R. *Nat. Mater.* **2010**, *9* (2), 172–178.

(5) Fujita, M.; Kwon, Y. J.; Washizu, S.; Ogura, K. *J. Am. Chem. Soc.* **1994**, *116* (3), 1151–1152.

(6) Lee, J.; Farha, O. K.; Roberts, J.; Scheidt, K. A.; Nguyen, S. T.; Hupp, J. T. *Chem. Soc. Rev.* **2009**, *38* (5), 1450–1459.

(7) Liu, J.; Chen, L.; Cui, H.; Zhang, J.; Zhang, L.; Su, C.-Y. *Chem. Soc. Rev.* **2014**, *43* (16), 6011–6061.

(8) Kreno, L. E.; Leong, K.; Farha, O. K.; Allendorf, M.; Van Duyne, R. P.; Hupp, J. T. *Chem. Rev.* **2012**, *112* (2), 1105–1125.

(9) Cui, Y.; Yue, Y.; Qian, G.; Chen, B. *Chem. Rev.* **2012**, *112* (2), 1126–1162.

(10) Campbell, M. G.; Sheberla, D.; Liu, S. F.; Swager, T. M.; Dincă, M. *Angew. Chem. Int. Ed.* **2015**, *54* (14), 4349–4352.

(11) Kobayashi, Y.; Jacobs, B.; Allendorf, M. D.; Long, J. R. *Chem. Mater.* **2010**, *22* (14), 4120–4122.

(12) Silva, C. G.; Corma, A.; García, H. *J. Mater. Chem.* **2010**, *20* (16), 3141–3156.

(13) Shekhah, O.; Liu, J.; Fischer, R. A.; Wöll, C. *Chem. Soc. Rev.* **2011**, *40* (2), 1081–1106.

(14) Sheberla, D.; Sun, L.; Blood-Forsythe, M. A.; Er, S.; Wade, C. R.; Brozek, C. K.; Aspuru-Guzik, A.; Dincă, M. *J. Am. Chem. Soc.* **2014**, *136* (25), 8859–8862.

(15) Stavila, V.; Talin, A. A.; Allendorf, M. D. *Chem. Soc. Rev.* **2014**, *43* (16), 5994–6010.

(16) Talin, A. A.; Centrone, A.; Ford, A. C.; Foster, M. E.; Stavila, V.; Haney, P.; Kinney, R. A.; Szalai, V.; Gabaly, F. E.; Yoon, H. P.; Léonard, F.; Allendorf, M. D. *Science* **2014**, *343* (6166), 66–69.

(17) Park, S. S.; Hontz, E. R.; Sun, L.; Hendon, C. H.; Walsh, A.; Van Voorhis, T.; Dincă, M. *J. Am. Chem. Soc.* **2015**, *137* (5), 1774–1777.

(18) Wiers, B. M.; Foo, M.-L.; Balsara, N. P.; Long, J. R. *J. Am. Chem. Soc.* **2011**, *133* (37), 14522–14525.

(19) Morozan, A.; Jaouen, F. *Energy Environ. Sci.* **2012**, *5* (11), 9269–9290.

(20) Horike, S.; Umeyama, D.; Kitagawa, S. *Acc. Chem. Res.* **2013**, *46* (11), 2376–2384.

(21) Zhang, Z.; Yoshikawa, H.; Awaga, K. *J. Am. Chem. Soc.* **2014**, *136* (46), 16112–16115.

(22) Aubrey, M. L.; Ameloot, R.; Wiers, B. M.; Long, J. R. *Energy Environ. Sci.* **2014**, *7* (2), 667–671.

(23) Li, J.-R.; Kuppler, R. J.; Zhou, H.-C. *Chem. Soc. Rev.* **2009**, *38* (5), 1477–1504.

(24) Bae, T.-H.; Lee, J. S.; Qiu, W.; Koros, W. J.; Jones, C. W.; Nair, S. *Angew. Chem. Int. Ed.* **2010**, *49* (51), 9863–9866.

(25) Zhang, C.; Lively, R. P.; Zhang, K.; Johnson, J. R.; Karvan, O.; Koros, W. J. *J. Phys. Chem. Lett.* **2012**, *3* (16), 2130–2134.

(26) Brown, A. J.; Johnson, J. R.; Lydon, M. E.; Koros, W. J.; Jones, C. W.; Nair, S. *Angew. Chem. Int. Ed.* **2012**, *51* (42), 10615–10618.

(27) Sumida, K.; Rogow, D. L.; Mason, J. A.; McDonald, T. M.; Bloch, E. D.; Herm, Z. R.; Bae, T.-H.; Long, J. R. *Chem. Rev.* **2012**, *112* (2), 724–781.

(28) Bloch, E. D.; Queen, W. L.; Krishna, R.; Zadrozny, J. M.; Brown, C. M.; Long, J. R. *Science* **2012**, *335* (6076), 1606–1610.

(29) Zhang, K.; Lively, R. P.; Zhang, C.; Chance, R. R.; Koros, W. J.; Sholl, D. S.; Nair, S. *J. Phys. Chem. Lett.* **2013**, *4* (21), 3618–3622.

(30) Brown, A. J.; Brunelli, N. A.; Eum, K.; Rashidi, F.; Johnson, J. R.; Koros, W. J.; Jones, C. W.; Nair, S. *Science* **2014**, *345* (6192), 72–75.

(31) Eddaoudi, M.; Kim, J.; Rosi, N.; Vodak, D.; Wachter, J.; O'Keeffe, M.; Yaghi, O. M. *Science* **2002**, *295* (5554), 469–472.

(32) Rosi, N. L.; Eckert, J.; Eddaoudi, M.; Vodak, D. T.; Kim, J.; O'Keeffe, M.; Yaghi, O. M. *Science* **2003**, *300* (5622), 1127–1129.

(33) Millward, A. R.; Yaghi, O. M. *J. Am. Chem. Soc.* **2005**, *127* (51), 17998–17999.

(34) Shekhah, O.; Wang, H.; Zacher, D.; Fischer, R. A.; Wöll, C. *Angew. Chem. Int. Ed.* **2009**, *48* (27), 5038–5041.

(35) Goesten, M. G.; Stavitski, E.; Juan-Alcañiz, J.; Martiñez-Joaristi, A.; Petukhov, A. V.; Kapteijn, F.; Gascon, J. *Operando IV 4th Int Congr Operando Spectrosc* **2013**, *205*, 120–127.

(36) Férey, G.; Haouas, M.; Loiseau, T.; Taulelle, F. *Chem. Mater.* **2014**, *26* (1), 299–309.

(37) Patterson, J. P.; Abellan, P.; Denny, M. S.; Park, C.; Browning, N. D.; Cohen, S. M.; Evans, J. E.; Gianneschi, N. C. *J. Am. Chem. Soc.* **2015**, *137* (23), 7322–7328.

(38) Chalati, T.; Horcajada, P.; Gref, R.; Couvreur, P.; Serre, C. *J. Mater. Chem.* **2011**, *21* (7), 2220–2227.

(39) Doris, S. E.; Lynch, J. J.; Li, C.; Wills, A. W.; Urban, J. J.; Helms, B. A. *J. Am. Chem. Soc.* **2014**, *136* (44), 15702–15710.

(40) Friščić, T.; Fábián, L. *CrystEngComm* **2009**, *11* (5), 743–745.

(41) Yue, Y.; Mehio, N.; Binder, A. J.; Dai, S. *CrystEngComm* **2015**, *17* (8), 1728–1735.

(42) Reboul, J.; Furukawa, S.; Horike, N.; Tsotsalas, M.; Hirai, K.; Uehara, H.; Kondo, M.; Louvain, N.; Sakata, O.; Kitagawa, S. *Nat. Mater.* **2012**, *11* (8), 717–723.

(43) Zanchetta, E.; Malfatti, L.; Ricco, R.; Styles, M. J.; Lisi, F.; Coghlan, C. J.; Doonan, C. J.; Hill, A. J.; Brusatin, G.; Falcaro, P. *Chem. Mater.* **2015**, *27* (3), 690–699.

(44) Stassen, I.; Campagnol, N.; Fransaer, J.; Vereecken, P.; Vos, D. D.; Ameloot, R. *CrystEngComm* **2013**, *15* (45), 9308–9311.

(45) Zhan, W.; Kuang, Q.; Zhou, J.; Kong, X.; Xie, Z.; Zheng, L. *J. Am. Chem. Soc.* **2013**, *135* (5), 1926–1933.

(46) McDonald, T. M.; Lee, W. R.; Mason, J. A.; Wiers, B. M.; Hong, C. S.; Long, J. R. *J. Am. Chem. Soc.* **2012**, *134* (16), 7056–7065.

(47) McDonald, T. M.; Mason, J. A.; Kong, X.; Bloch, E. D.; Gygi, D.; Dani, A.; Crocellà, V.; Giordanino, F.; Odoh, S. O.; Drisdell, W. S.; Vlaisavljevich, B.;

Dzubak, A. L.; Poloni, R.; Schnell, S. K.; Planas, N.; Lee, K.; Pascal, T.; Wan, L. F.; Prendergast, D.; Neaton, J. B.; Smit, B.; Kortright, J. B.; Gagliardi, L.; Bordiga, S.; Reimer, J. A.; Long, J. R. *Nature* **2015**, *519* (7543), 303–308.

(48) Lee, W. R.; Jo, H.; Yang, L.-M.; Lee, H.; Ryu, D. W.; Lim, K. S.; Song, J. H.; Min, D. Y.; Han, S. S.; Seo, J. G.; Park, Y. K.; Moon, D.; Hong, C. S. *Chem. Sci.* **2015**, *6* (7), 3697–3705.

(49) Wu, D.; McDonald, T. M.; Quan, Z.; Ushakov, S. V.; Zhang, P.; Long, J. R.; Navrotsky, A. *J. Mater. Chem. A* **2015**, *3* (8), 4248–4254.

(50) Drisdell, W. S.; Poloni, R.; McDonald, T. M.; Pascal, T. A.; Wan, L. F.; Pemmaraju, C. D.; Vlaisavljevich, B.; Odoh, S. O.; Neaton, J. B.; Long, J. R.; Prendergast, D.; Kortright, J. B. *Phys. Chem. Chem. Phys.* **2015**, *17* (33), 21448–21457.

(51) Vlaisavljevich, B.; Odoh, S. O.; Schnell, S. K.; Dzubak, A. L.; Lee, K.; Planas, N.; Neaton, J. B.; Gagliardi, L.; Smit, B. *Chem. Sci.* **2015**, *6* (9), 5177–5185.

(52) Rochelle, G. T. *Science* **2009**, *325* (5948), 1652–1654.

(53) Deng, H.; Grunder, S.; Cordova, K. E.; Valente, C.; Furukawa, H.; Hmadeh, M.; Gándara, F.; Whalley, A. C.; Liu, Z.; Asahina, S.; Kazumori, H.; O'Keeffe, M.; Terasaki, O.; Stoddart, J. F.; Yaghi, O. M. *Science* **2012**, *336* (6084), 1018–1023.

(54) Prout, E. G.; Tompkins, F. C. *Trans. Faraday Soc.* **1944**, *40* (0), 488–498.

(55) Chen, Y.; Johnson, E.; Peng, X. *J. Am. Chem. Soc.* **2007**, *129* (35), 10937–10947.

(56) Schladt, T. D.; Graf, T.; Tremel, W. *Chem. Mater.* **2009**, *21* (14), 3183–3190.

(57) Seo, W. S.; Shim, J. H.; Oh, S. J.; Lee, E. K.; Hur, N. H.; Park, J. T. *J. Am. Chem. Soc.* **2005**, *127* (17), 6188–6189.

(58) Nam, K. M.; Shim, J. H.; Han, D.-W.; Kwon, H. S.; Kang, Y.-M.; Li, Y.; Song, H.; Seo, W. S.; Park, J. T. *Chem. Mater.* **2010**, *22* (15), 4446–4454.

(59) Ning, J.; Xiao, G.; Wang, L.; Zou, B.; Liu, B.; Zou, G. *Nanoscale* **2011**, *3* (2), 741–745.

(60) Fominykh, K.; Feckl, J. M.; Sicklinger, J.; Döblinger, M.; Böcklein, S.; Ziegler, J.; Peter, L.; Rathousky, J.; Scheidt, E.-W.; Bein, T.; Fattakhova-Rohlfing, D. *Adv. Funct. Mater.* **2014**, *24* (21), 3123–3129.

Chapter 5

Sub-Micron Polymer-Zeolitic Imidazolate Framework Layered Hybrids via Controlled Chemical Transformation of Naked ZnO Nano-crystal Films

Adapted with permission from *Chem. Mater*. **2015**, *27* (22), pp 7673–7679. **Copyright 2015 American Chemical Society.**

Introduction

A hybrid material can exhibit functional properties greater than the sum of its parts when its components are chosen and arranged rationally[1,2]. Assembling such a composite requires attention to the chemistry, size, and morphology of each component. Furthermore, the dimensional complexity of the composite also necessitates consideration of component interfaces and their respective length scales. While there are many examples of functional composites with a dispersed phase in a host matrix (e.g., mechanically-reinforced polymer composites[3–5], composite electrodes for electrochemical devices[6,7], and switchable photonic displays[8,9]), those with layered architectures are fewer and are often more difficult to fabricate. This is the case with zeolitic imidazolate framework (ZIF)/polymer composites, where producing layered composites is more time-consuming and less controllable than the formation of mixed-matrix composites[10–14].

Zeolitic imidazolate frameworks (ZIF) are a sub-class of MOFs. Metal centers in ZIFs are tetrahedrally-coordinated to form 145° bonds with imidazoles, which are topographically similar to zeolites' Si-O-Si bonds[13,15]. ZIFs do not have active metal sites available, thus their primary mode of operation in regulating transport of different molecules is through molecular sieving[13], unlike the aforementioned extended MOF-74, or M_2(dobpdc), which can facilitate transport along aligned channels[16]. Having rigid frameworks with only a few degrees of linker rotational freedom, with pore size which are commensurate with the kinetic diameters of industrially-relevant gas molecules[17], ZIFs are uniquely positioned to effect high-throughput gas separation via size discrimination.

Here we show that sub-micron-thick ZIF films can be grown in a controllable manner via a ZnO-to-ZIF dissolution-crystallization scheme carried out on polymers of intrinsic microporosity (PIMs), yielding layered microporous composites for the first time (**Figure 5.1**). ZIFs are robust materials demonstrating great promise in a variety of applications including separations, catalysis, sensing, and electronics[13,18–20]. The ultrathin films reported here are especially promising for asymmetric membranes, where thin selective layers provide high selectivity without sacrificing flux. The morphology of these ZIF films on polymer is strongly influenced by the reaction conditions used to interconvert nanocrystalline ZnO to either ZIF-7 or ZIF-8, highlighting the deterministic role solvent plays on ZnO dissolution as well as ZIF nucleation and growth. The unique layered architecture made possible by these synthetic advances required us to develop and apply synchrotron X-ray techniques to understand the structure and composition of the composite in a quantitative manner. Through the use of these techniques, we were able to directly probe the nanoscale ZIF films rather than relying on the products of analogous bulk reactions.

Our implementation of cationic naked ZnO nanocrystals as precursors to sub-micron-thick ZIF films is unique and overcomes several challenges previously encountered with direct growth methods from solution-phase precursors. In those cases, ZIF films with thicknesses of microns or even tens of microns are more common[10,12,21–25]. Thinner films, which help shorten molecular diffusion paths, generally require multi-step layer-by-layer strategies (e.g., SURMOFs), and while 100 nm ZIF-8 films have been grown solvothermally on glass and silicon, extending this technique to polymers requires substrate modification[26–30]. In the present scheme, we limit the total Zn(II) available for ZIF formation simply by controlling the ZnO nanocrystal film thickness, and as the ZIF growth is directed by the ZnO nanocrystal layer, no functionalization of the polymer is necessary. We also hypothesize that the high surface area inherent to these 0D nanostructures aids in conversion rate and efficacy. In that regard, our results are complementary to previous work reporting ZIF growth on nanoscopic ZnO and $Zn(OH)_2$ materials, which have been transformed into both 1D and 2D ZnO-ZIF hybrids[31–40]. Metal oxides have also been used to grow other classes of porous crystals, including various MOFs via pseudomorphic replication[41,42]. Common to these schemes is the etching of the metal oxide by the ligand (i.e., dissolution) and subsequent nucleation and growth of the framework material (i.e., crystallization).

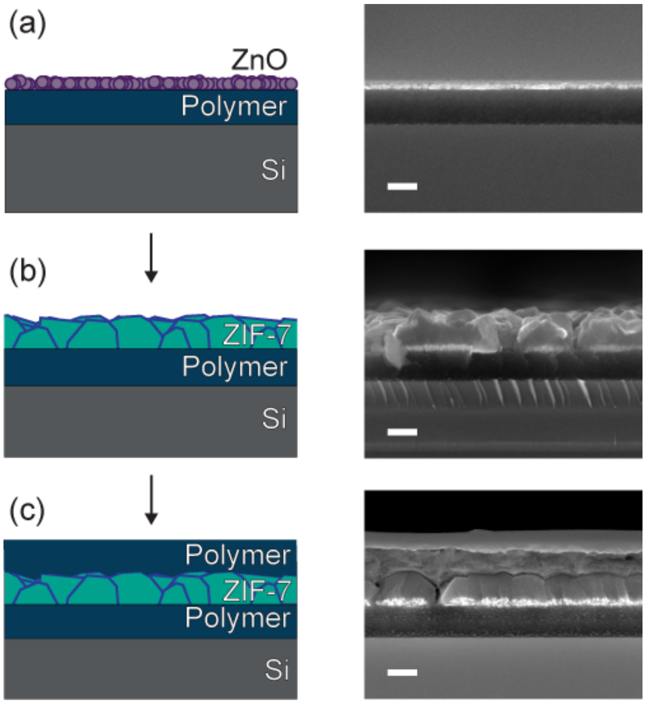

Figure 5.1 Scheme and cross-sectional SEM images depicting (a) ZnO nanocrystals on a polymer film, (b) a ZIF-7 film grown from the sacrificial ZnO nanocrystals, and (c) a PIM/ZIF-7/PIM trilayer structure. Scale bars are 200 nm.

Results and Discussion

We found that the interconversion of cationic naked ZnO nanocrystal films (28 ± 5 nm thick) to either ZIF-7 or ZIF-8 coatings (100–500 nm thick) on cross-linked films of PIM-1 (~200 nm thick) proceeded readily using a low-temperature microwave reaction (**Figure 5.1** a & b). Typically, ZnO nanocrystals were spin-coated on a cross-linked polymer film atop a silicon substrate. The nanocrystal-coated polymer film was submerged face-down in a solution of either benzimidazole or 2-methylimidazole in a water/DMF mixture ($[\text{imidazole ligand}]_0 = 1.11$ M) to induce transformation to ZIF-7 or ZIF-8, respectively. The vessel was subjected to microwave radiation without stirring to maintain an internal solution temperature of 50 °C for 30 min. Substrates were then retrieved and washed by dipping in a solvent bath (DMF for ZIF-7 films; deionized water for ZIF-8 films) to remove excess ligand. A sandwich structure with the ZIF between two layers of polymer was generated by spin-coating another layer of PIM-1 over the ZIF surface (**Figure 5.1**c). Unusual ZIF-8/ZIF-7 multilayers could also be prepared on cross-linked PIM-1 films by our method through the sequential deposition and transformation of ZnO nanocrystal films (**Figure 5.S1**) with 2-methylimidazole and benzimidazole in turn. Notably, in no cases was surface modification of PIM-1 necessary to adhere the ZnO nanocrystals or ZIF films, where in previous work, amine-functionalization of the polymer was needed to promote heterogeneous nucleation and adhesion of the ZIF[30].

Since these were some of the thinnest ZIF composite films ever made, conventional techniques for bulk materials were not suitable. Consequently, this work was as much about synthesis and processing as it was about technique development. In doing so, we have brought many thin film materials techniques into ZIF/MOF analysis, a traditionally inorganic synthesis field, in hopes of enriching the toolkit available. Specifically we relied heavily upon the cross-examination of imaging (scanning electron microscopy) and synchrotron techniques (grazing incidence X-ray diffraction / wide angle X-ray scattering (GIXD/GIWAXS) and X-ray absorption spectroscopy (XAS)). My contribution to this work has been focused on enabling synchrotron techniques, both in experimental execution and data analysis, at both Stanford Synchrotron Radiation Lightsource (beamline 11-3, GIXD/GIWAXS) and the Advanced Light Source (beamline 7.3.3, GIXD/GIWAXS; beamline 10.3.2, XAS).

Cross-sectional and top-down SEM were used to study the resultant film morphology. Contrast differences between residual ZnO nanocrystals and the overlying ZIF made each phase readily distinguishable. Crystalline ZIF-7 or ZIF-8 within the layered hybrid was detected using powder X-ray diffraction (PXRD) and synchrotron grazing incidence X-ray diffraction (GIXD) (**Figure 5.2**). GIXD patterns provided high signal-to-noise crystallographic identification with increased surface sensitivity, mitigating the overwhelming baseline from the amorphous polymer seen in the PXRD data[43]. This allowed us to directly collect diffraction patterns of ZIF on the polymer films^{43}. The 2D GIXD diffraction patterns were isotropic, revealing no preferential ZIF orientation with respect to the plane of the film (**Figure 5.S2**). To provide further insight into the fundamental steps in the present scheme, we explored in greater detail the reaction conditions that influenced ZIF film formation on PIM-coated substrates.

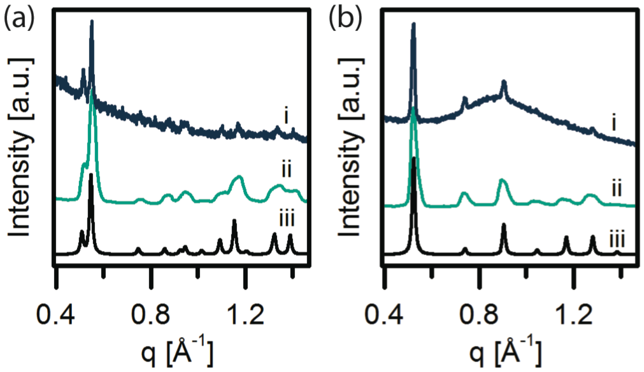

Figure 5.2 Diffraction patterns of (a) ZIF-7 and (b) ZIF-8 thin films on PIM-1 polymer supports, including (i) PXRD, (ii) GIXD, and (iii) simulated diffraction patterns.

Our systematic investigation of the reaction conditions used for the ZnO-to-ZIF-8 film transformation revealed significant control over film thickness and grain size with changes to the reaction solvent: here, mixtures of water and DMF (**Figure 5.3**). If all the ZnO were successfully transformed, a 30 nm nanocrystal layer would produce a ~320 nm thick ZIF-8 film^{44}. Transformations employing reaction mixtures up to 50 vol% DMF yielded smooth, continuous ZIF-8 films as thick as ~150 nm; un-incorporated Zn(II) is presumed to be lost to solution or retained as residual ZnO. The continuous nature of the films under these reaction conditions suggests the formation of many ZIF-8 nuclei and comparatively slow crystal growth. As the water content of the reaction mixture increased beyond 50 vol%, significantly less ZnO was visible in the cross-sectional SEM images and the ZIF-8 grain size also increased. In these cases, the ZIF-8 coatings ceased to be continuous; instead, the growth of faceted, isolated crystals adhered to the polymer surface was observed. In all cases, the equilibrium rhombic dodecahedral ZIF-8 crystal morphology was primarily observed, rather than the kinetically favored cubic morphology^{45}. Reactions in pure DMF were not reproducible, which we attribute to the ease in which naked ZnO nanocrystals re-disperse in this solvent.

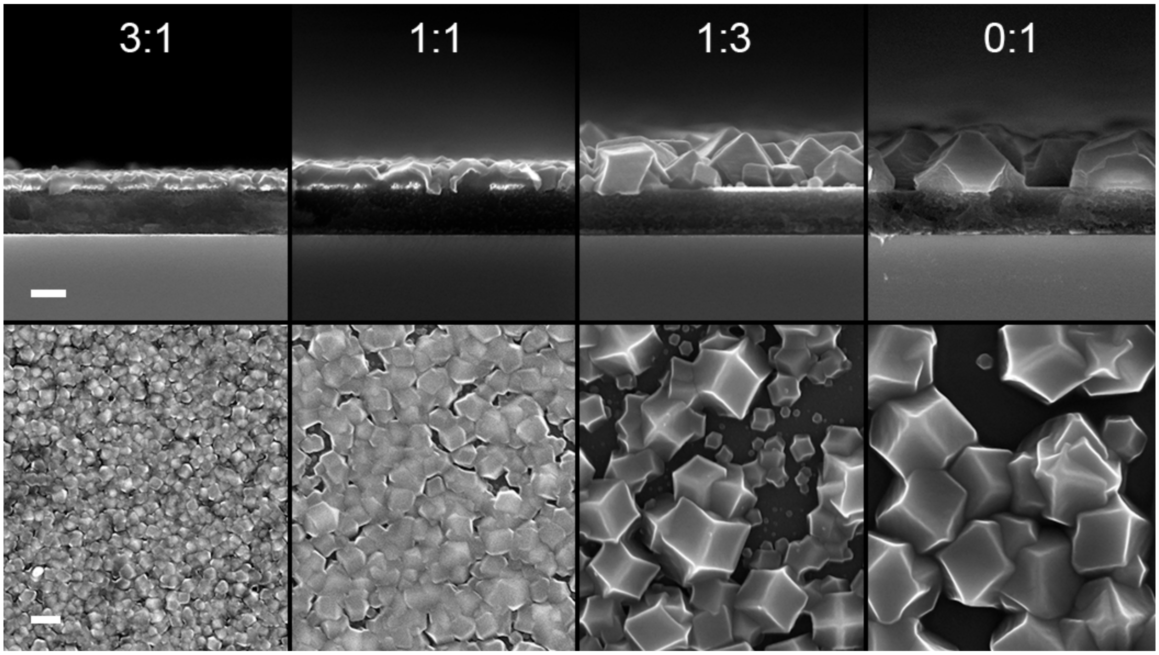

Figure 5.3 SEM images of ZIF-8 films transformed from sacrificial ZnO coatings at various DMF:water (*v/v*) ratios. Both cross-sectional (top row) and top-down (bottom row) views are shown. Scale bars are 200 nm.

In order to quantify the purity of ZIF-8 layers produced in different solvent mixtures (i.e., with respect to any residual ZnO), X-ray absorption near edge structure (XANES) spectra of representative samples produced in four DMF:water mixtures were compared to reference spectra for either ZnO nanocrystals or ZIF-8. XANES total fluorescence yield spectra of the Zn K-edge are well-suited to the analysis of our hybrid films: they are unaffected by the presence of the underlying PIM-1 film; the probe depth is micron-scale; and the absorption cross-sections of Zn atoms in different electronic environments, here ZnO and ZIF-8, are the same (see Experimental for more information). XANES spectra were collected from each sample at multiple spots near the center of the film and averaged together to faithfully represent the sample composition and to reduce beam damage on the ZIF-8 (**Figure 5.4**a). Principle component analysis (PCA) was performed on the dataset. The two principle components best expressing change in the dataset were compared against reference spectra taken of ZnO and ZIF-8 (**Figure 5.4**b). Both exhibit excellent agreement, suggesting the Zn content of the films can be accurately modeled as a mixture of only ZIF-8 and ZnO. Least-squares fits of the reference spectra to each experimental film provided a quantitative fraction of the total Zn present in each crystalline phase (**Figure 5.4**c). The XANES fits reveal that, as the volume fraction of water in the reaction medium increases, the films tend toward pure ZIF-8, which is in good agreement with the phenomenological interpretation of the SEM cross-sections. Phase-pure ZIF is not measured at the polymer surface in any sample.

While several metal oxide-to-MOF chemical transformations have been reported in the literature, the mechanism of this interconversion is still under investigation. Different metal oxide/ligand pairs and the conditions in which they are carried out may change the mechanism of MOF formation[33,41]. Clearly, the metal oxide-to-MOF coating conversion depends on the competing rates of several processes: (1) metal-oxide dissolution, (2) metal-ion diffusion away from the polymer surface, (3) MOF nucleation, (4) MOF growth, and (5) Ostwald ripening (**Figure 5.S3**). The relative rates of these processes dictate the overall kinetics of the reaction and the resultant morphology and composition of the product.

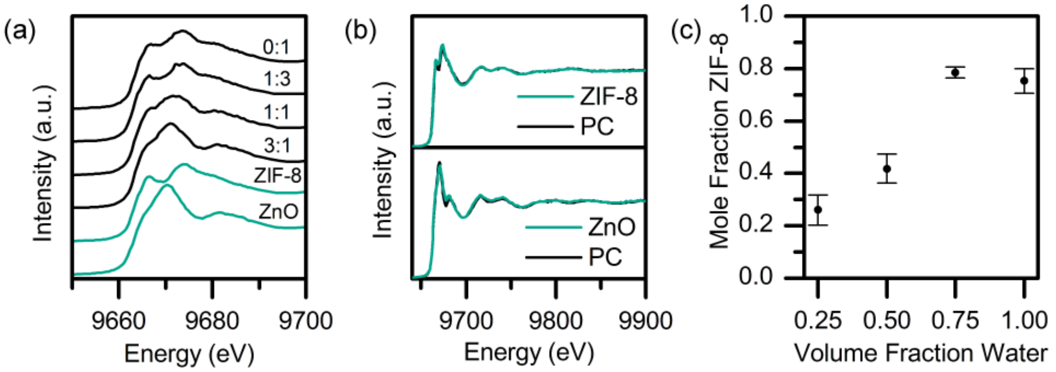

Figure 5.4 Quantitative XANES characterization of ZIF-8 films transformed from ZnO coatings at various DMF:water (*v/v*) ratios. (a) Spectra of bulk ZnO and ZIF-8 (green) and of ZIF-8 films (black). (b) The first two principle components (PC) of the experimental data set (black) match experimentally collected bulk ZIF-8 and ZnO spectra (green). (c) Mole fraction of Zn in ZIF-8 in films transformed using different solvent mixtures. Error bars show the standard error between samples identically prepared (n = 3 or 4).

In the scheme presented here, water and DMF each affect these competing rates. The transforming solutions show an increase in pH with increasing water content, from pH 9 at 25 vol% water to pH 11 at 100 vol% water. Increasing the vol% of water results in faster etching of the amphoteric ZnO, increased proton mobility overall, and more facile deprotonation of the ZIF crystal surfaces, which in turn promotes crystal growth over nucleation of new crystallites[46]. DMF, aside from regulating etching by modulating pH, may also be responsible for inhibiting ZIF growth as has been reported in some solvothermal ZIF-8 syntheses[47]. Finally, we considered whether differences in microwave adsorption might affect the energy available to the system. However, since water and DMF have similar loss tangent values, both solvents can be expected to behave similarly under microwave radiation[48].

Since phase-pure ZIF at the polymer surface was not measured in any of the XANES experiments, we reasoned that residual metal oxide may be necessary for a local ZIF nucleation event, consistent with a heterogeneous nucleation mechanism. ZnO has been reported previously as an effective templating agent for the solvothermal growth of ZIF films[11,39,49]. If ZnO is needed for heterogeneous nucleation here, the voids between crystals due to rapid nanocrystal dissolution are concomitant with fewer nucleation sites in those regions on PIM-1. This is consistent with our observation that voids account for greater fractions of the surface area in films formed under high water content solutions, where ZnO dissolution is more rapid.

Finally, studying the time-evolution of ZIF-8 film growth in a 75 vol% water solution provided further insight into the contributing and competing influences of ZIF-8 nucleation, growth, and Ostwald ripening (**Figure 5.S4**). Large crystals, seen in films grown from 75 vol% or pure water solutions, form when nucleation is slow relative to crystal growth. Nucleation occurs as long as ZnO is exposed to the solution, and crystal growth stops when all accessible Zn(II) is depleted, explaining the increased ZIF-8 polydispersity observed in reactions with a high water content. After microwave irradiation for 10 min, few nucleation sites have formed and the surface is primarily ZnO. By 30 min, the surface ZnO has been depleted or covered in ZIF-8. The crystal size is static over longer reaction times, demonstrating that Ostwald ripening is likely not a significant factor in film formation and that the 30 min reaction time is sufficient to obtain the final film morphology.

Conclusion

Sub-micron ZIF-7 and ZIF-8 coatings and bilayers on microporous polymer substrates were obtained through the chemical conversion of naked ZnO nanocrystal precursor films. The high surface area of the nanocrystal films facilitated a rapid conversion under mild conditions to ZIF coatings with morphologies that were controlled by choice of solvent. Crystal structures were confirmed by GIXD, and the morphological and chemical composition of the ZIF-8 films formed under varying reaction conditions were measured using SEM and XANES spectroscopy, respectively. Sub-micron-thick ZIF films encased on both sides by polymer and ZIF-8/ZIF-7 multilayers were accessible, demonstrating an attractive and versatile new methodology to fabricate layered composite architectures. These composite architectures may be well suited to applications in selective separations and sensing. In that the deposition of metal oxide nanocrystals within or on other materials is foreseeable, our techniques may also be applicable to ZIF-polymer composites in a variety of porous polymer formats, including hollow polymer fibers, polymer monoliths, polymer membranes, and polymer beads. Our unique access to ZIF-on-ZIF multilayers likewise suggests new avenues for selective species transport.

Experimental

Grazing Incidence X-ray Diffraction: GIXD was performed at two beamlines. Data were collected at the Stanford Synchrotron Radiation Laboratory (SSRL) beamline 11-3 with a photon energy of 12.7 keV. A MAR345 2D detector was used at a sample-detector distance of 175 mm. Integration of the diffraction peak areas was performed with the software WxDiff[50]. Additional data were collected at beamline 7.3.3 of the Advanced Light Source, Lawrence Berkeley National Laboratory, using a photon energy of 10 keV, a sample-detector distance of 280 mm, and a Pilatus 2M detector[51]. These diffraction peak areas were integrated with the software package Nika for Igor Pro[52]. The incident angle at both beamlines was fixed at 0.12° and all experiments were conducted in a He atmosphere.

X-ray Absorption Near Edge Structure Spectroscopy: XANES Zn K-edge spectra were collected at the Advanced Light Source (ALS) beamline 10.3.2[53]. The incident angle was ~15° and the spot size ~40 x 3 µm. Scans were taken at between 4 and 20 spots on each sample, until adequate signal to noise was achieved, from 9.56 to 10.00 keV using a solid state Ge detector Canberra 7-element UltraLEGe or Amp-Tek silicon drift diode detector and averaged together. Spectra of bulk ZnO and ZIF-8 nanocrystals were used in least squares linear fits of each sample. Monochromator drift was accounted for by making E0 a parameter of the fit. The absorption length was estimated using the Hephaestus software package and was found to be 88.7 µm for ZIF-8, assuming a density of 1.45 g cm^{-1}, and 8.7 µm for ZnO, assuming a density of 5.61 g cm^{-1} [54,55]. At an incident angle of 15°, the path length of the beam through the sample was well below this limit, and over-absorption was considered negligible. All other data processing was completed using software provided at the beamline.

Supporting Information

Materials

Zinc acetate dihydrate ($Zn(OAc)_2 \cdot 2H_2O$, 99.999% or ≥99%), oleic acid (90%), tetrafluoroterephthalonitrile (99%), 5,5’,6,6’-tetrahydroxy-3,3,3’,3’-tetramethyl-1,1’-spirobisindane (96%), 2-methylimidazole (2-HMIm, 99%), benzimidazole (BIM, 98%), were purchased from Sigma Aldrich. Oleylamine (80–90%), boron trifluoride-etherate (BF_3-etherate, *ca.* 48% BF_3), and chloroform-*d* ($CDCl_3$, >99.6%) were purchased from Acros Organics. Potassium hydroxide (KOH) was purchased from BDH Chemicals, 2,6-Bis(4-azidobenzylidene)cyclohexanone (wetted with 30% water by weight, >90%) from TCI chemicals, and potassium carbonate (K_2CO_3, >99.9%) from Fischer Scientific. Benzimidazole solutions were passed through a 0.45 μm filter to remove any insoluble contaminants; all other chemicals were used as received. All solvents were HPLC grade and used as received. A Biotage Initiator microwave was used for the chemical transformations. 4 mL of the relevant reaction solution was used for each transformation. SEM images were obtained with a Zeiss Gemini Ultra-55 analytical scanning electron microscope equipped with an in-lens detector at an accelerating voltage of 5 kV. Prior to imaging, samples were coated with a few nanometers of amorphous carbon using an Electron Microscopy Sciences 150T ES high vacuum carbon evaporator. Images were adjusted for brightness and contrast using the levels tool in Adobe Photoshop. EDX measurements were obtained on the same microscope using the equipped EDAX detector. XRD patterns for the ZIF films were recorded using a Bruker D8 Advance diffractometer with Göbel-mirror monochromated Cu-Kα source operating at 40 kV and 40 mA, and those for the ZnO and bulk ZIF-8 nanocrystals were recorded on a Bruker Gadds-8 diffractometer with Cu-Kα source operating at 40 kV and 20 mA. Diffraction patterns were simulated using the Mercury 3.5.1 software package[56]. TEM images of the nanocrystal precursors were taken on a Ziess Libra 120 TEM at 200 kV and 100 k magnification. TGA measurements were taken using a TA Instruments Q5000 IR Thermogravimetric Analyzer. Samples were held at 160 ˚C for 60 min to drive off solvent then ramped at 20 ˚C/min to 500 ˚C. Syntheses of the ZnO nanocrystals[57,58], PIM-1[59,60], and ZIF-8[61] used as the standard for the XANES experiment were followed from literature procedures.

Naked Zinc Oxide (ZnO) Nanocrystal Stripping: Ligand stripping was adapted from Doris *et al*[57]. DMF (500 μL) charged with BF_3-etherate (10 μL) was mixed with the ZnO nanocrystal dispersion in hexanes (100 μL, ~60 mg/mL) under nitrogen. Toluene (3.5 mL) was added to crash out the nanocrystals. The crystals were isolated by centrifugation and washed in 1:1:7 DMF:hexanes:toluene (*v/v/v*) twice and dispersed in

DMF. The stripped ZnO nanocrystals were characterized by PXRD, EDX, TGA, and TEM, and they had an average particle size of 7±1 nm.

Polymer Support Fabrication: The polymer cross-linking chemistry was adapted from Du *et al*[62]. Typically, PIM-1 (M_n = 19.3 g mol^{-1}, M_w = 52.1 g mol^{-1}, M_w / M_n = 2.70, 70 mg) was dissolved in chlorobenzene (1700 μL) and chloroform (300 μL) before adding 2,6-bis(4-azidobenzylidene)cyclohexanone (17 mg). This mixture (200 μL) was passed through a 0.2 μm PTFE filter onto a 1.8 x 1.8 cm single crystal silicon wafer and spin coated. The resulting films were annealed under vacuum at 175° C for 7 h. The cross-linked films were insoluble in solutions of heated DMF.

Additional Figures

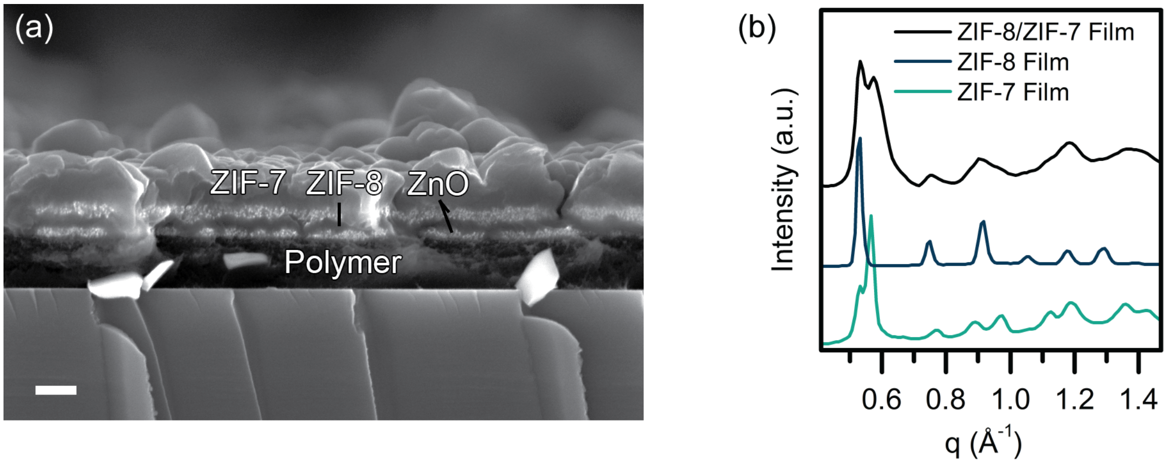

Figure 5.S1 (a) Cross-sectional scanning electron micrograph and (b) GIXD of a layered composite comprised of PIM-1, ZIF-8, ZIF-7, and ZnO. ZIF-7 layer was grown from ZnO NCs deposited on a ZIF-8 coating. Scale bar is 200 nm. GIXD traces were baseline-corrected and normalized.

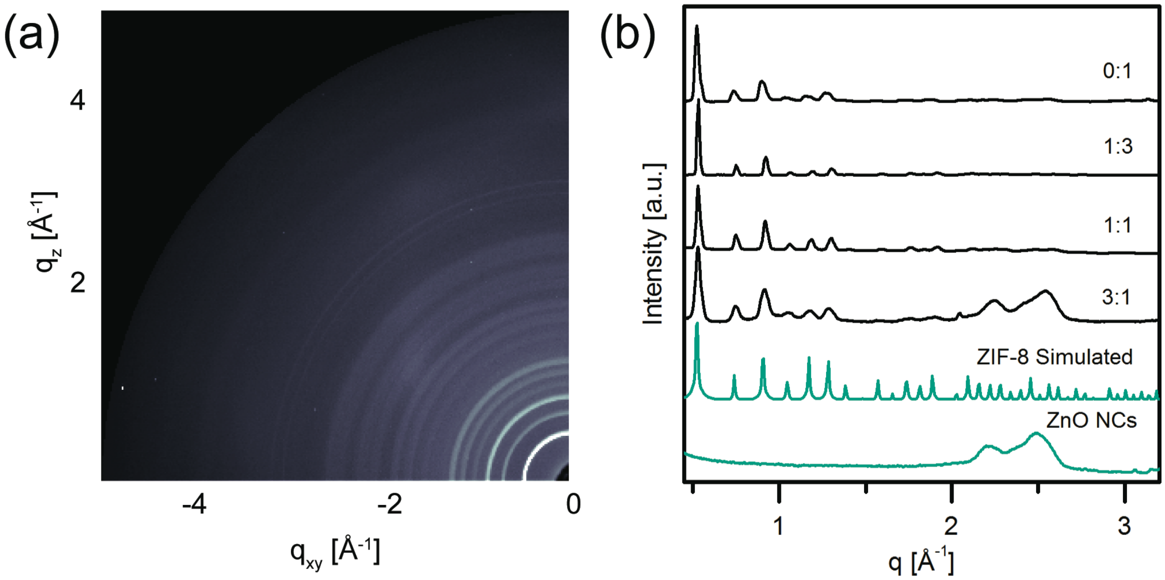

Figure 5.S2 Synchrotron X-ray diffraction data from ZIF-8/ZnO coatings. a) The 2D GIWAXS pattern is fully isotropic, revealing no preferential crystal orientation with respect to the plane of the support. b) 1D GIXD data, calculated by integrating a wedge of a 2D GIWAXS pattern, for ZIF-8 films fabricated in each of the four DMF:water (*v/v*) ratios studied by XAS. Traces were baseline-corrected and normalized.

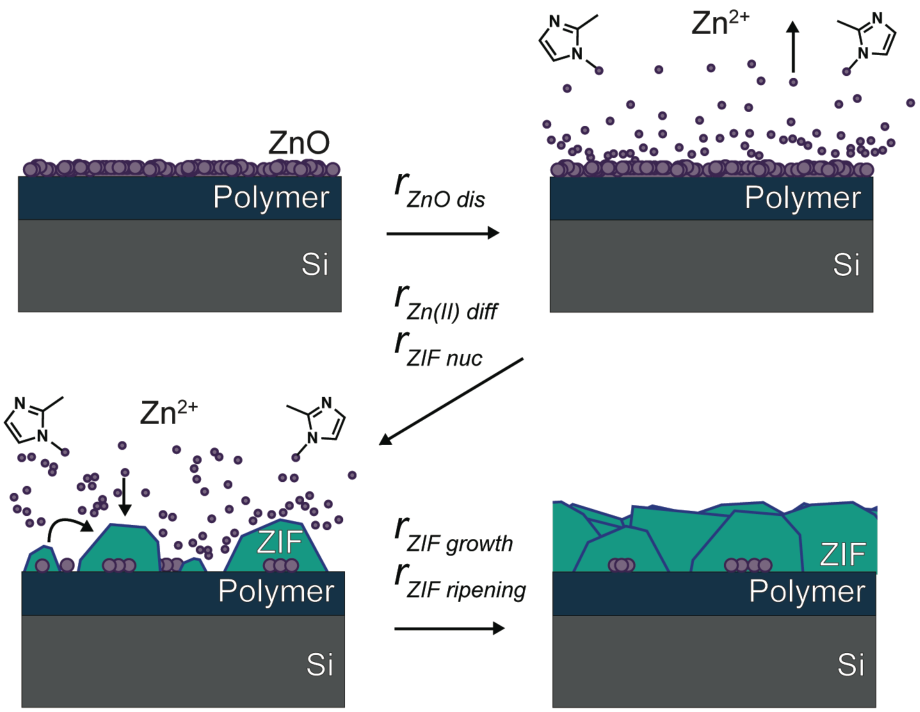

Figure 5.S3 Scheme detailing the competitive processes informing the morphology and composition of ZIF films accessed via ZnO nanocrystal precursors. The competing rates are (1) metal-oxide dissolution, (2) metal-ion diffusion away from the polymer surface, (3) ZIF nucleation, (4) ZIF growth, and (5) Ostwald ripening.

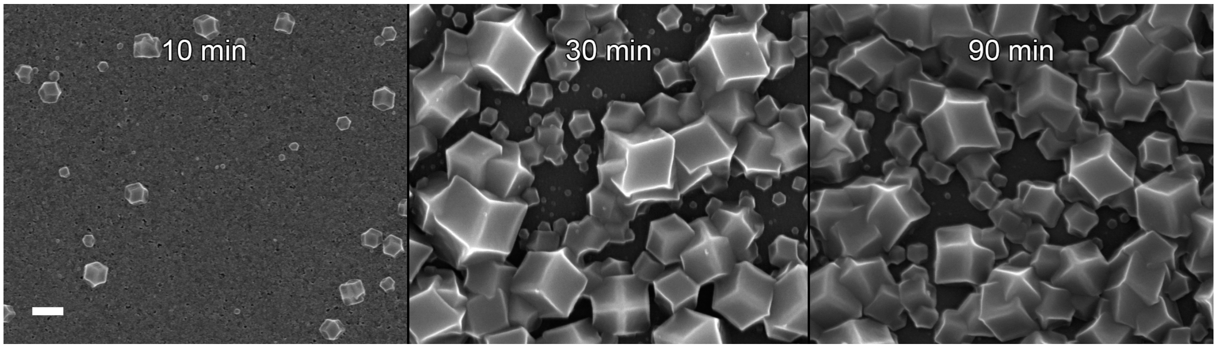

Figure 5.S4 Top-down SEM images showing the time-evolution of ZIF-8 films grown from ZnO NCs in 75 vol% water solutions. The slow appearance of ZIF-8 nuclei followed by rapid crystal growth is observed, suggesting ZIF-8 polydispersity is a result of different growth times before the Zn(II) source is consumed. The lack of morphological evolution after 30 min suggests Ostwald ripening is slow. Scale bar is 200 nm.

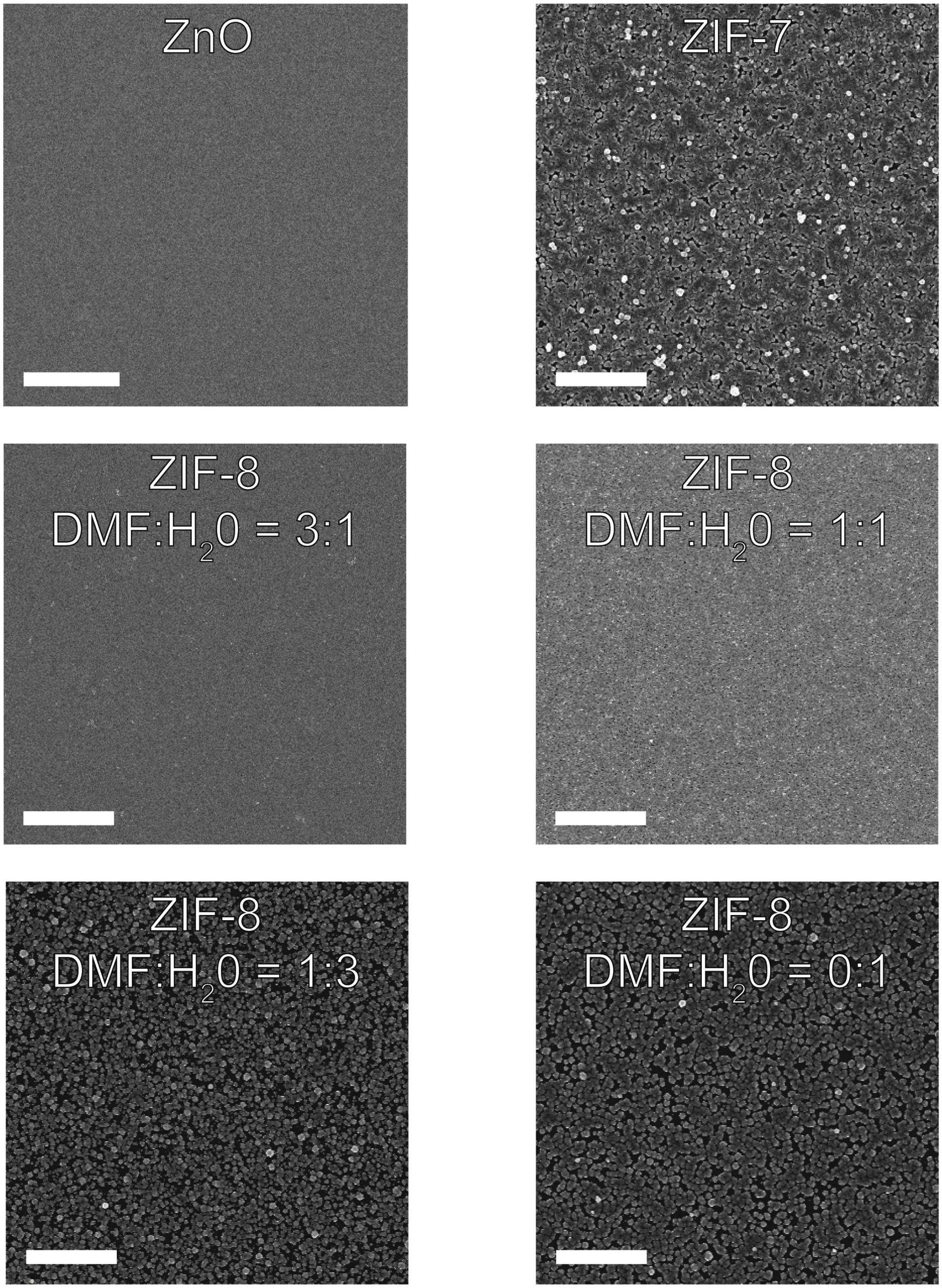

Figure 5.S5 Top-down SEM images of ZnO and ZIF coatings demonstrating large-scale uniformity. Top row: ZnO precursor film and ZIF-7 film. Middle and bottom rows: ZIF-8 films fabricated in each of the four DMF:water (*v/v*) ratios studied by XAS. All scale bars are 10 μm.

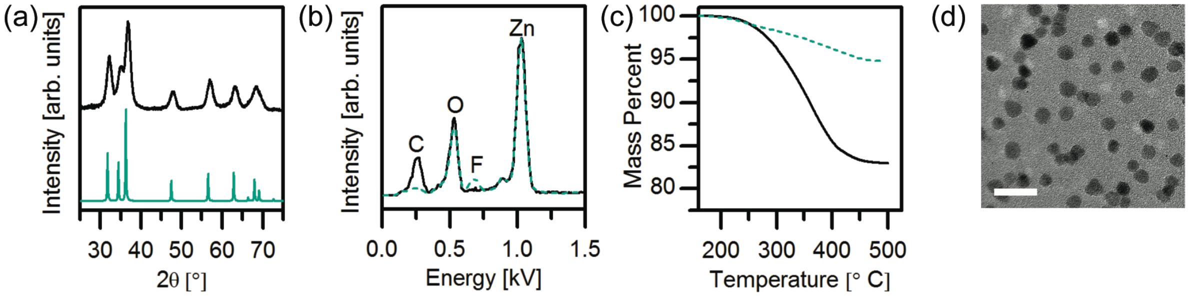

Figure 5.S6 Characterization of ZnO nanocrystals. (a) Baseline subtracted PXRD pattern for naked nanocrystals (top, black) and the simulated powder pattern (green, bottom). (b) EDX spectra of as-synthesized nanocrystals (black, solid) and naked nanocrystals (green, dashed) shows the loss of a carbon signal from the organic ligands and the appearance of a fluorine peak from the BF4– counter ion after ligand stripping. Normalized to the Zn peak for clarity. (c) TGA mass-loss normalized to the weight at 160 °C is lower for naked nanocrystals (green, dashed) than for the as-synthesized nanocrystals (black, solid), demonstrating the effective removal of organics during ligand-stripping. (d) TEM images of naked ZnO nanocrystals. Particles are monodisperse and 7±1 nm in diameter. Scale bar is 20 nm.

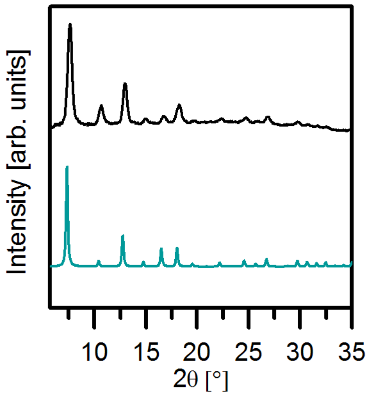

Figure 5.S7 PXRD of the bulk ZIF-8 used as the standard for the XANES experiment (top, black) and the simulated pattern (bottom, green).

References

(1) Sanchez, C.; Julián, B.; Belleville, P.; Popall, M. *J. Mater. Chem.* **2005**, *15* (35-36), 3559–3592.

(2) Thompson, R. B.; Ginzburg, V. V.; Matsen, M. W.; Balazs, A. C. *Science* **2001**, *292* (5526), 2469–2472.

(3) Coleman, J. N.; Khan, U.; Blau, W. J.; Gun'ko, Y. K. *Carbon* **2006**, *44* (9), 1624–1652.

(4) Bauer, J.; Hengsbach, S.; Tesari, I.; Schwaiger, R.; Kraft, O. *Proc. Natl. Acad. Sci. U. S. A.* **2014**, *111* (7), 2453–2458.

(5) Liff, S. M.; Kumar, N.; McKinley, G. H. *Nat. Mater.* **2007**, *6* (1), 76–83.

(6) Aricò, A. S.; Bruce, P.; Scrosati, B.; Tarascon, J.-.; Van Schalkwijk, W. *Nat. Mater.* **2005**, *4* (5), 366–377.

(7) Kim, J.; Ong, G. K.; Wang, Y.; LeBlanc, G.; Williams, T. E.; Mattox, T. M.; Helms, B. A.; Milliron, D. J. *Nano Lett.* **2015**.

(8) Arsenault, A. C.; Míguez, H.; Kitaev, V.; Ozin, G. A.; Manners, I. *Adv. Mater.* **2003**, *15* (6), 503–507.

(9) Arsenault, A. C.; Puzzo, D. P.; Manners, I.; Ozin, G. A. *Nat. Photonics* **2007**, *1* (8), 468–472.

(10) Brown, A. J.; Brunelli, N. A.; Eum, K.; Rashidi, F.; Johnson, J. R.; Koros, W. J.; Jones, C. W.; Nair, S. *Science* **2014**, *345* (6192), 72–75.

(11) Li, W.; Meng, Q.; Li, X.; Zhang, C.; Fan, Z.; Zhang, G. *Chem. Commun.* **2014**, *50*, 9711–9713.

(12) Yao, J.; Dong, D.; Li, D.; He, L.; Xu, G.; Wang, H. *Chem. Commun.* **2011**, *47* (9), 2559–2561.

(13) Chen, B.; Yang, Z.; Zhu, Y.; Xia, Y. *J. Mater. Chem. A* **2014**, *2*, 16811–16831.

(14) Bushell, A. F.; Attfield, M. P.; Mason, C. R.; Budd, P. M.; Yampolskii, Y.; Starannikova, L.; Rebrov, A.; Bazzarelli, F.; Bernardo, P.; Carolus Jansen, J.; Lanč, M.; Friess, K.; Shantarovich, V.; Gustov, V.; Isaeva, V. *J. Membr. Sci.* **2013**, *427*, 48–62.

(15) Phan, A.; Doonan, C. J.; Uribe-Romo, F. J.; Knobler, C. B.; O'Keeffe, M.; Yaghi, O. M. *Acc. Chem. Res.* **2010**, *43* (1), 58–67.

(16) McDonald, T. M.; Mason, J. A.; Kong, X.; Bloch, E. D.; Gygi, D.; Dani, A.; Crocellà, V.; Giordanino, F.; Odoh, S. O.; Drisdell, W. S.; Vlaisavljevich, B.; Dzubak, A. L.; Poloni, R.; Schnell, S. K.; Planas, N.; Lee, K.; Pascal, T.; Wan, L. F.; Prendergast, D.; Neaton, J. B.; Smit, B.; Kortright, J. B.; Gagliardi, L.; Bordiga, S.; Reimer, J. A.; Long, J. R. *Nature* **2015**, *519* (7543), 303–308.

(17) Breck, D. W. *Zeolite molecular sieves: structure, chemistry, and use*; R.E. Krieger, 1984.

(18) Park, K. S.; Ni, Z.; Côté, A. P.; Choi, J. Y.; Huang, R.; Uribe-Romo, F. J.; Chae, H. K.; O'Keeffe, M.; Yaghi, O. M. *Proc. Natl. Acad. Sci. U. S. A.* **2006**, *103* (27), 10186–10191.

(19) Kreno, L. E.; Leong, K.; Farha, O. K.; Allendorf, M.; Van Duyne, R. P.; Hupp, J. T. *Chem. Rev.* **2012**, *112* (2), 1105–1125.

(20) Sorribas, S.; Gorgojo, P.; Téllez, C.; Coronas, J.; Livingston, A. G. *J. Am. Chem. Soc.* **2013**, *135* (40), 15201–15208.

(21) Huang, X.; Zheng, B.; Liu, Z.; Tan, C.; Liu, J.; Chen, B.; Li, H.; Chen, J.; Zhang, X.; Fan, Z.; Zhang, W.; Guo, Z.; Huo, F.; Yang, Y.; Xie, L.-H.; Huang, W.; Zhang, H. *ACS Nano* **2014**, *8* (8), 8695–8701.
(22) Lu, G.; Hupp, J. T. *J. Am. Chem. Soc.* **2010**, *132* (23), 7832–7833.
(23) Kwon, H. T.; Jeong, H.-K. *J. Am. Chem. Soc.* **2013**, *135*, 10763–10768.
(24) Cacho-Bailo, F.; Seoane, B.; Téllez, C.; Coronas, J. *J. Membr. Sci.* **2014**, *464*, 119–126.
(25) Bux, H.; Liang, F.; Li, Y.; Cravillon, J.; Wiebcke, M.; Caro, J. *J. Am. Chem. Soc.* **2009**, *131* (44), 16000–16001.
(26) Shekhah, O.; Wang, H.; Zacher, D.; Fischer, R. A.; Wöll, C. *Angew. Chem. Int. Ed.* **2009**, *48* (27), 5038–5041.
(27) Arslan, H. K.; Shekhah, O.; Wohlgemuth, J.; Franzreb, M.; Fischer, R. A.; Wöll, C. *Adv. Funct. Mater.* **2011**, *21* (22), 4228–4231.
(28) Heinke, L.; Tu, M.; Wannapaiboon, S.; Fischer, R. A.; Wöll, C. *Microporous Mesoporous Mater.* **2015**, *216*, 200–215.
(29) Lu, G.; Farha, O. K.; Zhang, W.; Huo, F.; Hupp, J. T. *Adv. Mater.* **2012**, *24* (29), 3970–3974.
(30) Shamsaei, E.; Low, Z.-X.; Lin, X.; Mayahi, A.; Liu, H.; Zhang, X.; Liu, J. Z.; Wang, H. *Chem Commun* **2015**, *51*, 11474–11477.
(31) Yue, Y.; Qiao, Z.-A.; Li, X.; Binder, A. J.; Formo, E.; Pan, Z.; Tian, C.; Bi, Z.; Dai, S. *Cryst. Growth Des.* **2013**, *13* (3), 1002–1005.
(32) Stassen, I.; Campagnol, N.; Fransaer, J.; Vereecken, P.; Vos, D. D.; Ameloot, R. *CrystEngComm* **2013**, *15* (45), 9308–9311.
(33) Li, S.; Zhang, W.; Zhu, Y.; Zhao, Q.; Huo, F. *Cryst. Growth Des.* **2015**, *15*, 1017–1021.
(34) Zhan, W.; Kuang, Q.; Zhou, J.; Kong, X.; Xie, Z.; Zheng, L. *J. Am. Chem. Soc.* **2013**, *135* (5), 1926–1933.
(35) Yang, J.; Xie, Z.; Yin, H.; Wang, J.; Xu, J.; Wang, J.; Lu, J.; Yin, D.; Zhang, Y. *Microporous Mesoporous Mater.* **2014**, *198*, 263–270.
(36) Li, J.; Cao, W.; Mao, Y.; Ying, Y.; Sun, L.; Peng, X. *CrystEngComm* **2014**, *16* (42), 9788–9791.
(37) Drobek, M.; Bechelany, M.; Vallicari, C.; Chaaya, A. A.; Charmette, C.; Salvador-Levehang, C.; Miele, P.; Julbe, A. *J. Membr. Sci.* **2015**, *475*, 39–46.
(38) Khaletskaya, K.; Turner, S.; Tu, M.; Wannapaiboon, S.; Schneemann, A.; Meyer, R.; Ludwig, A.; Van Tendeloo, G.; Fischer, R. A. *Adv. Funct. Mater.* **2014**, *24* (30), 4804–4811.
(39) Zhang, X.; Liu, Y.; Li, S.; Kong, L.; Liu, H.; Li, Y.; Han, W.; Yeung, K. L.; Zhu, W.; Yang, W.; Qiu, J. *Chem. Mater.* **2014**, *26* (5), 1975–1981.
(40) Yue, Y.; Mehio, N.; Binder, A. J.; Dai, S. *CrystEngComm* **2015**, *17* (8), 1728–1735.
(41) Reboul, J.; Furukawa, S.; Horike, N.; Tsotsalas, M.; Hirai, K.; Uehara, H.; Kondo, M.; Louvain, N.; Sakata, O.; Kitagawa, S. *Nat. Mater.* **2012**, *11* (8), 717–723.
(42) Zanchetta, E.; Malfatti, L.; Ricco, R.; Styles, M. J.; Lisi, F.; Coghlan, C. J.; Doonan, C. J.; Hill, A. J.; Brusatin, G.; Falcaro, P. *Chem. Mater.* **2015**, *27* (3), 690–699.

(43) Schmidt, R.; Oh, J. H.; Sun, Y.-S.; Deppisch, M.; Krause, A.-M.; Radacki, K.; Braunschweig, H.; Könemann, M.; Erk, P.; Bao, Z.; Würthner, F. *J. Am. Chem. Soc.* **2009**, *131*, 6215–6228.
(44) Tan, J. C.; Bennett, T. D.; Cheetham, A. K. *Proc. Natl. Acad. Sci.* **2010**, *107* (22), 9938–9943.
(45) Cravillon, J.; Schröder, C. A.; Bux, H.; Rothkirch, A.; Caro, J.; Wiebcke, M. *CrystEngComm* **2012**, *14* (2), 492–498.
(46) McCarthy, M. C.; Varela-Guerrero, V.; Barnett, G. V.; Jeong, H.-K. *Langmuir* **2010**, *26* (18), 14636–14641.
(47) Bustamante, E. L.; Fernández, J. L.; Zamaro, J. M. *J. Colloid Interface Sci.* **2014**, *424*, 37–43.
(48) Schmink, J. R.; Leadbeater, N. E. In *Microwave Heating as a Tool for Sustainable Chemistry*; Leadbeater, N. E., Ed.; CRC Press: Boca Raton, 2010; p 4.
(49) Zhang, X.; Liu, Y.; Kong, L.; Liu, H.; Qiu, J.; Han, W.; Weng, L.-T.; Yeung, K. L.; Zhu, W. *J. Mater. Chem. A* **2013**, *1* (36), 10635–10638.
(50) Mannsfeld, S. C. Stanford Synchrotron Radiation Lightsource 2009.
(51) Hexemer, A.; Bras, W.; Glossinger, J.; Schaible, E.; Gann, E.; Kirian, R.; MacDowell, A.; Church, M.; Rude, B.; Padmore, H. *J Phys Conf Ser* **2010**, *247*, 012007.
(52) Ilavsky, J. *J. Appl. Crystallogr.* **2012**, *45* (2), 324–328.
(53) Marcus, M. A.; MacDowell, A. A.; Celestre, R.; Manceau, A.; Miller, T.; Padmore, H. A.; Sublett, R. E. *J. Synchrotron Radiat.* **2004**, *11* (3), 239–247.
(54) Ravel, B.; Newville, M. *J. Synchrotron Radiat.* **2005**, *12* (4), 537–541.
(55) Cao, S.; Bennett, T. D.; Keen, D. A.; Goodwin, A. L.; Cheetham, A. K. *Chem. Commun.* **2012**, *48* (63), 7805–7807.
(56) Macrae, C. F.; Bruno, I. J.; Chisholm, J. A.; Edgington, P. R.; McCabe, P.; Pidcock, E.; Rodriguez-Monge, L.; Taylor, R.; van de Streek, J.; Wood, P. A. *J. Appl. Crystallogr.* **2008**, *41* (2), 466–470.
(57) Doris, S. E.; Lynch, J. J.; Li, C.; Wills, A. W.; Urban, J. J.; Helms, B. A. *J. Am. Chem. Soc.* **2014**, *136* (44), 15702–15710.
(58) Sun, D.; Wong, M.; Sun, L.; Li, Y.; Miyatake, N.; Sue, H.-J. *J. Sol-Gel Sci. Technol.* **2007**, *43* (2), 237–243.
(59) Budd, P. M.; Elabas, E. S.; Ghanem, B. S.; Makhseed, S.; McKeown, N. B.; Msayib, K. J.; Tattershall, C. E.; Wang, D. *Adv. Mater.* **2004**, *16* (5), 456–459.
(60) Patel, H. A.; Yavuz, C. T. *Chem. Commun.* **2012**, *48* (80), 9989–9991.
(61) Cravillon, J.; Münzer, S.; Lohmeier, S.-J.; Feldhoff, A.; Huber, K.; Wiebcke, M. *Chem. Mater.* **2009**, *21* (8), 1410–1412.
(62) Du, N.; Park, H. B.; Robertson, G. P.; Dal-Cin, M. M.; Visser, T.; Scoles, L.; Guiver, M. D. *Nat. Mater.* **2011**, *10* (5), 372–375.

Chapter 6

A Polysulfide-Blocking Microporous Polymer Membrane Tailored for Hybrid Li-Sulfur Flow Batteries

Adapted with permission from *Nano Lett.* **2015**, *15* (9), pp 5724–5729. **Copyright 2015 American Chemical Society.**

Introduction

Membranes (or separators) are critical for ionic conduction and electronic isolation in many electrochemical devices. For cell architectures that utilize redox-active species that are dissolved, dispersed, or suspended in electrolyte—from fuel cells[1–3] (FCs) to redox flow batteries[4–11] (RFBs)—it is also imperative that the membrane prevent active material crossover that would otherwise contribute to device shorting, electrode fouling, or irrevokable loss in capacity. Unfortunately, commercial battery separators, which feature shape-persistent mesopores, are freely permeable to most active materials used in RFBs[12]. Alternative membrane separators have thus far relied heavily on variants of aqueous single-ion conductors, e.g., Nafion®[13–15], which may ultimately restrict the use of certain types of flowable electrodes. Considerably less attention has been paid to size-sieving as a mechanism to achieve membrane selectivity, although success in this regard would allow greater flexibility in battery chemistries. Despite the wide availability of porous materials[16] that might serve effectively as membrane components—including zeolites[17], metal organic frameworks[18–20], covalent organic frameworks[21], carbon nanotubes[22–24], cyclic peptide nanotubes[25–27], and microporous polymers[28,29]—rational design rules for achieving ion-selective transport via sieving in flow battery membranes have not been established.

Guided by theoretical calculations, we apply here polymers of intrinsic microporosity (PIMs) as a membrane platform for achieving high-flux, ion-selective transport in non-aqueous electrolytes. These polymers are synthesized in a single step and easily cast into large-area sheets with well-controlled pore structure and pore chemistry (**Figure 6.1**)[30–34]. The unique micropore architecture of PIMs arises primarily from two molecular characteristics: 1) PIMs do not feature rotating bonds along their backbone; and 2) they incorporate rigid sharp bends into at least one of the constituent monomers at regular intervals along the polymer chain. Both features contribute to frustrated packing of polymer chains in the solid state[35]. As a result, PIMs are amorphous yet exhibit high intrinsic microporosity (< 2 nm) and high surface area (300–1500 m^2 g^{-1})[36–38]. The open pore architecture of PIMs suggested to us that they might be uniquely positioned for selective species transport in electrochemical devices via sieving.

We highlight here new opportunities for PIMs to serve as ion-selective membranes in RFBs[39–45], using lithium-sulfur (Li-S) as a model battery chemistry. Here the lithium anode is stationary and separated, by the membrane, from the flowable sulfur-containing catholyte[46,47]. This RFB features a high theoretical specific energy capacity of 1,670 mAh g^{-1} of S and operating voltage that exceeds 2.0 V[48–55]. While these are desirable characteristics, this battery chemistry suffers from low Coulombic efficiency and rapid capacity fade when lithium polysulfides (PS) crossover to and react with the metal anode surface. Strategies seeking to mitigate PS crossover in Li-S batteries have included the use of sacrificial anode-protecting additives (e.g., $LiNO_3$)[56–59], single-ion conducting membranes[13,14], conductive interlayers[59–61], permselective barriers[62], and even polysulfide adsorbates[63–67]. Nonetheless, continuous Li consumption upon cycling remains a problem. Our demonstration here that PIM membranes block PS crossover, while allowing ions in the supporting electrolyte to traverse the membrane with minimal impedance, indicates a direct solution to the PS crossover problem is feasible; we also show dramatically improved battery performance when PIM membranes are in place, rather than conventional battery separators.

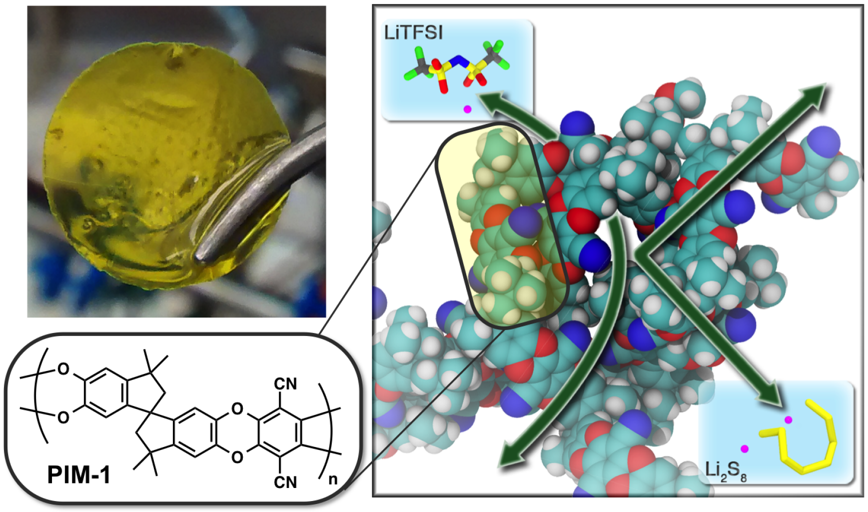

Figure 6.1 Ion-selective transport across membranes fabricated from PIM-1. For Li-S batteries, both stationary and hybrid flow, blocking Li_2S_x (where $x \geq 4$) crossover is critical to sustaining peak battery performance. We show that membranes based on PIM-1 achieve high transport selectivity for LiTFSI by reducing the membrane pore dimensions to sub-nanometer regimes, which shuts down polysulfide crossover via a sieving mechanism. Ion flux across the membrane is tied to overall microporosity, pore architecture, and electrolyte formulation.

Results and Discussion

To inform the rational design of a membrane platform capable of achieving high transport selectivity for supporting electrolyte (Lithium bis(trifluoromethane)sulfonimide, LiTFSI) *vs.* PS in Li-S RFBs, we carried out molecular dynamics (MD) simulations of each species' solvated structures in different ethereal solvents – diglyme (G2), triglyme (G3), and tetraglyme (G4) – as these are commonly used in Li-S RFBs[68–70]. The simulated effective sizes of these solvated complexes were determined by the radii of gyration (R_g) of the solute and the first solvation shell. These shells were typically composed of two solvent molecules, as exemplified by the average snapshots shown in **Figure 6.2**a. We also calculated the size of elemental sulfur, which exhibits no explicit solvent coordination in our simulations. For this singular case, we determined a size for

S_8 using its atoms' van der Waals solvent-excluded radii. Our determinations of R_g provide size-ranges for selective ion transport (**Figure 6.2**b). As the primary contributors to the shuttling currents are lithium polysulfides Li_2S_x where $x \geq 4$, the membrane pore dimensions should be smaller than 1.2–1.7 nm in order to achieve ion-selective transport.

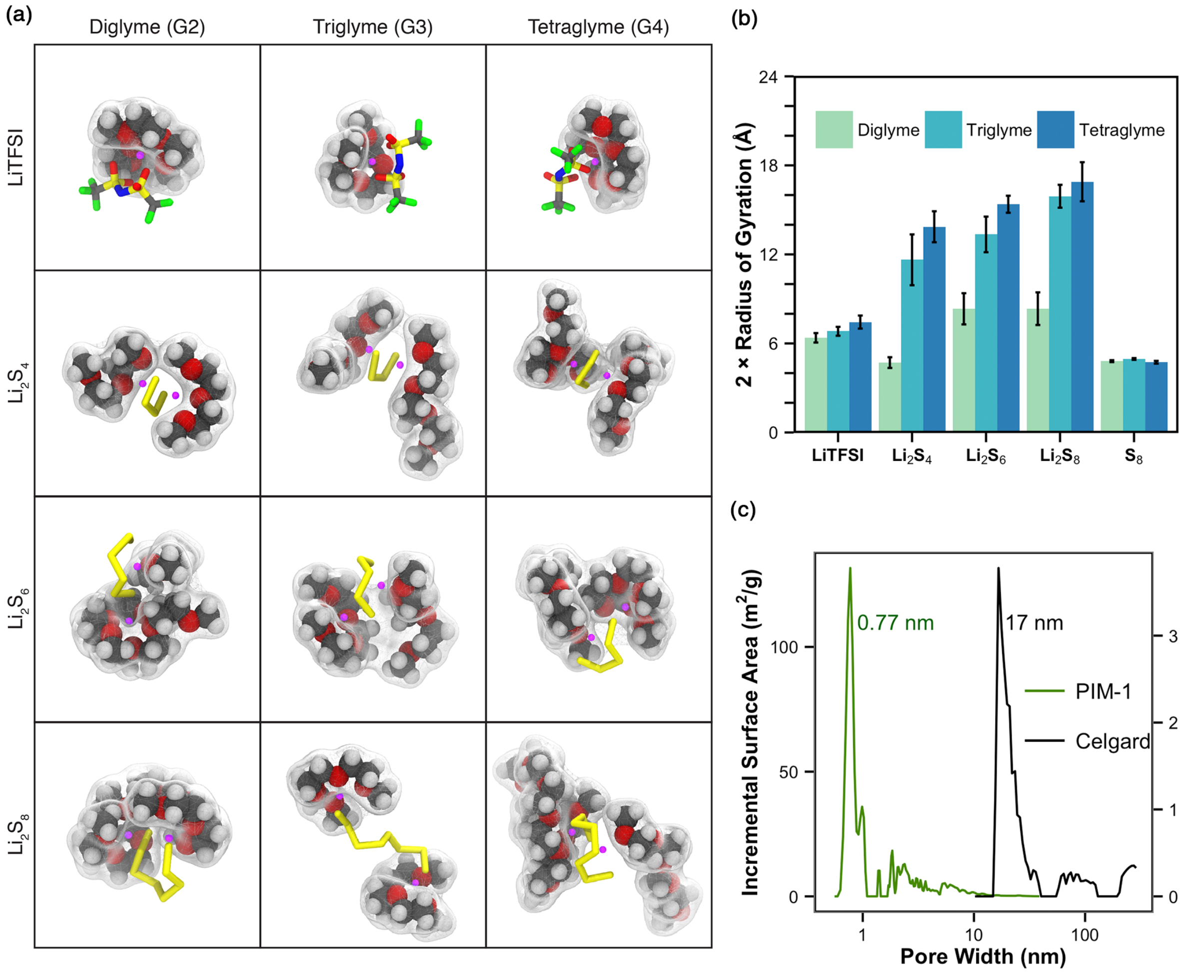

Figure 6.2 (a) Snapshots from MD simulations nearest to the average size of solvated LiTFSI and Li_2S_x (x = 4, 6, and 8) in diglyme, triglyme, and tetraglyme. (b) Calculated radii of gyration (R_g) for Li_2S_4, Li_2S_6, and Li_2S_8 – along with their first solvation shells – in diglyme, triglyme, and tetraglyme as determined by MD simulations. (c) Pore size distributions for microporous PIM-1 *vs*. mesoporous Celgard polymer membranes.

Directed by our MD simulations, we identified PIM-1[30] as a possible PS-blocking membrane material for Li-S hybrid flow cells. PIM-1 is the progenitor of a family of non-networked ladder polymers that are mechanically[71] and thermally[72] robust; pertinent to their use here, their pore dimensions are sub-nm. PIM-1 was synthesized (200 kg mol^{-1})

on a multi-gram scale from inexpensive, commercially available monomers and cast from solution into flexible free-standing membranes (~10 μm thick) (**Figure 6.1** & **Figure 6.S1**). We determined the specific surface area (795 m^2 g^{-1}) and pore size distribution of PIM-1 using nitrogen adsorption isotherms (**Figure 6.2**c). PIM-1 membranes had a nominal pore size of 0.77 nm, which is ideal for selective transport of LiTFSI and PS blocking. This stands in stark contrast with commercially available Celgard 2325, which has a much larger pore size of 17 nm: far too large for size-selective transport (**Figure 6.2**c). Celgard 2325 and similar mesoporous polymer separators[12] are commonly used in Li-S cells and serve as a useful benchmark for new membrane materials[46]. A total porosity of ~25% was determined for PIM-1 membranes using ellipsometric porosimetry, which is comparable to the porosity of Celgard 2325. As PIM-1 membranes are expected to swell to a degree upon introduction of electrolyte, this determination should be considered a lower limit to the available free volume.

We hypothesized that during battery operation the free volume in PIM-1 (and PIMs generally) would become swollen and infiltrated with electrolyte, creating an ionically percolating solution-phase conductive network. As a result, ion flux would be solely carried by (and be dependent on) the solution conductivity within the pores; polymer chain dynamics, which are orders of magnitude slower, would no longer dictate the membrane's ionic conductivity. To test this hypothesis, we evaluated PIM-1's membrane ionic conductivities in glymes of different oligomer lengths—diglyme (G2), triglyme (G3) and tetraglyme (G4)—containing 0.50 M LiTFSI. We noted a strong correlation between the membrane ionic conductivity and the bulk solution ionic conductivity[73] of the electrolyte (**Figure 6.3**a). These results indicate that the ion current is indeed carried by the infiltrating electrolyte, as predicted. This behavior was also observed in Celgard separators (**Figure 6.3**a). By comparing the membrane ionic conductivities for Celgard and PIM-1, we found that reducing the pore dimensions from 17 nm to 0.77 nm, respectively, only decreased membrane ionic conductivity ten-fold. We also found that electrolytes based on diglyme provided the highest membrane ionic conductivity for both platforms, and was thus chosen as the supporting electrolyte for all subsequent experiments.

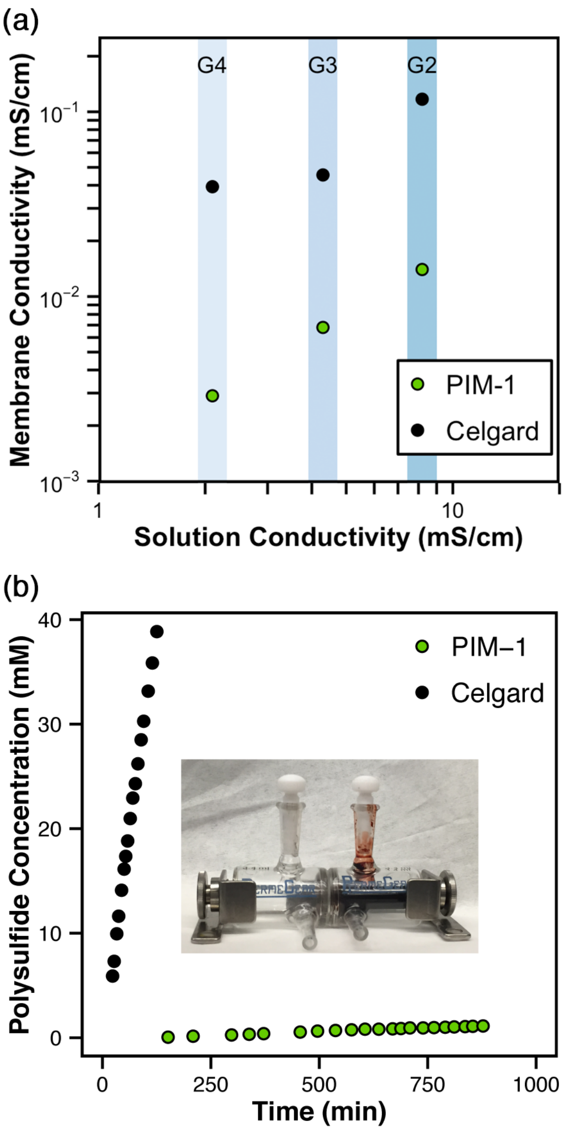

Figure 6.3 (a) Ambient temperature ionic conductivity of microporous PIM-1 *vs*. mesoporous Celgard membranes infiltrated with different electrolyte formulations: 0.50 M LiTFSI in either diglyme (G2), triglyme (G3), or tetraglyme (G4). (b) Time-evolution of the concentration of PS in the permeate (left) of H-cells configured with either a Celgard (*black*) or a PIM-1 (*green*) membrane. The retentate was charged with an initial concentration of 2.5 M S as Li_2S_8 in diglyme containing 0.50 M LiTFSI and 0.15 M $LiNO_3$. The concentration of PS in the permeate was determined electrochemically.

To quantify the polysulfide-blocking ability of PIM-1 *vs.* Celgard, we performed membrane crossover experiments in H-cells configured with dissolved PS (2.5 M S as Li_2S_8 in diglyme containing 0.50 M LiTFSI and 0.15 M $LiNO_3$) on the retentate side and PS-free electrolyte on the permeate side (**Figure 6.3**b, *inset*). The concentration of PS over time was then monitored electrochemically on the permeate side using either cyclic voltammetry or square wave voltammetry, where current could be correlated to concentration of PS via a calibration curve (**Figure 6.S2** & **Figure 6.S3**). Using an initial rate approximation, the diffusion coefficient of PS across the membrane was calculated to be 6.8×10^{-8} cm^2 s^{-1} for Celgard and 1.3×10^{-10} cm^2 s^{-1} for PIM-1 (~500-fold reduction). This is compelling evidence that PS are screened by a size-sieving mechanism within PIM-1's ionically-percolating micropore network, as hypothesized. This PS-blocking ability comes at minimal expense to overall membrane ionic conductivity compared to Celgard, thus highlighting the value in guiding membrane design through careful examination of the solvated structures of ions *vs.* redox active species in the electrolyte.

Given the outstanding PS-blocking ability of the PIM-1 membrane, their performance in Li-S batteries was tested employing soluble sulfur catholytes. To do so, Swagelok cells were assembled with Li-metal anodes, polysulfide catholytes (2.5 M S as Li_2S_8 in diglyme containing 0.50 M LiTFSI) and Celgard or PIM-1 membranes. Lithium anodes were scraped to reveal a fresh surface prior to cell assembly. Seeking to isolate the membrane's influence on mitigating PS shuttling currents, $LiNO_3$ additives were deliberately avoided in the electrolyte formulation. Moreover, to improve sulfur utilization, 5 wt% Ketjenblack was employed as an embedded current collector in the catholyte[42,46]. Three break-in cycles at C/10 were used to equilibrate PIM-1's membrane microenvironments before cycling at a C/8 rate. Overall, higher capacity fade was observed for both types of cells during the break-in due to the ample time allowed for polysulfide shuttling. The Li-S cells configured with Celgard membranes exhibited a drastic capacity fade from ~150 Wh L^{-1} after the break-in cycles to less than 20 Wh L^{-1} within the first 20 cycles, all at a C/8 rate. In contrast, batteries configured with PIM-1 membranes exhibited higher capacity at all cycles, sustaining 50 Wh L^{-1} at the end of 50 cycles (**Figure 6.4**a). The performance of PIM-1 membranes was further improved with the addition of $LiNO_3$ as an anode-protecting additive, with a sustained capacity of approximately 100 Wh L^{-1} after 50 cycles (**Figure 6.4**a) and stable cycling at rates as high as C/4 (**Figure 6.4**b). These results represent improvements in capacity retention over related work with Li-S flow cells, particularly in the absence of $LiNO_3$, and highlight the possibility for combining our membrane approach with other strategies to mitigate the effects of polysulfide crossover[59,74].

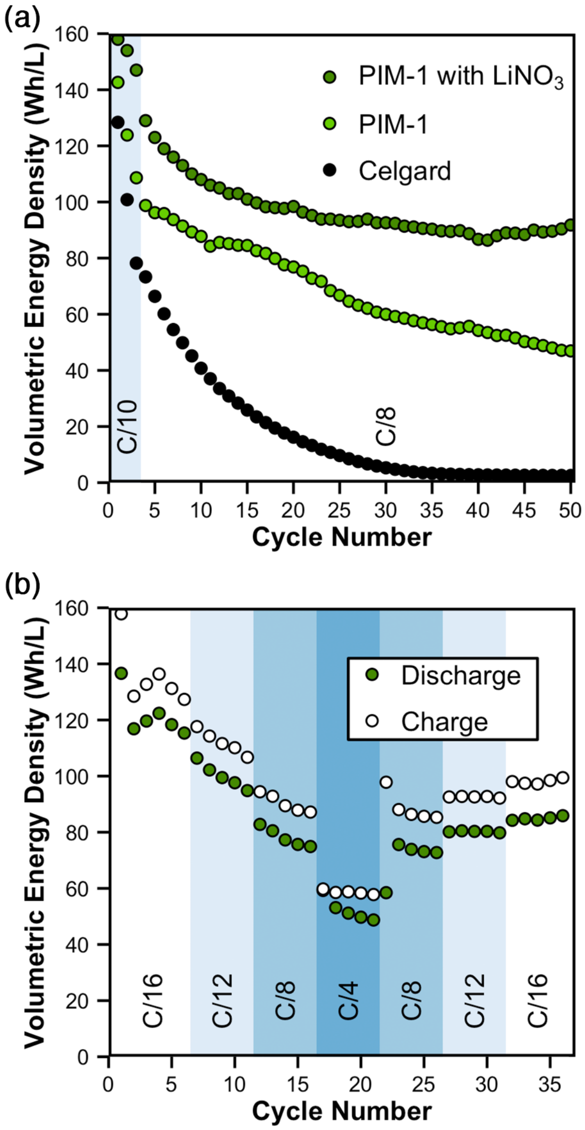

Figure 6.4 (a) Volumetric energy density as a function of cycle number for Celgard membrane with no $LiNO_3$ (*black circles*), PIM-1 membrane with no $LiNO_3$ (*light green circles*), and PIM-1 membrane with $LiNO_3$ additive (*dark green circles*). (b) Rate performance of PIM-1 membrane with $LiNO_3$ additive.

Preliminary application of PIM-1 as an active PS-blocking membrane in a flow-battery setup has been carried out in our collaborator's lab space at MIT. Frank Fan in Dr. Yet-Ming Chiang's lab graciously lent me his time and energy in assessing the viability of the membrane under flow conditions. The experiment was carried out in a custom-built flow cell, shown below in **Figure 6.5**. The parameters of the experiments (polarization and potentiostatic cycling) undertaken herein and the flow cell construction have been described by Fan *et. al.*[46] previously.

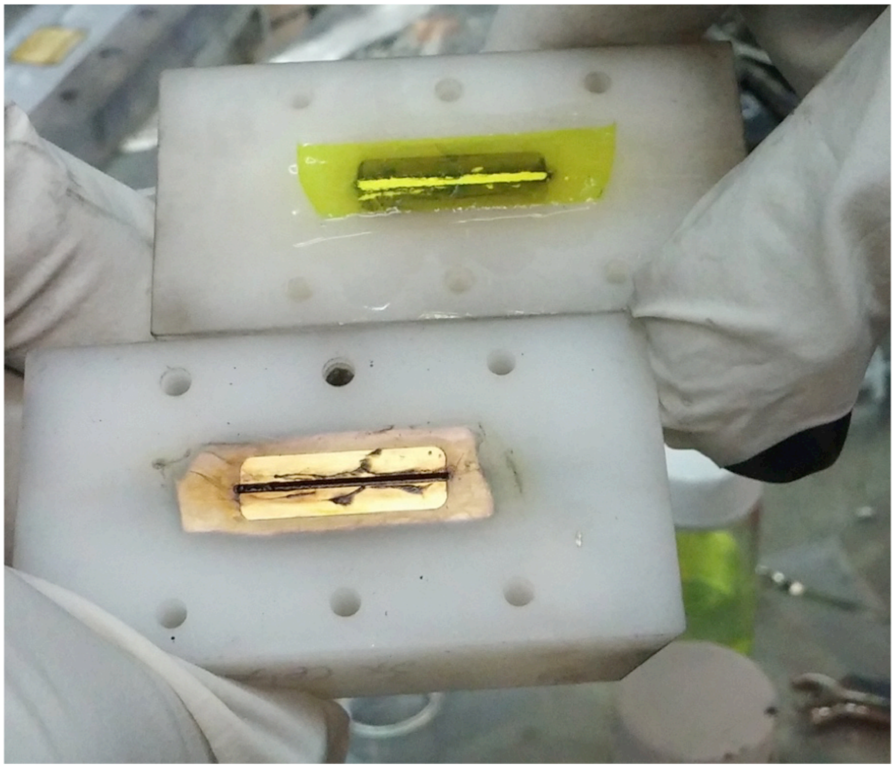

Figure 6.5 Li-PS flow cell before assembly. The lower half of the cell contains the cathodic channel in which PS slurry, the active material, flows. The upper half of the cell contains lithium anode strip, over which a PIM-1 membrane assembly rests.

Upon assembly, polarization tests were used to gauge the relative membrane impedance present in PIM-1 cells and Celgard cells. As expected, PIM-1 cells displayed greater membrane overpotential, permitting approximately half of the ionic current as Celgard (**Figure 6.6**) under both flowing and static conditions. The result echoed the ionic conductivity shown in **Figure 6.3**. Battery cycling performance, measured potentiostatically in the same fashion as in Fan *et. al.*[46], were compared without the addition of $LiNO_3$. Celgard battery shows reproducible charging plateaus at ~ +0.15 mA, indicative of PS shuttling **Figure 6.7**. Charging current was used to counteract the auto-discharge due to shuttling, thus never reaching the current limit for the cycling experiment. On the other hand, PIM-1 battery with drastically mitigated shuttling effect can successful accomplish multiple charge/discharge cycles within 20 hours (**Figure 6.8**). There was however noticeably lower starting capacity and gradual capacity loss, which was reminiscent of the precipitous capacity drop shown in Swagelok cell cycling behaviors (**Figure 6.4**). Experiments done by my colleagues have suggested there is non-negligible chemical reactivity between PIM-1 and the PS active material. The chemical reaction might be responsible for the permanent loss of capacity/active material and increased permeability of PS active materials. Long term stability and the exact mechanism of chemical changes involved are under active investigation within my group and is thus outside of the scope of this dissertation.

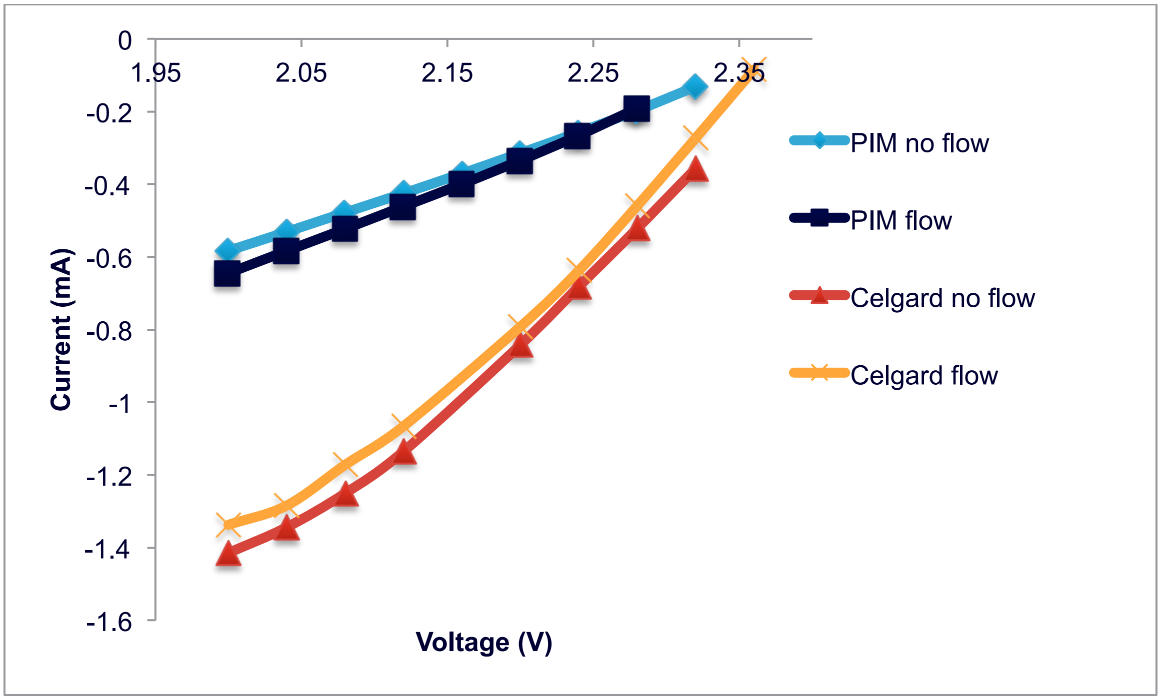

Figure 6.6 Polarization test for PIM-1- and Celgard-equipped flow cells.

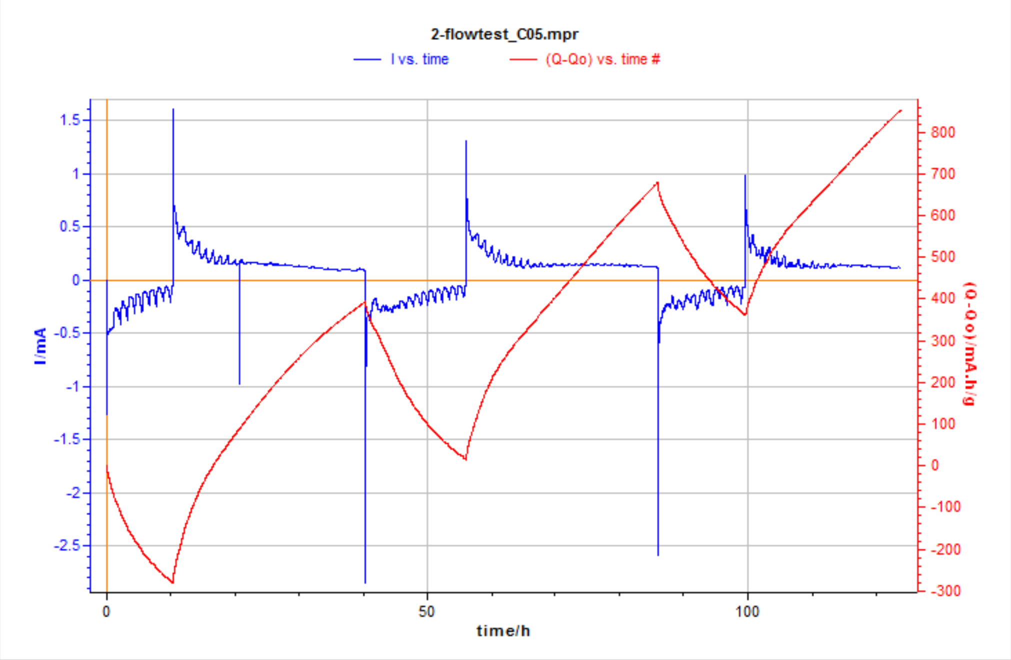

Figure 6.7 Potentiostatic cycling of a Celgard-equipped battery. Blue trace indicates the current passed when the cell is subjected to an external voltage. Red trace indicates the net charge passed in/out of the flow cell.

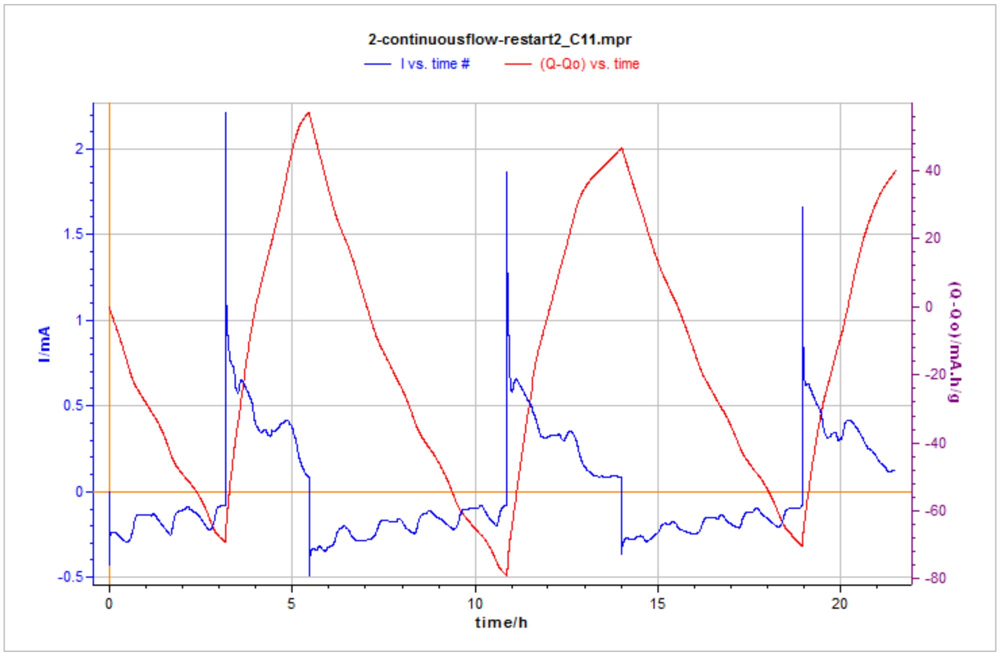

Figure 6.8 Potentiostatic cycling of a PIM-1-equipped battery. Blue trace indicates the current passed when the cell is subjected to an external voltage. Red trace indicates the net charge passed in/out of the flow cell.

Conclusion

Redox flow batteries present unique opportunities for low-cost, multi-hour energy storage—but also limitations. In order for RFBs to mature as a deployable technology, their longevity should be greatly improved for battery chemistries offering high-power performance. Toward that end, we highlighted the transport needs for membranes employed in non-aqueous Li-S cells, where the cathode was formulated as an energy-dense, flowable solution of polysulfides with Ketjenblack as an embedded current collector. We showed that rational principles for membrane design emerge from molecular dynamics simulations of the solvated structures of S_8, Li_2S_x (x = 8, 6, or 4), and LiTFSI in different electrolytes, and more specifically, that their calculated radius of gyration places an upper limit of 1.2–1.7 nm on the pore dimensions required for polysulfide blocking. Indeed, we showed that membranes processed from polymers of intrinsic microporosity exhibited unprecedented blocking characteristics for soluble polysulfides owing to their sub-nm pore dimensions. This blocking ability led to significantly improved device performance with respect to capacity fade and other important metrics. Given that the pore size, pore chemistry, and overall porosity for PIM membranes are tunable using molecular engineering and polymer processing, the membrane's transport characteristics can be tailored to suit a broad spectrum of electrochemical devices, including stationary batteries and fuel cells. Our success suggests a revolution in ion-transporting membranes is within reach.

Supporting Information

Experimental Details

Materials: Tetraglyme (G4), triglyme (G3), diglyme (G2), 3,3,3',3'-tetramethyl-1,1'-spirobiindane-5,5',6,6'-tetraol and tetrafluoroterephthalonitrile were purchased from Sigma Aldrich. Lithium nitrate, sulfur (Puratronic, 99.9995 % (metals basis)), lithium sulfide (99.9 % (metals basis)), and lithium metal were purchased from Alfa Aesar. Lithium bis(trifluoromethanesulfonyl)imide (LiTFSI) was purchased from 3M. Celgard 2535 membrane was purchased from MTI Corporation. Ketjenblack EC-600JD was purchased from AkzoNobel.

General methods: Nuclear magnetic resonance (NMR) spectra were taken on a Bruker Avance II 500 MHz NMR spectrometer. Analysis of the polymer's molecular weight distribution was carried out using size exclusion chromatography on a Malvern Viscotek TDA 302 system. Residual water content for various solvents was determined by a Mettler Toledo C20 Coulometric Karl Fischer titrator. Electrochemical experiments and battery testing were conducted with a BioLogic VMP3 potentiostat. Scanning electron micrographs were obtained with a Zeiss Gemini Ultra-55 analytical scanning electron microscope equipped with in-lens and secondary electron detectors at a beam energy of 2 keV.

Electrode details: Swagelok batteries were constructed using Swagelok unions purchased from Swagelok Northern California. Associated electrodes were made in-house from nickel 200 rods with outer diameters of 1.27 cm. Wells, which were 0.635 cm in diameter and 0.508 mm deep, were machined into the cathode current collectors. Gold was sputtered onto the cathode current collector surface. Anode current collectors were flat, bare nickel 200 surfaces.

Membrane preparation: PIM-1 was synthesized using a literature procedure[38,46]. PIM-1 was dissolved in chloroform at a concentration of 12.5 mg mL^{-1}. Films of PIM-1 were cast by depositing 1 mL of solution into a 3.5 cm diameter Teflon well. The solvent was left to evaporate in a closed vacuum chamber under ambient pressure for 1 h or until dryness. The films were further dried *in vacuo* overnight. The dried films were punched into 7/16-inch circles. Celgard® 2325 membranes were punched into 1/2-inch circles. All membranes were soaked in relevant electrolytes overnight before use.

Ionic conductivity measurements: Soaked membranes were sandwiched between two stainless steel blocking electrodes. Potentio electrochemical impedance spectroscopy (PEIS) was used with 50 mV AC bias scanning from 1 MHz to 100 mHz. The high frequency *x*-axis intercept is taken to be the resistance of the membrane. The membrane conductivity was then calculated taking into account the cell geometry.

Electrolyte and polysulfide preparation: The supporting electrolyte formulation for all battery cycling and conductivity measurements was 0.50 M LiTFSI. $LiNO_3$ was added to the electrolyte only for the crossover experiments detailed below. LiTFSI was dried for 16 h under vacuum at 150 ˚C. $LiNO_3$ was dried for 16 h under vacuum at 110 ˚C. Diglyme was tested for peroxides prior to use; if any were measured, it was stirred with alumina, filtered, and sparged with argon. Diglyme was dried with activated 3 Å molecular sieves until it measured < 20 ppm H_2O. Electrolyte was tested for water content and confirmed to contain < 30 ppm water before use. Solutions of Li_2S_8 (2.50 mol S L^{-1} in electrolyte) were prepared by mixing Li_2S (0.287 g, 6.25 mmol), sulfur (1.40 g, 5.47 mmol), and 20 mL of electrolyte and heating at 60 ˚C until all solids were dissolved. Li_2S_8 solutions were kept at 60 ˚C in order to prevent precipitation of insoluble species and cooled to room temperature prior to use. Cathode slurry with 5% *w/w* conductive additive was made by adding 30.8 mg of Ketjenblack to 500 µL of Li_2S_8 solution and mixed for 15 min.

Crossover experimental methods: Crossover measurements were made by placing respective membranes between the cell halves of a PermeGear Side-Bi-Side diffusion cell. Next, to the retentate side of the cell was added 2.5 mL of supporting electrolyte (0.15 M $LiNO_3$, 0.5 M LiTFSI in diglyme) and 2.5 mL of 2.5 M Li_2S_8 electrolyte was added to the permeate side. In this case, due to the presence of lithium as a reference electrode, $LiNO_3$ was necessary to prevent the reaction of polysulfides with the lithium. Crossover was determined by cyclic voltammetry and square wave voltammetry measurements of the permeate side of the cell. Cyclic voltammetry allowed concentrations between 5.0–60 mM to be measured while square wave voltammetry allowed for measurements of concentrations ranging from 0.20–1.0 mM. Given the different rates of crossover between the two materials, both techniques were necessary as the Celgard crossover was too fast to be measured accurately with the SWV, and the PIM crossover was too slow to be measured in a convenient time frame with CV. A glassy carbon disc electrode (1 mm) was obtained from BAS Inc. (West Lafayette, IN), polished before use and used as the working electrode. Lithium metal was used as the reference and counter electrodes. A calibration curve for each electrochemical technique was obtained by measuring the current as a function of voltage for a set of known concentration polysulfide solutions (**Figure 6.S2** & **Figure 6.S3**). The concentration of polysulfide *vs.* time for the crossover measurements was then calculated using the linear equation determined from the calibration curves.

Battery cycling: Cathode slurry was spread evenly into the cathode well. Lithium chip was punched using a 7/16-inch bore and pressed onto the anode. Due to the safety concern of dendrite formation, membranes were sandwiched between two Celgard layers to isolate them from the lithium polysulfide slurry and the lithium anode surface. The trilayer membrane was then pressed in between the two electrodes to assemble a Swagelok battery.

Computational Methods

First-Principles molecular dynamics simulations: The S_8/Li-TFSI/Li_2S_x-TEGDME systems were simulated using a modified version of the mixed Gaussian and plane wave code[75] CP2K/Quickstep[76]. We employed a triple-ζ basis set with two additional sets of polarization functions (TZV2P)[77] and a 320 Ry plane-wave cutoff. The unknown exchange-correlation potential is substituted by the revised PBE generalized gradient approximation[78,79], and the Brillouin zone is sampled at the Γ-point only. Interactions between the valence electrons and the ionic cores are described by norm-conserving pseudopotentials[80,81]. The Poisson problem is tackled using an efficient Wavelet-based solver[82]. We overcome the poor description of the short-range dispersive forces within the PBE-GGA exchange-correlation functional by employing the DFTD3 empirical corrections of Grimme *et al.*[83]. In order to equilibrate the systems, we performed 10 ps of NPT dynamics, using a Nose-Hoover thermostat (temperature damping constant of 100 fs) and an Anderson barostat (pressure damping constant of 2 ps). Snapshots of the system were saved every step. The snapshot with a volume closest to the average of the last 5 ps of MD was then selected as input for an additional 20 ps simulation in the constant volume, constant temperature (canonical or NVT) ensemble.

Structural analysis: We estimated the “size” of the solvated lithium polysulfide species as the sum of two terms: 1) the radius of gyration of the solute (R_{gyr}) and 2) the size of the glyme solvation shell. All structural analyses were performed for every 10 snapshots from the last 20 ps of the NVT AIMD simulations (4,000 for each system). The R_{gyr} was computed as

$$R_{gyr} = \sqrt{\frac{1}{M}\sum_i m_i\left(r_i - r_{cm}\right)^2} \qquad \textbf{(Eq. 6.4)}$$

where M is the total mass of the solute, R_{cm} is the center of mass and the sum is over all r_i atoms in the solute.

The solvation environment around each dissolved polysulfide was obtained calculating the Li – glyme (oxygen atom) and S – glyme pair distribution functions (PDF) from the last 20 ps NVT MD simulation. The 1st solvation shell was obtained from the minimum in the PDF after the first peak, and the number of solvent molecules obtained by simple integration.

Additional Figures

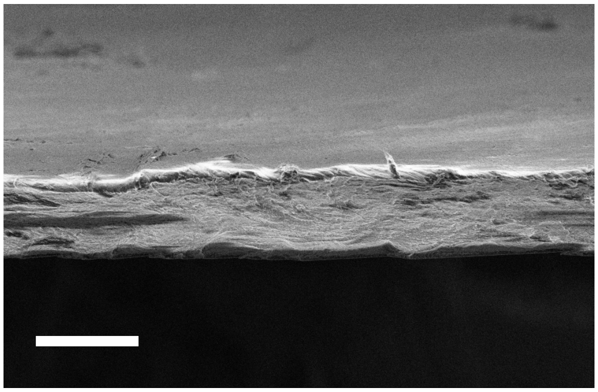

Figure 6.S1 Cross-sectional scanning electron micrograph of a freestanding PIM-1 membrane. The scale bar is 10 μm.

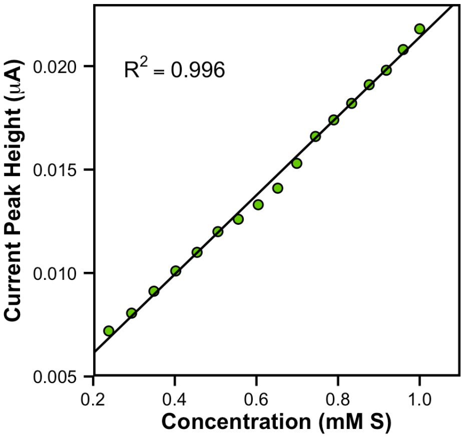

Figure 6.S2 Calibration curve of current *vs.* concentration obtained via square wave voltammetry for the lower concentration regime.

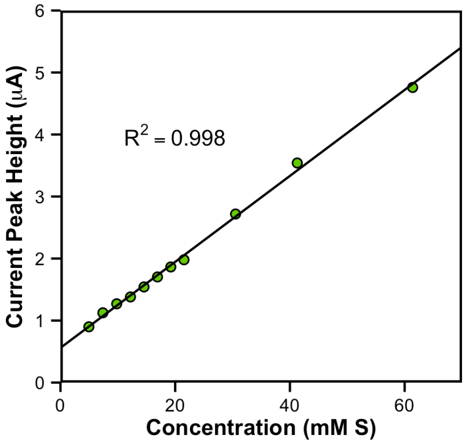

Figure 6.S3 Calibration curve of current *vs.* concentration obtained via cyclic voltammetry for the higher concentration regime.

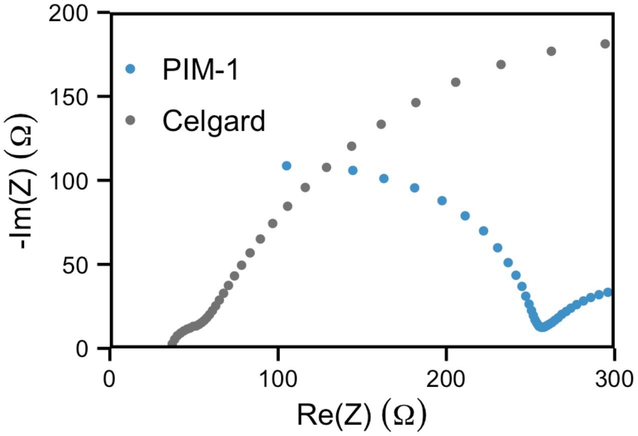

Figure 6.S4 Electrochemical impedance spectroscopy (EIS) of Li-S cells configured with PIM-1 and Celgard as membranes, respectively. The membrane ionic conduction kinetics are represented by the sizes of high-frequency semicircles, which are 20.1 Ohms and 215.1 Ohms for Celgard and PIM-1, respectively.

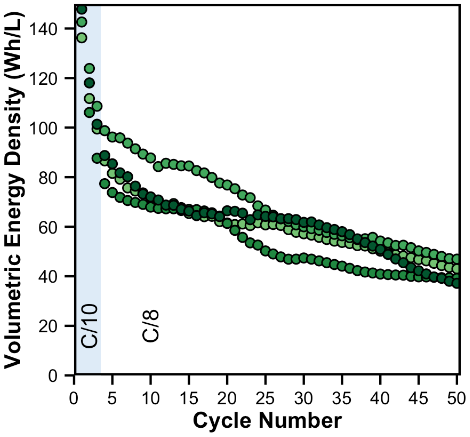

Figure 6.S5 Volumetric energy densities of all batteries tested (*catholyte formulation:* 2.5 M S as Li_2S_8 in diglyme containing 0.50 M LiTFSI) with either PIM-1 membrane (*green circles, left panel*) or Celgard membrane (*purple circles, right panel*).

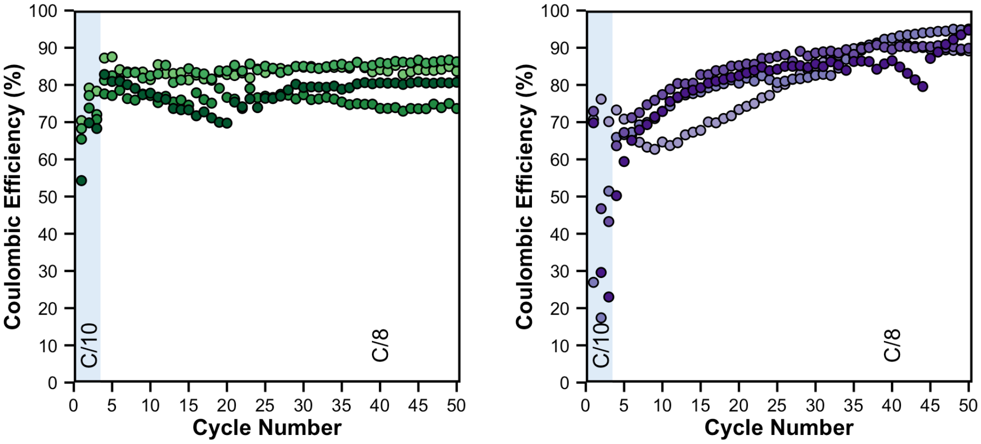

Figure 6.S6 Coulombic efficiencies of all batteries tested (*catholyte formulation:* 2.5 M S as Li_2S_8 in diglyme containing 0.50 M LiTFSI) with either PIM-1 membrane (*green circles, left panel*) or Celgard membrane (*purple circles, right panel*).

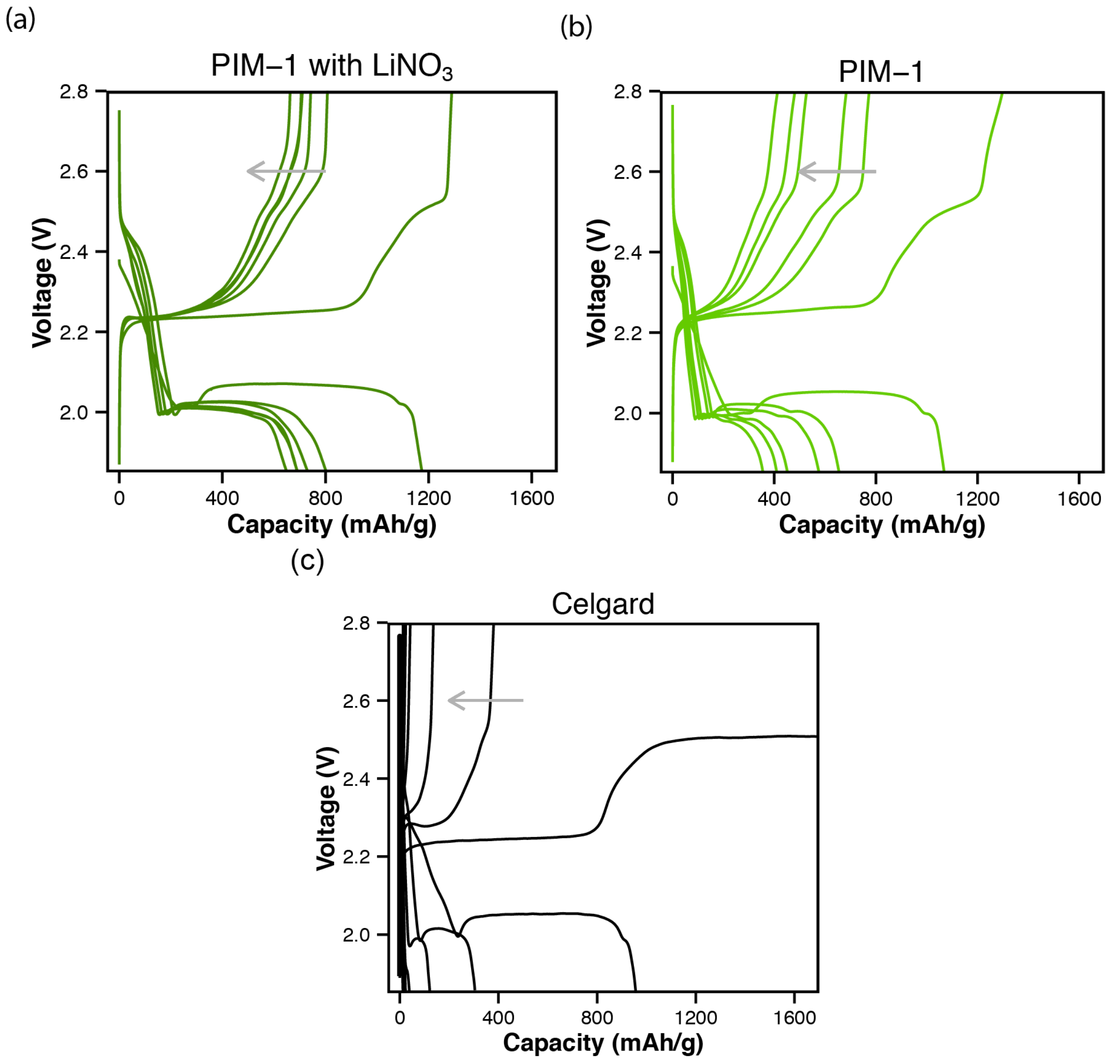

Figure 6.S7 Discharge and charge profiles for LI-S batteries configured with: (a) PIM-1 membrane separators and $LiNO_3$ electrolyte additive; (b) PIM-1 membrane separators without $LiNO_3$ electrolyte additive; and (c) Celgard separators without $LiNO_3$ additive at the 1st, 10th, 20th, 30th, 40th, and 50th cycles. The arrows indicate the direction of higher cycle number.

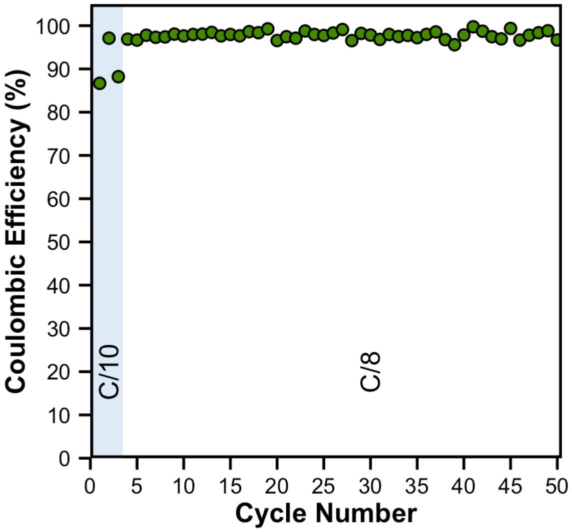

Figure 6.S8 Representative Coulombic efficiency of a Li-S battery configured with a PIM-1 membrane separator and $LiNO_3$ as an electrolyte additive.

References

(1) Steele, B. C. H.; Heinzel, A. *Nature* **2001**, *414* (6861), 345–352.

(2) Kerres, J. A. *J. Membr. Sci.* **2001**, *185* (1), 3–27.

(3) Borup, R.; Meyers, J.; Pivovar, B.; Kim, Y. S.; Mukundan, R.; Garland, N.; Myers, D.; Wilson, M.; Garzon, F.; Wood, D.; Zelenay, P.; More, K.; Stroh, K.; Zawodzinski, T.; Boncella, J.; McGrath, J. E.; Inaba, M.; Miyatake, K.; Hori, M.; Ota, K.; Ogumi, Z.; Miyata, S.; Nishikata, A.; Siroma, Z.; Uchimoto, Y.; Yasuda, K.; Kimijima, K.; Iwashita, N. *Chem. Rev. Wash. DC U. S.* **2007**, *107*, 3904–3951.

(4) Skyllas-Kazacos, M.; Rychcik, M.; Robins, R. G.; Fane, A. G.; Green, M. A. *J. Electrochem. Soc.* **1986**, *133* (5), 1057–1058.

(5) Lopez-Atalaya, M.; Codina, G.; Perez, J. R.; Vazquez, J. L.; Aldaz, A. *J. Power Sources* **1992**, *39* (2), 147–154.

(6) Fabjan, C.; Garche, J.; Harrer, B.; Jörissen, L.; Kolbeck, C.; Philippi, F.; Tomazic, G.; Wagner, F. *Electrochimica Acta* **2001**, *47* (5), 825–831.

(7) Joerissen, L.; Garche, J.; Fabjan, C.; Tomazic, G. *J. Power Sources* **2004**, *127* (1–2), 98–104.

(8) Weber, A. Z.; Mench, M. M.; Meyers, J. P.; Ross, P. N.; Gostick, J. T.; Liu, Q. *J. Appl. Electrochem.* **2011**, *41* (10), 1137–1164.

(9) Dunn, B.; Kamath, H.; Tarascon, J.-M. *Science* **2011**, *334* (6058), 928–935.

(10) Wang, W.; Luo, Q.; Li, B.; Wei, X.; Li, L.; Yang, Z. *Adv. Funct. Mater.* **2013**, *23*, 970–986.

(11) Huang, Q.; Wang, Q. *ChemPlusChem* **2015**, *80*, 312–322.

(12) Arora, P.; Zhang, Z. (John). *Chem. Rev.* **2004**, *104* (10), 4419–4462.

(13) Huang, J.-Q.; Zhang, Q.; Peng, H.-J.; Liu, X.-Y.; Qian, W.-Z.; Wei, F. *Energy Environ. Sci.* **2013**, *7* (1), 347–353.

(14) Bauer, I.; Thieme, S.; Brückner, J.; Althues, H.; Kaskel, S. *J. Power Sources* **2014**, *251*, 417–422.

(15) Jin, Z.; Xie, K.; Hong, X.; Hu, Z.; Liu, X. *J. Power Sources* **2012**, *218*, 163–167.

(16) Thomas, A. *Angew. Chem. Int. Ed.* **2010**, *49* (45), 8328–8344.

(17) Caro, J.; Noack, M. *Microporous Mesoporous Mater.* **2008**, *115*, 215–233.

(18) Yaghi, O. M.; O'Keeffe, M.; Ockwig, N. W.; Chae, H. K.; Eddaoudi, M.; Kim, J. *Nature* **2003**, *423* (6941), 705–714.

(19) Kitagawa, S.; Kitaura, R.; Noro, S. *Angew. Chem. Int. Ed.* **2004**, *43*, 2334–2375.

(20) Chung, T.-S.; Jiang, L. Y.; Li, Y.; Kulprathipanja, S. *Prog. Polym. Sci.* **2007**, *32* (4), 483–507.

(21) Colson, J. W.; Dichtel, W. R. *Nat. Chem.* **2013**, *5*, 453–465.

(22) Che, G.; Lakshmi, B. B.; Fisher, E. R.; Martin, C. R. *Nature* **1998**, *393* (6683), 346–349.

(23) Hinds, B. J.; Chopra, N.; Rantell, T.; Andrews, R.; Gavalas, V.; Bachas, L. G. *Science* **2004**, *303* (5654), 62–65.

(24) Geng, J.; Kim, K.; Zhang, J.; Escalada, A.; Tunuguntla, R.; Comolli, L. R.; Allen, F. I.; Shnyrova, A. V.; Cho, K. R.; Munoz, D.; Wang, Y. M.; Grigoropoulos, C. P.; Ajo-Franklin, C. M.; Frolov, V. A.; Noy, A. *Nat. Lond. U. K.* **2014**, *514*, 612–615.

(25) Ghadiri, M. R.; Granja, J. R.; Buehler, L. K. *Nature* **1994**, *369*, 301–304.

(26) Xu, T.; Zhao, N.; Ren, F.; Hourani, R.; Lee, M. T.; Shu, J. Y.; Mao, S.; Helms, B. A. *ACS Nano* **2011**, *5*, 1376–1384.

(27) Hourani, R.; Zhang, C.; van der Weegen, R.; Ruiz, L.; Li, C.; Keten, S.; Helms, B. A.; Xu, T. *J. Am. Chem. Soc.* **2011**, *133* (39), 15296–15299.

(28) McKeown, N. B.; Budd, P. M. *Chem. Soc. Rev.* **2006**, *35* (8), 675.

(29) Budd, P. M.; McKeown, N. B. *Polym. Chem.* **2010**, *1*, 63–68.

(30) Budd, P. M.; Ghanem, B. S.; Makhseed, S.; McKeown, N. B.; Msayib, K. J.; Tattershall, C. E. *Chem. Commun.* **2004**, No. 2, 230–231.

(31) Budd, P. M.; Msayib, K. J.; Tattershall, C. E.; Ghanem, B. S.; Reynolds, K. J.; McKeown, N. B.; Fritsch, D. *J. Membr. Sci.* **2005**, *251* (1–2), 263–269.

(32) Staiger, C. L.; Pas, S. J.; Hill, A. J.; Cornelius, C. J. *Chem. Mater.* **2008**, *20* (8), 2606–2608.

(33) McKeown, N. B.; Budd, P. M. *Macromolecules* **2010**, *43* (12), 5163–5176.

(34) Du, N.; Dal-Cin, M. M.; Pinnau, I.; Nicalek, A.; Robertson, G. P.; Guiver, M. D. *Macromol. Rapid Commun.* **2011**, *32*, 631–636.

(35) Heuchel, M.; Fritsch, D.; Budd, P. M.; McKeown, N. B.; Hofmann, D. *J. Membr. Sci.* **2008**, *318* (1–2), 84–99.

(36) Du, N.; Park, H. B.; Robertson, G. P.; Dal-Cin, M. M.; Visser, T.; Scoles, L.; Guiver, M. D. *Nat. Mater.* **2011**, *10* (5), 372–375.

(37) Carta, M.; Malpass-Evans, R.; Croad, M.; Rogan, Y.; Jansen, J. C.; Bernardo, P.; Bazzarelli, F.; McKeown, N. B. *Science* **2013**, *339* (6117), 303–307.

(38) Shamsipur, H.; Dawood, B. A.; Budd, P. M.; Bernardo, P.; Clarizia, G.; Jansen, J. C. *Macromolecules* **2014**, *47* (16), 5595–5606.

(39) Li, X.; Zhang, H.; Mai, Z.; Zhang, H.; Vankelecom, I. *Energy Environ. Sci.* **2011**, *4* (4), 1147–1160.

(40) Gu, M.; Lee, J.; Kim, Y.; Kim, J. S.; Jang, B. Y.; Lee, K. T.; Kim, B.-S. *RSC Adv.* **2014**, *4* (87), 46940–46946.

(41) Liu, Q.; Sleightholme, A. E. S.; Shinkle, A. A.; Li, Y.; Thompson, L. T. *Electrochem. Commun.* **2009**, *11* (12), 2312–2315.

(42) Duduta, M.; Ho, B.; Wood, V. C.; Limthongkul, P.; Brunini, V. E.; Carter, W. C.; Chiang, Y.-M. *Adv. Energy Mater.* **2011**, *1* (4), 511–516.

(43) Leung, P.; Li, X.; León, C. P. de; Berlouis, L.; Low, C. T. J.; Walsh, F. C. *RSC Adv.* **2012**, *2* (27), 10125–10156.

(44) Shin, S.-H.; Yun, S.-H.; Moon, S.-H. *RSC Adv.* **2013**, *3* (24), 9095–9116.

(45) Huang, Q.; Li, H.; Graetzel, M.; Wang, Q. *Phys. Chem. Chem. Phys.* **2013**, *15*, 1793–1797.

(46) Fan, F. Y.; Woodford, W. H.; Li, Z.; Baram, N.; Smith, K. C.; Helal, A.; McKinley, G. H.; Carter, W. C.; Chiang, Y.-M. *Nano Lett.* **2014**, *14* (4), 2210–2218.

(47) Yang, Y.; Zheng, G.; Cui, Y. *Energy Environ. Sci.* **2013**, *6* (5), 1552–1558.

(48) Rauh, R. D.; Abraham, K. M.; Pearson, G. F.; Surprenant, J. K.; Brummer, S. B. *J. Electrochem. Soc.* **1979**, *126* (4), 523–527.

(49) Bruce, P. G.; Freunberger, S. A.; Hardwick, L. J.; Tarascon, J.-M. *Nat. Mater.* **2012**, *11* (1), 19–29.

(50) Cuisinier, M.; Cabelguen, P.-E.; Evers, S.; He, G.; Kolbeck, M.; Garsuch, A.; Bolin, T.; Balasubramanian, M.; Nazar, L. F. *J. Phys. Chem. Lett.* **2013**, *4*, 3227–3232.

(51) Barghamadi, M.; Kapoor, A.; Wen, C. *J. Electrochem. Soc.* **2013**, *160* (8), A1256–A1263.

(52) Assary, R. S.; Curtiss, L. A.; Moore, J. S. *J. Phys. Chem. C* **2014**, *118*, 11545–11558.

(53) Vijayakumar, M.; Govind, N.; Walter, E.; Burton, S. D.; Shukla, A.; Devaraj, A.; Xiao, J.; Liu, J.; Wang, C.; Karim, A.; Thevuthasan, S. *Phys. Chem. Chem. Phys.* **2014**, *16*, 10923–10932.

(54) Manthiram, A.; Fu, Y.; Chung, S.-H.; Zu, C.; Su, Y.-S. *Chem. Rev.* **2014**, *114* (23), 11751–11787.

(55) Wu, H.-L.; Huff, L. A.; Gewirth, A. A. *ACS Appl. Mater. Interfaces* **2015**, *7*, 1709–1719.

(56) Aurbach, D.; Pollak, E.; Elazari, R.; Salitra, G.; Kelley, C. S.; Affinito, J. *J. Electrochem. Soc.* **2009**, *156* (8), A694–A702.

(57) Zhang, S. S. *Electrochimica Acta* **2012**, *70*, 344–348.

(58) Rosenman, A.; Elazari, R.; Salitra, G.; Markevich, E.; Aurbach, D.; Garsuch, A. *J. Electrochem. Soc.* **2015**, *162* (3), A470–A473.

(59) Su, Y.-S.; Manthiram, A. *Nat. Commun.* **2012**, *3*, 1166.

(60) Zhou, G.; Pei, S.; Li, L.; Wang, D.-W.; Wang, S.; Huang, K.; Yin, L.-C.; Li, F.; Cheng, H.-M. *Adv. Mater.* **2014**, *26*, 625–631.

(61) Yao, H.; Yan, K.; Li, W.; Zheng, G.; Kong, D.; Seh, Z. W.; Narasimhan, V. K.; Liang, Z.; Cui, Y. *Energy Environ. Sci.* **2014**, *7*, 3381–3390.

(62) Huang, J.-Q.; Zhuang, T.-Z.; Zhang, Q.; Peng, H.-J.; Chen, C.-M.; Wei, F. *ACS Nano* **2015**, *9*, 3002–3011.

(63) Hart, C. J.; Cuisinier, M.; Liang, X.; Kundu, D.; Garsuch, A.; Nazar, L. F. *Chem. Commun.* **2015**, *51* (12), 2308–2311.

(64) Pang, Q.; Kundu, D.; Cuisinier, M.; Nazar, L. F. *Nat. Commun.* **2014**, *5*, 4759.

(65) Tao, X.; Wang, J.; Ying, Z.; Cai, Q.; Zheng, G.; Gan, Y.; Huang, H.; Xia, Y.; Liang, C.; Zhang, W.; Cui, Y. *Nano Lett.* **2014**, *14* (9), 5288–5294.

(66) Wang, Z.; Dong, Y.; Li, H.; Zhao, Z.; Wu, H. B.; Hao, C.; Liu, S.; Qiu, J.; Lou, X. W. *Nat. Commun.* **2014**, *5*, 5002.

(67) Zhang, Q.; Wang, Y.; Seh, Z. W.; Fu, Z.; Zhang, R.; Cui, Y. *Nano Lett.* **2015**, *15*, 3780–3786.

(68) Henderson, W. A.; Brooks, N. R.; Young, V. G. *Chem. Mater.* **2003**, *15* (24), 4685–4690.

(69) Henderson, W. A.; McKenna, F.; Khan, M. A.; Brooks, N. R.; Young, Victor G.; Frech, R. *Chem. Mater.* **2005**, *17* (9), 2284–2289.

(70) Pascal, T. A.; Wujcik, K. H.; Velasco-Velez, J.; Wu, C.; Teran, A. A.; Kapilashrami, M.; Cabana, J.; Guo, J.; Salmeron, M.; Balsara, N.; Prendergast, D. *J. Phys. Chem. Lett.* **2014**, *5*, 1547–1551.

(71) Song, J.; Du, N.; Dai, Y.; Robertson, G. P.; Guiver, M. D.; Thomas, S.; Pinnau, I. *Macromol. Wash. DC U. S.* **2008**, *41*, 7411–7417.

(72) Budd, P. M.; Elabas, E. S.; Ghanem, B. S.; Makhseed, S.; McKeown, N. B.; Msayib, K. J.; Tattershall, C. E.; Wang, D. *Adv. Mater.* **2004**, *16* (5), 456–459.

(73) Choquette, Y.; Brisard, G.; Parent, M.; Brouillette, D.; Perron, G.; Desnoyers, J. E.; Armand, M.; Gravel, D.; Slougui, N. *J. Electrochem. Soc.* **1998**, *145* (10), 3500–3507.

(74) Chen, H.; Zou, Q.; Liang, Z.; Liu, H.; Li, Q.; Lu, Y.-C. *Nat. Commun.* **2015**, *6*, 5877.

(75) Lippert, B. G.; Hutter, J.; Parrinello, M. *Mol. Phys.* **1997**, *92* (3), 477–488.
(76) van de Vondele, J.; Krack, M.; Mohamed, F.; Parrinello, M.; Chassaing, T.; Hutter, J. *Comput. Phys. Commun.* **2005**, *167* (2), 103–128.
(77) van de Vondele, J.; Hutter, J. *J. Chem. Phys.* **2007**, *127* (11), 114105.
(78) Perdew, J. P.; Burke, K.; Ernzerhof, M. *Phys. Rev. Lett.* **1996**, *77* (18), 3865–3868.
(79) Zhang, Y.; Yang, W. *Phys. Rev. Lett.* **1998**, *80* (4), 890–890.
(80) Goedecker, S.; Teter, M.; Hutter, J. *Phys. Rev. B* **1996**, *54* (3), 1703–1710.
(81) Krack, M. *Theor. Chem. Acc.* **2005**, *114* (1-3), 145–152.
(82) Genovese, L.; Deutsch, T.; Goedecker, S. *J. Chem. Phys.* **2007**, *127* (5), 054704.
(83) Grimme, S.; Antony, J.; Ehrlich, S.; Krieg, H. *J. Chem. Phys.* **2010**, *132* (15), 154104.

Chapter 7

Outlook and Conclusion

Outlook

As clean energy technologies grow in diversity, the separation demands inevitably become more exotic and complex. Currently we see two main directions for microporous membrane developments as applied to present and emerging technologies – an exploration of microporosity in 2-D materials as well as more seamless integration of optimized microporous sieving components into composites with controlled architecture.

Microporous 2-D Selective Layers

While graphene has ushered in an era of 2-D materials research,[1,2] it has found limited success in the laboratory as a selective membrane[3,4]. Otherwise impermeable, graphene requires treatment with high-energy ions, electrons and photons to introduce microporosity[3]. All of these techniques are either very limited in scale (e.g., small area) or pore density, with no control over the chemistry of the perforated pore[3]. Significant advances in synthetic methods will be required before their advantages are realized. Nonetheless, microporous monolayer graphene and 2-D materials alike are ideal sieving platforms with high selectivity and permeability. Selectivity can be as sharp as the pore size distribution is narrow. Permeability can be maximized with high pore density and practically non-existent analyte-wall interactions. Despite the noted synthetic limitations, graphene-based sieving membranes have shown their initial promise in gas separation[5–7] and nanofiltration[2,7–9].

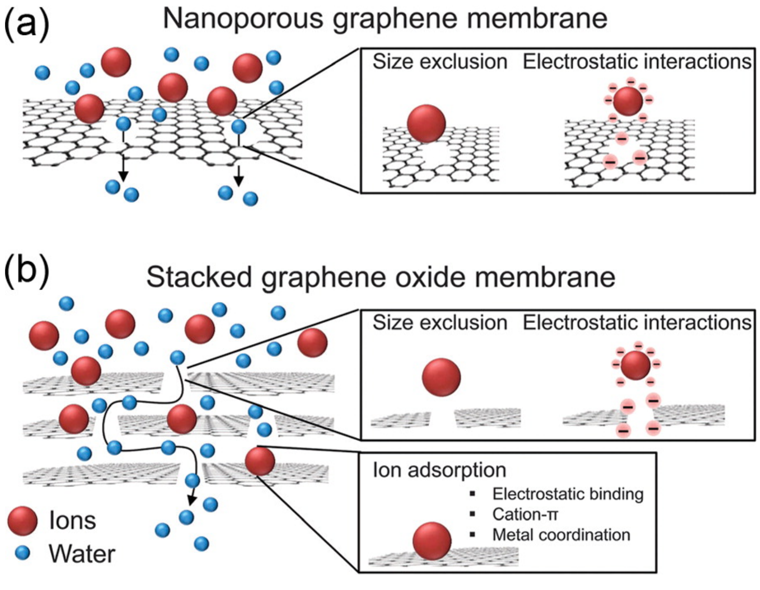

Figure 7.1 The transport pathways in graphene and graphene oxide membranes[3]. The image is reproduced with permission from the cited reference.

It is worth noting that similar 2-D materials have also been prepared to be microporous molecular sieves[10]. They are attractive for the same reason why graphene as a membrane is desirable – ultrathin membrane results in ultrafast kinetics. In particular, there is a recent endeavour to create 2-D polymers[11]. This can be achieved either through synthetic control by confining the growth only to within a 2-D plane, sometimes followed by post-synthetic exfoliation, a method well-known in association with graphene[12]. Covalent organic frameworks (COFs), due to the synthetic control over the bonding arrangements of both of the secondary building units (SBUs), have been successfully synthesized and delaminated as a 2-D material with pores ranging from 1.5 nm to upward of 2 nm[13–16]. Other porous 2-D polymers with only one type of monomer have also been synthesized[17,18], with occasional aid of metal coordination[19–21]. Instead of adopting purely planar moieties as monomers or COF SBUs, the Schlüter and King groups adopted 3-D self-assembled monomers based on π-π interactions. The pre-organization and subsequent polymeration afforded porous sheets amenable to exfoliation[22–24]. Aside from COFs, a separate effort in producing 2-D zeolite sheets is also ongoing. As zeolites are innately 3-D constructs, delamination is necessary to obtain 2-D flat sheets. To date, a select few types of zeolites have been successfully exfoliated[25–27]. Molecular sieve membranes have been fabricated using these nanosheets, via Langmuir-Schaefer deposition[28], as seeds for secondary growth[29], or simply by filtration[26,30]. Interested readers are directed to the literature on the 2-D- material-based membranes[31].

While graphene may be difficult to manipulate, graphene oxide carries less stringent usage conditions. Graphene oxide is partially oxidized graphene flakes commonly produced by subjecting graphite to strongly oxidizing conditions[32]. Unlike all of the previously mentioned microporous materials, the limiting dimension that effects sieving is the gap between the layers, and analyte transport mainly take place in the interlayer solvent environment[33]. The surface is composed of hydrophilic defect sites, pristine hydrophobic graphene surfaces and pores. Though pristine patches of graphene surface exist[34,35], evidence suggests that the oxygen-rich hydrophilic defects sites are highest in areal density and are most likely interacting with analytes[36]. Due to the weak inter-plane interactions, graphene oxide is a rather dynamic system in the absence of cross-linking. The state of hydration[37], annealing conditions[38] and the crosslinking agents[39–42] can all affect the sieving dimension.

Chemistry for Controlling the Structure and Dynamics of Component Interfaces

A major shortcoming with many of the microporous sieving components considered in this dissertation is their poor processibility. Solid-in-solid dispersions are increasingly sought after, where microporous sieving components are dispersed within a matrix. Such dispersions feature incredibly large interfacial area between components. Poor control over these interfaces can yield a percolating network of non-selective pathways with minimal resistance, bypassing any permselective characteristics of either sieving component. In the other extreme, strong binding leads to rigidified chains and pore blockage, isolating the sieving elements from the transport considerations[43]. Thus this calls for proper interface tuning is required to ensure reliable adhesion between these two components. To this end, chemical and thermal treatments have been utilized to enhance the interfacial properties. Heat restructures the polymer chain packing, leading to densified polymer matrix, including near the interface[44–47]. Separately, chemical functionalization, be it tethered to the sieving element or embodied in a small molecule co-dispersant, can also promote interfacial adhesion[44,48–50]. Another example of interfacial engineering was for carbon nanotubes. Though technically not a mixed matrix membrane, carbon nanotube membranes have been fabricated leveraging the high wettability by polystyrene[51]. The active field has been reviewed periodically[43,52].

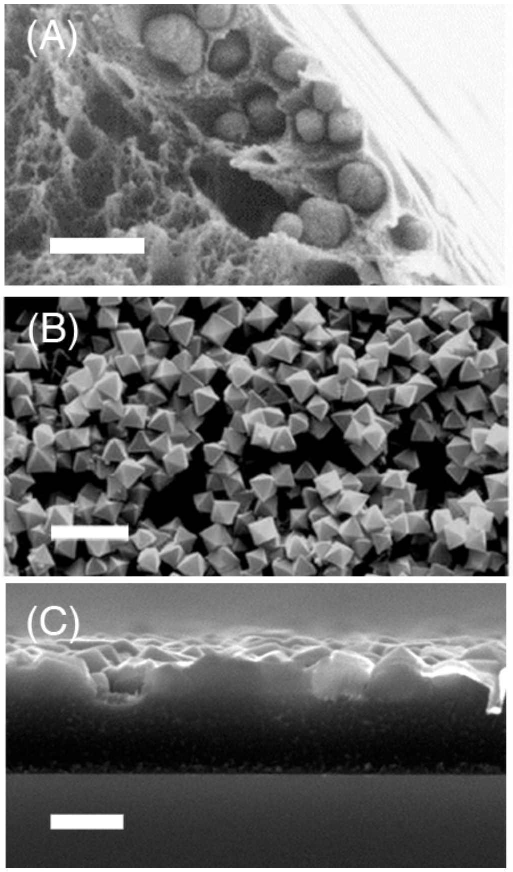

Figure 7.2 Different mixed matrix membrane compositing constructions. (A) Zeolite in polymer solid dispersion mixed matrix membrane[53]. Scale bar is 1 μm. Reprinted from *Journal of Membrane Science*, Vol 288, Husain, S.; Koros, W. J., Mixed matrix hollow fiber membranes made with modified HSSZ-13 zeolite in polyetherimide polymer matrix for gas separation, 195-207, Copyright 2007, with permission from Elsevier. (B) MOF in polymer membrane at high filler loading[54]. Scale bar is 2 μm. Reprinted from *Angewandte Chemie International Edition*, Vol 54, Denny, M. S.; Cohen, S. M., In Situ Modification of Metal–Organic Frameworks in Mixed-Matrix Membranes, 9029-9032, Copyright 2015, with permission from Elsevier. (C) Planar ZIF on polymer membrane, grown *in situ*[55]. Scale bar is 0.2 μm. Reprinted with permission from Meckler, S. M.; Li,

C.; Queen, W. L.; Williams, T. E.; Long, J. R.; Buonsanti, R.; Milliron, D. J.; Helms, B. A. *Chem. Mater.* **2015**. Copyright 2015 American Chemical Society.

In addition to zipping up these defects, an alternative strategy to minimize transport along defects would be to reduce the dimensionality of the defects. By replacing a solid dispersion with a layered structure, interfacial defects are no longer a percolating 3D network but a 2D plane. The added advantage of a layered structure is that the interface is oriented the orthogonal to the gas flow, reducing its negative impact as a result. There have been lots of interests in creating planar ZIF structures, such as at the interfaces of two immiscible liquids[56] and on the hollow membrane interior surface[57]. Our group's recent effort in preparing 2-D layered MOFs from metal oxide precursors are described in Chapter 2-5 of this dissertation and also in publication[55].

Conclusion

In conclusion, in this dissertation I have presented leading-edge research and development of microporous (or molecular sieving) membrane materials across gas, liquid, and ion transports, which are foundational to many clean energy technologies. With such a huge variety of industrially relevant mixtures, be it gas pairs, water and salt, ions of varying sizes, or liquids, it is impossible to conjure up a panacea material that can solve all the problems. Therefore it is without a doubt that tailor-made materials, empowered by the rapid improvements of synthetic techniques, fabrication processes and computational capabilities, will have to be made for each transport case separately, such that perfect size and shape selectivity and frictionless pore wall permits simultaneous high selectivity and conductivity. With the advent of reticular and polymer chemistry, equipped with the foresight of computational chemistry, microporous materials are currently in a golden prolific era, with innumerable new structures being discovered since the emergence of their respective prototypical materials, be it MOFs, COFs, PIMs or TRs. Combined with other long-standing molecular sieves, they form a crucial toolset to tackle the many selective-transport-based technologies of tomorrow, one mixture at a time.

References

(1) Jiang, D.; Cooper, V. R.; Dai, S. *Nano Lett.* **2009**, *9* (12), 4019–4024.

(2) Surwade, S. P.; Smirnov, S. N.; Vlassiouk, I. V.; Unocic, R. R.; Veith, G. M.; Dai, S.; Mahurin, S. M. *Nat. Nanotechnol.* **2015**, *10* (5), 459–464.

(3) Huang, L.; Zhang, M.; Li, C.; Shi, G. *J. Phys. Chem. Lett.* **2015**, *6* (14), 2806–2815.

(4) Liu, G.; Jin, W.; Xu, N. *Chem. Soc. Rev.* **2015**, *44* (15), 5016–5030.

(5) Koenig, S. P.; Wang, L.; Pellegrino, J.; Bunch, J. S. *Nat. Nanotechnol.* **2012**, *7* (11), 728–732.

(6) Wang, L.; Drahushuk, L. W.; Cantley, L.; Koenig, S. P.; Liu, X.; Pellegrino, J.; Strano, M. S.; Bunch, J. S. *Nat. Nanotechnol.* **2015**, *10* (9), 785–790.

(7) Celebi, K.; Buchheim, J.; Wyss, R. M.; Droudian, A.; Gasser, P.; Shorubalko, I.; Kye, J.-I.; Lee, C.; Park, H. G. *Science* **2014**, *344* (6181), 289–292.

(8) O'Hern, S. C.; Jang, D.; Bose, S.; Idrobo, J.-C.; Song, Y.; Laoui, T.; Kong, J.; Karnik, R. *Nano Lett.* **2015**, *15* (5), 3254–3260.

(9) O'Hern, S. C.; Boutilier, M. S. H.; Idrobo, J.-C.; Song, Y.; Kong, J.; Laoui, T.; Atieh, M.; Karnik, R. *Nano Lett.* **2014**, *14* (3), 1234–1241.

(10) Zhao, Y.; Xie, Y.; Liu, Z.; Wang, X.; Chai, Y.; Yan, F. *Small* **2014**, *10* (22), 4521–4542.

(11) Sakamoto, J.; van Heijst, J.; Lukin, O.; Schlüter, A. D. *Angew. Chem. Int. Ed.* **2009**, *48* (6), 1030–1069.

(12) Novoselov, K. S.; Geim, A. K.; Morozov, S. V.; Jiang, D.; Zhang, Y.; Dubonos, S. V.; Grigorieva, I. V.; Firsov, A. A. *Science* **2004**, *306* (5696), 666–669.

(13) Côté, A. P.; Benin, A. I.; Ockwig, N. W.; O'Keeffe, M.; Matzger, A. J.; Yaghi, O. M. *Science* **2005**, *310* (5751), 1166–1170.

(14) Zwaneveld, N. A. A.; Pawlak, R.; Abel, M.; Catalin, D.; Gigmes, D.; Bertin, D.; Porte, L. *J. Am. Chem. Soc.* **2008**, *130* (21), 6678–6679.

(15) Berlanga, I.; Ruiz-González, M. L.; González-Calbet, J. M.; Fierro, J. L. G.; Mas-Ballesté, R.; Zamora, F. *Small* **2011**, *7* (9), 1207–1211.

(16) Colson, J. W.; Woll, A. R.; Mukherjee, A.; Levendorf, M. P.; Spitler, E. L.; Shields, V. B.; Spencer, M. G.; Park, J.; Dichtel, W. R. *Science* **2011**, *332* (6026), 228–231.

(17) Grill, L.; Dyer, M.; Lafferentz, L.; Persson, M.; Peters, M. V.; Hecht, S. *Nat. Nanotechnol.* **2007**, *2* (11), 687–691.

(18) Bieri, M.; Treier, M.; Cai, J.; Aït-Mansour, K.; Ruffieux, P.; Gröning, O.; Gröning, P.; Kastler, M.; Rieger, R.; Feng, X.; Müllen, K.; Fasel, R. *Chem. Commun.* **2009**, No. 45, 6919.

(19) Amo-Ochoa, P.; Welte, L.; González-Prieto, R.; Sanz Miguel, P. J.; Gómez-García, C. J.; Mateo-Martí, E.; Delgado, S.; Gómez-Herrero, J.; Zamora, F. *Chem. Commun.* **2010**, *46* (19), 3262.

(20) Abel, M.; Clair, S.; Ourdjini, O.; Mossoyan, M.; Porte, L. *J. Am. Chem. Soc.* **2011**, *133* (5), 1203–1205.

(21) Bauer, T.; Zheng, Z.; Renn, A.; Enning, R.; Stemmer, A.; Sakamoto, J.; Schlüter, A. D. *Angew. Chem. Int. Ed.* **2011**, *50* (34), 7879–7884.

(22) Kissel, P.; Erni, R.; Schweizer, W. B.; Rossell, M. D.; King, B. T.; Bauer, T.; Götzinger, S.; Schlüter, A. D.; Sakamoto, J. *Nat. Chem.* **2012**, *4* (4), 287–291.

(23) Kissel, P.; Murray, D. J.; Wulftange, W. J.; Catalano, V. J.; King, B. T. *Nat. Chem.* **2014**, *6* (9), 774–778.

(24) Kory, M. J.; Wörle, M.; Weber, T.; Payamyar, P.; Poll, S. W. van de; Dshemuchadse, J.; Trapp, N.; Schlüter, A. D. *Nat. Chem.* **2014**, *6* (9), 779–784.

(25) Corma, A.; Fornes, V.; Pergher, S. B.; Maesen, T. L. M.; Buglass, J. G. *Nature* **1998**, *396* (6709), 353–356.

(26) Varoon, K.; Zhang, X.; Elyassi, B.; Brewer, D. D.; Gettel, M.; Kumar, S.; Lee, J. A.; Maheshwari, S.; Mittal, A.; Sung, C.-Y.; Cococcioni, M.; Francis, L. F.; McCormick, A. V.; Mkhoyan, K. A.; Tsapatsis, M. *Science* **2011**, *334* (6052), 72–75.

(27) Choi, M.; Na, K.; Kim, J.; Sakamoto, Y.; Terasaki, O.; Ryoo, R. *Nature* **2009**, *461* (7261), 246–249.

(28) Rangnekar, N.; Shete, M.; Agrawal, K. V.; Topuz, B.; Kumar, P.; Guo, Q.; Ismail, I.; Alyoubi, A.; Basahel, S.; Narasimharao, K.; Macosko, C. W.; Mkhoyan, K. A.; Al-Thabaiti, S.; Stottrup, B.; Tsapatsis, M. *Angew. Chem. Int. Ed.* **2015**, *54* (22), 6571–6575.

(29) Agrawal, K. V.; Topuz, B.; Pham, T. C. T.; Nguyen, T. H.; Sauer, N.; Rangnekar, N.; Zhang, H.; Narasimharao, K.; Basahel, S. N.; Francis, L. F.; Macosko, C. W.; Al-Thabaiti, S.; Tsapatsis, M.; Yoon, K. B. *Adv. Mater.* **2015**, *27* (21), 3243–3249.

(30) Agrawal, K. V.; Topuz, B.; Jiang, Z.; Nguenkam, K.; Elyassi, B.; Francis, L. F.; Tsapatsis, M.; Navarro, M. *AIChE J.* **2013**, *59* (9), 3458–3467.

(31) Kim, W.; Nair, S. *Chem. Eng. Sci.* **2013**, *104*, 908–924.

(32) Chen, D.; Feng, H.; Li, J. *Chem. Rev.* **2012**, *112* (11), 6027–6053.

(33) Huang, L.; Li, Y.; Zhou, Q.; Yuan, W.; Shi, G. *Adv. Mater.* **2015**, *27* (25), 3797–3802.

(34) Nair, R. R.; Wu, H. A.; Jayaram, P. N.; Grigorieva, I. V.; Geim, A. K. *Science* **2012**, *335* (6067), 442–444.

(35) Boukhvalov, D. W.; Katsnelson, M. I.; Son, Y.-W. *Nano Lett.* **2013**, *13* (8), 3930–3935.

(36) Zhang, Q.; Zheng, H.; Geng, Z.; Jiang, S.; Ge, J.; Fan, K.; Duan, S.; Chen, Y.; Wang, X.; Luo, Y. *J. Am. Chem. Soc.* **2013**, *135* (33), 12468–12474.

(37) Joshi, R. K.; Carbone, P.; Wang, F. C.; Kravets, V. G.; Su, Y.; Grigorieva, I. V.; Wu, H. A.; Geim, A. K.; Nair, R. R. *Science* **2014**, *343* (6172), 752–754.

(38) Qiu, L.; Zhang, X.; Yang, W.; Wang, Y.; Simon, G. P.; Li, D. *Chem. Commun.* **2011**, *47* (20), 5810.

(39) Hu, M.; Mi, B. *Environ. Sci. Technol.* **2013**, *47* (8), 3715–3723.

(40) Han, Y.; Jiang, Y.; Gao, C. *ACS Appl. Mater. Interfaces* **2015**, *7* (15), 8147–8155.

(41) Hung, W.-S.; Tsou, C.-H.; De Guzman, M.; An, Q.-F.; Liu, Y.-L.; Zhang, Y.-M.; Hu, C.-C.; Lee, K.-R.; Lai, J.-Y. *Chem. Mater.* **2014**, *26* (9), 2983–2990.

(42) Srinivas, G.; Burress, J. W.; Ford, J.; Yildirim, T. *J. Mater. Chem.* **2011**, *21* (30), 11323–11329.

(43) Chung, T.-S.; Jiang, L. Y.; Li, Y.; Kulprathipanja, S. *Prog. Polym. Sci.* **2007**, *32* (4), 483–507.

(44) Widjojo, N.; Chung, T.-S.; Kulprathipanja, S. *J. Membr. Sci.* **2008**, *325* (1), 326–335.

(45) Jiang, L. Y.; Chung, T. S.; Kulprathipanja, S. *J. Membr. Sci.* **2006**, *276* (1–2), 113–125.

(46) Jiang, L. Y.; Chung, T. S.; Kulprathipanja, S. *AIChE J.* **2006**, *52* (8), 2898–2908.

(47) Vu, D. Q.; Koros, W. J.; Miller, S. J. *J. Membr. Sci.* **2003**, *211* (2), 311–334.

(48) Vankelecom, I. F. J.; Van den broeck, S.; Merckx, E.; Geerts, H.; Grobet, P.; Uytterhoeven, J. B. *J. Phys. Chem.* **1996**, *100* (9), 3753–3758.

(49) Yong, H. H.; Park, H. C.; Kang, Y. S.; Won, J.; Kim, W. N. *J. Membr. Sci.* **2001**, *188* (2), 151–163.

(50) Venna, S. R.; Lartey, M.; Li, T.; Spore, A.; Kumar, S.; Nulwala, H. B.; Luebke, D. R.; Rosi, N. L.; Albenze, E. *J Mater Chem A* **2015**, *3* (9), 5014–5022.

(51) Hinds, B. J.; Chopra, N.; Rantell, T.; Andrews, R.; Gavalas, V.; Bachas, L. G. *Science* **2004**, *303* (5654), 62–65.

(52) Goh, P. S.; Ismail, A. F.; Sanip, S. M.; Ng, B. C.; Aziz, M. *Sep. Purif. Technol.* **2011**, *81* (3), 243–264.

(53) Husain, S.; Koros, W. J. *J. Membr. Sci.* **2007**, *288* (1–2), 195–207.

(54) Denny, M. S.; Cohen, S. M. *Angew. Chem. Int. Ed.* **2015**, *54* (31), 9029–9032.

(55) Meckler, S. M.; Li, C.; Queen, W. L.; Williams, T. E.; Long, J. R.; Buonsanti, R.; Milliron, D. J.; Helms, B. A. *Chem. Mater.* **2015**.

(56) Ameloot, R.; Vermoortele, F.; Vanhove, W.; Roeffaers, M. B. J.; Sels, B. F.; De Vos, D. E. *Nat. Chem.* **2011**, *3* (5), 382–387.

(57) Brown, A. J.; Brunelli, N. A.; Eum, K.; Rashidi, F.; Johnson, J. R.; Koros, W. J.; Jones, C. W.; Nair, S. *Science* **2014**, *345* (6192), 72–75.